Research and Development in Novel Alternative Renewable Energy Technology

Zheming Wen

A thesis is submitted in partial fulfilment of the requirements of Bournemouth University for the degree of Doctor of Philosophy

October 2015

Faculty of Science and Technology

Bournemouth University

Abstract

Fossil fuels have become the main energy source for human after the Industrial Revolution. However, with ever-increasing energy consumption, they are not sustainable in terms of their finite reserves, pollutions to the environment and contributions to climate change. Driven by these problems, the EU and UK have together set a mutual objective to generate renewable energy as 20% of the total energy supply by 2020. This research project, fully funded by Future Energy Source Ltd, is a direct response to the needs of developing novel alternative renewable energy technologies.

This project concerns about the research and development of a large scale flat plate solar collector (LSFPSC) with serpentine tubing that can be fully integrated into building envelops. The project work focuses on design improvements for increasing thermal performance, enhancing reliability and minimising costs of the LSFPSC. This is accomplished by employing a three-stage approach combining both experimental testing and simulation studies.

An experimental facility was designed and built for testing the LSFPSC prototype with comprehensive monitoring equipment for collecting important data such as temperature and flow rates. The 1st stage experimental results and mathematical analyses showed that the unglazed LSFPSC prototype has an operating efficiency of 28.55%.

In the 2nd stage, research was done to propose suitable improvements which were then tested experimentally. These improvements include changing the heat transfer mechanism between the absorber and the circulation system, enhancing the bond conductivity and minimising convective losses. The improved prototype showed increased operating efficiencies of 43.50% (unglazed configuration) and 46.07% (glazed configuration).

In the 3rd stage, the experimental and analysis data from the 2nd stage were employed to design TRNSYS simulation that was used to simulate the LSFPSC's performance using weather data from 36 different locations in 22 countries. The simulation results showed the LSFPSC is capable of producing mean useful output of 1.29 GJ/m^2/year (glazed) and 1.00 GJ/m^2/year (unglazed). Further economic evaluation showed the LSFPSC has much shorter payback period (2.4 to 6.5 years) than the typical commercial flat plate collectors (8 to 12 years) indicating that the LSFPSC is an economical solution for low/medium temperature applications.

List of Publications

Journal Publications

1. **Wen Z.,** Khan Z., Camfield, T., 2015. *Experimental study of a large scale flat plate solar collector with continuous serpentine tubing configuration for building integration.* Energy for Sustainable Development (Submitted)
2. **Wen Z.,** Khan Z., Camfield, T., 2015. *Simulation study of a large scale flat plate solar collector with continuous serpentine tubing configuration and building envelope integration for domestic hot water pre-heating and space heating*. Solar Energy (Submitted)

Abstracts in Conference Proceedings

3. Khan Z., **Wen Z.,** 2014. *An Experimental Study of a Novel Solar-Thermal System for Domestic and Commercial Applications*. ASME 2014 International Mechanical Engineering Congress. 14th – 20th November 2014, Montreal, Canada.
4. **Wen Z.,** Khan Z., Camfield T., Hadfield, M., 2014. *Research and Development in Novel Alternative Renewable Energy Technology*. 6th University Annual PG Conference 22nd – 23rd January 2014, Bournemouth University

Poster Conferences

5. **Wen Z.,** Khan Z., Camfield T., Hadfield, M., 2013. *Research and Development in Novel Alternative Renewable Energy Technology*. Prize Winner of the 6th PGR Poster Conference, 22nd May 2013, School of Design Engineering and Computing, Bournemouth University.
6. **Wen Z.,** Khan Z., Camfield T., Hadfield, M., 2014. *Research and Development in Novel Alternative Renewable Energy Technology*. Prize Winner of the 6th University Annual PG Conference 22nd – 23rd January 2014, Bournemouth University
7. **Wen Z.,** Khan Z., Camfield T., Hadfield, M., 2014. *Efficiency Enhancement through Thermal Optimisation and Materials Design for a Novel Renewable Energy Technology*. 7th PGR Poster Conference, 21st May 2014, School of Design Engineering and Computing, Bournemouth University.

Table of Contents

List of Figures

List of Tables

Nomenclature

A	area	m^2
C_P	specific heat capacity	J/K
D	diameter	m
F	view factor	
F_R	collector removal factor	
G	irradiance	W/m^2
I	solar irradiation	W/m^2
Nu	Nusselt number	
Pr	Prandtl number	
Q	heat transfer rate	W
Ra	Rayleigh number	
Re	Reynolds number	
T	temperature	K
U	heat loss coefficient	W/m^2K
V	velocity	$m\ s^{-1}$
b	bond width	m
g	gravitational constant	$m\ s^{2}$
h	heat transfer coefficient	W/m^2K
k	thermal conductivity	$W/m\ K$
$\dot{m}$	mass flow rate	$kg\ s^{-1}$
v	kinematic viscosity	$m^2\ s^{-1}$

Greek symbols

α	absorptivity	
α'	thermal diffusivity	$m^2\ s^{-1}$
ε	emissivity	
λ	wavelength	μm
η	efficiency	
σ_{sb}	Stefan-Boltzmann constant	$5.67 \times 10^{-8}\ W/m^2K^4$
τ	transmittance	
β	collector tilt	deg
β'	volumetric coefficient of expansion	$1/K$
γ	bond thickness	m
δ	thickness	m

Subscripts

ab	absorber
a/am	ambient
b	bond
bot	bottom
c	collector
ci	collector inlet
$circ$	circulation system
co	collector outlet
$cond$	conduction
$conv$	convection
ex	exchange chamber
f	heat transfer fluid
gl	glazing
htf	heat transfer fluid
i	inlet
in	input
inf	infrared radiation
ins	insulation
L	loss
o	outlet
out	output
p	pipe
pl	plate
rad	radiation
$refl$	reflection
st	storage tank
seg	segment
u	useful energy
w	wind

Abbreviations

$LSFPSC$	large scale flat plate solar collector
DHW	domestic hot water
SH	space heating
GL	glazed
$UNGL$	unglazed

Acknowledgements

I would like to express my earnest gratitude to Dr. Zulfiqar Khan, who provided me the opportunity to work on this exciting project. His continuous support and guidance have been a strong source of inspiration and confidence for me to overcome obstacles to pursue my goals in academic research.

I would also like to thank Mr Tony Camfield and Mr Robert Heffer, Future Energy Source Ltd, for fully funding this project and providing facility to conduct large scale experiments on prototype testing.

I am also thankful to Mr Brian Camfield. His experience in Mechanical and Electrical Engineering was vital in setting up the experiments.

I also appreciate the general support from Professor Mark Hadfield.

At last I would like to show my deepest gratitude to my parents for their continuous and selfless supports.

Author’s Declaration

This report contains the original work of the author except otherwise indicated. All contents of this report except materials from external sources are subjected to confidentiality as set out within the agreement between BU and FES Ltd.

CHAPTER 1

1. Introduction

1.1 A Brief History of Energy Use in Human Society

Energy has played a fundamental role in the development of human civilization, as its use is essential for survival and shapes the conditions of human life. Certainly, production and consumption of energy are among the most important activities in the modern world, and the evolution of civilization throughout history has been directly linked to available energy sources that can be converted for human use (Ostwald, 1907).

Primitive man, found in East Africa 1 million years ago, simply converted food (chemical energy) into muscle power (kinetic energy) and calories (heat energy) for his survival. His daily consumption of energy is estimated by Cook (1971) to be 2000 kcal. People gradually learned to use the bow and arrow (mechanical energy) to hunt animals, and later began using domesticated animals to produce crops from lands. With this discovery of agriculture, humans started producing more energy than necessary for survival, moved out of caves into intentionally constructed homes with more comforts, and began to use some of their time in ways other than for pure survival. People started to devote time into science, arts and commerce etc., all of which further led to the advancement of civilization (Ristinen and Kraushaar, 2006). Figure 1.1 shows the different energy consumption demands at different historical points.

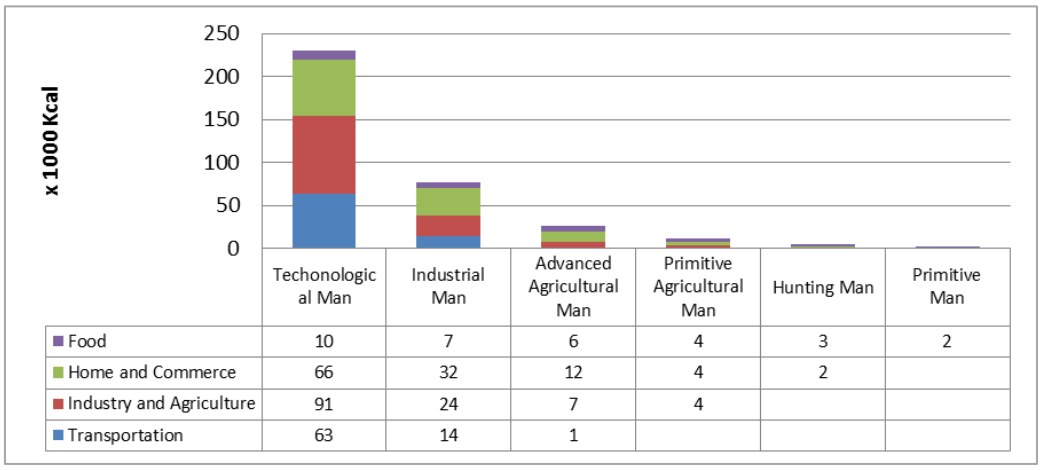

	Techonological Man	Industrial Man	Advanced Agricultural Man	Primitive Agricultural Man	Hunting Man	Primitive Man
Food	10	7	6	4	3	2
Home and Commerce	66	32	12	4	2	
Industry and Agriculture	91	24	7	4		
Transportation	63	14	1			

Figure 1.1: Estimated human energy consumption demands per capita at different historical points (Cook, 1971)

The expansion of civilization has demanded increasing energy consumption to meet the needs of changing living conditions and increasing populations. This increased demand has inevitably led to the advancement of energy production technologies. The vertical waterwheel was discovered around 200 AD and was employed in water mills to utilize water energy (kinetic energy) in production (mechanical energy). Water mills were used to perform a variety of early industrial processes such as crushing grains, smelting and shaping metal, sawing wood, and so forth. Water mills grew to become a central

element in Western technology (Reynolds, 2002). During the Middle Ages, numerous large water mills were built across Europe, along with dams and canals, displaying a basic energy system that consisted of energy production units, energy transportation channels and energy storage facilities. The advancement in water mills indicated the industrial dependence on water energy at that time to meet the expanding demands of human civilization.

However, geographical inflexibility limited the use of water energy. Another form of water energy, steam energy, was found to have more geographical flexibility and was more versatile in meeting different energy demands. The age of steam, began with the invention of the first successful steam engine by Thomas Newcomen in 1712. Improved by James Watt in the late 1700s, the steam engine flourished as an energy production source throughout the nineteenth century. Steam energy powered the Industrial Revolution, not only by replacing water energy in production and manufacturing, but also by leading to the development of a new transportation system, railways. The Industrial Revolution, the cradle of capitalism, shaped human society into a new form and changed people's lifestyles dramatically. It is observed by Barbour et al. (1982) that the usage of steam energy established a permanent link between fossil fuels and industrialization.

1.2 Current Energy Problems

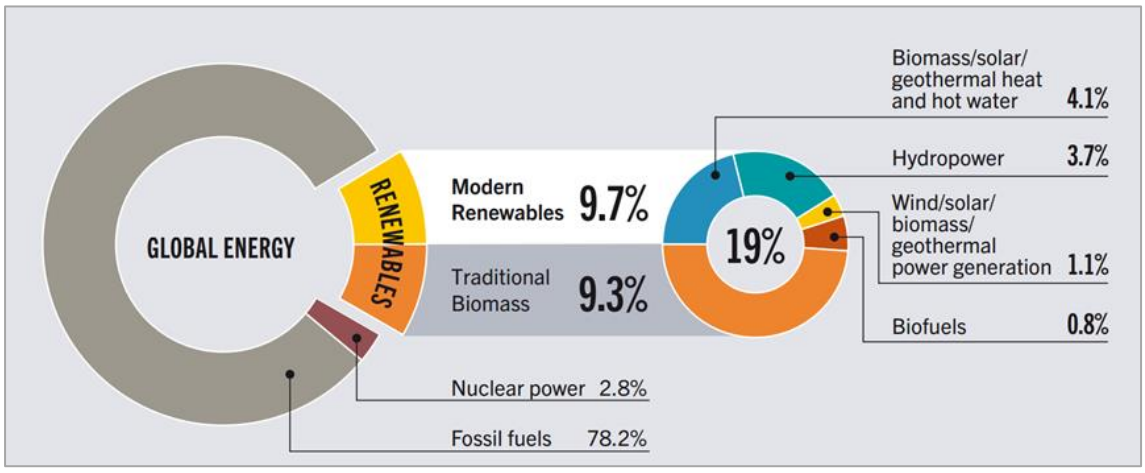

Figure 1.2: Global Energy Market Shares By Technologies in 2011 (REN21, 2012)

Fossil fuels are now the most important energy source for human civilisation, accounting for 78.2% of the current energy market, as shown in Figure 1.2. Fossil fuels are used in powering transportation, producing chemicals and polymers, and for the generation of electricity. Resulting from our dependence on fossil fuels, there are several existing and emerging problems that must be considered.

One such problem is related to climate change. Carbon dioxide (CO_2) is a by-product of the combustion of fossil fuels. Statistics reveal that fossil fuels contributed approximately 63% of global human-induced CO_2 emissions during 2000 – 2004, where 36% were from oil, 35% from coal and 20% from natural gas (Raupach et al., 2007). CO_2 is known to be a "greenhouse gas" that contributes to global warming by trapping heat in the earth's atmosphere. Global warming can increase the average temperature

on the earth sufficiently to cause substantial melting of the polar ice caps. This in turn can lead to a rise in sea level and threaten the very existence of our coastal cities. Droughts, flood and other detrimental ecological changes can also be caused by global warming.

A second set of environment problems results from the extraction, refining and usage of fossil fuels. During these processes, numerous air and water pollutants are created, with clear negative effects to the environment as a consequence. Additionally, activities like coal mining can cause mine subsidence, land disturbance and underground water pollution. Coal contains a range of impurities, among which the most notorious one is sulphur. Combustion of coal can release detrimental gaseous oxides of sulfur (SO_2) and nitrogen (NO_x), toxic hydrides (i.e. HCN) and nitrides (i.e. SNO_3) and also particulate emissions that can severely damage the human respiratory system (WCA, 2013). Extraction and combustion of oil causes similar problems; however, at a level less severe than for coal, mostly due to advanced refinery technologies. However, a serious environmental problem associated with oil is oil spillage from tankers or other transportation methods. When oil is released directly into environment, it can contaminate water and disturb marine ecology. It is noticed by Dunnet et al. (1982) that most birds affected by an oil spill will die unless there is human intervention.

Thirdly, the earth holds a finite capacity of fossil fuel reserves. The formation of fossil fuels takes millions of years through natural processes, such as anaerobic decomposition of buried organic materials, and sometimes this formation can exceed 650 million years to be accomplished (Mann et al., 2005). Fossil fuels on the earth are thus considered to be non-renewable in terms of the human lifespan. Table 1.1 shows proved reserve and human annual consumption amounts of oil, coal and natural gas in 2010 (BP, 2011).

Table 1.1: Estimated depletion time of fossil fuels based on proved reserves and world annual consumption amounts in 2010 (BP, 2011)

	Oil	Gas	Coal
Proved Reserves	1383.2 billion barrels	187.1 trillion cubic metres	860.94 trillion tons
Annual Consumption	31.89 billion barrels	3.17 trillion cubic metres	6.93 trillion tons
Estimated Depletion Time	43.37 years	59.04 years	124.21 years

The estimated depletion times, as shown in Table 1.1, are not realistic, as annual consumption will vary in the future, and new reserves may be discovered. However it is instructive to show that based on our current consumption rate, two of our major fossil fuels (oil and gas) will deplete in less than one century.

Yet a forth problem is associated directly with human society. Fossil fuels, oil in particular, play a very important role in our economics, and their prices can influence our daily lives. Political activities, commercial activities and wars can impose

fluctuations on oil prices. By the end of 2012, oil price has increased about four times more than that in 2000, illustrated in Figure 1.3 (OPEC, 2013). Even though he oil price has dropped significantly in the past few years, it may rise up in the future.

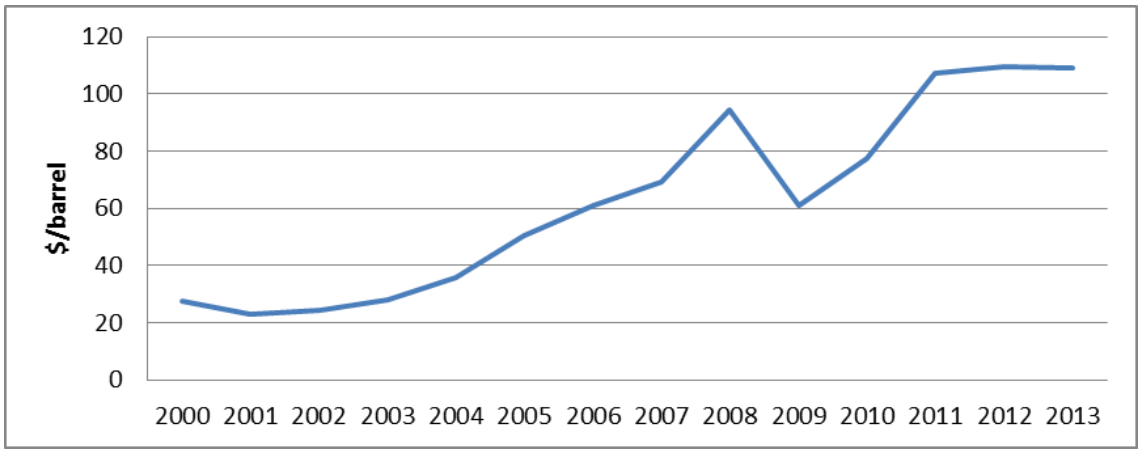

Figure 1.3: OPEC Oil Reference Basket Price from 2000 to 2013 (OPEC, 2013)

During these ten years, two nationwide fuel protests took place in the UK. The protests in 2005 caused panic buying from people that led to consequential oil supply disruptions (Laville, 2005). Similar protests took places in other countries, indicating that changes of oil prices can cause unhappiness and instability in our society. The resource shortage and higher costs of extracting oil from unconventional sites will also be expected to increase oil prices in the future. When oil reserves reach certain levels close to exhaustion, it will no longer be affordable for the public. This may lead to chaos in society or even collapse of our economic system.

It is obvious that the energy provided by fossil fuels is not sustainable for the development of human civilization. Therefore, finding cheap alternative energy sources are essential for our future.

1.3 Alternative Energy Sources

Nuclear energy is an important energy source. Current nuclear energy is generated by sustained nuclear fission of uranium producing radioactive wastes that are hazardous to people and the environment. If nuclear fusion can be employed to generate energy safely, it can be a very promising sustainable energy source for the future, since it uses hydrogen as fuel. However, due to the technical difficulties of controlling and containing the power of nuclear fusion, it may take another few decades before nuclear fusion energy can be utilised safely. In the past decades, humans have developed technologies to employ other renewable energy sources, such as wind power, hydropower, biomass, bio-fuel, geothermal energy, tidal energy and solar energy. Solar energy appears to be the most promising energy source, and its potential is recognized by the International Energy Agency (IEA): "the development of affordable, inexhaustible and clean solar energy technologies will have huge longer-term benefits. It will increase countries' energy security through reliance on an indigenous, inexhaustible and mostly import-independent resource, enhance sustainability, reduce pollution, lower the costs

of mitigating climate change, and keep fossil fuel prices lower than otherwise. These advantages are global" (IEA, 2011).

The potential of solar energy is also recognized by governments in many countries. Many governments have invested public funds in the development of solar power stations and encourage installation of solar energy facilities on residential buildings. One example is the UK government, which is currently employing a feed-in tariff scheme to pay incentives to citizens who install solar photovoltaic (PV) electricity generating facilities on their houses (EST, 2013). Another example is an incentive plan implementing by the Chinese government to partially subsidize the costs of purchasing solar water heating systems for its citizens (CCGP, 2012).

1.4 Current Solar Industry

With supports from governments, the usage of solar PV has increased significantly in the past decade. The electricity produced by solar PV has increased from 0.99 TWh (terawatt-hour) in 1996 to 87.11 TWh in 2010. That's an increase from less than 0.01% to 0.41% of total world electricity generation, as shown in Figure 1.4 (BP, 2011)

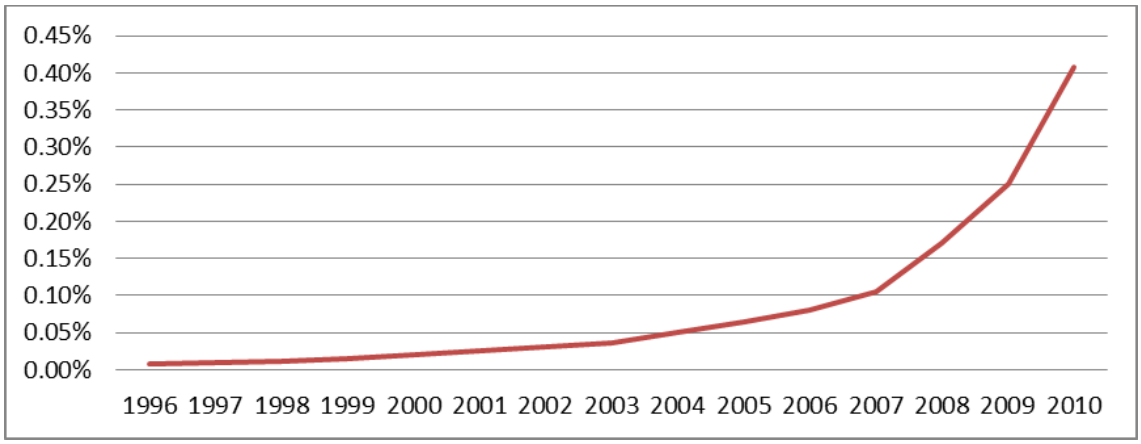

Figure 1.4: % of Solar Electricity in Total World Electricity Generation (BP, 2011)

Similar growth of usage was seen in solar thermal systems. By the end of 2010, the global annual installed capacities of solar heat collectors have increased 6 times (from 6.5GW_{th} to 40.5GW_{th}, illustrated in Figure 1.5) since 2000 (Weiss and Mahthner, 2012)

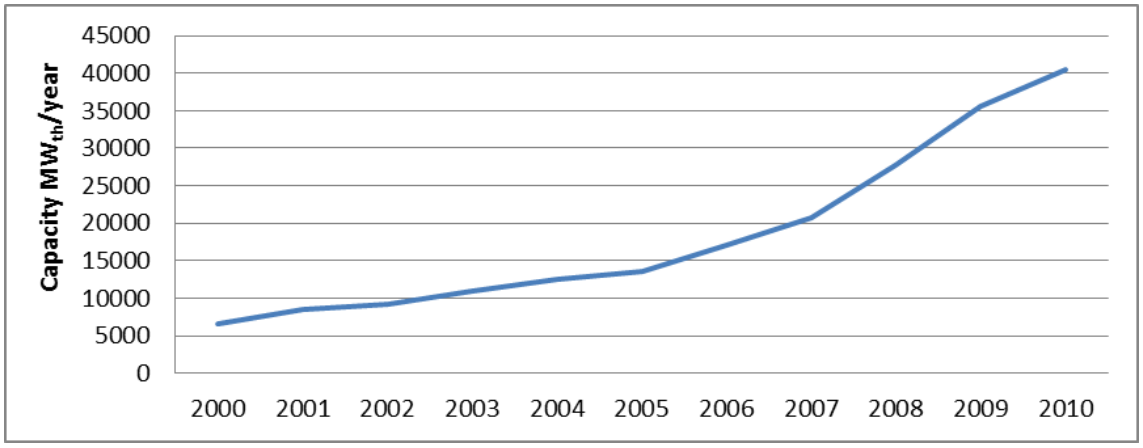

Figure 1.5: Annual Installed Capacities of Solar Heat Collectors (Weiss and Mahthner, 2012)

However, comparing to fossil fuels, the costs of solar PV technologies are still too high to be affordable for the public without government supports. Table 1.2 shows the typical costs of electricity produced by conventional energy sources (nuclear and fossil fuels) (NEA and OECD, 2010). Table 1.3 shows estimated typical capital costs of commissioning and energy costs of solar PV and solar thermal from a comprehensive report conducted by Renewable Energy Policy Network for the 21st Century (REN21) in 2012. Based on the data from a detailed survey conducted by Nuclear Energy Agency (NEA) and Organisation for Economic Co-operation and Development (OCED),

Table 1.2: Costs of Electricity Generated by Nuclear and Fossil Fuels (NEA and OECD, 2010)

	Typical Energy Costs £/kWh
Nuclear	0.07
Coal	0.07
Gas	0.06

Table 1.3: Capital Costs and Energy Costs of Solar PV and Solar Thermal (REN21, 2012)

Solar PV	Capital Cost £/kW		Typical Energy Costs £/kWh	
	Min	Max	Min	Max
Rooftop	1,612	2,126	0.14	0.29
Utility Scale	1,190	1,528	0.13	0.24
Solar Thermal	**Capital Cost £/kW**		**Typical Energy Costs £/kWh**	
	Min	Max	Min	Max
Concentrating Solar Power	2,932	6,842	0.12	0.19
Solar Thermal	**Capital Cost £/kW_{th}**		**Typical Energy Costs £/kWh Equivalent**	
	Min	Max	Min	Max
Water Heating (China)	96	412	0.01	0.18
Water and Space Heating	403	1,375	0.03	0.47

It is clear that the costs of solar PV energy are 2 – 4 times more expensive than conventional energy while solar thermal energy could be the cheapest. Moreover, the capital costs of solar PV are much higher than solar thermal, which is mainly due to their energy-intensive extraction, production and manufacturing processes together with their usage of expensive rare earth minerals (REM). The prices of REM have soared in the past decade and are expected to increase further with China's recent restrictions on their REM exports since China is responsible for more than 95% of the REM used in solar PV, reported by Vidal (2012). As a competitive alternative to Solar PV, solar thermal technology has shown significant increase in usage during the past decade (Figure 1.6).

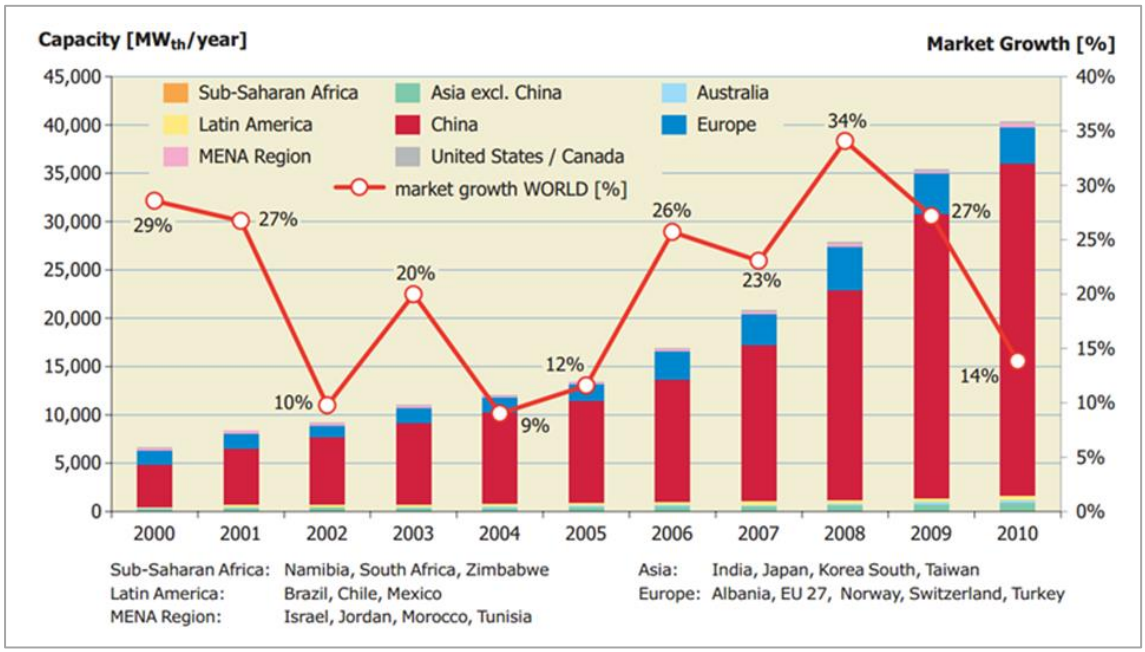

Figure 1.6: Annual Installed Capacity of Solar Heat Collector from 2000 – 2010 (IEA, 2011)

Solar thermal technologies are commonly used in heating/cooling applications and are also capable in electricity generation.

1.5 Potentials of Building-Integrated Solar Heating Systems

About 40% of the world's energy is used in the building sector for the purpose of heating, cooling, ventilation and sanitary hot water of which two-thirds are consumed by households where heating alone accounts for more than 50% (IEA, 2007). Apart from space heating, hot water is also used for many domestic purposes (e.g. showers, utensils) and water is generally heated by commercial fuels (e.g. electricity, natural gas) in urban areas. In this regard, the utilisation of solar energy through solar water heating systems can contribute greatly to reduce the usage of fossil fuels and their associated environmental problems. Additionally, comparing to centralised energy generation methods (i.e. power stations), the utilisation of decentralised solar water heating systems for residential applications can provide savings on energy transportation and increase energy availability for users in remote areas.

Many of the commercially available solar heat collectors are manufactured as individual units to be installed on rooftops using mounting racks or supportive frames which could incur high material and installation costs at the same time intruding aesthetic beauty. Researches have shown that the mass production and the integration of solar collectors into the building envelope (e.g. replacing the classic facade or the roof elements) can lower the costs per unit area and increase the quantity of energy for harvesting with larger collecting area (Medved et al., 1994, Bartelsen et al., 1999, Arkar et al., 1999, Palmero-Marrero and Oliveira, 2006). It is also shown that the solar collectors can be integrated into the building envelope with a range of colours to comply with other elements to retain aesthetic values at the same time producing satisfactory outputs (Tripanagnostopoulos et al., 2000, Kalogirou, 2004a). Furthermore, if no complicated techniques or coupling/bonding elements are to be employed to integrate the solar collectors into the building envelope, the installation process would be quicker and simpler which reduces material and labouring costs.

1.6 Motivation for Work

The development of a low-cost solar heating system that is capable of being fully integrated into the building envelope with non-complicated installation techniques can generate significant economic benefits by providing an affordable and sustainable energy solution. The research and development works on a novel solar thermal system will also make great contribution to knowledge in the fields of solar industry, architectural design and thermodynamics.

1.7 Research Question

The research question of this project is: how solar heat collector can be designed to utilise roof as absorber to harvest solar energy efficiently and cost-effectively with flexible scalability and minimal maintenance?

1.8 Aims and Objectives

This project is concerned about improving the performance of a roof-integrated novel solar heat collector using an experimental approach with mathematical modelling and evaluating its performance under various conditions using computer simulation. The improved solar collector will have the advantages of easier installation, cheaper costs and less maintenance over those commercially available ones with the capability of producing large amount of outputs in different regions of the world. The objectives listed below were set to be achieved by the end of this project:

1. Design and develop an experimental facility that can be employed to conduct indoor tests for the novel solar collector prototype
2. Design and develop a monitoring mechanism for capturing the significant performance parameters of the prototype
3. Investigate and understand how various parameters and components' design contribute to the prototype performance
4. Measure the prototype performance experimentally and analyse the acquired data to develop efficient mathematical models

5. Devise and implement improvements/modifications to increase the prototype performance based on mathematical modelling and practicality assessment
6. Design and develop simulation models to simulate the prototype performance using actual weather data to assess its suitability of deployment throughout worldwide locations.

1.9 Novelty

There are two main novelties involved in this research:

1. Research and development of a new design of a large scale flat plate solar collector (LSFPSC) that replaces roofing elements with full integration into building envelops. In comparison with typical flat plate solar collectors, the LSFPSC can produce larger quantity of heat energy (due to more available collecting area) and it has much lower unit costs. In addition, the LSFPSC employs continuous serpentine tubing design that eliminates the presence of joints minimising the risks of leaking. Hence, the required maintenance is significantly reduced. The LSFPSC can be installed on existing buildings as retrofit or installed as an integral part of new buildings. The scalability of the LSFPSC is very flexible as customised numbers of installations can be employed to meet various energy demands.
2. Design and development of new TRNSYS simulation models to reflect the performance of the components consisting of the LSFPSC for the applications of domestic hot water heating and space heating. The Koppen-Greiger climate classification system was used to select locations covering a diverse range of climate conditions. The weather data of the selected locations were employed in the TRNSYS models allowing the performance of the LSFPSC to be evaluated for assessing its suitability of deployment in different regions.

1.10 Thesis Outline

Chapter 1 introduces background, objectives and novelty of the research. An overview of human energy industry is provided from the perspectives of the past, present and future. The problems associated with the usage of fossil fuels are described to give an understanding of our future demands in clean and renewable energy sources. The current market of solar industry is analysed to give an understanding of its commercial benefits and existing problems.

Chapter 2 gives an overview of the solar industry and a foundation of literature review for the proposed research. The solar energy is introduced in terms of its annual quantity, global distribution and regional variation. Main solar harvesting technologies are described with focus on non-concentrating solar thermal technologies. Many efforts have been put in the studies of solar water heating systems, which are specifically explored in the areas of system configurations and designs of flat-plate collectors. Mathematical analyses of a typical flat-plate solar water heating system are discussed to understand the effects of the three main components (solar collector, heat exchanger and storage tank) and their efficiencies.

Chapter 3 introduces experimental plan, designs and methods. Progressive targets were identified and described for different stages of the project together with plans to achieve them. Design of experiment set-up is described in relation to the selection of parameters, roles of the measuring instruments and data acquisition methods. Two important experiment scenarios are discussed in terms of the difference between their input parameters.

Chapter 4 describes the experimental scenario used in the 1st Stage and elaborates the performance analysis of the LSFPSC prototype. The energy balance equations of the system are identified. Each component of the system is analysed in terms of thermal gains/losses via two major heat transfer mechanisms: radiation and convection. A summary of their contribution is given in the end of this chapter showing efficiencies of the collector, the heat exchanger and the overall system.

Chapter 5 describes several modifications that were proposed to improve the performance of the LSFPSC prototype during the 2nd Stage of the project. These modifications include: employing glazing and using conduction instead of convection. Relevant mathematical models were developed to predict the benefits of these modifications.

Chapter 6 describes how proposed improvements from Chapter 5 were implemented on the LSFPSC prototype and how it was then subjected to performance tests to acquire new data for comparative study. This chapter presents the experimental results and mathematical models of the improved prototype together with parametric analysis of important factors such as wind speed and flow rates.

Chapter 7 describes the design of the TRNSYS simulation that simulates the performance of the LSFPSC under various climate conditions using weather data from world locations selected based on the Koppen-Greiger climate classification. An economic evaluation is given to show the payback period of the LSFPSC.

Chapter 8 presents discussion of results, conclusions and recommendations for future research works.

Appendices, References and Bibliographies are presented at the end of this thesis.

CHAPTER 2

2. Literature Review

2.1 An Introduction to Solar Energy

Our sun is an enormous natural fusion reactor. Each second, the fusion reactions in the sun convert more than four million tons of its mass (hydrogen and helium) into energy, producing radiant light and heat emitted into all directions. A very tiny fraction of this emitted energy, about half a trillionth, reaches Earth as solar energy (IEA, 2011).

Solar radiation provides the essential energy for life to flourish on Earth. The oceans and atmosphere absorb this solar energy, and the temperature increases. Water then evaporates from the seas and rises with warm air to cause atmospheric circulation. When the wet warm air reaches higher altitudes where temperature is low, condensation takes place to turn water vapour into clouds, which then rain onto Earth's surface, completing the water cycle. Absorption of solar energy by the oceans and landmasses maintains the average temperature on Earth's surface at about 14^{o}C (Treut et al., 2007). Living organisms convert solar energy into chemical energy through the photosynthesis process that produces oxygen, as well as the biomass from which fossil fuels are derived (Vermass, 1998).

The average amount of solar energy that reaches the earth's outer atmosphere is approximately 342 W/m^2, but only 198 W/m^2 (57.9%) hits the earth's surface. 67 W/m^2 (19.6%) is absorbed by the atmosphere, and the remaining 77 W/m^2 (22.5%) is reflected back to space by clouds, aerosols and the atmosphere (Treut et al., 2007). A total of 885 million tera-watthours (TWh) reaches Earth's surface in a year, which is 6200 times of the energy consumed by humankind in 2008 (IEA, 2011). Figure 2.1 demonstrates the difference in scales between the annual human energy consumption (small box on top) and the annual solar energy together with other energy sources.

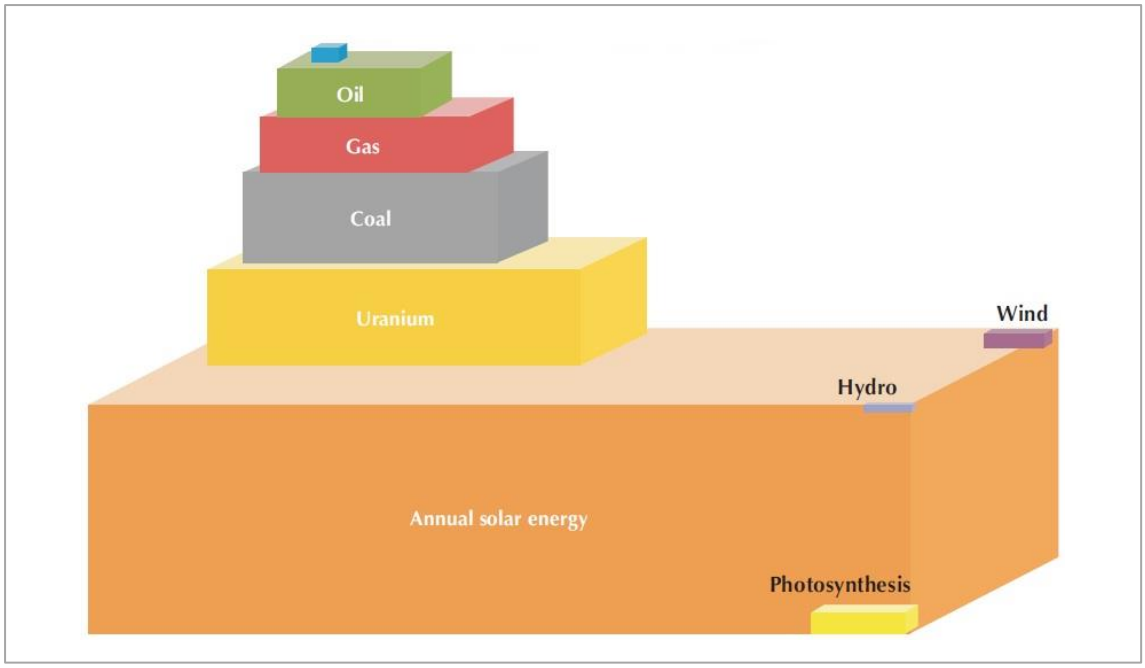

Figure 2.1: Total World Energy vs. Annual Solar Energy (IEA, 2011)

Therefore, if we can develop technologies to capture and distribute one tenth of one per cent of the available solar energy, our current energy requirements can be met.

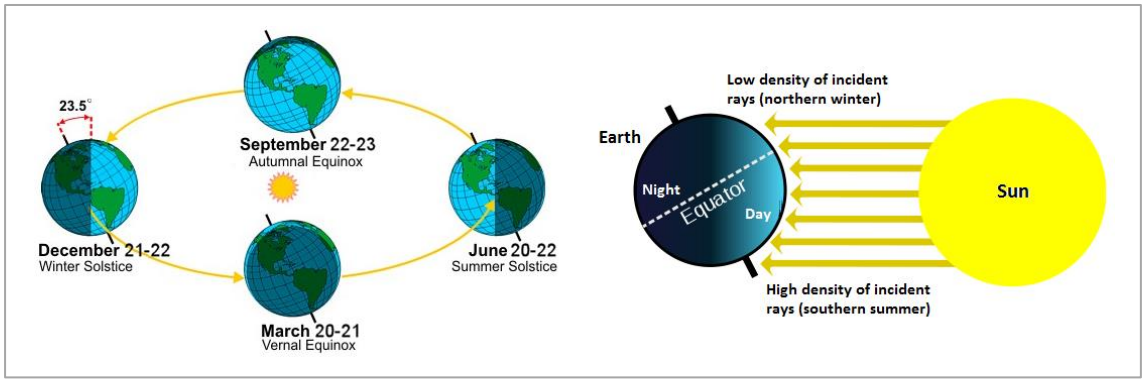

Figure 2.2: Tilted Earth in Relation to the Rotational Plane around the Sun (NWS, 2013)

The earth's rotational plane is not perpendicular to its orbital plane. For half the year , the southern hemisphere tilts facing the sun while the nouthern hemisphere tilts away (see Figure 2.2). Therefore, regions of higher altitudes receive less sunlight in winder and more sunlight in summer while the regions near the equator receive year-long constant sunlight. This is the reason why obvious season changes occur at regions of higher altitudes and the solar irradiance distribution is uneven across the globe.

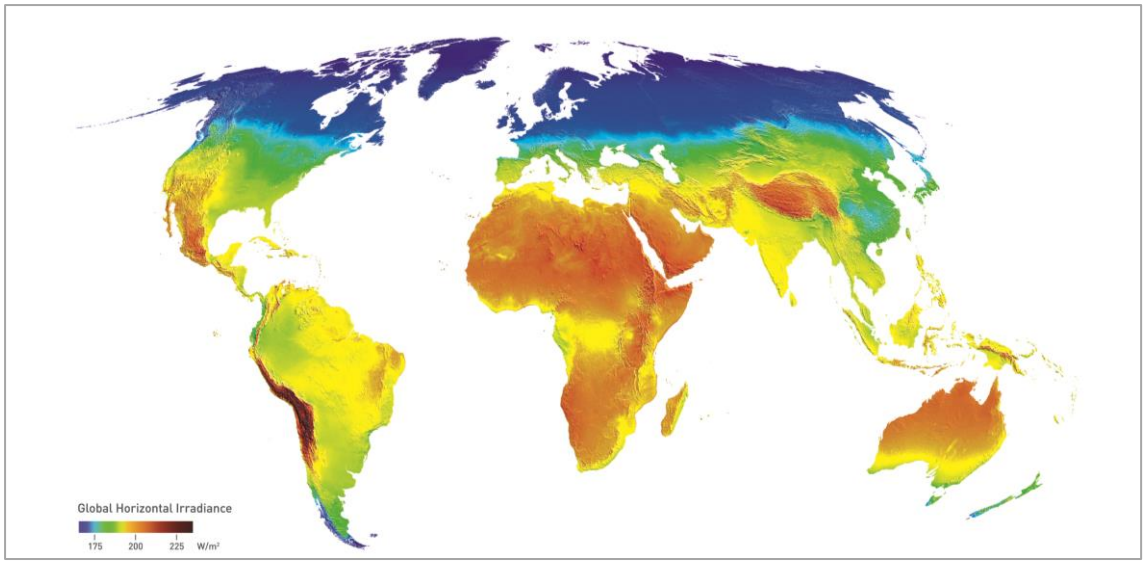

Figure 2.3: Satellite-derived Global Mean Solar Resource Map (3tier, 2013)

The amount of theoretically available solar radiation at the earth's surface is illustrated by averaged solar irradiance maps such as the one shown in Figure 2.3. These maps can indicate potentials of solar resources to help identifying suitable solar technologies for specific regions.

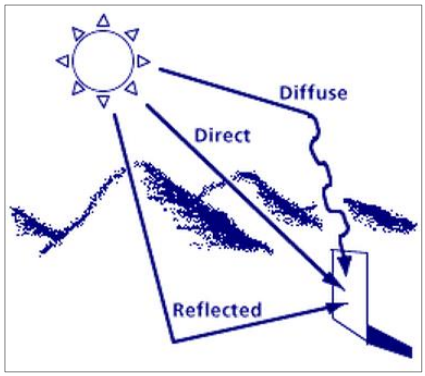

Figure 2.4: Three Types of Solar Radiations (Source: inforse.org)

As sunlight travels through the earth's atmosphere, part of it is absorbed or scattered by air molecules, water vapour, aerosols, and clouds. The sunlight that travels through directly to the earth's surface is called direct (beam) solar radiation. The part of sunlight that has been scattered out of the direct beam is called diffuse solar radiation. The solar radiation received at the earth's surface is always a mixture of direct (beam) radiation and diffuse radiation (Chen, 2011), illustrated in Figure 2.4. In general, the proportion of diffuse radiation increases as the climate gets cloudier. Since direct radiation and diffuse radiation behave differently, climate patterns should be assessed to determine appropriate solar technologies for a specific region. A third type of radiation, ground-reflected radiation, can also be utilised by certain types of solar technologies.

2.2 Solar Technologies Overview

According to quantum mechanics, radiation, such as sunlight, has wave-particle duality (Greiner, 2001). This means solar radiation can be viewed both as being electromagnetic waves with different wavelengths and frequencies, and as a flux of electromagnetic particles (photons). This wave-particle behaviour provides us with two basic ways of capturing the sun's energy:

1. the radiation can be directly converted to electrical energy through the use of photovoltaic (PV) cells, and

2. the radiation can be absorbed by gaseous, liquid or solid materials in which the resulting heat energy can be converted into kinetic energy, electrical energy or chemical energy.

2.2.1 Solar PV Technologies

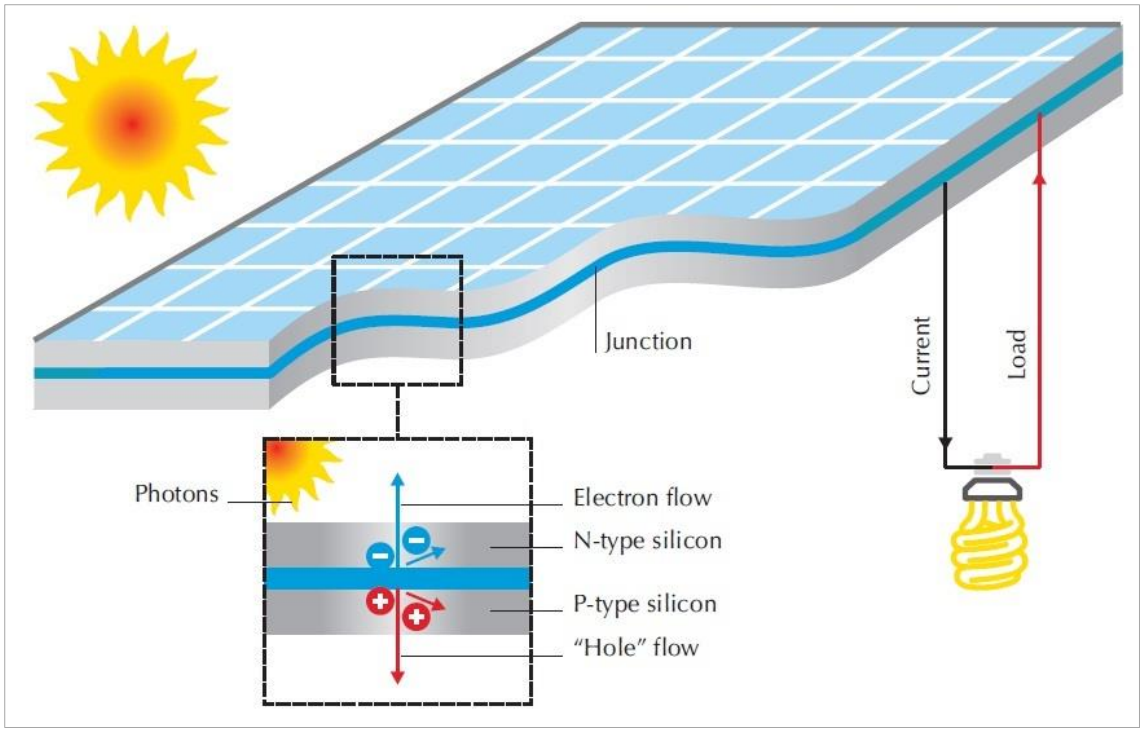

Figure 2.5: Schematic of a Typical Solar PV Cell (IEA, 2011)

Energy carried by solar photons can produce electrical conduction in semiconductors to generate electricity in solar photovoltaic (PV) cells, of which basic mechanism is shown in Figure 2.5. Since solar PV cells can convert sunlight directly into useful electricity, their use offers great industrial/commercial potentials in energy production even in remote areas. Its potential has been recognized by governments and technology companies worldwide in the past decade, as shown in significant increases in solar PV installation capacities and decreases in solar PV cell prices.

2.2.2 Solar Thermal Technologies

There are two categories in solar thermal technologies: concentrating and non-concentrating. The former employs only direct solar radiation while the latter could utilise direct, diffuse and ground-reflected solar radiations. In terms of functions, concentrating solar power (CSP) is mainly used in electricity generation and occasionally used in solar fuels production; non-concentrating solar power is most commonly seen in solar water heating (SWH) applications and occasionally in space heating systems.

Concentrating Solar Power

As the name implies, concentrating solar power (CSP) technologies focus sunlight received on a large aperture area to a much smaller area by using lenses or mirrors.

Current CSP technologies can be categorised into four types by the way they focus the sunlight and the mechanism used to receive the concentrated light (Figure 2.6).

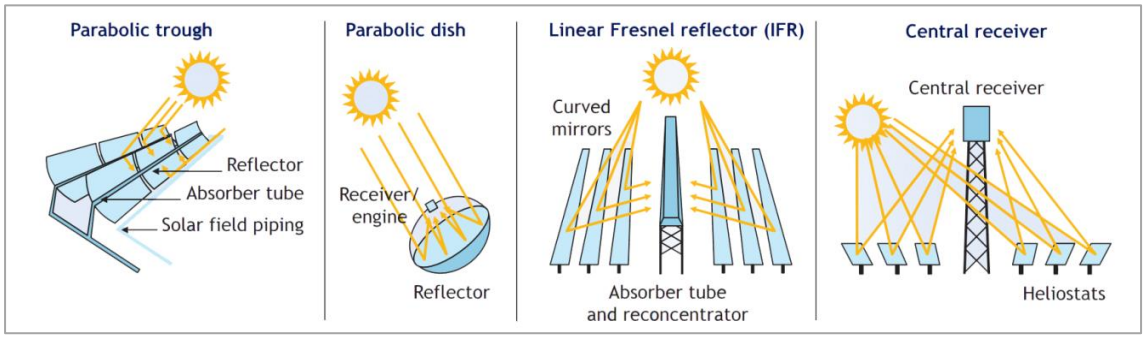

Figure 2.6: Concentrating Solar Power (CSP) Technologies (GreenpeaceInt et al., 2009)

The concentrated light can produce very high temperatures (up to 900^{o}C): the maximum temperature is proportionally related to the concentration ratio (Vignarooban et al., 2015). Therefore, CSP technologies are mainly used to deliver high-temperature heat to drive steam turbine and produce electricity (See Figure 2.7).

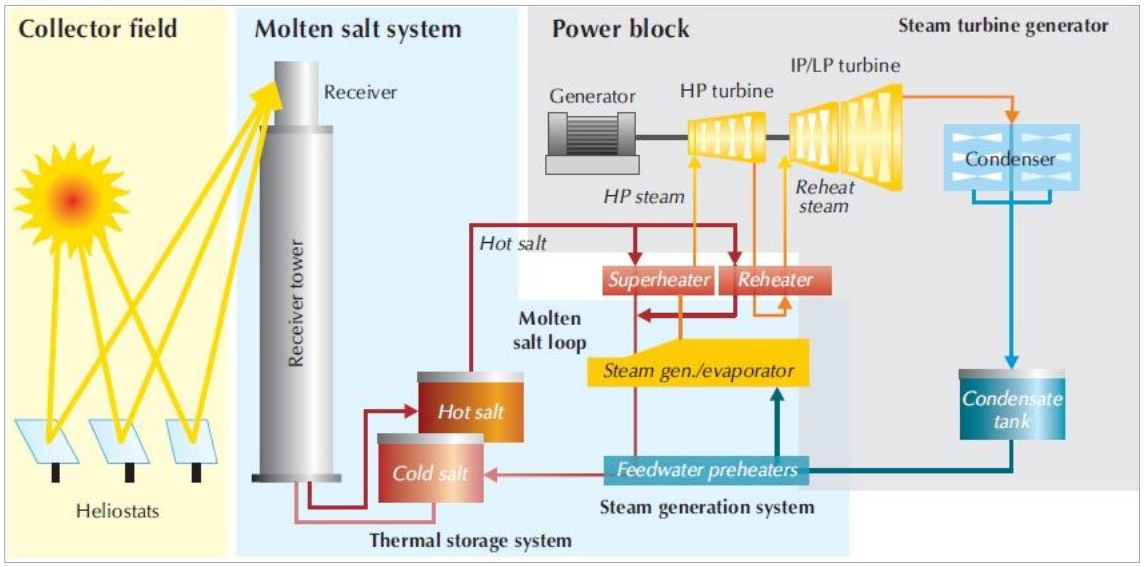

Figure 2.7: Solar Thermal Electricity Generation using Central Receiver Tower (IEA, 2011)

They are also seen in heat applications (e.g. desalination) with surplus heat that can be utilised in combined heat and electricity (sometimes also solar fuel) production installations (See Figure 2.8).

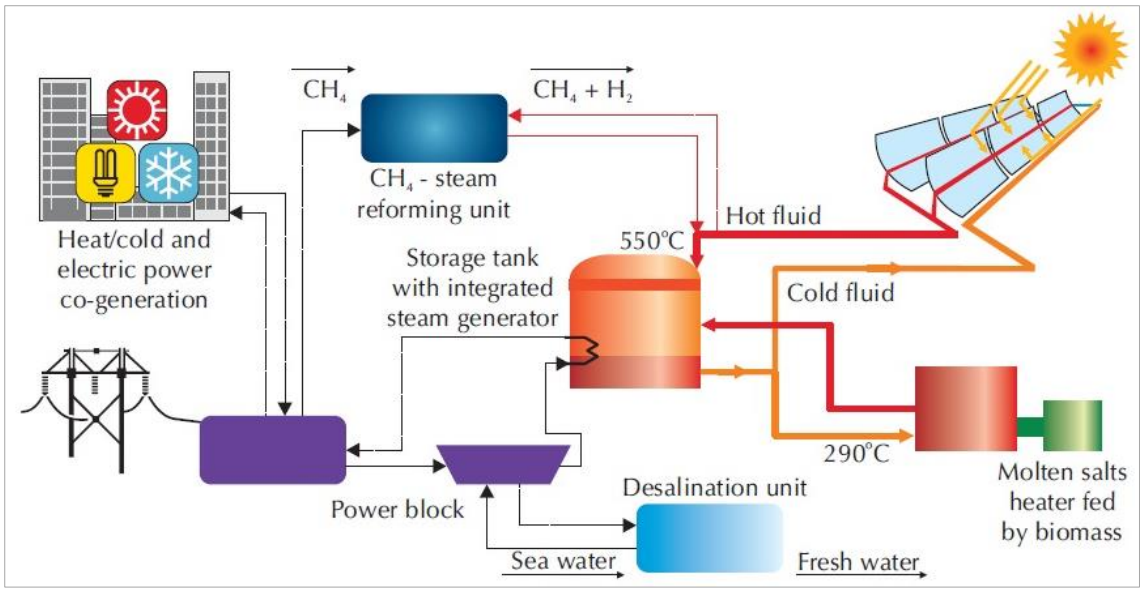

Figure 2.8: Solar Fuel/Heat/Electricity Generation using Parabolic Trough (IEA, 2011)

The solar energy employed by CSP technologies is measured as direct normal irradiance (DNI), which is the energy received directly from the sun on a surface tracked perpendicular to the sun's rays (IEA, 2010). It is necessary for CSP technologies to operate under clear skies with sufficient DNI to reach optimal performance. This requirement limits favourable regions for their deployments. CSP technologies are normally employed in utility scale applications and not widely used for residential applications due to potential health and safety risks posed by their high operating temperatures.

Non-Concentrating Solar Thermal Technologies

The broad variety of non-concentrating solar thermal collectors can be divided into two main types: flat-plate, which can be glazed or unglazed; and evacuated tubes. A wide range of collector designs are available but they have many components in common.

The absorber is used to collect incoming near-infrared and visible solar radiation. Absorbers with dark colours are normally preferred as dark surfaces have particularly high degree of sunlight absorption. The wavelengths of solar radiation received at the absorber's surface are mainly shorter than 2500nm. The solar radiation is then partly re-emitted in greater wavelengths than 2500 nm as infrared which carry away energy from the absorber surface. Most absorbers have selective coatings to ensure as much as thermal energy is retained. A selective coating provides a structured, layered surfrace that 'traps' the re-emitted radiation.

A circuit carrying heat transfer fluid (gas or liquid) is present in all collectors. The heat exchange efficiency between this circuit and the absorber must be maximised to minimise heat losses and maximise system efficiency. Since the faster rate of heat removal from the absorber, the less heat is lost to the surroundings and the more useful heat can be extracted. To achieve this, a common design is to locate the absorber directly on the external surface of the circuit.

Most non-concentrating collectors have a housing, apart from unglazed collectors used for swimming pool heating and air heating. The housing can reduce energy losses to the surroundings from both the absorber and the circuit while also providing protection against degradation, corrosion and damages. Clearly, transparent materials (e.g. glass) must be used as the housing cover to allow solar radiation to reach the absorber.

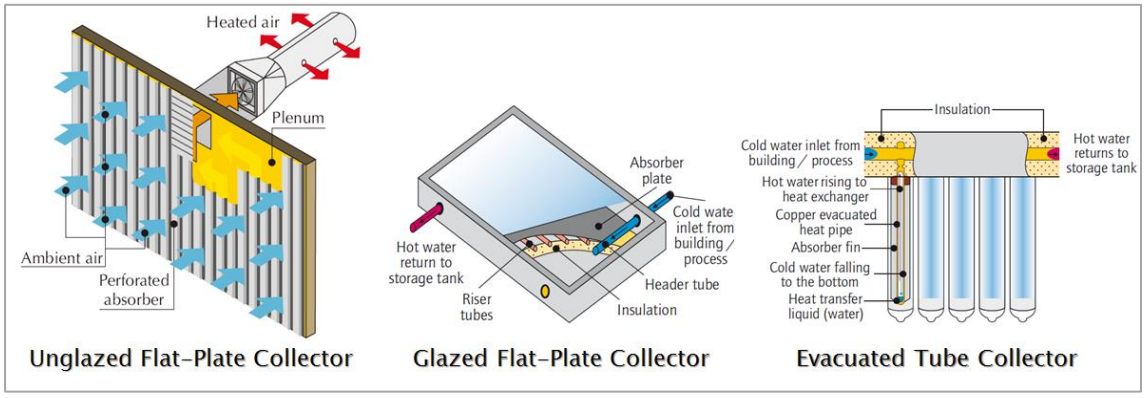

Figure 2.9: Non-Concentrating Solar Thermal Technologies (IEA, 2011)

Unglazed flat-plate collectors consist of a metal or plastic absorber without covering (Figure 2.9 left). They are commonly seen in heating swimming pool and ambient, non-recirculated air.

Glazed flat-plate collectors employ housing of shallow box shape, comprising:

- a casing, made of aluminium, steel, plastic or sometimes wood, and
- insulation materials (e.g. mineral wool) or vacuum to reduce thermal losses on the back of the collector, and
- one or two transparent layers of low iron, tempered glass that sometimes include anti-reflective coating capable of increasing transmittance of the cover (See Figure 2.9 middle).

They are used for domestic solar water heating systems, recirculated air heating and space heating in residential and commercial applications.

Evacuated tube collectors, where the housing is a glass tube with vacuum inside that keeps the heat losses to the environment on a very low level (See Figure 2.9 right). Since they are well insulated, they are suitable in solar water heating applications requiring higher temperatures with lower ambient temperatures. They also perform better than flat-plate collectors in low irradiation conditions.

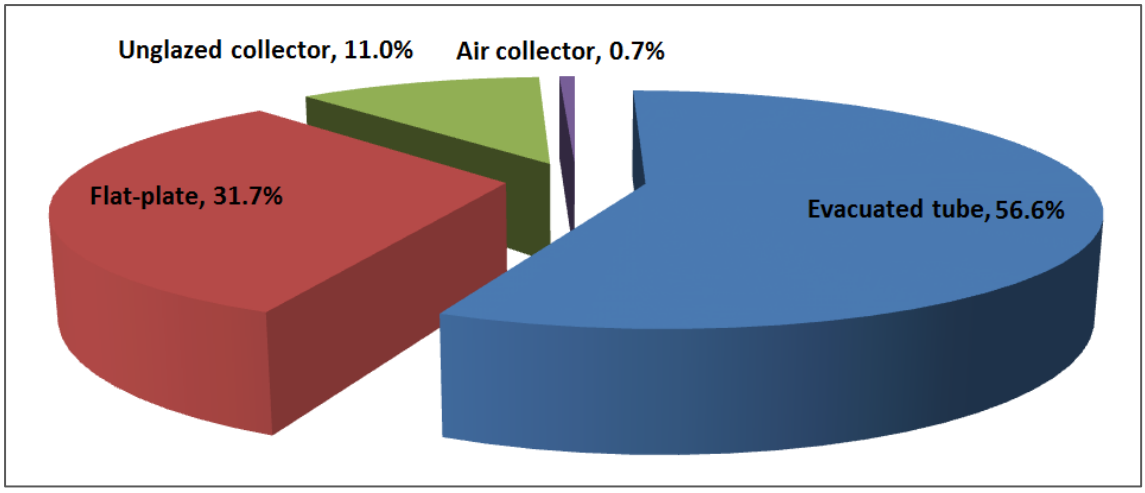

Figure 2.10: Distribution of Worldwide Installed Capacity in Operation by Collector Type in 2010 (Weiss and Mahthner, 2012)

By the end of 2010, the non-concentrating solar thermal collector capacity in operation worldwide reached approximate 195.8 GW_{th}, corresponding to 279.7 million m^2; it was estimated to have grown by 25% to 245 GW_{th} by the end of 2011 (Weiss and Mahthner, 2012). Of this, 56% comprised evacuated tube collectors, 31.9% glazed flat-plate collectors, 11% unglazed water collectors and 0.7% air collectors (Figure 2.10).

2.3 Solar Water Heating Systems

Non-concentrating solar thermal technologies were mainly employed in solar water heating (SWH) systems to produce hot water for industrial and residential uses. In terms of circulation methods and applications, SWH systems can be broadly categorised as passive SWH systems and active SWH systems. A review of a variety of SWH systems is given below with a discussion on their recent designs and modifications.

2.3.1 Passive Solar Water Heating Systems

The circulation of water or heat transfer fluid (HTF) in passive solar water heating systems depends on natural convection driven by heat. There are two main categories of these passive systems: the integrated collector storage and the thermosyphon SWH systems.

Integrated collector storage solar water heaters (ICSSWH) employ a tank that acts as both a solar heat collector and storage. They are sometimes known as 'batch' SWH systems. The basic design of ICSSWH systems consists of a simple dark-coloured tank enclosed with a glass cover. However, the main drawback of simple ICSSWH designs is heat loss, which is significant during night time. Effective improvements such as selective absorber surface coatings, insulating materials and additional glazing covers can be utilised to reduce heat losses.

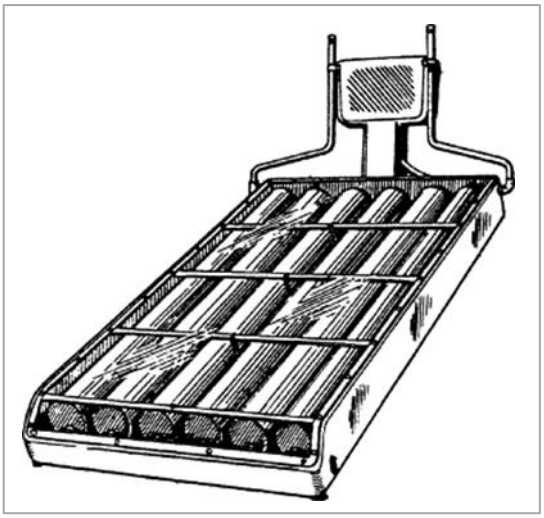

Figure 2.11: The stainless steel closed pipe type solar water heater (Tanishta 1970)

In early 1950s, the first commercialised ICSSWH system was marketed in Japan with a 'closed-pipe' design as illustrated in Figure 2.11 (Smyth et al., 2006). This concept was further improved with the introduction of cylindrical vessels (combining both functions of collector and storage), which can still be seen in many commercial designs today. Smyth et al. (2005) observed that rectangular vessels could function and perform on similar levels as cylindrical vessels. ICSSWH systems with triangular geometries were also introduced and found to have higher heat transfer rates due to increased natural convection currents (Ecevit et al., 1989, Kaushik et al., 1994). Together with attempts on various geometrical designs, many studies have been conducted on insulation materials (e.g. fibre glass, inorganic glass foams, honey comb structures) to enhance the thermal performance of the ICSSWH systems (Goetzberger and Rommel, 1987, Rehim, 1998).

Baffles were introduced to further improve the system efficiency by guiding the direction of the flowing fluid to separate the vessel into an outer collecting volume and an inner storage volume. Sokolov and Vaxman (1983) carried out the first numerical and experimental studies on baffle plates in triangular and rectangular ICSSWH systems. Kaushik et al. (1995) conducted similar studies in a triangular system, illustrated in Figure 2.12.

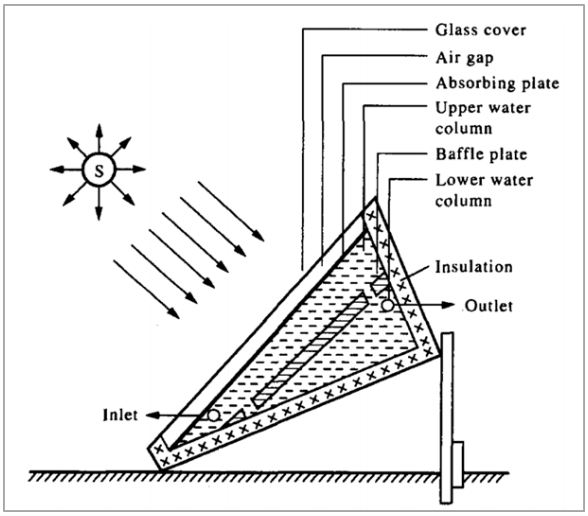

Figure 2.12: Triangular built-in storage water heater (Kaushik et al., 1995)

These studies showed that the inclusion of the baffle plate had prominent effects on improving the system's performance, especially during non-collecting periods. They also showed that the thickness and material of the baffle had small impact on the system performance. Due to their simplicity and inexpensive costs, ICSSWH systems are popular in developing countries with non-freezing climates.

A simple open-loop thermosyphon system, shown schematically in Figure 2.13, transports HTF from the collector to the storage using natural convection flow (Kalogirou, 2004b).

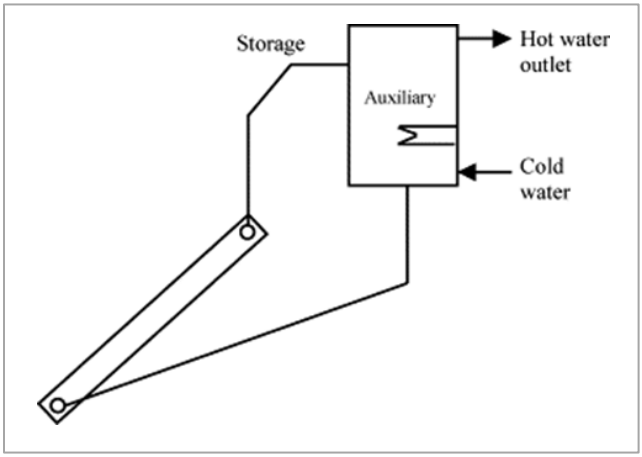

Figure 2.13: Schematic diagram of a thermosyphon solar water heater (Kalogirou, 2004b)

That is, HTF expands becoming less dense when heated, and rises through the collector into the top of the storage tank. Then it is replaced by colder, denser cold water from the bottom of the storage. Solar heating will maintain this density difference in the system to allow continuous circulation.

Numerous analytical and experimental studies have been conducted on the analysis of the performance of the thermosyphon SWH systems. Some of the most important are shown here.

Gupta and Garg (1968) developed one of the first fundamental models for thermal performance of a thermosyphon SWH with no drain-off and no load conditions. Their studies represented solar radiation and ambient temperature by Fourier series, and were able to predict daily performance. Their theoretical approach was validated substantially with experiments.

It appeared that the first detailed studies on thermosyphon SWH systems were conducted by Ong. In his first study (Ong, 1974), Ong developed a mathematical approach that employs 'finite-difference method' (FDM) assuming the entire system is consisted of finite number of sections, each individual section having a uniform mean temperature. His second study (Ong, 1976), improved his mathematical approach to become more compliant to experimental conditions

Kudish et al. (1985) conducted a study to analyse the effect of flow rate in thermosyphonic collector efficiency. Based on the thermosyphon flow data gathered, they constructed a standard efficiency test curve showing that this technique can be applied in testing thermosyphonic collectors. Their study also determined the instantaneous collector efficiency as a function of time of day.

A study of system modelling and operation characteristics was conducted Morrison and Braun (1985) on thermosyphon SWH systems with vertical or horizontal storage tank. Their study showed that the system performance is optimised when the daily collector volume flow is approximately equal to the daily load flow. It was noticed that the system with horizontal tank did not perform as well as a vertical one.

Apart from conventional solar flat-plate collector, studies have also been carried out on the use of the evacuated tube collector in thermosyphon SWH systems. Budihardjo and Morrison (2009) conducted a thorough simulation study to analyse the optical and thermal characteristics of a water-in-glass solar water heater (Figure 2.14).

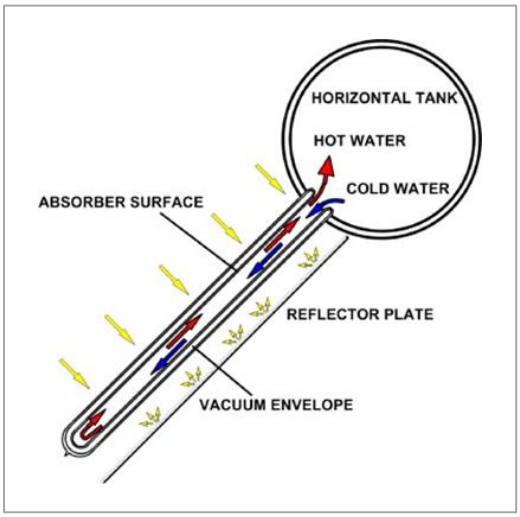

Figure 2.14: Flow driven by natural convection in a water-in-glass solar water heater (Budihardjo and Morrison, 2009)

They concluded that there is much less temperature stratification present in the horizontal storage tank used in their system leading to much smaller effect on the system performance in comparison with the cylindrical tanks used with common flat-

plate collectors. However, the system has limited tolerance for high pressure which can only be used in low ambient temperature conditions.

2.3.2 Active Solar Water Heating Systems

Unlike passive systems, active systems employ one or more pumps to circulate water or HTF within the system. Active systems can be categorized into direct circulation and indirect water heating systems. In the direct systems, water from the storage tank is directly circulated to the solar collector to be heated, whereas in the indirect active system the HTF is circulated through the collector and releases heat through a heat exchanger to the water in the storage tank.

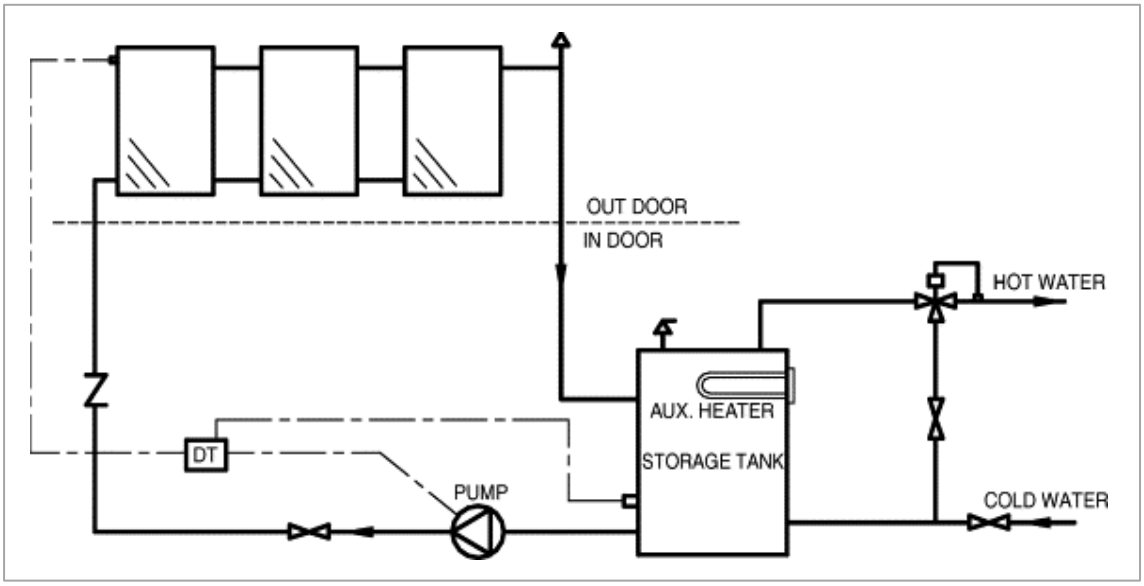

Figure 2.15: Direct circulation system (Kalogirou, 2004b)

In terms of operation, direct systems are simple and could provide hot water of moderate temperature (~50–60 °C), but they are vulnerable to freezing damages (Kalogirou, 2004b). Many design modifications have been adopted to overcome the freezing issues. One of such modifications is to operate the direct circulation system in drain-back mode; a temperature differential controller-integrated pump is employed to circulate water from the storage tank to the solar collectors. Numerous research studies were conducted on the direct active SWH systems. Only some of the more recent investigations are discussed here.

More recently, evacuated tube collectors (ETC) have been used extensively for domestic water heating purposes. It has been observed that the performance of ETCs is much higher than flat-plate collector because of its lower convection heat losses to surroundings. Li et al. (2010) developed a heat transfer model to evaluate the performance of all-glass ETC incorporated in a direct circulation system. This simplified model combined both natural circulation in single glass tube and forced flow circulation in the manifold header. Flow equations were obtained by analysing the frictional losses and buoyancy forces inside the tube. A mere 5% deviation was observed between the predicted and experimental collector outlet temperatures.

Apart from the collector types discussed above, Chong et al. (2012) researched a cost-effective new V-trough SWH system that employed direct circulation. It was observed that integrating a solar absorber with a V-shaped trough reflector could substantially improve the thermal performance of SWH. Different insulating materials were tested on the system with and without glazing. The prototype was reported to be capable of achieving an optical efficiency of 71% with a maximum outlet water temperature of 82 °C and 67 °C with and without insulation, respectively.

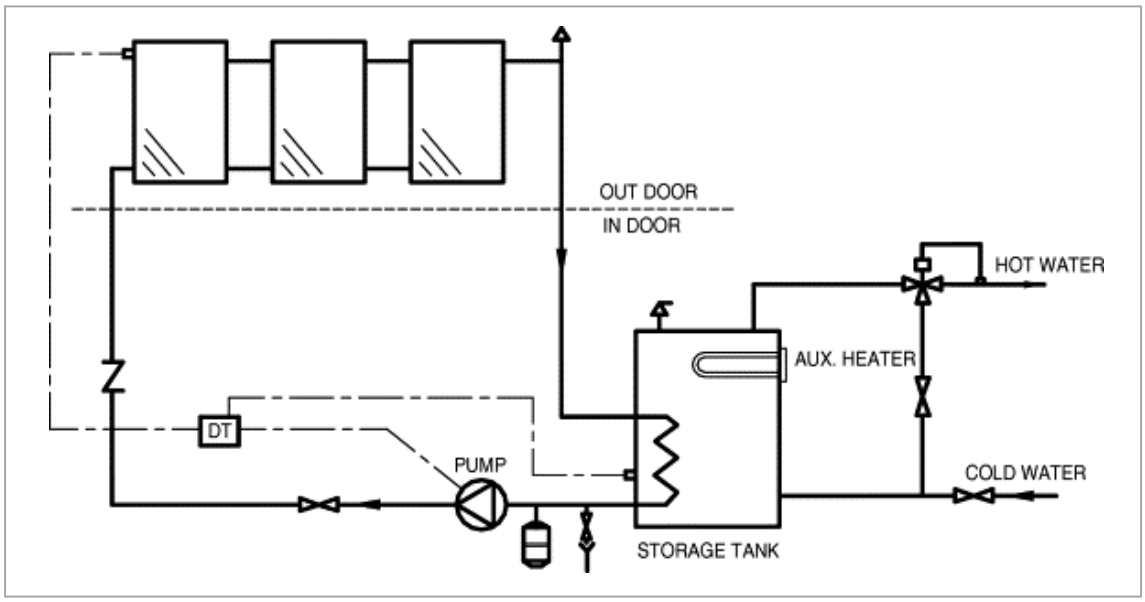

Figure 2.16: Indirect circulation system (Kalogirou, 2004b)

In general, direct heating systems are commonly employed in regions with abundant sunshine and moderate ambient temperatures. Indirect water heating systems are more beneficial in regions with less sunshine hours and low ambient temperatures. Indirect systems have reliable operation records and effective freezing protection (Kalogirou, 2004b). Heat transfer fluid (HTF), such as ethylene glycol is circulated between the collector and the heat exchanger, along with anti-freezes and corrosion inhibitors. Many indirect SWH systems operate on a heat pump (HP) mode to supplement the solar energy gained from solar collector. Hot water is produced utilizing waste heat or other low temperature sources such as ground heat. An exclusive working fluid is circulated in the collector and its heat gain is released through a heat exchanger to cold water in storage. The main drawback for solar assisted HP system is that its performance is very low when the ambient temperature is low. Some of the recent studies on indirect SWH systems are discussed.

A variable capacity direct expansion solar-assisted HP system (DX-SAHPS) for water heating purposes was tested by Chaturvedi et al. (1998). In their experiment set-up, a bare solar collector was used as an evaporator for the HP system. The system was tested under changing ambient conditions with varying compressor speed controlled by a frequency drive. The test results showed that lowering the speed of the compressor when the ambient temperatures were higher can lead to extensive increase of the coefficient of performance (COP) of the system. Hence, such systems could perform better in summer compared to winter.

Kuang et al. (2003) proposed another design of DX-SAHPS. Their proposed system employed a bare flat-plate collector acting as a heat source as well as an evaporator for the refrigerant, illustrated in Figure 2.17. From the simulation model it was concluded that the monthly average COP varied between 4 and 6, and the collector efficiency was about 40–60%. A similar work was conducted by Li et al. (2007) to present another experimental study on the DX-SAHP. Their results showed that the proposed system can attain a maximum COP of 6.61 on a clear sunny day (T_a = 17.1 °C, I = 955 W/m^2). Even during cloudy and rainy nights, the system could perform moderately with a COP of 3.11.

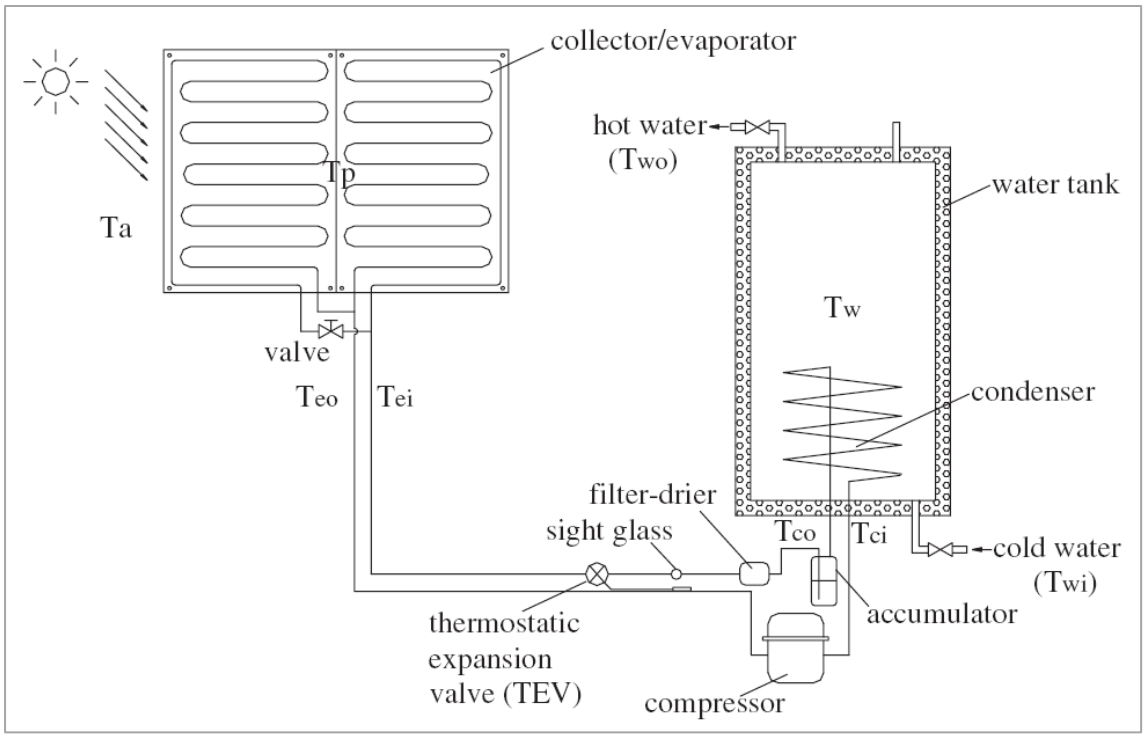

Figure 2.17: Schematic diagram of DX-SAHP water heater (Kuang et al., 2003)

Using heat pipes is another approach to further enhance the system performance. A heat-pipe water heater was fabricated and tested/modelled by Huang et al. (2005). The overall COP of the system was calculated based on the performance of the combined solar heat pipe collector and conventional HP. When solar radiation was low, the system operated in HP mode. During clear sunny days, the heat-pipe mode operated independently of electrical energy input to achieve higher thermal efficiency. The results showed that the COP of the hybrid-mode of operation could attain as high as 3.32, with 28.7% higher efficiency compared to using the HP mode alone.

2.4 Designs of Flat-Plate Collectors

The solar collector is the most important component of any SWH system. It absorbs incoming solar energy and transfers absorbed energy to the heat transfer fluid flowing through the collector as useful heat. The fundamental design parameters associated with solar collectors such as efficiency factor (F') and heat removal factor (F_R) were first developed by Hottel and Whillier (1955). They were later expanded and improved by

Duffie and Beckman (2013) to become the theoretical core of recent designs of solar thermal collectors. The efficiency of a SWH system is mainly influenced by the effectiveness of the solar collector. Therefore the majority of research has been focused on improving the performance of the collector. Important studies on the design modifications of the flat-plate collectors are discussed below.

A typical flat-plate collector (FPC) consists of:

- a flat absorber plate with selective coating,
- a transparent cover that reduces top heat-losses,
- heat transfer fluid (HTF) that removes heat from the absorber plate,
- tubes/pipes/passages for the flow of HTF,
- an insulating layer/support that reduces back heat losses,
- and a protective casing that protects the collector from dust, moisture and animals.

Many studies have been conducted on the design and development of FPC. Matrawy and Farkas (1997) reported that the tubing configuration of the collector can significantly influence its thermal performance. One of the most commonly employed configurations is the parallel-tube collector design, in which pipes (risers) are integrated with the absorber plate forming an integral part of the plate structure (Figure 2.18a). The first thermal performance analysis of parallel tube collectors was conducted by Hottel and Whillier (1955). For this type of collector designs, Duffie and Beckman (2013) developed a thermal analysis procedure that comprised of two steps: evaluation of the heat conduction from the plate to the tubing based on the fin efficiency factor; estimation of the convection heat transfer to the fluid in the tubing based on the heat removal factor. This procedure was later adapted and further developed by many researchers. There were several disadvantages associated with parallel tubing design, such as: non-uniform temperature distribution across the surface of the absorber plate, unequal distribution of the working fluid through the collector risers, and increased heat losses when the absorber plate has higher temperatures under low flow rate conditions. A serpentine tube collector design was introduced to overcome these problems, especially in compensating low flow rate conditions (Figure 2.18b). This design allows the total mass of HTF to pass through the whole area of the collector with uniform flow rates, increasing the heat transfer coefficient (Matrawy and Farkas, 1997).

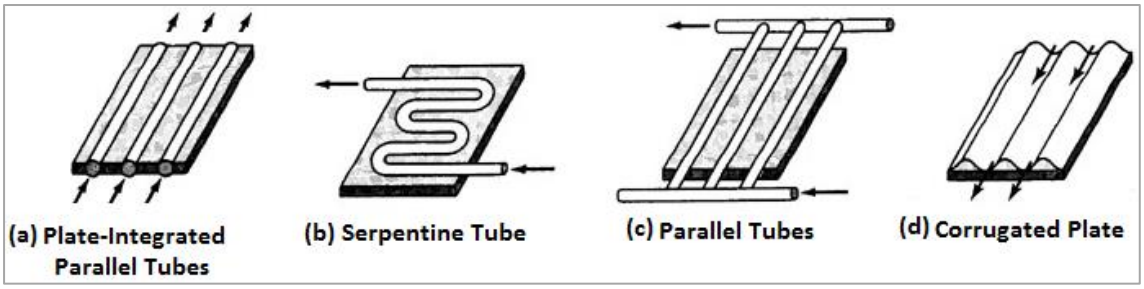

Figure 2.18: Internal piping arrangement in flat-plate collectors (Murdoch University 2008)

An improved tubing design employing two connected sets of parallel-tube collectors (Figure 2.18c) was tested and compared against other two designs (Matrawy and Farkas, 1997). The results show that the efficiency of the improved design is 6% higher

than the serpentine configuration and 10% more than a single parallel tube collector, under similar testing conditions. Other geometric designs include a fin-and-tube collector (Figure 2.18d), in which the corrugated absorbing plate acts as flow channels allowing the HTF to have direct contact with solar collecting surface (Rommel and Moock, 1997, Alvarez et al., 2010).

The absorber plate is the core component of the flat-plate collector, of which thermal performance is influenced by its material properties and design parameters. Kovarik (1978) reported that the parabolic shape is one of the most efficient designs because of its heat output per unit volume is higher than other shape geometries. Hollands and Stedman (1992) introduced a rectangular profile with a step change in local thickness (RPSLT), in which the fin is thinner far from the tube permitting savings in material content. They carried out a thermal analysis reporting that to maximise heat transfer, the fin area must be maximised for a given fin volume (m^2/m^3). Kundu (2002) conducted a further comparative study between absorber plates with RPSLT, rectangular and trapezoidal profiles. His results showed that the RPSLT profile is superior over the others due to its optimal performance efficiency, excellent heat transfer rate per unit volume and less difficulty in fabrication (Figure 2.19).

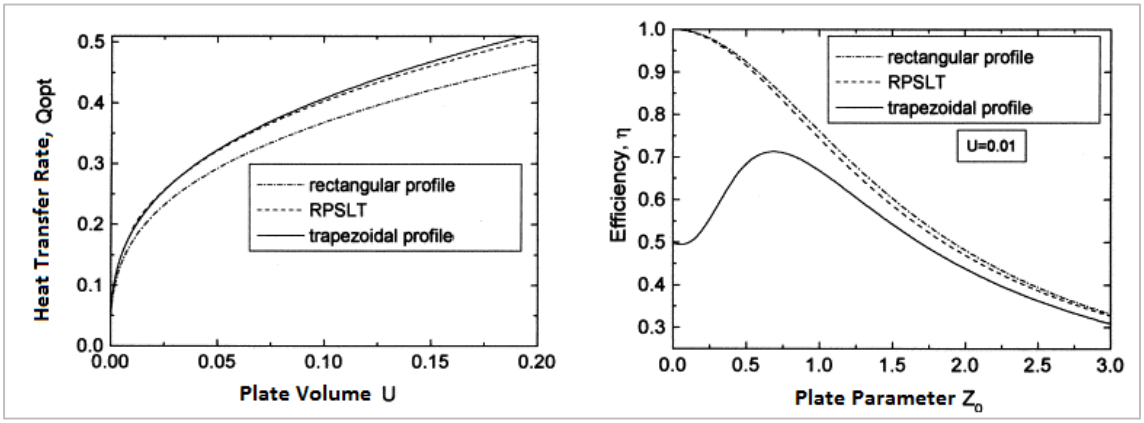

Figure 2.19: Comparison of heat transfer rate and efficiency between different profiles of absorber

Metals are most commonly used in absorber plates but they are susceptible to corrosion, making them difficult to maintain performance over a long period of time. For better resistance against internal and external corrosions, the use of polymer-based absorbers has been increasing. Apart from their non-corrosive properties, polymer-based absorbers are also light weight, cheaper and easier to fabricate than the metal ones. Polymers are generally known to be prone to UV degradation, but suitable polymer materials have been developed to withstand long exposure to sunlight, such as ethylene propylene diene monomer (EPDM) (O'Brien-Bernini and McGowan, 1984). Sopian et al. (2002) conducted experimental studies on a flat-plate solar collector using a commercially available blend of thermoplastic natural rubber (TPNR) in the absorber plate. In the experiments, they tested the TPNR absorber plate under the conditions indicated by international standard organisations. Their results concluded that the TPNR absorber plate has the potentials to be employed in commercial domestic thermosyphon hot water system (Figure 2.20).

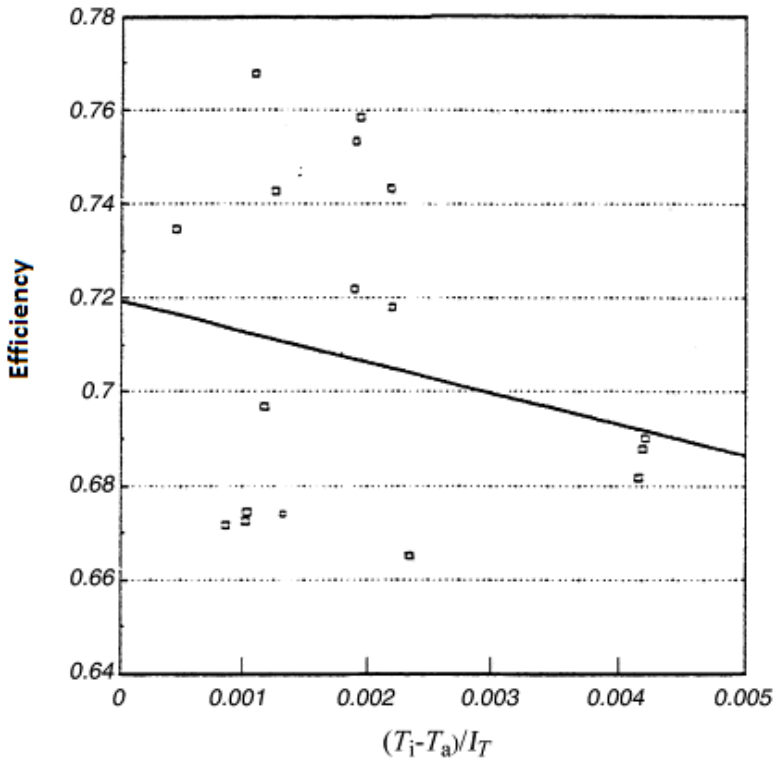

Figure 2.20: Performance curve of the TPNR collector (Sopian et al., 2002)

Polymer flat-plate collectors were also introduced in European regions with freezing climates due to their flexibility and tolerance against volume expansion during freezing. Hence plain water could be used as heat transfer fluid without the addition of antifreeze. Another advantage of these collectors is that they can be connected directly to the storage tank, avoiding the usage of a heat exchanger that can lower the system efficiency. Using polymer-based components can lead to cheaper fabrication costs than metal ones, evidenced by Liu et al. (2000a)'s study showing the cost of a conventionally designed nylon solar absorber was about 20% cheaper than a similar copper one. However, in comparison with metal collectors, polymer collectors have much lower thermal conductivity and can only be used for moderate temperature applications as they cannot sustain deterioration and deformation under high temperatures (Kalogirou, 2004b).

Transparent insulating materials are generally used as glazing in solar collectors to reduce top heat losses by convection and radiation, hence improving collector efficiency and ensuring high temperature performance (Duffie and Beckman, 2013). Glass is one of the most widely used glazing materials in solar collectors due to its low costs and good transmittance up to 90% (Kalogirou, 2004b). Anti-reflection coatings can be applied to increase the solar transmittance of glass, resulting in improved collector efficiency (Figure 2.21) (Furbo and Shah, 2003).

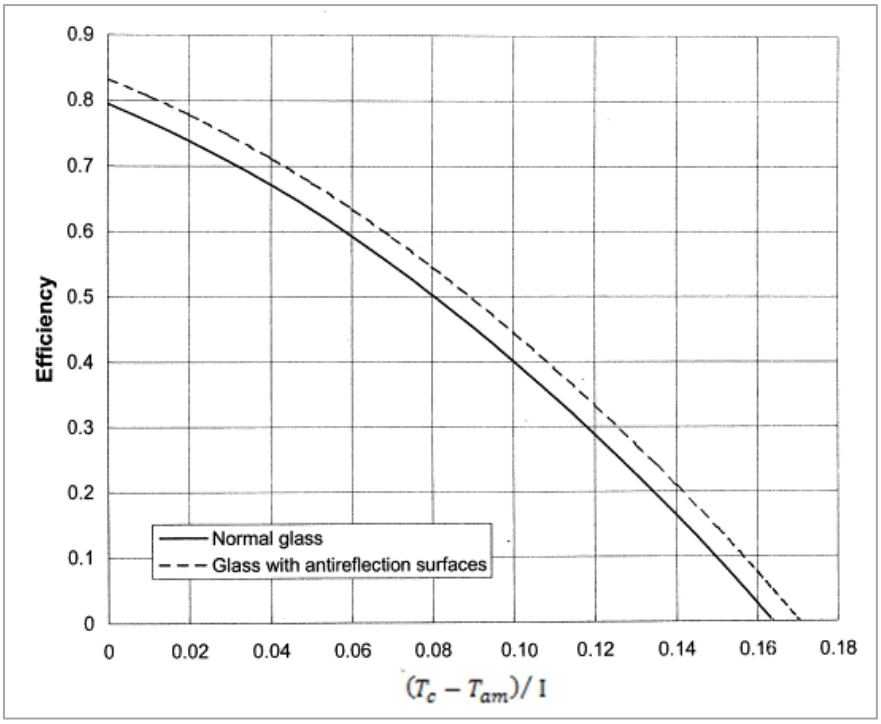

Figure 2.21: Variations of the efficiency with the combined factor ($T_c - T_{am}$) / I for collectors with different glazing (Furbo and Shah, 2003)

Using multiple glazing covers can further enhance collector efficiency by creating additional air gaps that act as insulation layers to reduce convective heat losses (Akhtar and Mullick, 2007). Plastic thin films and sheets can also be used as glazing materials with their high shortwave transmittance and reasonable transmittance for thermal radiation. Compare to glass glazing, plastic glazing is lower in mass and much more flexible to withstand impacts of hails or stones (Kalogirou, 2004b). However, their usage is limited due to their susceptibility to UV degradation and deterioration under high temperatures.

Rectangular, circular and hexagonal geometries are common design profiles of transparent insulating materials. As an attempt to further reduce convective heat losses, honeycomb structure was introduced. Abdullah et al. (2003) investigated the effects of different honeycomb arrangements on the collector efficiency and compared them with non-honeycomb insulation. Their results confirmed that the top heat losses were considerably reduced (49% - 56%) but marginal decrease of optical efficiency (15% - 32%) was also observed.

The optical properties of different collector components such as absorptivity and emissivity play important roles in dictating the collector efficiency. Hellstrom et al. (2003) conducted a simulation research to study the impact of several optical parameters on the annual performance of a solar collector at 50^{o}C operating temperature. Their results showed that, by changing absorptivity from 0.95 to 0.97 and emissivity from 0.10 to 0.05, an increase of 6.7% in the annual performance was achieved. It was found that treating the glass glazing with anti-reflection coating increased the annual output by 6.5%. An increase of 5.6% in annual performance was obtained by employing a

secondary cover made of Teflon. If instead a Teflon honeycomb cover is installed, a twice as high performance increase is obtained 12.1%.

Different types of reflectors could be employed to direct additional solar radiation onto the collector (Figure 2.22) that increases thermal input hence improving the collector performance. Tripanagnostopoulos et al. (2000) experimentally investigated and showed that using booster reflector could lead to substantial increases in the collector performance.

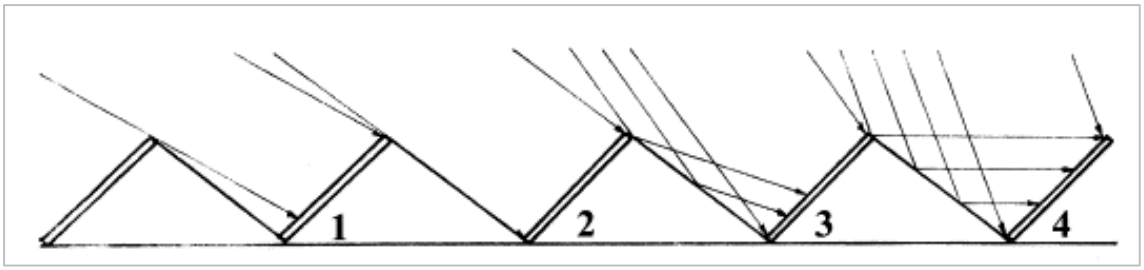

Figure 2.22: Effect of booster reflectors to collectors regarding the direction of solar rays (Tripanagnostopoulos et al., 2000)

RÖNnelid and Karlsson (1999) developed a corrugated reflector as an attempt to further utilise reflected solar radiation by creating more reflection surfaces for solar rays. Their experimental results showed that the corrugated reflector directed 10% more radiation to the collector compared to the flat one, which was estimated to result in a 3% increase in the annual collector output.

2.5 Building-Integrated Solar Heat Collectors

For residential and commercial applications, the majority of solar heat collectors are produced as individual units to be installed with mounting options shown in Figure 2.23.

Figure 2.23: Different mounting options of solar heat collectors (Source: Sunmaxxsolar)

The Free-Standing Mounting option is employed for flat or pitched roofs where the pitch angle is not high enough (less than 35 degrees) to deliver maximum collector performance. It provides additional tilt to collectors increasing their ability to capture sunlight and deliver higher performance. The Ballast Mounting Add-on can provide extra safety to the solar collector installation by minimising potentials of roof penetrations or leak damage. The Flush Mounting option is normally employed for

pitched roofs with high tilting angle (more than 35 degrees) that are optimum for sunlight harvesting. The appearances of the most mounted solar collectors don't comply with the aesthetics of buildings as they are normally seen to be intruding "patches" on roofs (Figure 2.24 and 2.25).

Figure 2.24: Free-standing mounted solar heat collectors on roof (Source: homepower.com)

Figure 2.25: Flush mounted solar heat collectors on roof (Source: solaruk.com)

Researches have been done to explore the advantages of building-integrated solar collectors over mounted solar collectors. Bartelsen et al. (1999) conducted experiments on unglazed collector prototypes with absorbers made of corrugated metal roof sheets which were used for roofs and facades. Their results showed the absorbers made of roof sheets have thermal performance close to typical flat plate collectors with only a slightly lower zero-loss efficiency η_0 value. However, their prototypes were designed to place the circulation systems outside of the roof sheets making them susceptible to damages. Additionally, they have similar casing as typical collectors that cannot be fully integrated within building envelopes.

Aesthetics is important in residential and commercial applications, thus the integration of solar collectors in buildings should be compatible with the architectural design. Metal roof sheets are produced to meet architectural standards with different colours for aesthetic requirements. Tripanagnostopoulos et al. (2000) investigated the performances of three flat-plate collectors that used black, blue and red-brown absorbers with/without glazing, with/without rear insulation and with/without booster reflectors under similar operating conditions. Illustrated in Figure 2.26, the results showed that coloured absorbers had only marginally lower efficiencies than the black absorber. It thus concluded that dark tone coloured absorbers could perform similarly as the black absorber and able to meet aesthetic requirements.

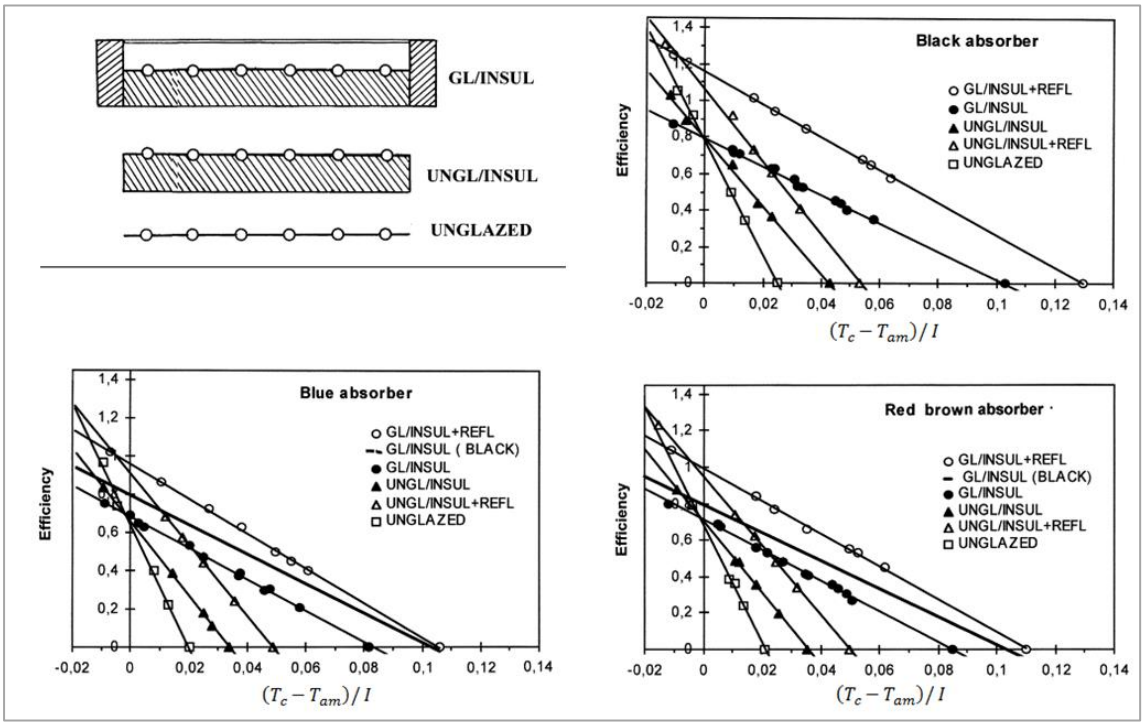

Figure 2.26: Variations of the efficiency with the combined factor ($T_c - T_{am}$) / I for tested solar collectors (Tripanagnostopoulos 2000)

Medved et al. (2003) designed and developed large panel roof-integrated unglazed solar collectors with a range of industrially produced metal roof sheets for the application of heating water in an indoor swimming pool. Their experimental and modelling results showed that the steady-state efficiency of the collectors η_0 is in the range between 0.26 and 0.74, and the heat loss factors are 2.9 – 7.9 under no-wind

conditions. They conducted analyses to show the influences of wind speed and heat transfer fluid mass flow rate on the collector efficiency to identify the optimum operating conditions.

In the EU project Endothermic Technology for Energy Efficient Housing, Stojanović et al. (2010) studied the long-term performance of a full-scale Solar-Assisted Heat Pump System (SAHPS) for residential heating in Nordic climatic conditions. The SAHPS consists of a roof-integrated flat plate unglazed solar collector with internal ducts for carrying heat transfer fluids. The SAHPS is illustrated in Figure 2.27. Their research showed that the SAHPS was successful in two years of full operations to fulfil heating requirements with system performance, indicated by Seasonal Performance Factor (SPF), to be $\mathrm{SPF}_{\mathrm{HeatPump}} = 2.85$ and $\mathrm{SPF}_{\mathrm{SAHPS}} = 2.09$. However, it was noticed that the square-shaped internal ducts were highly susceptible to leaking.

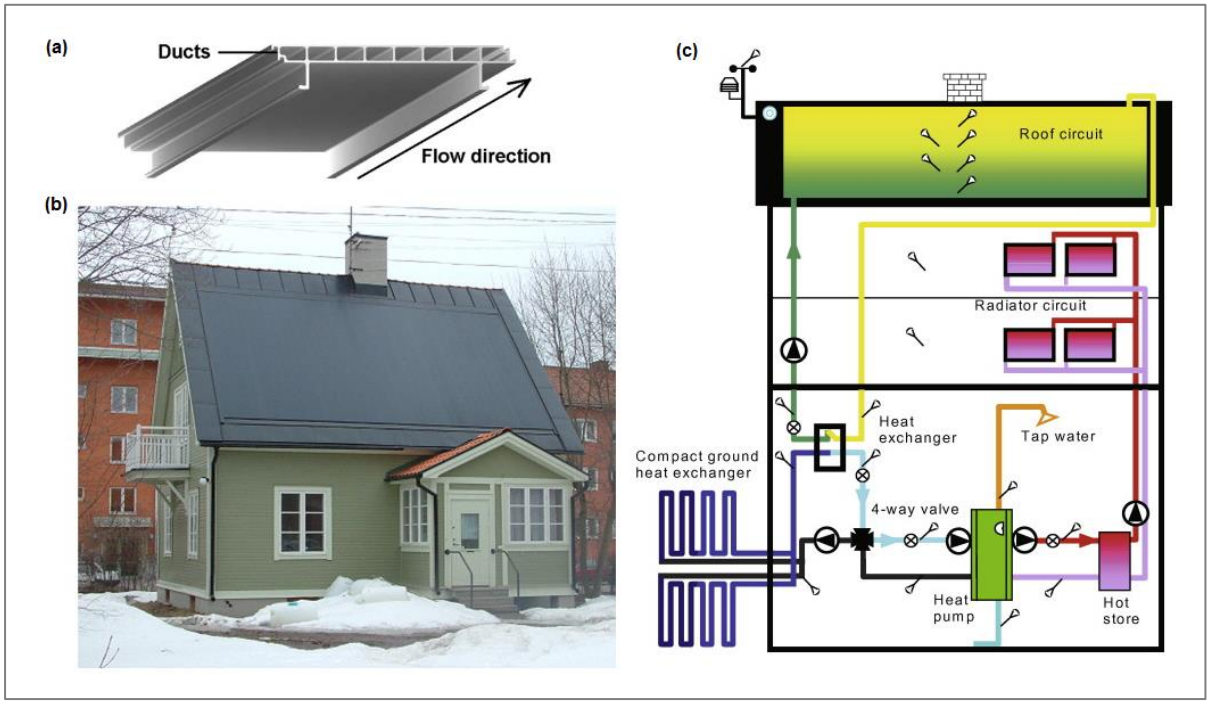

Figure 2.27: Illustration of the unglazed absorber with internal ducts (a), picture of the collector integrated with a house in Sandviken, Sweden (b), and the schematic of the solar-assisted heat pump system (c) (Stojanović et al., 2010)

Ji et al. (2011) investigated a building-integrated dual-function solar collector that was able to provide water heating in warm seasons and passive space heating in cold winter, as illustrated in Figure 2.28. Their results showed that, on typical summer days, the collector can heat up water in storage tank to more than 40^{o}C with thermal efficiency above 50% and solar heat gain by water at around 3.4 MJ/m^2. For typical autumn days, the water temperature could reach 48 ^{o}C with a thermal efficiency of 48.4% and heat energy gain of 6.57 MJ/m^2.

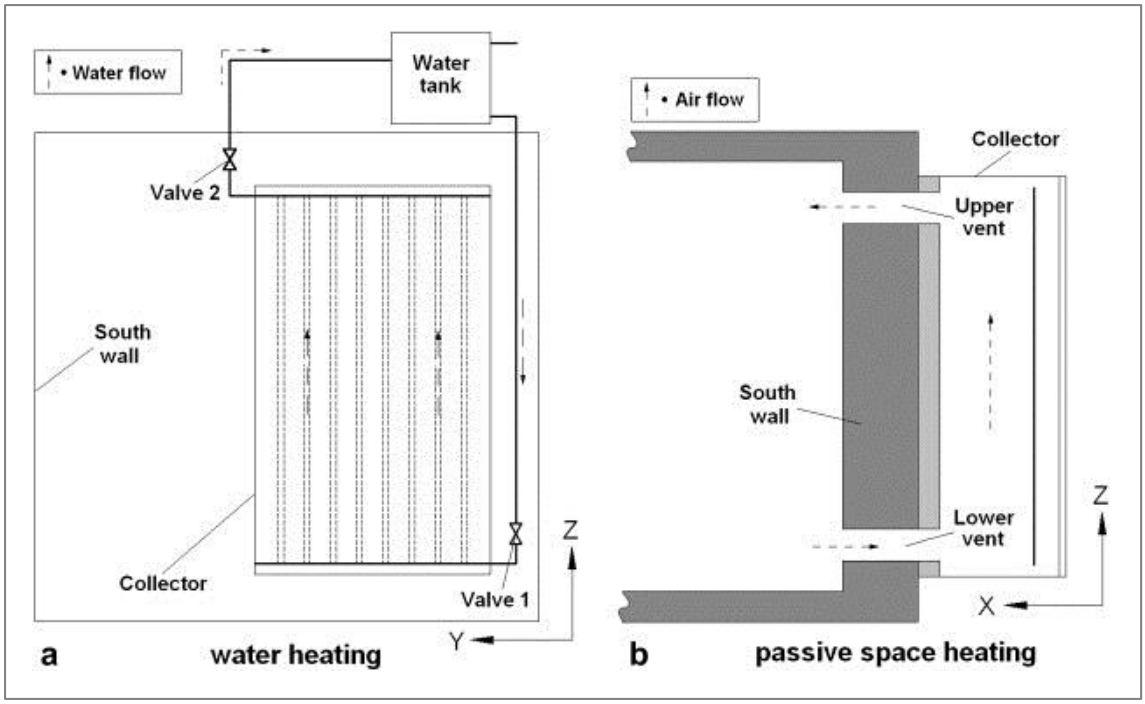

Figure 2.28: Illustration of a building-integrated, dual function solar collector (Ji et al., 2011)

The majority of solar thermal collectors employ metal absorbers which are relatively expansive to buy and install. There has been continuous research on developing polymeric solar collectors to reduce production and installation costs. Cristofari et al. (2002) studied the performance of a flat plate solar collector wholly made of a copolymer material and investigated the effects of various parameters including insulation thickness, flow rate and fluid layer thickness. Experimental results on a Mediterranean site showed yearly mean efficiencies of 56.5% without wind and about 49% for a wind speed of 5 m/s. It was also showed that employing polymeric materials can reduce the collector weight by 50%. Research conducted by Koehl et al. (2014) for the Task 39 of Solar Heating and Cooling Programme of the International Energy Agency exhibited designs, developments and optimisations of polymer based solar thermal systems. One of their partner companies, Aventa, developed an all-polymeric solar collector for building integration (Figure 2.29). The polymeric collector is based on extruded Polyphenylene Sulphide and Polycarbonate that can be manufactured in sizes from 205 to 580cm in length with a width of 60cm. Its flexible scalability allows it to be adjusted to fit onto various roof and façade structures. In addition, its design has fairly good aesthetics making it appealing for architectural applications.

The majority of existing researches of building-integrated solar thermal collectors focused on unglazed collectors that are used for low temperature applications. These unglazed collectors mainly employed manifold tubing configuration that are susceptible to leaking due to the presence of welded joints and were studied with weather data mostly from developed countries. In this research, the performance of building-integrated serpentine-tubed collectors (glazed/unglazed) under a wide range of weather conditions is studied to contribute new knowledge of collector designs and applications to the solar thermal industry.

Figure 2.29: Building-integrated polymeric collectors developed by Aventa (Koehl et al., 2014)

2.6 Mathematical Analysis

Duffie and Beckman (2013) conducted comprehensive researches on solar thermal collectors and have developed detailed mathematical models for design and prediction. Their reputed studies have been widely used by numerous researchers to derive and modify to obtain appropriate approaches for different designs and scenarios, (Yadav and Bhagoria, 2013, Viorel, 2007, Tooraj et al., 2012, Facão and Oliveira, 2006, Cadafalch, 2010, Altamush Siddiqui, 1997, Alireza and Kamran, 2009). The performance of a solar water heating system is dependent on the three main components: the solar collector, the heat exchanger and the storage tank.

2.6.1 Energy Balance of Solar Collector

The energy balance of flat-plate collectors was researched most extensively among all collector types with well-recognised outcome (Duffie and Beckman, 2013). The reason being that all solar thermal collectors have similar working mechanisms but flat-plate collectors have simpler geometries that can be easily adopted and modified to describe other more complicated geometries.

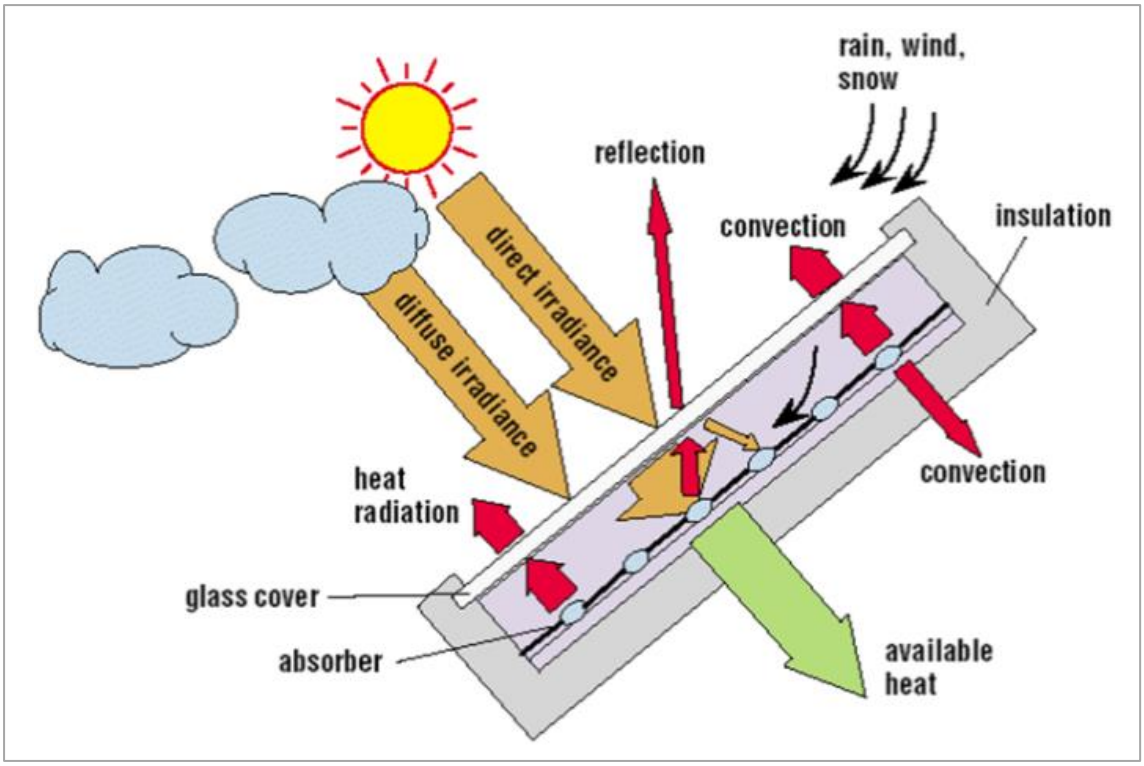

Figure 2.30: Schematic diagram of energy balance in a flat-plate collector (Quaschning, 2004)

The overall energy balance of a typical flat-plate collector at a steady state is illustrated in Figure 2.30 and could be expressed using energy transfer rate Q as:

$$Q_u = Q_{in} - Q_L \tag{2.1}$$

The solar input energy absorbed by the solar collector depends on the optical properties of its glazing cover and absorber plate, which can be estimated as:

$$Q_{in} = A_c I\ (\tau\alpha) \tag{2.2}$$

The heat loss Q_l from the collector to the ambient is:

$$Q_l = A_c U_L (T_c - T_{am}) \tag{2.3}$$

Substitute equation (2.2) and (2.3) into (2.1), we can obtain:

$$Q_u = A_c (I(\tau\alpha) - U_L (T_c - T_{am})) \tag{2.4}$$

It is generally assumed that heat losses are released through the top, bottom and sides of the collector. U_L is defined as the collector overall loss coefficient that is the sum of the top, bottom and edge loss coefficients:

$$U_L = U_{top} + U_{bot} + U_{edge}\ (W/m^2K) \tag{2.5}$$

The top loss coefficient U_{top} is a function of the number and properties of the glazing cover as well as the ambient temperature:

$$U_{top} = \left(\frac{N}{\frac{C}{T_c}\left[\frac{(T_c - T_{am})}{N+f}\right]^e} + \frac{1}{h_w} \right)^{-1} + \frac{\sigma_{sb}(T_c + T_{am})\left(T_c^2 + T_{am}^2\right)}{\frac{1}{\varepsilon_c + 0.00591 N h_w} + \frac{2N + f - 1 + 0.133\varepsilon_c}{\varepsilon_c} - N} \quad (2.6)$$

$N = number\ of\ glazing\ covers$

$f = (1 + 0.089h_w - 0.1166h_w\varepsilon_c)(1 + 0.07866N)$

$C = 520(1 - 0.000051\beta^2)$

$e = 0.43(1 - 100/T_c)$

The heat losses of back insulation are estimated to be released via conduction, which is determined by the thermal conductivity and thickness of the insulation material:

$$U_{bot} = \frac{k_{ins,bot}}{L_{ins,bot}} \quad (2.7)$$

The edge losses are estimated by assuming one-dimensional sideways heat flow around the perimeter of the collector system. The losses through the edge should be referenced to the collector area:

$$U_{edge} = \left(\frac{k_{ins,edge}}{L_{ins,edge}}\right)\left(\frac{A_{edge}}{A_c}\right) \quad (2.8)$$

Equation 2.4 can be used to calculate Q_u, but it is difficult to measure the mean temperature across the collector plate. Therefore, Hottel and Whillier (1955) and Bliss Jr (1959) introduced a collector removal factor F_R to calculate the useful heat gain Q_u, assuming that the collector temperature T_c is equal to the inlet fluid temperature T_{if}. The equation 2.4 can be reformulated as:

$$Q_u = A_c F_R\big(I(\tau\alpha) - U_L(T_i - T_{am})\big) \quad (2.9)$$

The useful heat gained by the heat transfer fluid can be estimated as:

$$Q_{u,f} = C_{p,f}\dot{m}_f(T_o - T_i) \quad (2.10)$$

The collector removal factor F_R is defined as the ratio of the heat gained by the working fluid to the heat gained in the condition that the mean collector temperature equals the inlet fluid temperature:

$$F_R = \frac{Q_{u,f}}{Q_u} = \frac{C_{p,f}\dot{m}_f(T_o - T_i)}{A_c\big(I(\tau\alpha) - U_L(T_i - T_{am})\big)} \quad (2.11)$$

The collector efficiency η is the ratio of the useful energy gained by the collector to the incident solar radiation energy on the collector during a specified period of time:

$$\eta = \frac{\int Q_u\, dt}{A_c \int I\, dt} \quad (2.12)$$

Adapted from equation 2.9, Cooper and Dunkle (1981) developed linear and non-linear relationships to determine the variation of the collector efficiency with the operating temperature depending on the characteristics of the collector. Their works lead to the following expressions for the instantaneous efficiency:

For a linear relationship: $\eta_i = F_R(\tau\alpha) - a\left(\frac{T_c - T_{am}}{I}\right)$ (2.13)

For a non-linear relationship: $\eta_i = F_R(\tau\alpha) - a\left(\frac{T_c - T_{am}}{I}\right) - b\left(\frac{(T_c - T_{am})^2}{I}\right)$ (2.14)

Where *a* and *b* are constants at a particular wind speed and other parameters with wind speed dependence that contribute to heat loss factors. Equation 2.10 and 2.11 can be used to express the variations of the efficiency with the combined factor of $\frac{T_c - T_{am}}{I}$ for typical solar collectors including unglazed flat-plate (pool heaters), single glazed flat-plate, double glazed flat-plate and evacuated tubes, illustrated in Figure 2.31.

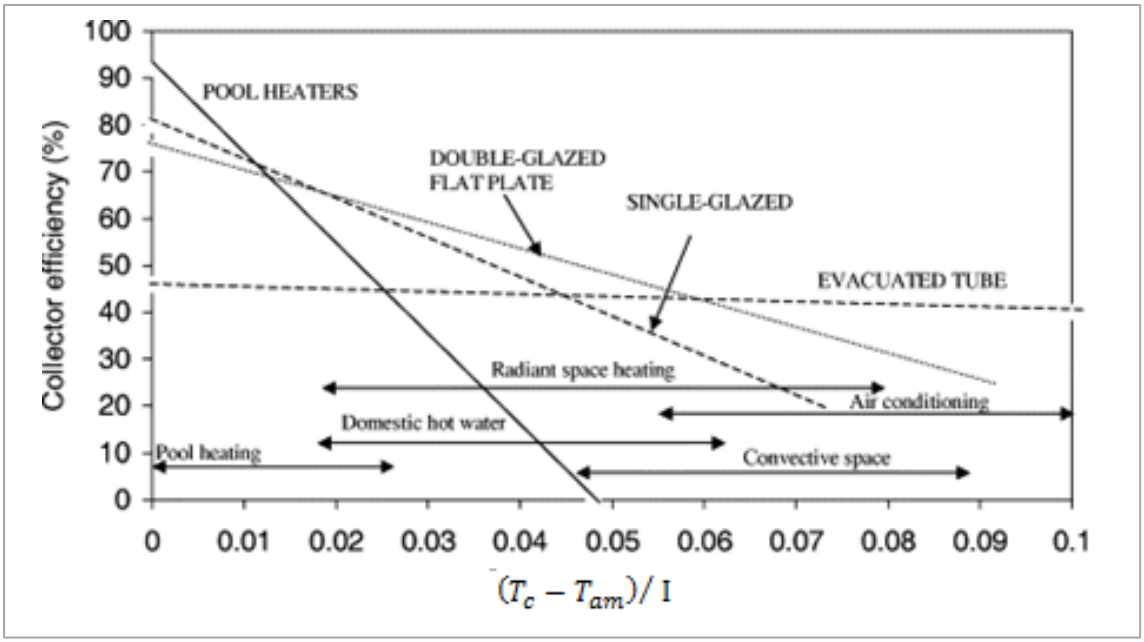

Figure 2.31: Variations of the efficiency with the combined factor ($T_c - T_{am}$) / I for typical solar collectors (Kalogirou, 2004b)

Figure 2.31 showed that reducing the solar input (I) would lead to decreases in collector efficiency. To represent temperature effects on the collector efficiency more clearly, IEA (2012) employed ($T_c - T_{am}$) as the function of collector efficiency in equations 2.13 and 2.14, their relationships are illustrated in Figure 2.32.

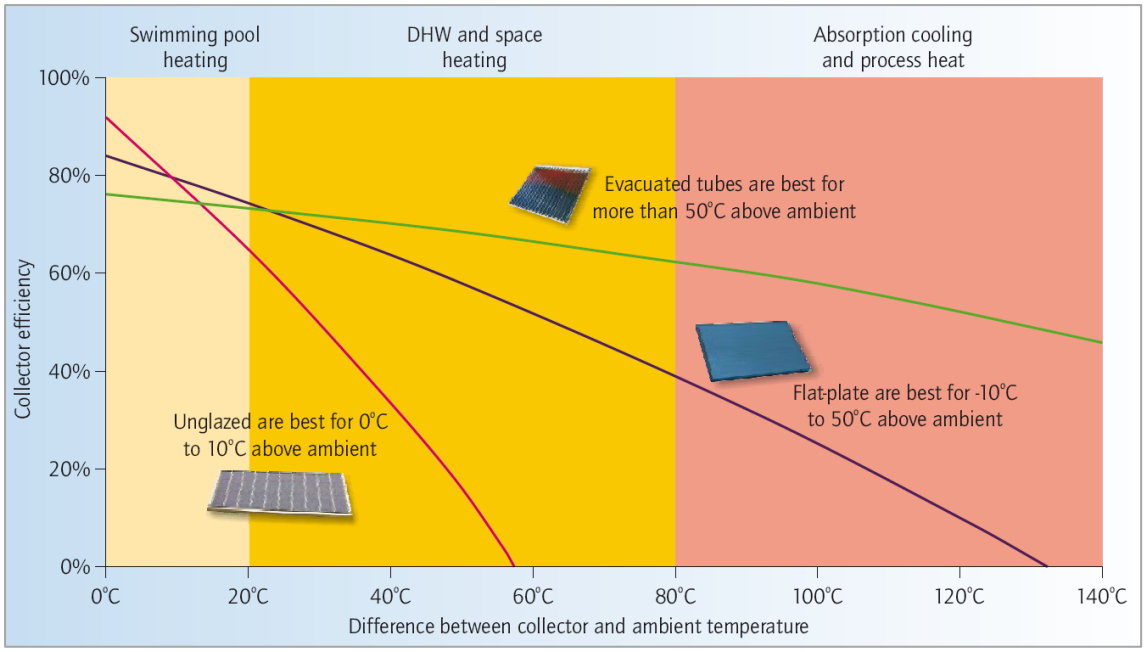

Figure 2.32: Variations of collector efficiency with ($T_c - T_{am}$) for typical solar collectors (IEA, 2012)

In Figure 2.32, the slopes of the lines represent their heat loss factors. The steeper the slope, the more the collector loses heat as its temperature increases. Unglazed collectors have the steepest slope due to its poor insulation. Evacuated tube collectors (ETC) generally begin with lower efficiency than flat-plate collectors (FTC). However, as the collector temperature increases, the efficiency in ETCs decreases less rapidly than that in FTCs, mainly because of their excellent insulation provided by vacuum.

2.6.2 Energy Balance of Heat Exchanger

In indirect type of solar thermal systems, collectors are used in combination with a heat exchanger between collector and storage allowing the use of antifreeze solutions in the collector loop. A common circuit of this type is shown in Figure 2.33 below.

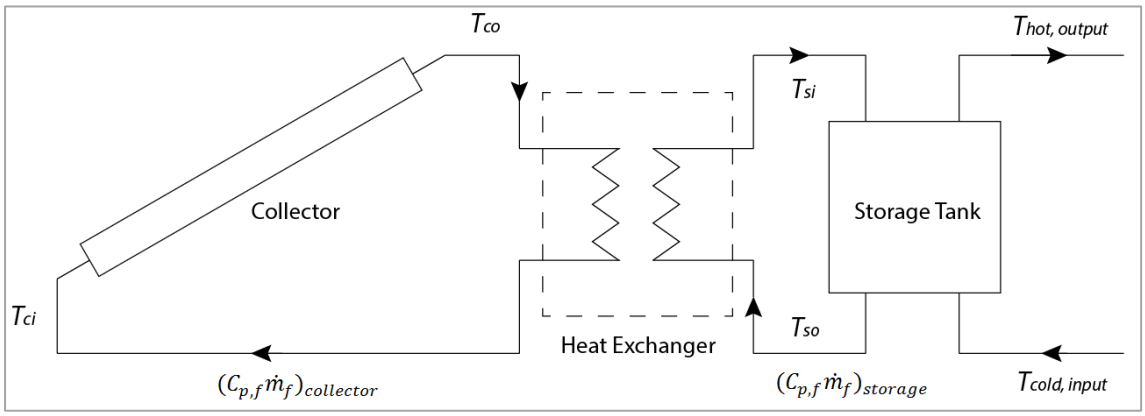

Figure 2.33: Schematic of a solar thermal system with a heat exchanger between collector and storage tank

The presence of heat exchanger can influence the performance of solar thermal system and the level of influence is affected by the heat exchanger effectiveness ε, which is defined as the ratio of the actual heat exchange rate to the maximum possible heat exchange rate. Kays and London (1998) developed an expression of heat exchanger performance in terms of effectiveness:

$$Q_{HX} = \varepsilon(C_{p,f}\dot{m}_f)_{min}(T_{co} - T_{so}) \quad (2.15)$$

Where $(C_{p,f}\dot{m}_f)_{min}$ is the smaller of the fluid capacitance rates (flow rate $\dot{m}_f$ times fluid heat capacity $C_{p,f}$) on the collector side $(C_{p,f}\dot{m}_f)_c$ and storage side $(C_{p,f}\dot{m}_f)_s$ of the heat exchanger, T_{co} is the outlet fluid temperature from the collector, and T_{so} is the outlet fluid temperature from the storage (close to the temperature of cold input fluid).

The useful gain of the collector is represented as:

$$Q_u = A_c F_R\big(I(\tau\alpha) - U_L(T_{co} - T_{ci})\big) \quad (2.16)$$

And also:

$$Q_u = C_{p,f}\dot{m}_f(T_{co} - T_{ci}) \quad (2.17)$$

de Winter (1975) derived a useful analytical combination of equations for the collector and the heat exchanger. Duffie and Beckman (2013) developed a single expression incorporating the collector equation and the heat exchanger equation combining equations 2.12, 2.13 and 2.14. The expression has similar form as the collector equation (2.13), but it has a reduced value of $F_R{}'$ due to the presence of heat exchanger:

$$Q_u = A_c F_R{}'\big(I(\tau\alpha) - U_L(T_{co} - T_{am})\big) \quad (2.18)$$

Where the modified collector heat removal factor $F_R{}'$ accounts for the presence of the heat exchanger and its ratio with F_R is given by:

$$\frac{F_R{}'}{F_R} = \left[1 + \left(\frac{A_c F_R U_L}{(C_{p,f}\dot{m}_f)_c}\right)\left(\frac{(C_{p,f}\dot{m}_f)_c}{\varepsilon(C_{p,f}\dot{m}_f)_{min}} - 1\right)\right]^{-1} \quad (2.19)$$

The ratio $F_R{}'/F_R$ can be regarded as a penalty indicator of the collector performance because the presence of heat exchanger causes the collector to operate at higher temperatures. From another point of view, the ratio $F_R/F_R{}'$ can be considered as the fractional increase in collector area needed for the system with the heat exchanger to produce the same amount of energy as the system without the heat exchanger.

2.6.3 Energy Balance of Storage Tank

In direct solar thermal systems, collectors are directly connected to the water storage tank without the presence of a heat exchanger. Figure 2.34 shows a typical direct solar thermal system using forced circulation (pumped).

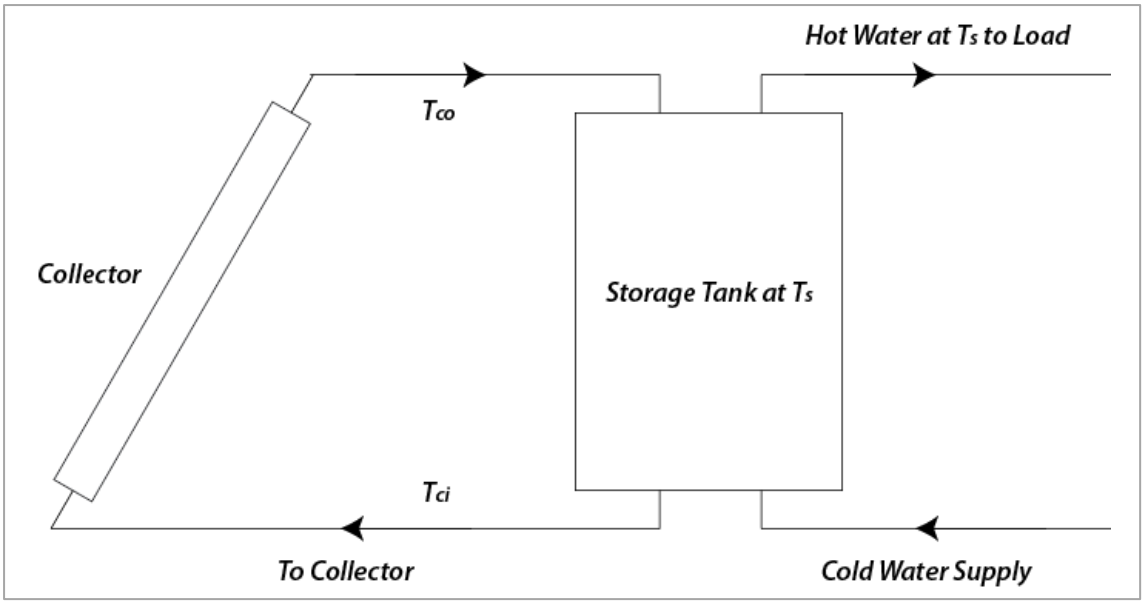

Figure 2.34: Schematic of a typical direct SWH system with collector connecting directly to storage tank

The water (or other fluid) stored in a fully mixed or unstratified storage tank has uniform temperature. The energy storage capacity of the storage tank operating over a finite temperature difference is given by:

$$Q_{st} = \left(C_{p,f} m_f\right)_{st} (T_o - T_{st}) \tag{2.20}$$

Where Q_{st} is the total heat energy capacity for a cycle operating through the temperature range $(T_o - T_{st})$ and m_f is the mass of water (or other fluid) in the storage. The lower limit of the operation temperature range for most applications is defined by the minimum temperature requirements of the process. The upper limit may be determined by the process, the vapour pressure of the liquid, or the collector heat loss. Illustrated in Figure 2.35, an energy balance of the un-stratified tank is given as:

$$\left(C_{p,f} m_f\right)_{st} \frac{dT_{st}}{dt} = Q_u - \dot{L}_{st} - (UA)_{st}(T_{st} - T'_{am}) \tag{2.21}$$

Where Q_u is the useful energy rate delivered from the collector and $\dot{L}_s$ is the removal rate of energy to the load and T'_a is the ambient temperature for the storage tank. The term $(UA)_{st}$ defines the energy loss from the storage to surroundings via its surface.

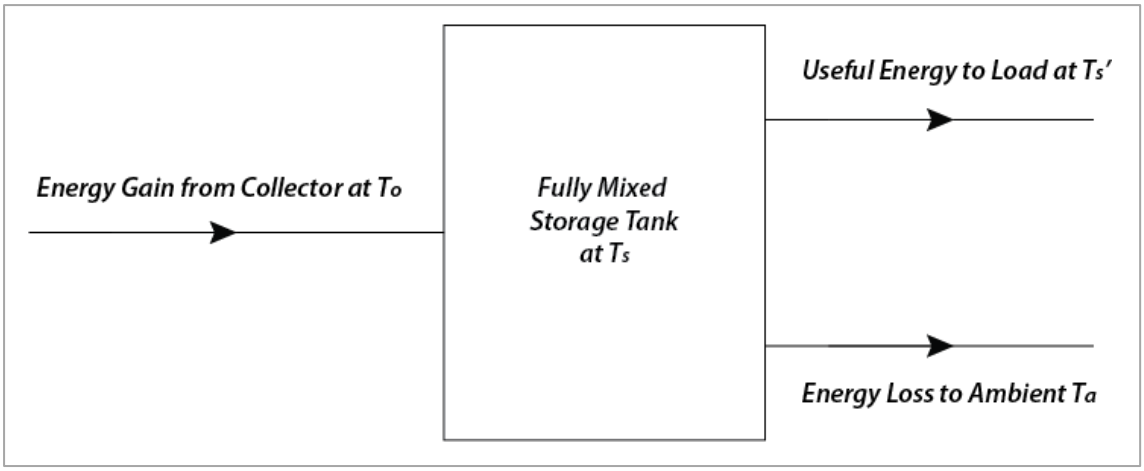

Figure 2.35: Energy balance of an un-stratified storage of mass m operating in ambient temperature T_a

For a not fully mixed (stratified) storage tank, it could be modelled by dividing the water into layers and establishing energy balance equation for each layer. Equation 2.21 can be integrated over time to determine the long-term performance of the storage tank:

$$T_{st}^{+} = T_{st} + \frac{\Delta t}{(C_{p,f} m_f)_{st}} [Q_u - L_{st} - (UA)_{st}(T_{st} - T_{am})] \quad (2.22)$$

Therefore, an entire day's useful energy, tank water temperature, load demand and contribution of the solar energy in meeting that demand can be obtained from various design parameters, e.g. collector area, tank capacity and time when auxiliary energy is needed.

2.7 Scope of Research

The scope of research for this project is defined to cover:

- Performance testing and analysis of the LSFPSC prototype
- Introducing modifications to the LSFPSC prototype for enhancing performance and improving structural integration
- Using mathematical modelling and computer simulation to assess the performance of the LSFPSC under various weather conditions for different applications

Based on the Scope of Research, next chapter elaborates the detailed Research and Development plan for this project with experimental designs.

CHAPTER 3

3. Methodology

3.1 Research and Development Plan

This project is mainly concerned about the research and development (R&D) of a building-integrated large scale flat plate solar collector (LSFPSC) with continuous serpentine tubing. The main target is to improve its design to achieve high efficiency and excellent cost effectiveness. To reach this target, the R&D process was designed with progressive targets which were then categorised into three stages:

1st Stage – Preliminary Experiments and Analyses

The aim of this stage was to develop a LSFPSC prototype based on the initial design and establish an experimental facility to run performance tests on the prototype to find out whether it meets the basic operating standards. The prototype must be able to perform without any safety issues and produce reasonable useful energy output consistently. A monitoring mechanism was developed to acquire performance data from different components of the prototype during testing for analysis. The analysis should be capable of providing identification of important parameters, understanding contribution of components to efficiency and an overall performance assessment of the prototype.

2nd Stage – Mathematical Modelling and Introducing System Improvements

This stage focuses on bringing improvements to the prototype to increase its performance, a cyclic process was used:

1. Performance analysis results were employed to build mathematical models and computer simulation to simulate actual performance of the prototype. The simulation can test improvement proposals (e.g. new designs, variation of important parameters) to evaluate their effects in system efficiency.
2. Together with feasible assessment of practicability and economic viability, the simulation results acted as guideline to decide if certain proposals are worthy to be tested in practice. This helped reducing costs of labour, materials and energy.
3. Chosen proposals were experimented with collected data for performance analysis to validate with simulation output and subjected to feasible assessment for final justification.
4. Justified modifications were integrated to become part of the final prototype design, and the process restarts at step 1 for further enhancements.

The cyclic process allowed improvements to be brought into the LSFPSC design continuously until an optimal solution is achieved.

3rd Stage – Advanced Modelling and Application Assessment

This stage began when the prototype was optimised with improvements to perform with desirable efficiency. The main purpose of this stage was to use the computer simulation

to assess the performance of the LSFPSC in actual applications (i.e. domestic hot water, space heating) under different climate conditions to determine the optimal regions for deployment. Economic evaluation was conducted to couple with the deployment suitability to provide a good indicator of the LSPFSC's commercial potentials.

3.2 Experimental Design

3.2.1 Experiment Set-up

Figure 3.1 shows the schematic of the experimental set-up, which was employed to test if the prototype can operate safely and produce output that meets the basic requirements of a solar thermal system. This set-up consists of a controllable testing environment and five main performing components:

- ***Testing room:*** built with highly insulating materials, can be opened for natural air flow or closed for artificial ventilation within the test room;
- ***Solar simulator:*** employed as an artificial light source to produce radiant energy, simulating the sun;
- ***LSFPSC prototype:*** absorbs the radiant energy and delivers it into the circulation system as heat energy;
- ***Circulation system:*** driven by a circulating pump, it carries heat transfer fluid (HTF) that removes heat from the solar collector;
- ***Heat exchanger:*** allows heated HTF to deliver its thermal energy into the colder water within the storage tank;
- ***Storage tank:*** acts as the secondary circuit that extracts heated water to be utilised as useful thermal energy.

The drain/filling valve allows heat transfer fluid to be filled into or drained out from the circulation system. An expansion vessel is connected to the primary circuit to accommodate volume expansion of heat transfer fluid under over-heating circumstances. Manual release of pressure and unnecessary gas in the circulation system can be done safely through an over-pressure safety valve. The flowmeter, pressure transmitter and temperature sensors are connected with a data acquisition unit (not shown in Figure 3.1) which monitors and records data on PC for performance analysis.

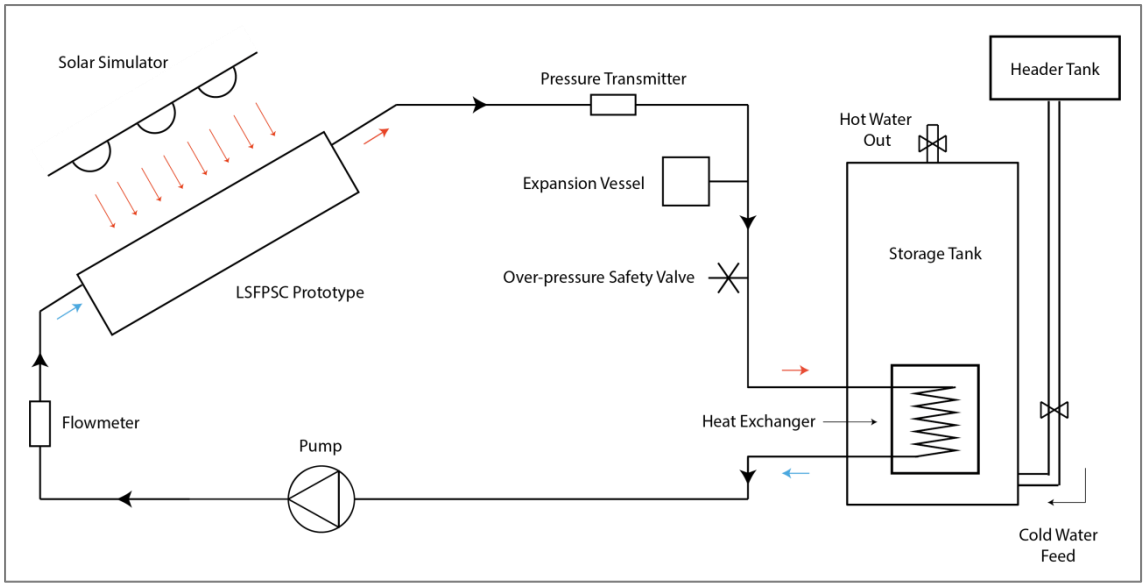

Figure 3.1: Experimental Set-up

In the following sections, the testing environment and the main components are elaborated in schematics with descriptions of their functions and importance. Similar experiment layouts and data logger configuration will be employed in the future stages with relevant modifications to meet stage-specified requirements.

3.2.2 Testing Room

The testing room was built with strong insulating materials in order to be isolated from the surroundings. It provides a controllable experimental environment that allows tests to be conducted for obtaining comparable results. As shown in Figure 3.2, the testing room has four walls each consists of three insulating boards and a sliding ventilation door with a removable roof. The LSFPSC prototype was placed in the centre with the circulation system that goes in and out through the north wall connecting to other measuring instruments and storage unit. The prototype can be experimented in the testing room with no wind or a ventilation fan could be used to create windy conditions.

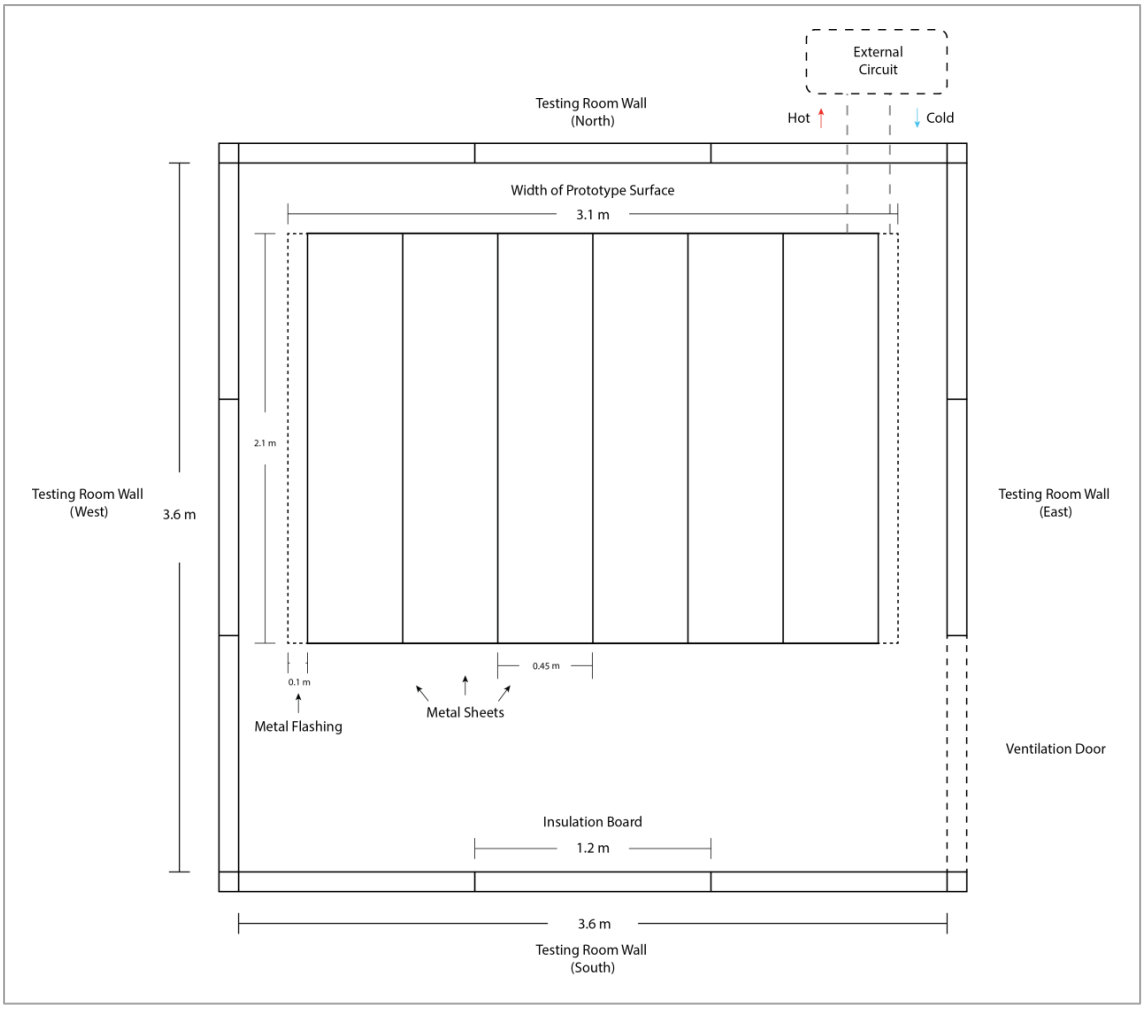

Figure 3.2: Basic Structure and Arrangements in Testing Room

3.2.3 Solar Collector

The LSFPSC prototype was built on a supporting frame that resembles a roof structure with a pitch angle of approximately 30^{o}, as shown in Figure 3.3. The prototype comprises with three components:

Absorber: absorbs incoming radiation and converts it into heat energy. It is formed by six stainless steel roof sheets (1mm in thickness) that are lightweight and have a fixing mechanism allowing them to be joined side-by-side easily by clamping to create a firm and strong surface.

Circulation system: carries heat transfer fluid to absorb and remove heat away from the exchange chamber. It goes into the collector from the bottom and leaves from the top providing a height gradient where thermosyphon effect can occur for natural circulation or compliment pumped circulation.

Back insulation: made of a rigid, compact and highly insulating material (Celotex) that is normally used in building applications as loft insulation with a thickness of 100mm. It insulates the collector, which works at high temperatures, to avoid overheating in the space underneath. This set-up allows the safety in future practical applications to be

assessed. The specification of Celotex is listed in Table B.4, Appendix B together with other alternative materials.

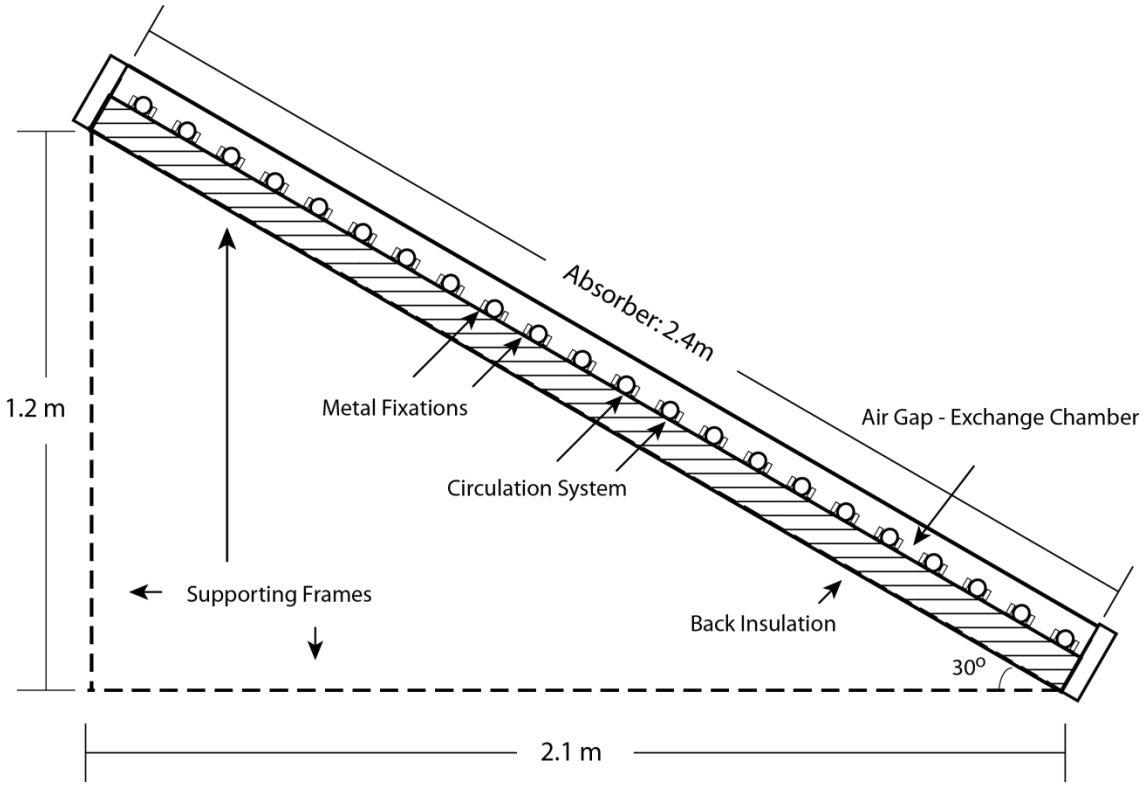

Figure 3.3: Cross-sectional view of the LSFPSC prototype for the 1st stage testing

3.2.4 Solar Simulator

The solar simulator employs two lighting machines each equipped with 6 x 1000W quartz-halogen lamps with spectral irradiance shown in Figure 3.4. Even though the lamp's spectrum is different from the solar spectrum but it has no impact on the accuracy of testing results as the total absorptivity of the black paint used on the prototype's absorber surface is about 0.90 for both visible and infrared spectrum range. Therefore, when two radiation beams arrive on the absorber surface that have the same irradiance (e.g. 1000 W/m^2) but with different spectrums (e.g. beam A has 30% visible and 70% infrared and beam B has 10% visible and 90% infrared), the prototype would absorb the same amount of energy from each beam (900 W/m^2).

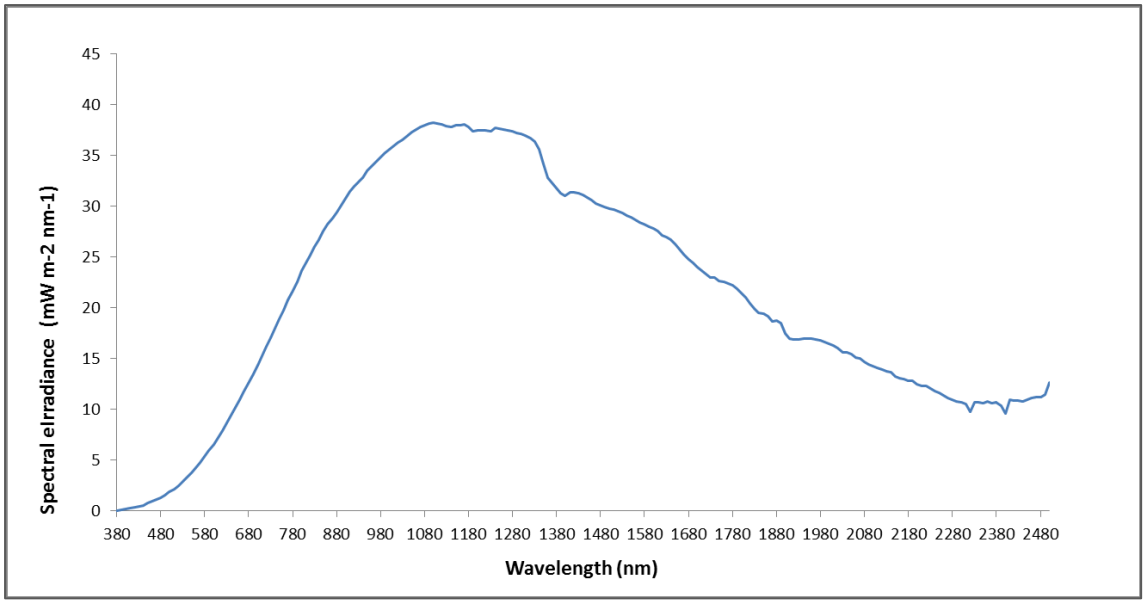

Figure 3.4: Spectral irradiance of the solar simulator

The simulator has built-in control system to set lighting time and vary the amount of energy output. They are positioned approximately 80cm away from the collector surface with an arrangement shown in Figure 3.5 to distribute their radiation evenly. For the testing in the 1st Stage, the irradiance on the prototype surface was estimated based on the known energy output of the lamps due to the limitation of instrument. For the testing in the 2nd Stage, the irradiance on the collector surface was measured by a Kipp & Zonen CMP3 pyranometer which is shown in Figure 3.6 and its specifications are listed in Table 3.1.

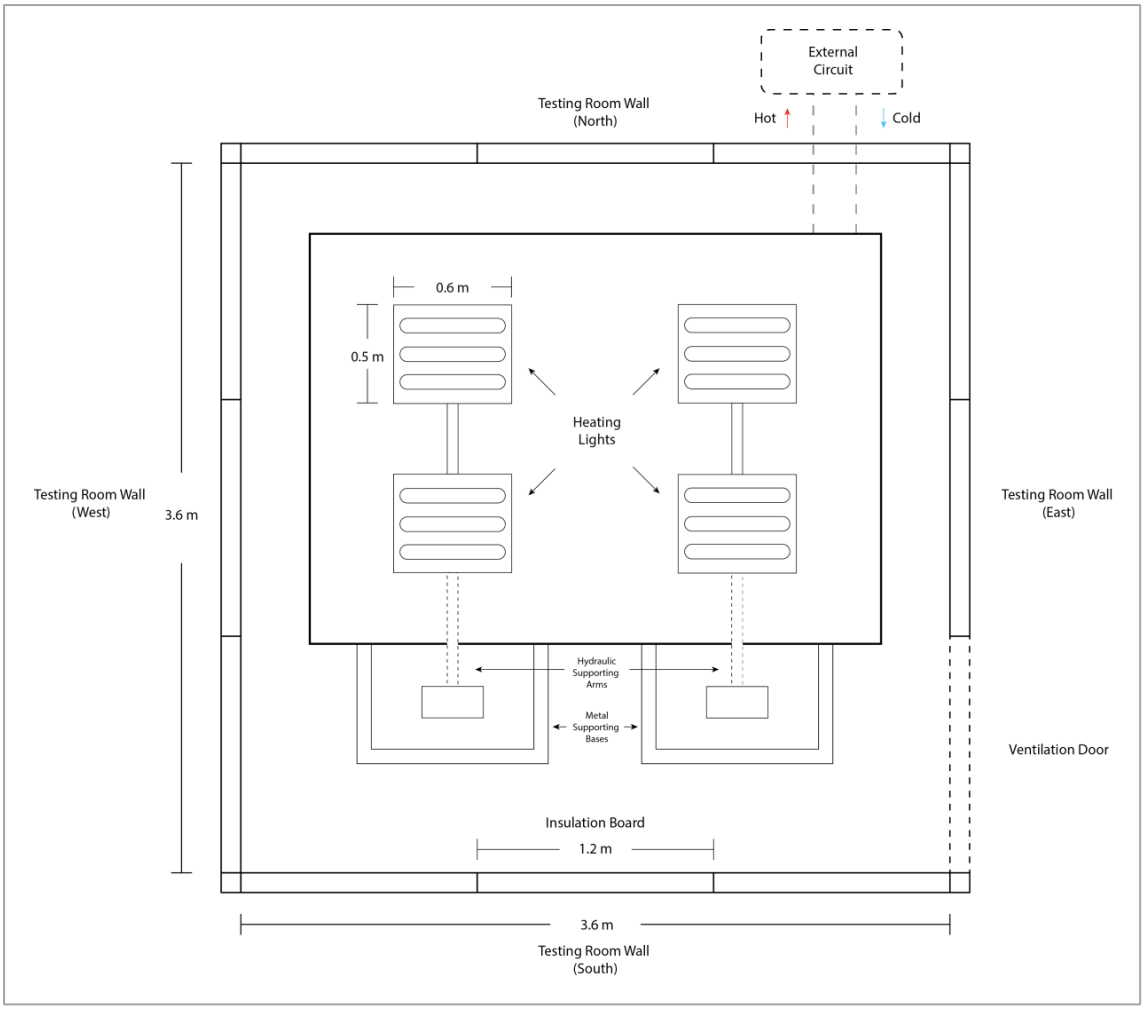

Figure 3.5: Arrangement of Heating Lights in the Testing Room

Figure 3.6: Kipp & Zonen CMP3 pyranometer (Source: Kipp & Zonen)

Table 3.1: Specifications of the Kipp & Zonen CMP3 pyranometer

Spectral range	300 to 2800 nm
Sensitivity	5 to 20 µV/W/m²
Response time	18 s
Operational temperature range	-40 °C to +80 °C
Maximum solar irradiance	2000 W/m²
Field of view	180 °

3.2.5 The Circulation System

The circulation system employed a serpentine tubing configuration as shown in Figure 3.7. Unlike normal manifold tubing configuration, the serpentine tubing was designed to have continuous length underneath the absorber without the presence of any welded or fitted joints where leaking are prone to occur. The tubing has a total length of 55m with 23 parallel segments and each segment is approximately 2.5m long. Tubing joints are only present in the outlet and inlet of the LSFPSC which are located in easy-to-access area (loft area) minimising efforts for maintenance. The serpentine tubing was placed and fixed firmly on the back insulation using metal clips. In terms of materials, three layered (PVC-Al-PVC) underground pipe was employed in the 1st Stage testing and copper pipe was employed in the 2nd Stage testing. Their specifications are shown in Table B.3, Appendix B, together with a selection of other identified alternative circulation system candidates.

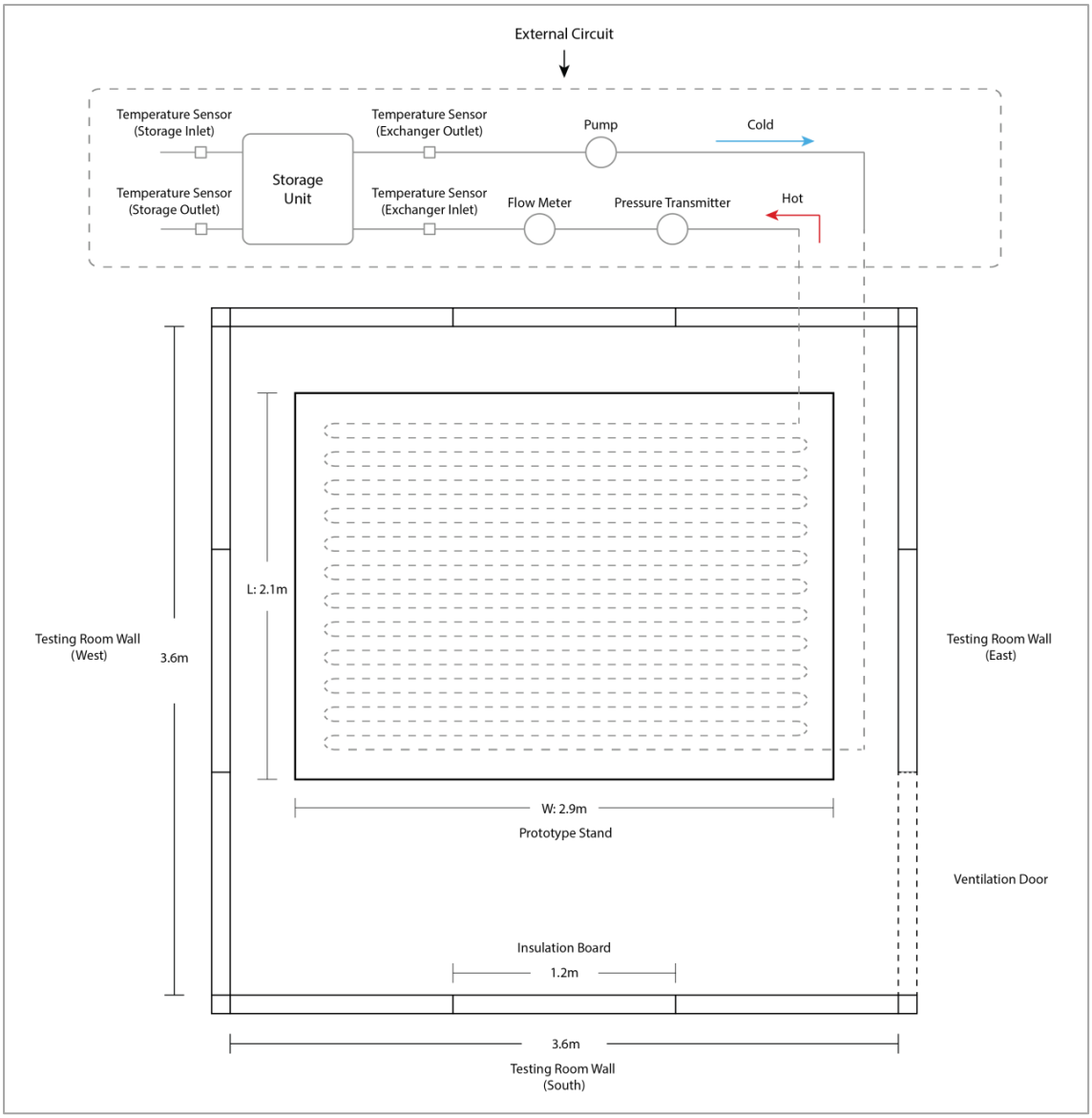

Figure 3.7: Arrangement of the Circulation System and External Circuit

3.2.6 Storage Tank

The storage tank has a volume of 118L with a copper-coiled heat exchanger where the circulation system connects to and delivers heat energy to its stored cold water. A header tank is employed to provide cold water supply and acts as a pressure source allowing hot water to be extracted.

3.2.7 Data Acquisition Unit

In order to monitor the temperature distributions of the LSFPSC, K-type thermocouples were installed crossed the collector surface, the circulation system and the interspace between the circulation system segments. Thermocouples were also installed on the inlet and outlet of the LSFPSC and the storage tank to collect temperature data for performance analysis.

A Titan FT2 Hall Effect flow meter was employed to measure the flow rates in the circulation system. It produces analogue data (frequency) proportional to flow which then was converted into current readings (mA) by an analogue converter. The flow meter and the analogue converter are shown in Figure 3.8 and their specifications are listed in Table 3.2.

Table 3.2: Specifications of Titan FT2 flow meter and analogue converter

Titan FT2 Flow Meter	
Flow range	2.50 – 30 L/min
Operational temperature range	-15 °C to +125 °C
Approximate K factor	550
Accuracy	99.25%
Analogue Converter	
Signal output range	4 – 20 mA
Operational temperature range	0 °C to +50 °C
Frequency detection range	0.25/0.5 to 1000Hz

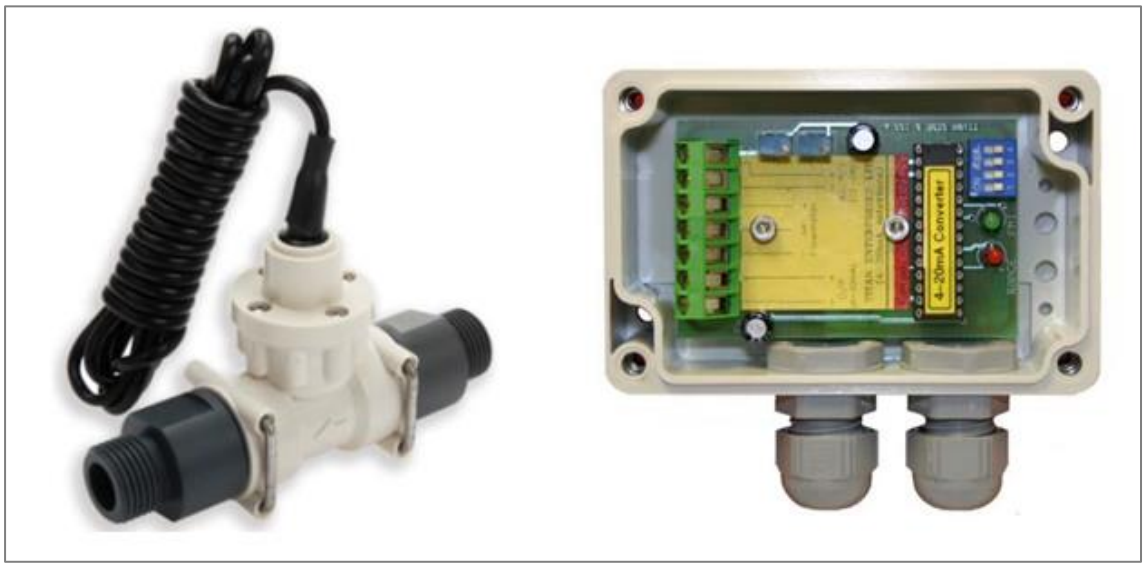

Figure 3.8: FT2 Hall Effect flow meter and analogue converter (Source: Titan Enterprise Ltd)

A Wika S-10 pressure transmitter was used to monitor the pressure within the circulation system for health and safety reasons. The pressure transmitter was installed with a cooling tower in order to avoid damages caused by the high temperature heat transfer fluid, both are shown in Figure 3.9 and the specifications are listed in Table 3.3.

Table 3.3: Specifications of Wika S-10 pressure transmitter

Wika S-10 Pressure Transmitter	
Pressure range	0 – 40 bar
Signal output range	4 – 20 mA
Operational temperature range	-30 °C to +100 °C
Accuracy	99.5%

Figure 3.9: Wika S-10 pressure transmitter and cooling tower (Source: Wika)

All these monitoring instruments were wired to multiplexers installed on an Agilent 34970A Data Acquisition Unit where data are recorded and transferred to the PC interface. The Data Acquisition unit and the multiplexer are shown in Figure 3.10. Each multiplexer has 20 voltage channels for thermocouple connections and 2 channels for the connections of flow meter and pressure transmitter. Three multiplexers were employed in total and their data channel configurations with the Data Acquisition unit and the instruments are shown in Appendix A.

Figure 3.10: Agilent 34970A Data Acquisition unit and 34901A Multiplexer (Source: Agilent)

For the 1st stage testing, the data acquisition unit had 40 communication channels (i.e. two multiplexers were employed) interfacing with measuring instruments, of which configuration is shown in Table A.1. For the 2nd stage testing, it was necessary to expand the communication capacity to the maximum (three multiplexers with 60 channels) to employed additional thermocouples to obtain more accurate data. Its detailed configuration is shown in Table A.2. Compare with the 1st stage configuration, the 2nd stage configuration employed nine thermocouples instead of six and on five locations (location 1 to 5) instead of three (location 1 to 3):

1. **Outer surface of the absorber:** is directly related to the amount of energy received by the absorber that is vital to understand the energy balance of the solar collector.
2. **Inner surface of the absorber:** is linked with the amount of energy delivered into the exchange chamber. The temperature gradient between the outer and the inner surfaces could be used as an indicator to determine convection effects.
3. **Air within the exchange chamber:** can be employed to understand energy loss and energy gain via convection within the exchange chamber.
4. **Air near the outer surface of the absorber:** can be used to analyse the convection loss from the outer surface of the absorber to the surrounding ambient air. It can also help on exploring the effectiveness of the insulation designs (e.g. glazing mechanisms).
5. **The circulation system:** will be the key on calculating the amount of useful energy delivered and estimating the overall system efficiency. The temperature distribution pattern can indicate whether heat saturation occurs within the solar collector i.e. the heat transfer fluid reaches a temperature cap without further noticeable increase before leaving the solar collector.

The expanded capacity allows thermal data to be collected from a more refined area and the additional monitoring locations acquires data for better understanding of temperature distribution to conduct more comprehensive performance of the LSFPSC.

Next chapter will present designs of experiment scenarios for preliminary testing and relevant performance analysis.

CHAPTER 4

4. 1st Stage – Preliminary Experiments and Analyses

4.1 Experiment Scenario Design

In order to assess actual performance of the LSFPSC, it is important for it to receive energy input from the solar simulator similar to the amount of actual solar energy received on the earth surface. Table 4.1 shows the solar radiation data collected by the UK Met Office in Bournemouth, 2011. From this data, two important parameters were adapted. One is the mean daily radiation (KJ/m^2), which is calculated by dividing the annual total global radiation with 365 days. Another one is the mean daily irradiance (W/m^2) that is calculated by dividing the mean daily radiation with mean daily sunshine hours. These two parameters were employed to design two experiment scenario for conducting preliminary testing on the LSFPSC prototype.

Table 4.1: Solar Radiation in Bournemouth, 2011 (Source: Met Office)

MONTH	Total Global Radiation (KJ/m^2)	Total Sunshine Hours	MONTH	Total Global Radiation (KJ/m^2)	Total Sunshine Hours
Jan	98206	52.3	July	505519	158.5
Feb	155267	42.8	Aug	478100	135.0
Mar	361382	145.0	Sep	363441	133.9
Apr	405714	217.5	Oct	193115	98.4
May	568712	189.2	Nov	109278	56.2
June	482357	172.7	Dec	79282	49.3
Annual Total Global Radiation				4030657	KJ/m^2
Mean Daily Radiation				11043	KJ/m^2
Mean Daily Sunshine Hours (Excl. Nov, Dec, Jan & Feb)				5	Hours
Mean Daily Irradiance				613	W/m^2

4.1.1 Scenario I

In this scenario, the solar simulator was set to 12000W output for approximately 100 minutes to generate a total amount of energy similar to the actual mean daily radiation (Table 4.2). It is expected that the output hot water temperature from the collector is much higher than the normal level as the prototype is subjected to higher radiation per unit area. Nevertheless, tests based on this scenario could provide good indications of the steady state efficiency of the LSFPSC prototype.

Table 4.2: Experiment Scenario I – Use of Mean Total Daily Radiation

Solar Simulator Output	12000	W
Testing Time (Approx.)	100	min
Collector Surface Area	6.96	m^2
Total Energy Received on the Collector during Testing Time	10345	KJ/m^2
Mean Irradiance on the Collector	1724	W/m^2

4.1.2 Scenario II

This scenario is designed to employ 4000W output from the solar simulator providing radiant energy similar to the actual mean daily irradiance (Table 4.3). It could provide a good approximation of the actual daily performance of the prototype, of which efficiency can be compared with results from scenario I for correlation.

Table 4.3: Experiment Scenario II – Use of Mean Daily Irradiance

Solar Simulator Output	4000	W
Testing Time (Approx.)	100	min
Collector Surface Area	6.96	m^2
Mean Irradiance on the Collector	575	W/m^2

4.2 Energy Balance of Solar Collector

Heat transfers of different components were identified to construct the energy balance of the LSFPSC prototype, as illustrated in Figure 4.1. In the 1st Stage of testing, the prototype employed has a large gap between the circulation system and the absorber which was about 5 – 10mm wide. This means the absorber and the circulation system were not in direct contact with each other. Therefore, the heat transfer from the absorber to the circulation system can only be done through the gap via convection in air and the gap was named 'exchange chamber' accordingly. In order to encourage convection to occur within the exchange chamber, the top and bottom of the LSFPSC were not fully sealed. However, in this case, convection could also take place from the exchange chamber to the surrounding to cause some heat loss. With the labelling convention for heat flows $Q_{modes,from-to}$, the energy balance equations of the LSFPSC can be written as:

$$Q_u = Q_{conv,c-circ} + Q_{rad,c-circ} = Q_{in} - Q_{rad,loss} - Q_{conv,loss} - Q_{loss,edge} \quad (4.1)$$

$$Q_{in} = I\alpha_c A_c = Q_{source} - Q_{refl,c-sur} \quad (4.2)$$

$$Q_{rad,loss} = Q_{rad,c-sur} + Q_{rad,c-ins} \quad (4.3)$$

$$Q_{conv,loss} = Q_{conv,c-sur} + Q_{conv,ex-sur} \quad (4.4)$$

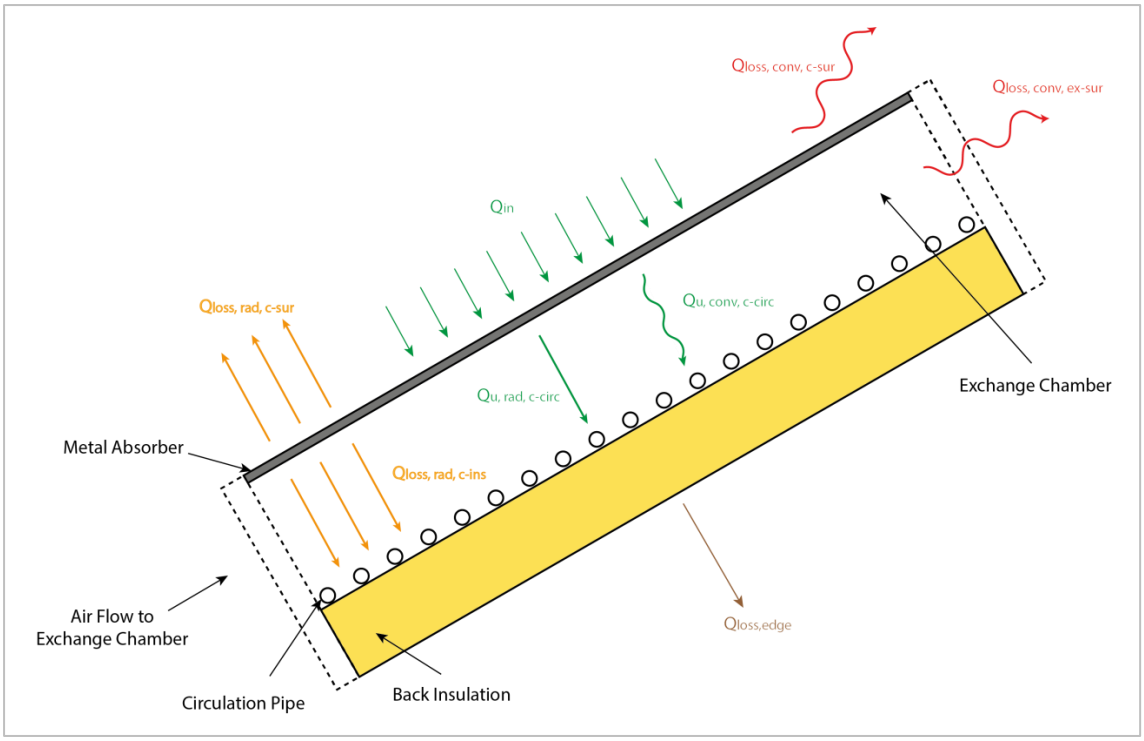

Figure 4.1: Energy Balance of the FES Solar Thermal System

Q_u is the total amount of useful energy delivered into the circulation system via convection and radiation. It can also be calculated based on the performance of the heat exchanger and the storage tank for comparative studies by adapting Equations (2.17) and (2.20):

$$Q_u = \left(C_{water} \mathrm{m}_{st}(T_{end} - T_{start})\right)/t_{test} \cong C_{htf}\dot{m}_{htf}(T_o - T_i) \qquad (4.5)$$

4.3 Energy Input

The value of Q_{source} is known due to the fact that the solar simulator is capable of producing a controllable amount of energy output. By using the equation (4.2), the energy input Q_{in} received by the absorber can be calculated using an absorber reflectance of 0.1 (based on the property of the black paint used on the absorber). The results are shown in Table 4.4 and 4.5.

Table 4.4: Energy Input Q_{in} for Scenario I

Energy output from the solar simulator (Q_{source})	12000	W
Energy loss due to reflection, assumed to be 10% ($Q_{refl,c-sur}$)	1200	W
Energy input received by the absorber (Q_{in})	10800	W

Table 4.5: Energy Input Q_{in} for Scenario II

Energy output from solar simulator (Q_{source})	4000	W
Energy loss due to reflection, assumed to be 10% ($Q_{refl,c-sur}$)	400	W
Energy input received by the absorber (Q_{in})	3600	W

4.4 Performance of Solar Collector, Heat Exchanger and Storage Tank

Under zero-loss conditions, the three main components in LSFPSC prototype (i.e. the collector, the heat exchanger and the storage tank) should have the same efficiency. However, when the heated HTF leaves the solar collector, it loses heat to the surroundings before it reaches the heat exchanger, causing less useful energy gain. With continuous operation, the decreasing temperature gradient between the HTF and the water storage makes the heat transfer less effective hence reducing the efficiency of the storage tank. Therefore, the actual efficiencies of the three main components can be placed in a descending order as:

$$\eta_c > \eta_{ex} > \eta_{st} \tag{4.6}$$

By measuring the useful energy gained by components, their efficiencies are given as:

$$\eta_c = Q_{u,c}/Q_{in} \tag{4.7}$$

$$\eta_{ex} = Q_{u,ex}/Q_{in} \tag{4.8}$$

$$\eta_{st} = Q_{u,st}/Q_{in} \tag{4.9}$$

4.5 Efficiency of Solar Collector

This section describes the thermal analysis of the solar collector identifying sources of energy losses and gains which are adapted to calculate the collector efficiency.

4.5.1 Radiant Heat Transfer

The circulation system directly gains energy, $Q_{rad,c-circ}$, from the radiation emitted by the heated collector. Radiation loss consists of $Q_{rad,c-sur}$, the radiant heat transfer from the collector to the surroundings and $Q_{rad,c-ins}$, the radiant heat transfer from the collector to the back insulation.

Radiation Loss from the Collector to the Surroundings

Once the collector gets heated, radiant heat transfer occurs between the collector and the surroundings due to the presence of temperature gradient. This rate of radiant heat transfer is given by:

$$Q_{rad,c-sur} = \varepsilon_c A_c \sigma_{sb} (T_c^4 - T_{sur}^4) \tag{4.10}$$

The parameters and calculated $Q_{rad,c-sur}$ are shown in Table 4.6 and Table 4.7.

Table 4.6: Parameters used in the calculation of $Q_{rad,c-sur}$ for Scenario I

Stefan-Boltzmann constant	5.67E-08	W/m^2 K^4
Emissivity of the collector	0.35	
Area of the collector	6.96	m^2
Mean temperature of the collector	384.6	K
Mean temperature of the surroundings	344.9	K
Mean rate of radiation loss	1102.9	W
Radiation loss to the surroundings (% of Q_{in})	10.21%	

Table 4.7: Parameters used in the calculation of $Q_{rad,c-sur}$ for Scenario II

Stefan-Boltzmann constant	5.67E-08	W/m^2 K^4
Emissivity of the collector	0.35	
Area of the collector	6.96	m^2
Mean temperature of the collector	327.8	K
Mean temperature of the surroundings	307.7	K
Mean rate of radiation loss	357.6	W
Radiation loss to the surroundings (% of Q_{in})	9.93%	

Radiation Loss from Collector to Back Insulation

Additional radiation loss occurs between the collector and the back insulation as they have different temperatures. Since they are both grey bodies with different emissivity and surface area, equation (4.10) is extended to include these two parameters along with view factor F_{c-ins} :

$$Q_{rad,c-ins} = \frac{\sigma_{sb}(T_c^4 - T_{ins}^4)}{\frac{1-\varepsilon_c}{\varepsilon_c A_c} + \frac{1}{A_c F_{c-ins}} + \frac{1-\varepsilon_{ins}}{\varepsilon_{ins} A_{ins}}} \quad (4.11)$$

Where: $F_{c-ins} = \frac{1+\cos\beta}{2}$ $and\ \beta\ is\ the\ tilted\ angle\ of\ the\ collector$

The parameters and calculated $Q_{rad,c-ins}$ are shown in Table 4.8 and 4.9.

Table 4.8: Parameters used in the calculation of $Q_{rad,c-ins}$ for Scenario I

Emissivity of the collector	0.35	
Emissivity of the back insulation	0.09	
Area of the collector	6.96	m^2
Area of the back insulation	5.75	m^2
Mean temperature of the collector	384.6	K
Mean temperature of the back insulation	353.8	K
View factor	0.933	
Titled angle (with respect to the horizon)	30	^{o}
Mean rate of radiation loss	151.23	W
Radiation loss to the back insulation (% of Q_{in})	1.40%	

Table 4.9: Parameters used in the calculation of $Q_{rad,c-ins}$ for Scenario II

Emissivity of the collector	0.35	
Emissivity of insulation	0.09	
Area of the collector	6.96	m^2
Area of the back insulation	5.75	m^2
Mean temperature of the collector	327.8	K
Mean temperature of the insulation	310.9	K
View factor	0.933	
Titled angle (with respect to the horizon)	30	^{o}
Mean rate of radiation loss	51.29	W
Radiation loss to the back insulation (% of Q_{in})	1.42%	

Radiation Gain from Collector to Circulation System

The principle of this radiation gain is similar to the radiant heat transfer between the collector and the back insulation. Hence equation (4.11) can be modified using the parameters of the circulation system, which is given as:

$$Q_{rad,c-circ} = \frac{\sigma_{sb}\left(T_c^4 - T_{circ}^4\right)}{\frac{1-\varepsilon_c}{\varepsilon_c A_c} + \frac{1}{A_c F_{c-circ}} + \frac{1-\varepsilon_{circ}}{\varepsilon_{circ} A_{circ}}} \tag{4.12}$$

The parameters and calculated $Q_{rad,c-circ}$ are shown in Table 4.10 and 4.11.

Table 4.10: Calculation Parameters of $Q_{rad,c-circ}$ for Scenario I

Emissivity of the collector	0.35	
Emissivity of the circulation system	0.9	
Radius of the circulation system	0.008	m
Total length of the circulation system	55	m
Total surface area of the circulation system	1.935	m^2
Area of the collector	6.96	m^2
Mean temperature of the collector	384.6	K
Mean temperature of the circulation system	353.8	K
View factor	0.933	
Mean rate of radiation gain	766.95	W
Useful energy gained via radiation (% of Q_{in})	7.10%	

Table 4.11: Calculation Parameters of $Q_{rad,c-circ}$ for Scenario II

Emissivity of collector	0.35	
Emissivity of the circulation system	0.9	
Radius of the circulation system	0.008	m
Total length of the circulation system	55	m
Total surface area of the circulation system	1.935	m^2
Area of the collector	6.96	m^2
Mean temperature of the collector	327.8	K
Mean temperature of the circulation system	310.9	K
View factor	0.933	
Mean rate of radiation gain	260.98	W
Useful energy gained via radiation (% of Q_{in})	7.25%	

4.5.2 Convective Heat Transfer

Convection Loss from Collector to Surrounding

As the collector was directly exposed to the ambient, $Q_{conv,c-sur}$, the convection from the collector surface to the surrounding was the main contributor to convective loss.

The friction and heat transfer coefficient for a flat plate can be determined by solving the conservation of mass, momentum, and energy equations. The Nusselt number, the non-dimensional heat transfer coefficient, can be expressed as:

$$\mathrm{Nu} = \frac{hL}{k} = C_{Nu} Re_L^m Pr^n \tag{4.13}$$

where C_{Nu}, m, and n are constants, h is heat transfer coefficient, k is the thermal conductivity of the flat plate and L is the length of the flat plate. Re is the Reynolds number which is the ratio of inertia forces to viscous forces in the fluid:

$$\mathrm{Re} = \frac{inertia\ forces}{viscous\ forces} = \frac{VL}{v} \tag{4.14}$$

The inertia forces are proportional to the density and the velocity of the fluid. At large Re numbers, the inertia forces become large relative to the viscous forces thus the viscous forces cannot prevent the random and rapid fluctuations of the fluid (turbulent regime). The Re number that defines the transition region for a flow to become turbulent is called the critical Reynolds number. The critical Re number for flow over flat plate is approximately 5 x 10^5 (Duffie and Beckman 2006). For laminar flow ($Re < 5 \times 10^5$), assuming the flat plate is isothermal, the average Nusselt number over the flat plate is given as:

$$\mathrm{Nu} = \frac{hL}{k} = 0.664 Re_L^{1/2} Pr^{1/3} \qquad 0.6 \leq Pr \tag{4.15}$$

For turbulent flow ($5 \times 10^5 < Re < 10^7$), the average Nusselt number over the isothermal flat plate is given as:

$$\mathrm{Nu} = \frac{hL}{k} = 0.037 Re_L^{4/5} Pr^{1/3} \qquad 0.6 \leq Pr \leq 60 \tag{4.16}$$

Pr is the Prandtl number which is a measure of relative thickness of the velocity and thermal boundary layer:

$$\mathrm{Pr} = \frac{kinematic\ viscosity}{thermal\ diffusivity} = \frac{v}{\alpha} \tag{4.17}$$

From equation (4.13), the expression for $Q_{conv,c-sur}$ can be adapted as:

$$Q_{conv,c-sur} = \frac{k_{air}}{L_c} A_c (T_c - T_{sur}) C_{Nu} Re_L^m Pr^n \tag{4.18}$$

Table 4.12 and 4.13 show the calculation parameters for $Q_{conv,c-sur}$. The Reynolds number was calculated to be 6.6 x 10^5 (with V = 5.5m/s, L = 2.4m and *v* = 2.01E-05 m^2/s) which is larger than 5 x 10^5 hence the flow was turbulent and equation (4.16) was applied.

Table 4.12: Calculation Parameters of $Q_{conv,c-sur}$ for Scenario I

Mean temperature of ambient air	344.95	K
Mean temperature of the collector	384.6	K
Kinematic viscosity of ambient air	2.01E-05	m^2/s
Thermal diffusivity of ambient air	2.90E-05	m^2/s
Thermal conductivity of ambient air	0.0296	W/m K
Area of the collector	6.96	m^2
Air travel length	2.4	m
Mean rate of energy loss to the surroundings	4190.65	W
Energy loss to the surroundings (% of Q_{in})	38.80%	

Table 4.13: Calculation Parameters of $Q_{conv,c-sur}$ for Scenario II

Mean temperature of ambient air	307.71	K
Mean temperature of the collector	327.8	K
Kinematic viscosity of ambient air	1.65E-05	m^2/s
Thermal diffusivity of ambient air	2.31E-05	m^2/s
Thermal conductivity of ambient air	0.0296	W/m K
Area of the collector	6.96	m^2
Air travel length	2.4	m
Mean rate of energy loss to the surroundings	1313.69	W
Energy loss to the surroundings (% of Q_{in})	36.49%	

Convection Gain from Collector to Circulation System via Heat Exchange Chamber

The air within the exchange chamber was first heated up by the absorber ($Q_{conv,c-ex}$), and then a large proportion of its energy was transferred into the circulation system ($Q_{conv,ex-circ}$) as useful energy while a smaller portion was lost to the surrounding ($Q_{conv,ex-sur}$). Therefore, the convection loss from the heat exchange chamber to the surrounding can be expressed by modifying Equation (4.18), which gives $Q_{conv,c-ex}$ as:

$$Q_{conv,c-ex} = \frac{k_{air}}{L_c} A_c (T_c - T_{ex}) C_{Nu} Re_L^m Pr^n \quad (4.19)$$

The parameters and calculated $Q_{conv,c-ex}$ are shown in Table 4.14 and 4.15.

Table 4.14: Calculation Parameters of $Q_{conv,c-ex}$ for Scenario I

Mean temperature of air in the exchange chamber	353.77	K
Mean temperature of the collector	384.6	K
Kinematic viscosity of air in the exchange chamber	2.096E-05	m^2/s
Thermal diffusivity of air in the exchange chamber	2.965E-05	m^2/s
Thermal conductivity of air in the exchange chamber	0.0299	W/m^2 K
Area of the collector	6.96	m^2
Air travel length	2.4	m
Mean rate of energy gained by the exchange chamber	3272.06	W
Energy gained by the exchange chamber (% of Q_{in})	30.29%	

Table 4.15: Calculation Parameters of $Q_{conv,c-ex}$ for Scenario II

Mean temperature of air in the exchange chamber	310.96	K
Mean temperature of the collector	327.8	K
Kinematic viscosity of air in the exchange chamber	1.68E-05	m^2/s
Thermal diffusivity of air in the exchange chamber	2.36E-05	m^2/s
Thermal conductivity of air in the exchange chamber	0.0299	W/m^2 K
Area of the collector	6.96	m^2
Air travel length	2.4	m
Mean rate of energy gained by the exchange chamber	1118.30	W
Energy gained by the exchange chamber (% of Q_{in})	31.06%	

Churchill and Bernstein (1977) developed a mathematical model to express the Nusselt number in convection through air flowing pass circular cylinders:

$$\mathrm{Nu}_D = 0.3 + \frac{0.62 Re_D^{1/2} Pr^{1/3}}{\left[1+(0.4/Pr)^{2/3}\right]^{1/4}} \left[1 + \left(\frac{Re_D}{282000}\right)^{5/8}\right]^{4/5} \quad (4.20)$$

This model can be used to describe the convection from the hot air within the heat exchange chamber to the circulation system:

$$Q_{conv,ex-circ} = \frac{k_{air}}{D_{circ}} A_{circ} (T_{ex} - T_{circ}) \left[0.3 + \frac{0.62 Re_D^{1/2} Pr^{1/3}}{\left[1+(0.4/Pr)^{2/3}\right]^{1/4}} \left[1 + \left(\frac{Re_D}{282000}\right)^{5/8}\right]^{4/5}\right] \quad (4.21)$$

The parameters and calculated $Q_{conv,ex-circ}$ are shown in Table 4.16 and 4.17.

Table 4.16: Calculation Parameters of $Q_{conv,ex-circ}$ for Scenario I

Mean temperature of air in the exchange chamber	353.77	K
Mean water temperature of circulation system output	333.36	K
Kinematic viscosity of air in the exchange chamber	2.1E-05	m^2/s
Thermal diffusivity of air in the exchange chamber	2.97E-05	m^2/s
Thermal conductivity of air in the exchange chamber	0.0299	W/m^2 K
Radius of the circulation system	0.008	m
Length of the circulation system	55	m
Area of the circulation system	1.935	m^2
Air travel length	0.016	m
Mean rate of energy gained by the circulation system	2316.70	W
Useful energy gained via convection (% of Q_{in})	21.45%	

Table 4.17: Calculation Parameters of $Q_{conv,ex-circ}$ for Scenario II

Mean temperature of air in the exchange chamber	310.96	K
Mean water temperature of circulation system output	303.56	K
Kinematic viscosity of air in the exchange chamber	1.68E-05	m^2/s
Thermal diffusivity of air in the exchange chamber	2.36E-05	m^2/s
Thermal conductivity of air in the exchange chamber	0.0299	W/m^2 K
Radius of the circulation system	0.008	m
Length of the circulation system	55	m
Area of the circulation system	1.935	m^2
Air travel length	0.016	m
Mean rate of energy gained by the circulation system	753.28	W
Useful energy gained via convection (% of Q_{in})	20.92%	

Convection Loss from Heat Exchange Chamber to Surrounding

With known results of $Q_{conv,ex-circ}$, the average $Q_{conv,ex-sur}$ can then be estimated as:

$$Q_{conv,ex-sur} = Q_{conv,c-ex} - Q_{conv,ex-circ} \quad (4.22)$$

For Scenario I:

$$Q_{conv,ex-sur} = Q_{conv,c-ex} - Q_{conv,ex-circ} = 3272.06 - 2316.70 = 955.36\,W$$

For Scenario II:

$$Q_{conv,ex-sur} = Q_{conv,c-ex} - Q_{conv,ex-circ} = 1118.30 - 753.28 = 365.02\,W$$

4.6 Energy Gain by the Heat Exchanger

The heat exchanger transfers thermal energy from hotter heat transfer fluid into colder water storage. Its useful energy gain, $Q_{u,ex}$, can be estimated using the second part of equation 4.5 and η_{ex} can then be calculated using equation 4.8. The mass flow rate was known from the volumetric flow rate recorded by the flow meter. The temperatures of the hot inlet and the cold outlet were also measured experimentally. A heat exchange effectiveness of 0.8 is used as recommended for solar thermal system simulation by Duffie and Beckman, 2013. Table 4.18 and 4.19 show the parameters and calculated $Q_{u,ex}$ and η_{ex}.

Table 4.18: Calculation Parameters of $Q_{u,ex}$ for Scenario I

Mean water temperature of heat exchanger inlet	333.37	K
Mean water temperature of heat exchanger outlet	303.68	K
Volumetric flow rate (min)	0.0018	m^3/min
Mass flow rate (s)	0.03	kg/s
Exchanger efficiency factor	0.8	
Mean energy exchange rate	2982.6	W
Efficiency of the heat exchanger (% of Q_{in})	27.62%	

Table 4.19: Calculation Parameters of $Q_{u,ex}$ for Scenario II

Mean water temperature of heat exchanger inlet	304.74	K
Mean water temperature of heat exchanger outlet	295.51	K
Volumetric flow rate (min)	0.0018	m^3/min
Mass flow rate (s)	0.03	kg/s
Exchanger efficiency factor	0.8	
Mean rate of energy exchange	927.9	W
Efficiency of the heat exchanger (% of Q_{in})	25.77%	

4.7 Efficiency Gain by the Storage Tank

The useful energy gain by the storage tank, $Q_{u,st}$, is determined by the amount of energy absorbed by the water within the storage tank using the first part of equation (4.5) and η_{st} can be calculated using equation (4.9). For the water in storage tank, its total mass, starting temperature and final temperature were measured experimentally. The parameters and calculated $Q_{u,st}$ and η_{st} are shown in Table 4.20 and 4.21.

Table 4.20: Calculation Parameters of $Q_{u,st}$ for Scenario I

Total testing time (minute)	135	min
Total testing time (second)	8100	s
Starting water temperature	19	C
Finishing water temperature	67	C
Total water mass in storage tank	118	kg
Water specific heat capacity	4187	J/kg K
Total energy gained by water in storage tank	23715168	J
Mean rate of useful energy gain through the test	2927.80	W
Efficiency of the storage tank (% of Q_{in})	27.11%	

Table 4.21: Calculation Parameters of $Q_{u,st}$ for Scenario II

Total testing time (minute)	90	min
Total testing time (second)	5400	s
Starting water temperature	18	C
Finishing water temperature	27	C
Total water mass in storage tank	118	kg
Water specific heat capacity	4187	J/kg K
Total energy gained by water in storage tank	4446594	J
Mean rate of useful energy gain through the test	823.44	W
Efficiency of the storage tank (% of Q_{in})	22.87%	

4.8 Discussion

The sources of energy gains and losses were identified for both scenarios which are summarised in Table 4.22 and 4.23 with useful energy gains of the collector, the heat exchanger and the storage tank. The fourth column of each table shows the % of Q_{in} for each calculated energy source.

Table 4.22: Energy Gains/Losses (Scenario I)

Energy input received by the absorber (Q_{in})	10800	W	
Radiation loss to the surroundings	1102.87	W	10.21%
Radiation loss to the back insulation	151.23	W	1.40%
Total radiation loss	1254.10	W	11.61%
Convection energy loss from collector to surroundings	4190.65	W	38.80%
Convection energy loss from exchange chamber to surroundings	955.36	W	8.85%
Total convection loss	5146.01	W	47.65%
Edge loss	1316.23	W	12.19%
Radiation gained by the circulation system	766.95	W	7.10%
Convection gained by the circulation system	2316.70	W	21.45%
Useful energy gained by the collector	3083.65	W	28.55%
Useful energy gained by the heat exchanger	2982.60	W	27.62%
Useful energy gained by the storage tank	2927.80	W	27.11%

Table 4.23: Energy Gains and Losses (Scenario II)

Energy input received by the absorber (Q_{in})	3600	W	
Radiation loss to the surroundings	357.60	W	9.93%
Radiation loss to the back insulation	51.29	W	1.42%
Total radiation loss	408.89	W	11.36%
Convection energy loss from collector to surroundings	1313.69	W	36.49%
Convection energy loss from exchange chamber to surroundings	365.02	W	10.14%
Total convection loss	1678.71	W	46.63%
Edge loss	498.13	W	13.84%
Radiation gained by the circulation system	260.98	W	7.25%
Convection gained by the circulation system	753.28	W	20.92%
Total useful energy gained by the collector	1014.26	W	28.17%
Useful energy gained by the heat exchanger	927.86	W	25.77%
Useful energy gained by the storage tank	823.44	W	22.87%

The LSFPSC prototype has shown similar performance in both scenarios with a collector efficiency to be around 28%. It is clear that the convection loss (~47%) is the major contributor to this low efficiency. Significant amount of energy was lost via air convection from the collector surface (~38%) as the collector was unglazed and the absorber was directly exposed to the surroundings. Additionally, as the exchange chamber was partly open to the ambient allowing convection to deliver useful energy to the circulation system, there was inevitable heat loss from the exchange chamber to the surroundings (~9%). The radiation energy loss (~10%) could be reduced by lowering the emissivity of the absorber sheets through the application of selective paints. The collector prototype was built on a supporting/fixing frame consisting of metal and composite materials. These materials could get heated up during practical tests by conduction and convection (e.g. contacts with collector and back insulation) losing heat to the ambient accounting for edge loss (~12%).

The results show that the efficiency decreases as the heat transfer fluid (HTF) leaves the collector to reach the heat exchanger to deliver thermal energy to the storage tank. The reasons were mentioned in section 4.3. The decrease was less obvious in scenario I as the HTF was heated to much higher temperatures than that in scenario II. This creates larger temperature gradients between the HTF and the water in storage tank allowing heat to be transferred more efficiently.

The identified deficient problems of the 1st Stage testing were analysed to propose improvements, which will be discussed in the next chapter.

CHAPTER 5

5. 2nd Stage – Mathematical Modelling

This chapter describes the mathematical models that use the testing data from previous chapter to propose improvements for enhancing the performance of the LSFPSC prototype. As results from both 1st stage experiment scenarios showed similar collector performances, only practical data and analysis results of scenario I were employed in the 2nd stage mathematical models.

5.1 Glazing Cover and Surface Convection Loss

The thermal analysis showed that the convection loss from the absorber surface to the surroundings accounted for the largest percentage of heat loss (~38%). Therefore, minimising this convection loss can lead to significant improvement of system efficiency. Glazing cover has been widely used in commercial solar collectors as an effective way of reducing convection loss. It reduces convection loss through two mechanisms:

1. Isolating solar absorber from the surroundings minimising the effects of forced convection caused by wind (air flow)
2. Creating a gap between the glazing cover and the absorber that is filled with air (low thermal conductivity) to act as an insulation layer.

The glazing cover can also contribute to reduce radiation loss:

1. Reflecting back the infrared radiation emitted by the absorber
2. The glazing cover normally has higher temperatures than the surroundings hence the radiant heat transfer from the absorber to the glazing is lower.

Two approaches were used to estimate the effects of glazing cover in thermal loss when applied on the prototype under the conditions of Scenario I.

The first approach is to calculate the heat transfer through radiation and convection from the absorber to the glass cover separately. The radiant heat transfer is given by:

$$Q_{rad,c-gl} = \frac{\sigma_{sb}\left(T_c^4 - T_{gl}^4\right)}{\frac{1-\varepsilon_c}{\varepsilon_c A_c} + \frac{1}{A_c F_{c-gl}} + \frac{1-\varepsilon_{gl}}{\varepsilon_{gl} A_{gl}}} \quad (5.1)$$

The recorded ambient temperatures were used as the temperatures of the glazing to predict the performance of the collector. F_{c-gc} is the view factor from the absorber to the cover, given as:

$$F_{c-gl} = \frac{1}{\pi x y}\left[\ln\frac{x_1^2 y_1^2}{x_1^2 + y_1^2 - 1} + 2x\left(y_1 \tan^{-1}\frac{x}{y_1} - \tan^{-1} x\right) + 2y\left(x_1 \tan^{-1}\frac{y}{x_1} - \tan^{-1} y\right)\right] \quad (5.2)$$

Where: $x = w/d$, $w\ is\ the\ width\ of\ the\ absorber$

$y = l/d$, $l\ is\ the\ length\ of\ the\ absorber$

$d =\ the\ distance\ between\ the\ absorber\ and\ the\ cover$

$x_1 = \sqrt{1 + x^2}$

$$y_1 = \sqrt{1 + y^2}$$

The parameters and calculated $Q_{rad,c-gl}$ are shown in Table 5.1.

Table 5.1: Calculation Parameters of $Q_{rad,c-gl}$ for Approach 1

Mean temperature of the absorber	384.61	K
Assumed mean temperature of the glazing cover	344.95	K
Emissivity of the absorber	0.35	
Emissivity of the glazing cover	0.8	
Area of the glazing cover	6.96	m^2
Area of the absorber	6.96	m^2
View factor	0.983	
Mean rate of radiation loss via the glazing cover	1008.52	W

The gap between the absorber and the glazing was assumed to be fully sealed from the surroundings, hence only natural air convection could occur. The natural convective heat transfer is given by:

$$Q_{conv,c-gl} = h_{c-gl} A_c \Delta T \tag{5.3}$$

$$h_{c-gl} = \frac{Nuk_{air}}{L} \tag{5.4}$$

$$Nu = 1 + 1.44\left[1 - \frac{1708(\sin 1.8\beta)^{1.6}}{Ra\cos\beta}\right]\left[1 - \frac{1708}{Ra\cos\beta}\right]^{+} + \left[\left(\frac{Ra\cos\beta}{5830}\right)^{1/3} - 1\right]^{+} \tag{5.5}$$

$$Ra = \frac{g\beta'\Delta T L^3}{v\alpha} \tag{5.6}$$

Where $h = heat\ transfer\ coefficient\ (W/m^2\,K)$
$L = spacing\ (m)$
$g = gravitational\ constant\ (m/s^2)$
$\beta' = volumetric\ coefficient\ of\ expansion\ (1/K)$
$\Delta T = temperature\ difference\ between\ the\ absorber\ and\ the\ glazing\ \ (K)$
$v = kinematic\ viscosity\ (m^2/s)$
$\alpha = thermal\ diffusivity\ (m^2/s)$

The parameters and calculated $Q_{conv,c-gl}$ are shown in Table 5.2.

Table 5.2: Calculation Parameters of $Q_{conv,c-gl}$ for Approach 1

Mean temperature of the absorber	384.61	K
Assumed average temperature of the glazing cover	344.95	K
Spacing between the absorber and the glazing cover	0.025	m
Tilt angle	30	o
Kinematic viscosity of air	2.01E-05	m^2/s
Thermal diffusivity of air	2.85E-05	m^2/s
Thermal conductivity of air	0.029	W/m K
Area of the absorber	6.96	m^2
Mean rate of energy loss via convection	854.68	W

The sum of the assumed radiant and convective loss with glazing is 1863.20 W, which is 17.25% of the energy input and it is much lower compared to the actual combined radiant and convective heat loss (5293.52W, 49.01%). However, the actual temperatures of the glazing cover should be higher than the ambient temperatures, so this approach can overestimate the total heat loss.

Therefore, **the second approach,** developed by Klein (1979), which incorporated both radiant and convective losses, and only considers collector and ambient temperatures, was used to give more accurate predictions of energy loss with glazing cover:

$$Q_{loss,c-am} = U_{c-am} A_c \Delta T \tag{5.7}$$

$$U_{c-am} = \left(\frac{N}{\frac{C}{T_c}\left[\frac{(T_c - T_{am})}{N+f}\right]^e} + \frac{1}{h_w} \right)^{-1} + \frac{\sigma (T_c + T_{am})(T_c^2 + T_{am}^2)}{\frac{1}{\varepsilon_c + 0.00591 N h_w} + \frac{2N + f - 1 + 0.133\varepsilon_c}{\varepsilon_{gl}} - N} \tag{5.8}$$

$N = number\ of\ glazing\ covers$
$f = (1 + 0.089 h_w - 0.1166 h_w \varepsilon_c)(1 + 0.07866 N)$
$C = 520(1 - 0.000051\beta^2)$
$e = 0.43(1 - 100/T_c)$
$h_w = wind\ heat\ transfer\ coefficient\ (W/m^2\ C)$

The parameters and calculated $Q_{loss,c-gl}$ are shown in Table 5.3.

Table 5.3: Calculation Parameters $Q_{total,c-gl}$ for Approach 2

Mean temperature of the absorber	384.61	K
Mean ambient temperature	344.95	K
Emissivity of the absorber	0.35	
Emissivity of the glazing cover	0.8	
Number of glazing covers	1	
Tilt angle of the absorber	30	^{o}
Wind heat transfer coefficient	10	W/m^2 K
Area of the absorber	6.96	m^2
Mean total heat loss (convection and radiation)	1143.39	W

The combined radiant and convective heat loss is estimated to be 1143.39 W, which is 10.59% of the input energy. This is compared with the actual combined loss (5293.52W, 49.01%) and illustrated in Figure 5.1. Based on these two approaches, it is estimated that if glazing cover is employed, the combined radiant and convective heat loss could be reduced significantly by 38.42% based on the assumption that the circulation system is capable of removing all the additional energy gain.

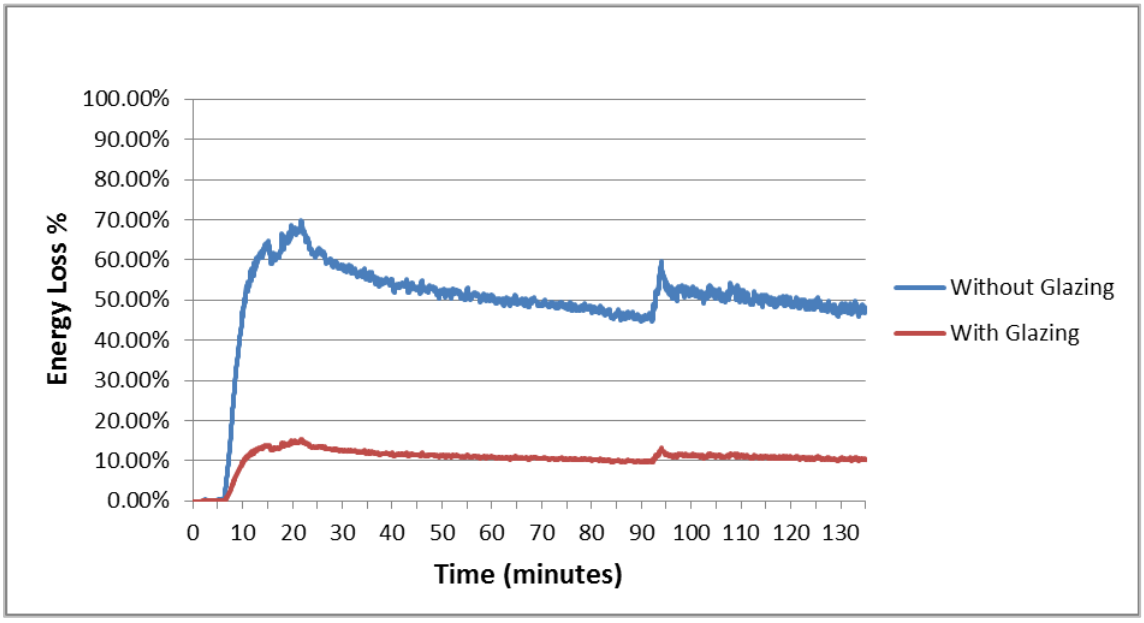

Figure 5.1: Combined Radiant and Convective Energy Loss from Collector Surface vs. Time

5.2 Thermal Conductivity and Absorber Thickness

The incoming radiation energy is converted to heat energy when it is received on the surface of the absorber. The heat energy is then conducted from the front side of the absorber to its back side, and be transferred into the exchange chamber via convection. It is noticed that this convection has higher dependence on the thermal conductivity of the flowing medium (air in this case) than the absorber. This is due to the fact that the flowing medium is the main driver in convective heat transfer and the absorber has very small thickness allowing heat to pass quickly.

It is important to study the relationship between the thermal conductivity of the absorber and the convective heat transfer rates. This can contribute to the material selection of absorber in terms of thermal conductivity and thickness. Optimal combinations of these two parameters would allow more configurations to be developed for a wider range of applications (e.g. producing useful hot air and hot water at the same time). A mathematical model is developed to understand the effects of these two parameters in the combined conduction and convection heat transfer as shown in Figure 5.2.

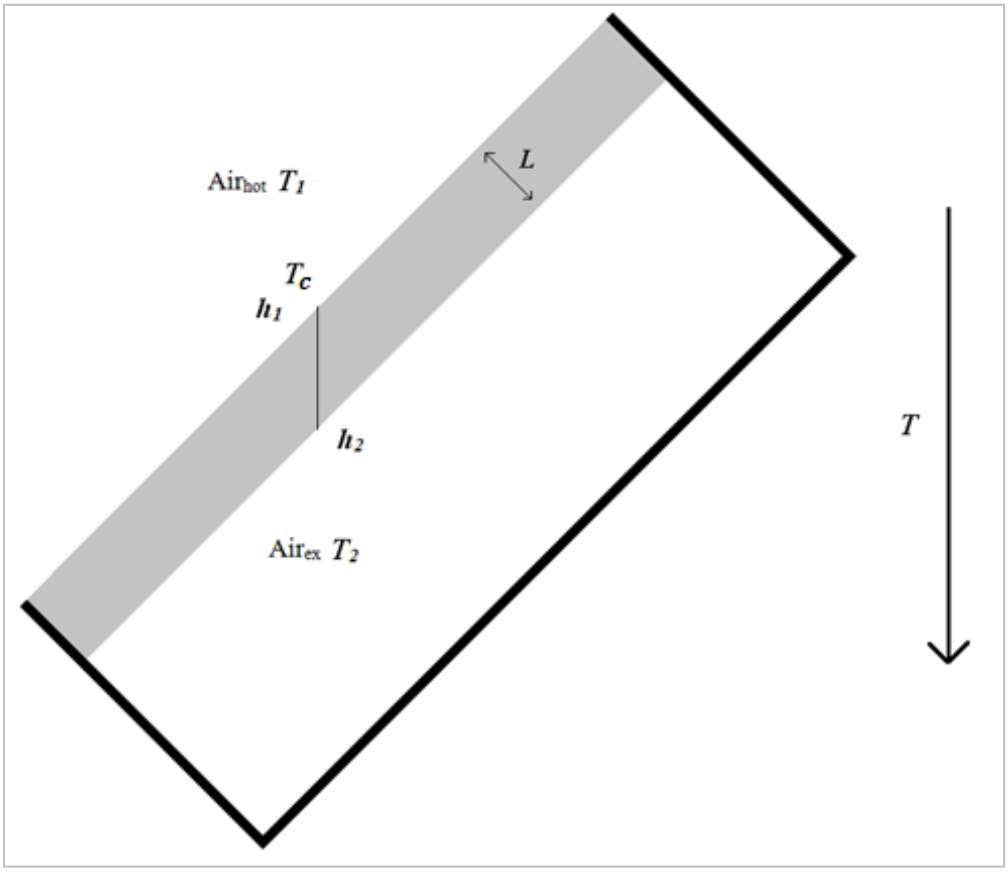

Figure 5.2 Conducting Absorber with Convective Heat Transfer

This model assumed that the absorber receives heat energy from surrounding hot air (acting as the source of heat input, with unknown temperature T_1) to reach its known temperature T_c with known heat transfer coefficient h_1 (adapted from previous thermal analysis). Then the heat transfer rate from the absorber to the exchange chamber Q_{c-ex} can be given as:

$$Q_{c-ex} = h_1 A_c (T_1 - T_c) \quad (5.9)$$

Q_{c-ex} is assumed to be uniform across the absorber, which can be expressed as:

$$Q_{c-ex} = \frac{T_1 - T_2}{\frac{1}{A_c h_1} + \frac{L}{A_c k_c} + \frac{1}{A_c h_2}} \quad (5.10)$$

By equating and re-arranging Equation 5.9 and 5.10, the expression for the hot air temperature can be written as:

$$T_1 = \frac{T_c\left(1 + \frac{Lh_1}{k_c} + \frac{h_1}{h_2}\right) - T_2}{\frac{Lh_1}{k_c} + \frac{h_1}{h_2}} \quad (5.11)$$

Where $h_1 = heat\ transfer\ coefficient\ between\ hot\ air\ and\ absorber$

$h_2 = heat\ transfer\ coefficient\ between\ absorber\ and\ air\ in\ exchange\ chamber$

$L = thickness\ of absorber$

The parameters h_1, h_2, k, L, T_c and T_2 are known from measurements, experiment data and previous analysis. Equation 5.11 is used to estimate T_1, which is then used in equation 5.10 to estimate Q_{c-ex} across the absorber, the results are shown in Table 5.4.

Table 5.4: Calculation and Estimation Results

Mean T_1	409.81	K
Mean T_2	353.77	K
Mean T_c	381.74	K
Thickness of the absorber	0.001	m
Thermal conductivity of the absorber	50	W/m K
Area of the absorber	6.96	m^2
h_1	15.18	W/m^2 K
h_2	15.24	W/m^2 K
Estimated Q_{c-ex}	2966.49	W
Actual Q_{c-ex}	3272.06	W
Difference	9.34%	

The estimation result is appropriate as it is not significantly deviated from the actual heat transfer rate. At the thickness of 1mm, the variation of heat transfer rate with thermal conductivity is extrapolated to give the relationship shown in Figure 5.3. It can be seen that, the thermal conductivity does not have significant influences on the heat transfer rate until it reaches a critical value (approximately 0.05). Materials with thermal conductivity below the critical value are normally categorised as insulators and not suitable to be used as solar heat collectors. There is a wide range of materials with thermal conductivity above the critical value (e.g. most metals, ceramics and plastics), which gives large flexibility of choosing economical materials as good-performing absorbers.

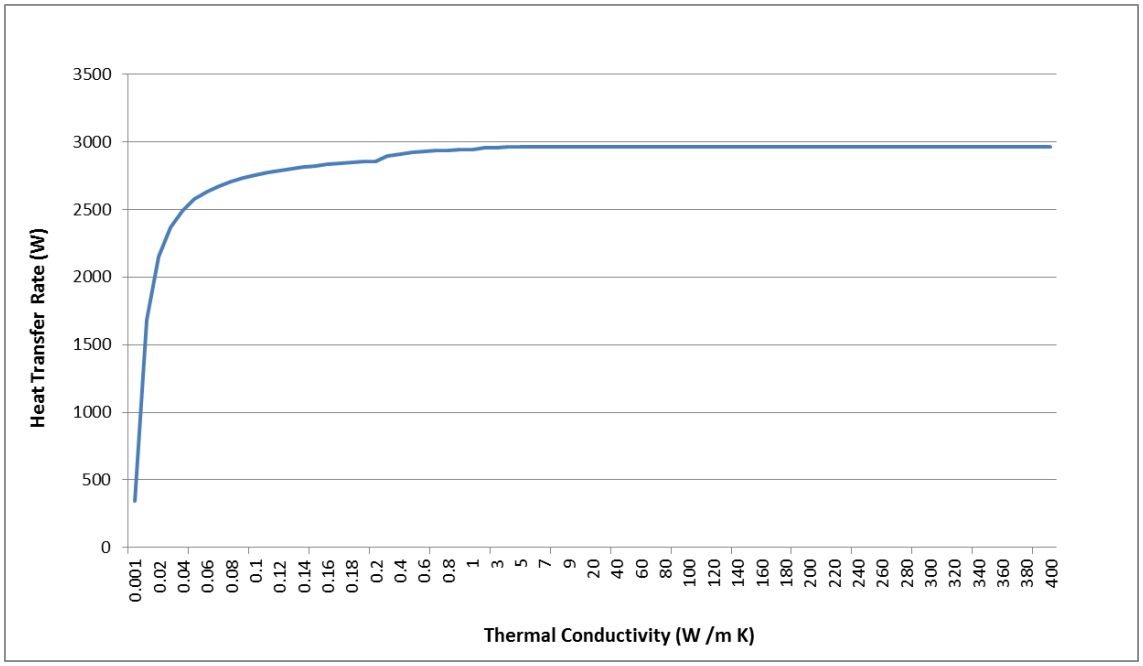

Figure 5.3 Collector Heat Transfer Rate vs. Collector Thermal Conductivity

The relationship between the heat transfer rate and the absorber thickness is also extrapolated for materials with different thermal conductivities (from highly conductive metal to insulator). Figure 5.4 shows the critical values of thickness, i.e. 1m for metal, 0.001 for ceramic and the insulator shows deficiency even at 0.0001m.

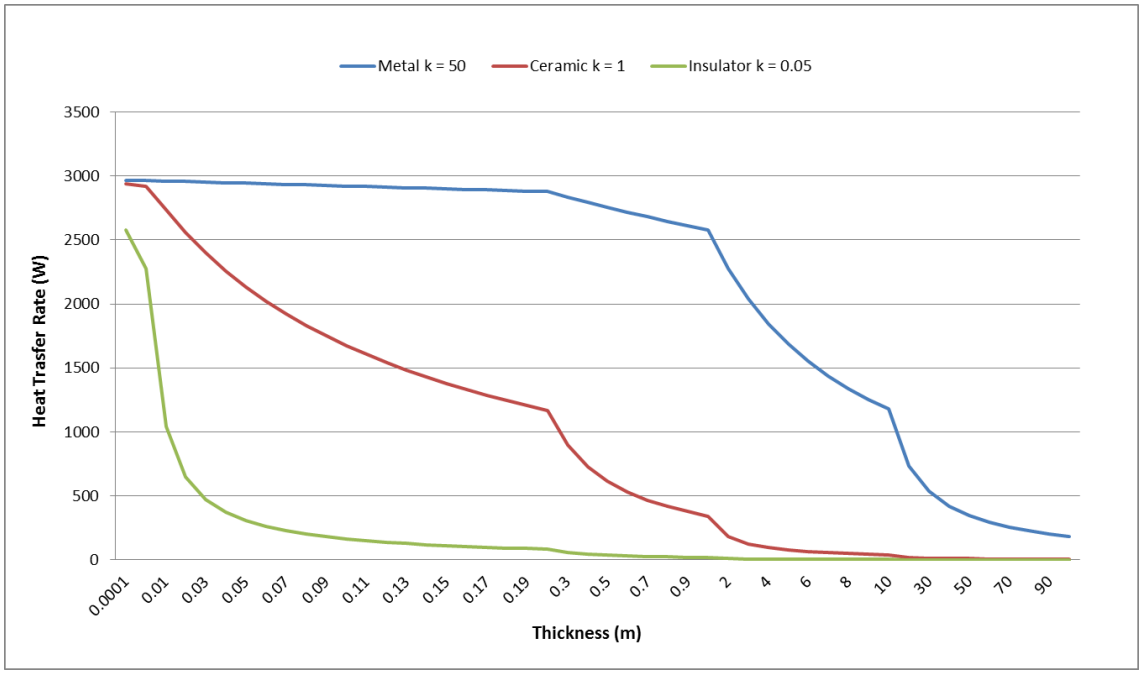

Figure 5.4 Heat Transfer Rate vs. Thickness (Metal, Ceramic and Insulator)

Expansive but highly conductive metal could be employed as solar absorbers in the form of thin foils (<0.001m) to save material costs while providing excellent performance. Relatively cheaper ceramics (cement, concrete,) with moderate thermal conductivity can also be used as solar absorbers. They have less strength than metals

hence they require more thickness to compensate for this drawback. This will lead to reduced performance. Insulators are not good candidates for solar absorbers. However, those employed in structural applications may be suitable to act as solar absorbers to provide cheap passive heating to buildings.

5.3 Conduction as the Main Heat Transfer Mechanism

The studies showed that convection is not an effective heat transfer mechanism as the open convection could cause heat loss to ambient while the closed convection could significantly reduce the collector efficiency. Thus, it was proposed to develop mechanisms to put circulation system in direct contact with the absorber allowing conduction to occur without the need of the exchange chamber. Hence it eliminates convective heat loss to the ambient and improves collector efficiency. Figure 5.5 shows several mechanisms using metal brackets to enable conduction:

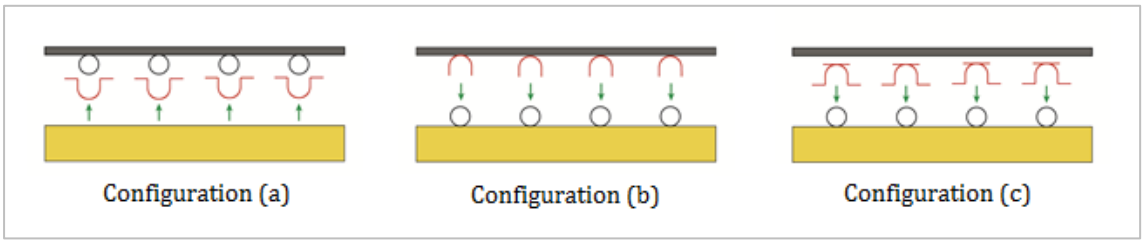

Figure 5.5: Mechanisms for creating direct conduction contacts

Configuration (a) is easy to implement but it may require additional glue or fixing to place the bracket fins in full contact with the absorber; configuration (b) shows the metal brackets could be manufactured or welded as part of the absorber to act as sockets for pipes to fit in easily; similar to (a), configuration (c) also uses independent metal brackets and it is easier to install but it requires more materials and the manufacturing process could be more complicated. Configuration (a) was chosen to be implemented experimentally so the metal brackets could easy be fixed and undone while configuration (b) was considered to be the optimal design for mass production. The cross-sectional view of the absorber-bracket-piping with ideal conduction contact is shown in Figure 5.6.

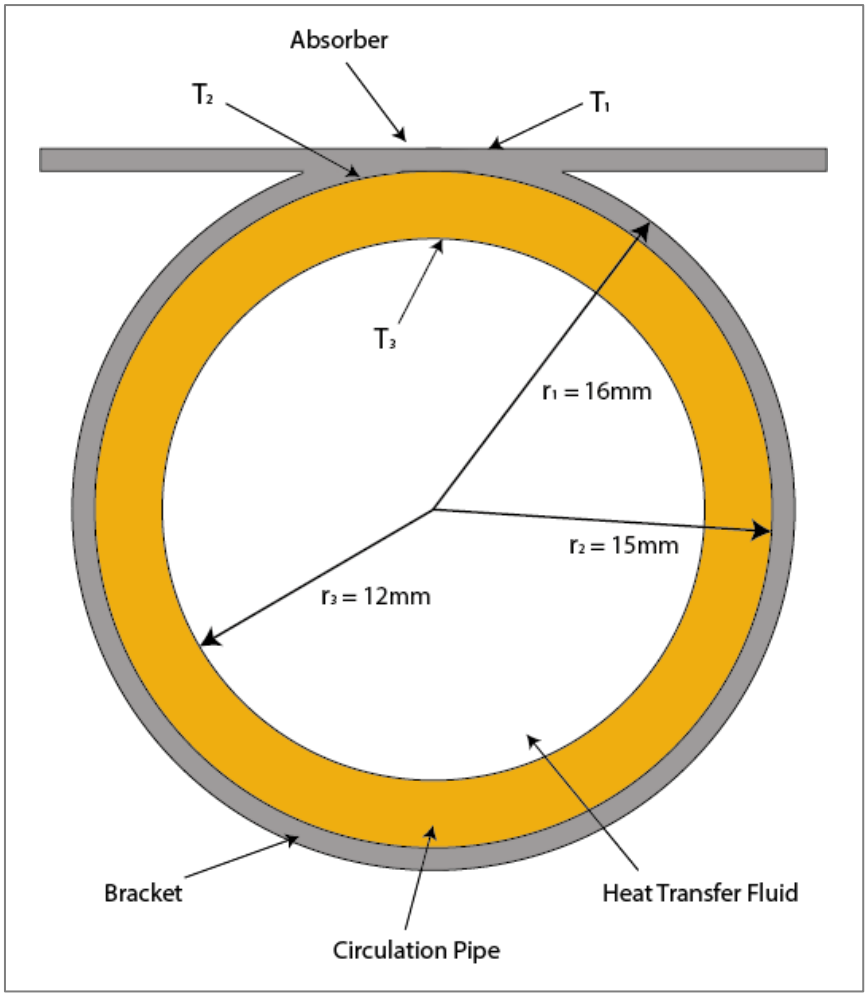

Figure 5.6: Cross sectional view of the ideal conduction contact

A mathematical model was developed to predict the performance of this new configuration using $Q_{gain,ex}$ (the known energy rate delivered into the exchange chamber, sum of the calculated $Q_{conv,c-ex}$ and $Q_{rad,c-circ}$ from Chapter 4 to estimate the temperatures that could be gained by heat transfer fluids via conduction.

T_1 is the temperature of the absorber surface, T_2 is the temperature at the interface between the absorber and the circulation system, and T_3 is the temperature at the interface between the circulation system and the heat transfer fluid. T_1 is known from experiment data and T_2 and T_3 can be estimated using the expressions below:

$$T_2 = T_1 - Q_{gain,ex}\frac{\ln(r_1/r_2)}{2\pi k_c L} \tag{5.12}$$

$$T_3 = T_2 - Q_{gain,ex}\frac{\ln(r_2/r_3)}{2\pi k_{circ} L} \tag{5.13}$$

Where $L = total\ length\ of\ the\ circulation\ system\ under\ the\ absorber$

$r_1 = radius\ of\ the\ bracket\ frame$

$r_2 = outer\ radius\ of\ the\ circulation\ system$

$r_3 = inner\ radius\ of\ the\ circulation\ system$

By combining Equation (5.12) and (5.13), the relationship between T_1 and T_3 can be obtained as:

$$T_3 = T_1 - Q_{gain,ex}\frac{\ln(r_1/r_2)}{2\pi k_c L} - Q_{gain,ex}\frac{\ln(r_2/r_3)}{2\pi k_{circ} L} \quad (5.14)$$

Table 5.5: Estimated T_2 and T_3

Actual mean energy input to the exchange chamber $Q_{gain,ex}$	3922.73	W
Radius of the absorber frame r_1	0.016	m
Outer radius of the circulation system r_2	0.015	m
Inner radius of the circulation system r_3	0.012	m
Thermal conductivity of the circulation system k_{circ}	0.15	W/m K
Thermal conductivity of the absorber k_c	50	W/m K
Mean T_1	381.74	K
Estimated mean T_2	381.72	K
Estimated mean T_3	364.84	K
Actual mean temperature of HTF at collector outlet	333.36	K

Results in Table 5.5 show that, with the same heat transfer rate $Q_{gain,ex}$, the estimated T_3 is much higher than the actual average temperature of the heat transfer fluid obtained during experiment. The comparison is illustrated in Figure 5.7.

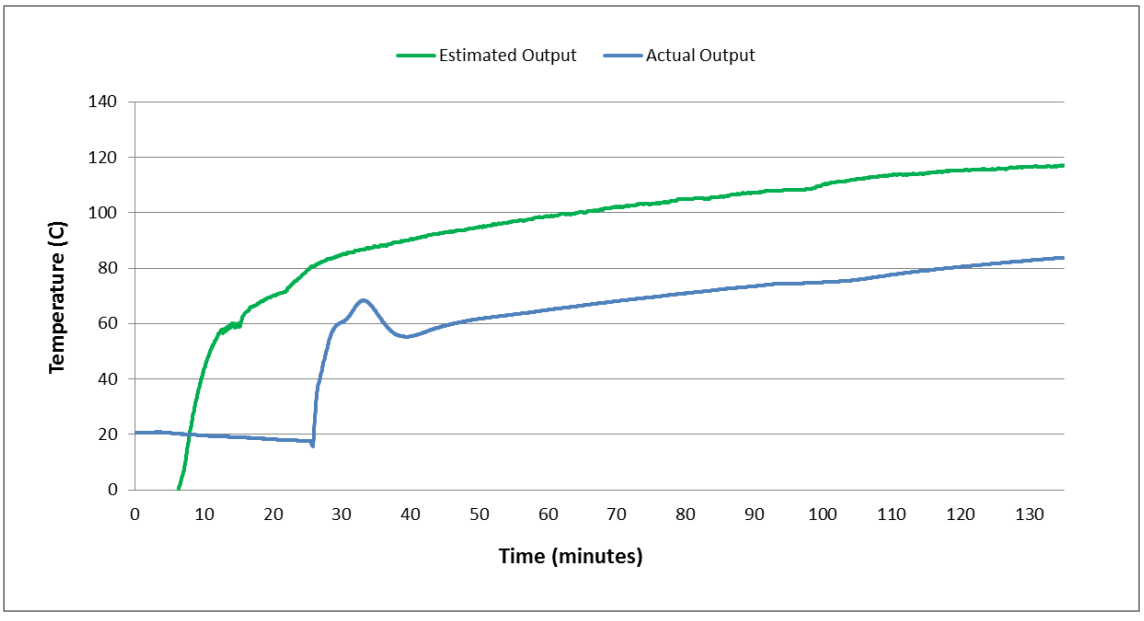

Figure 5.7: Estimated T_3 vs. Actual Output Temperatures of the Heat Transfer Fluid

Assuming the heat transfer fluid, with the mean actual temperature T_{in}, flows into the circulation system and leaves with temperatures equalling to T_3, its useful energy gain, $Q_{gain,circ-htf}$, can be estimated using the equation:

$$Q_{gain,circ-htf} = h_{p-htf}A_{circ}(T_3 - T_{in}) \quad (5.15)$$

$$h_{p-htf} = \frac{Nu_D \times k_{htf}}{D} \quad (5.16)$$

$$Nu_D = \frac{(f/8)(Re_D - 1000)Pr}{1 + 12.7(f/8)^{1/2}(Pr^{2/3} - 1)} \quad (5.17)$$

Where $h_{circ-htf} = heat\ transfer\ coeffient\ from\ the\ circulation\ system\ to\ the\ HTF$
$A_{circ} = unit\ inner\ surface\ area\ of\ the\ circulation\ system$
$D = diameter\ of\ the\ circulation\ system$
$f = the\ friction\ factor = (0.79 \ln Re_D - 1.64)^{-2}$
$Pr = Prandtl\ number = v/\alpha$
$Re_D = Reynolds\ number = Vd/v$
$v = kinematic\ viscosity$
$\alpha = thermal\ diffusivity$

The calculation parameters and results are shown in Table 5.6 and the comparison with actual energy gain is illustrated in Figure 5.8.

Table 5.6: Calculation Parameters and Result for Q'

Average actual temperature of the absorber	384.61	K
Average T_3	364.84	K
Average actual temperature of cold water inlet	303.68	K
Kinematic viscosity of water	3.12E-07	m^2/s
Thermal diffusivity of water	1.72E-07	m^2/s
Thermal conductivity of water	0.677	W/m K
Inner diameter of the circulation system	0.012	m
Average volumetric flow rate	0.265	m/s
Unit inner surface area of the circulation system	0.0379	m^2
Estimated average energy exchange rate Q'	6152.35	W

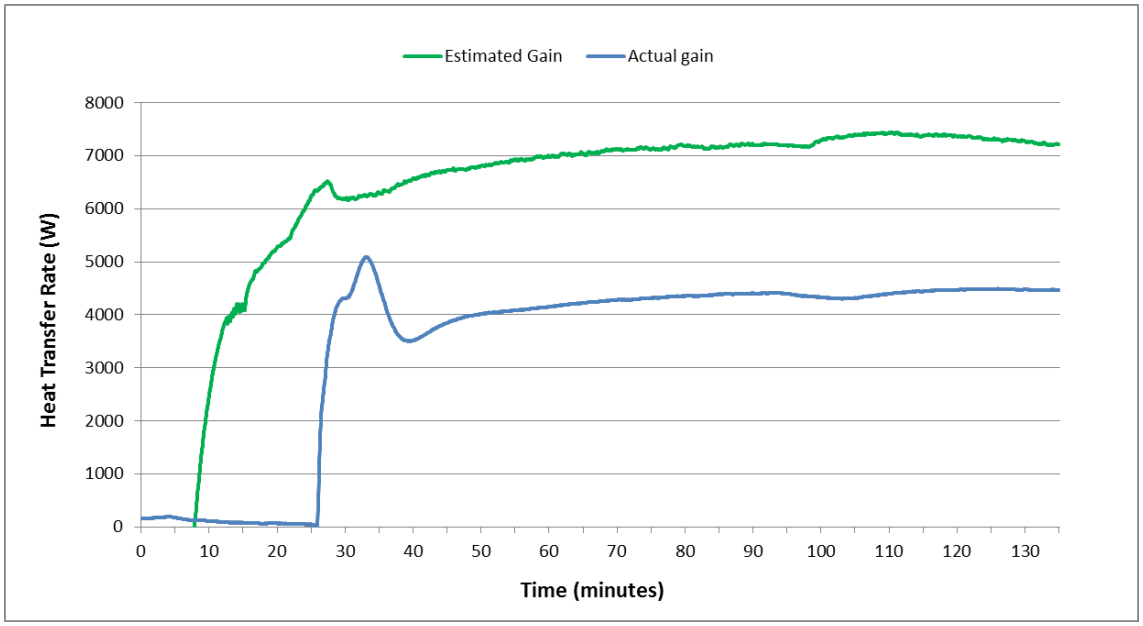

Figure 5.8: Estimated Energy Gain vs. Actual Energy Gain

Compare to the actual energy gain Q_{actual} $(3083.65W)$, the estimated energy gain Q' (6152.35W) indicated that using conduction could significantly improve the collector efficiency. This increase is contributed by the elimination of convection from the exchange chamber to the surroundings and the faster conduction via the direct contacts between the collector and the circulation system.

5.4 Summary

The mathematical modelling results showed that minimising the surface convection loss and changing the heat transfer mode from convection to conduction can lead to substantial increase in the performance of the LSFPSC. Next chapter will detail the implementation of improvements based on these two aspects. In addition, the analysis on thermal conductivity and absorber thickness indicated that apart from metal roofing, the LSFPSC can also utilise other roofing types (e.g. ceramic, plastics).

CHAPTER 6

6. 2nd Stage Improvement Testing and Modelling

6.1 Implemented Improvements

As discussed in Chapter 5, several modifications could be employed to improve the performance of the LSPFSC prototype. After conducting practicality assessment with the industrial partner, it was decided to implement glazing and conduction mechanism on the prototype as they contribute greatly to improving collector performance. PEX-AL-PEX pipe was used in the 1st stage testing but partial melting was observed to occur near where the pipe had close contacts with the absorber. Therefore, PEX-AL-PEX pipe is considered to be not suitable for the conduction mechanism where tight contacts are required between the absorber and the pipe. It was decided to replace the cheaper PEX-AL-PEX pipe with slightly more expansive copper pipe to avoid damages and leaks that may be caused by melting.

The supportive beams were adjusted to push the back insulation upward to leaving approximately 12mm space for inserting the circulation system plus aluminium brackets shaped as shown in Figure 5.5(a). With a set of mechanical tools, a copper pipe (D_{outer} = 10mm, D_{inner} = 8mm) that has a total length of 55m was bent into a uniform serpentine configuration with 23 parallel segments and each segment is 2.5m long. This is similar to the length and segments of the PEX-AL-PEX circulation system employed in the 1st stage testing. The aluminium brackets were manufactured from aluminium sheets which has a thickness of 1mm. Each bracket is about 10cm long and has a channel for inserting the pipe with a fin length of approximately 3cm. The fin provides additional area for transferring heat from the absorber to the circulation system. After inserting the pipe into the bracket channels, conductive silicone was used to fill the top gap which was then covered by a thin aluminium film. Using the conductive silicone could remove the low conductive air gaps and greatly improve the conduction between the absorber and the circulation system. The film was used to contain the silicone preventing it to be squeezed around making sticky mess on the absorber. A cross sectional view of the conduction mechanism is shown in Figure 6.1. The serpentine pipe was placed and fixed firmly on the back insulation using metal clips.

The absorber of the LSFPSC has a total collector area of 7 m^2 that consisted of six steel roofing sheets each with dimensions of W = 0.48m (total collector W = 2.9m), L = 2.4m, and thickness δ_{ab} = 1mm. The absorber surface was painted to achieve black matt finish that has high absorptivity α = 0.9 but it also has high emissivity ε_c = 0.9. These lightweight roofing sheets were joined via a locking mechanism side-by-side to create a firm and strong surface, which was then placed on top of the circulation system and clamped and screwed tightly to the supporting frame (i.e. top and bottom purlins).

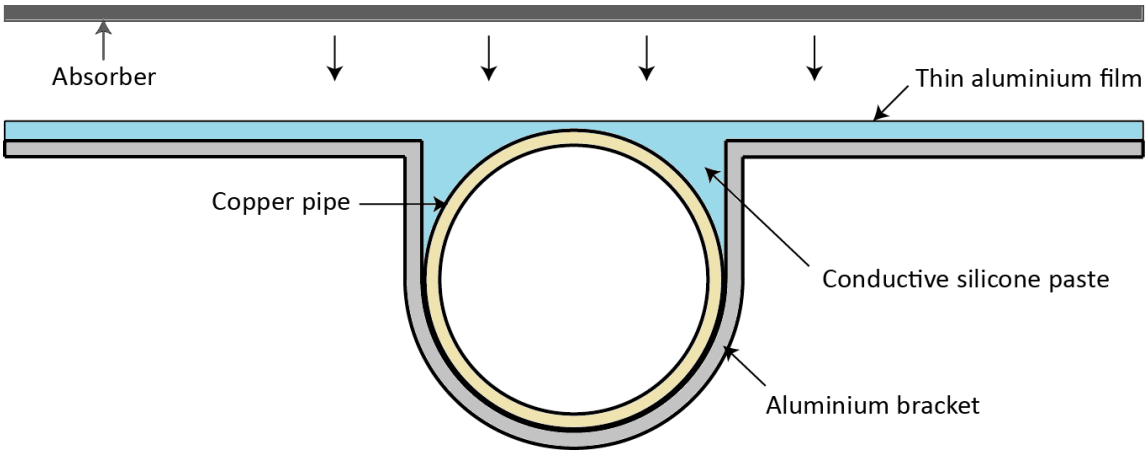

Figure 6.1: Cross sectional view of the contact mechanism using aluminium brackets

As described before, the prototype resembles a typical rooftop structure that has a pitch angle of 30^{o} with 100mm thick high-density back insulation ($k < 0.022$ W/ m K) supported by metal frames. The cross sectional view of the modified LSFPSC prototype is shown in Figure 6.2 with unglazed (up) or glazed (down) configurations. The glazing for the prototype consisted of three transparent glass sheets (emissivity $\varepsilon_{gl} = 0.92$ and transmittance $\tau = 0.9$) with dimensions W = 0.96m, L = 2.4m and thickness $\delta_{gl} = 2$mm. With vertical supportive beams, the glass sheets were placed on top of the absorber and fixed onto the purlins and then sealed with silicone, illustrated in Figure 6.3.

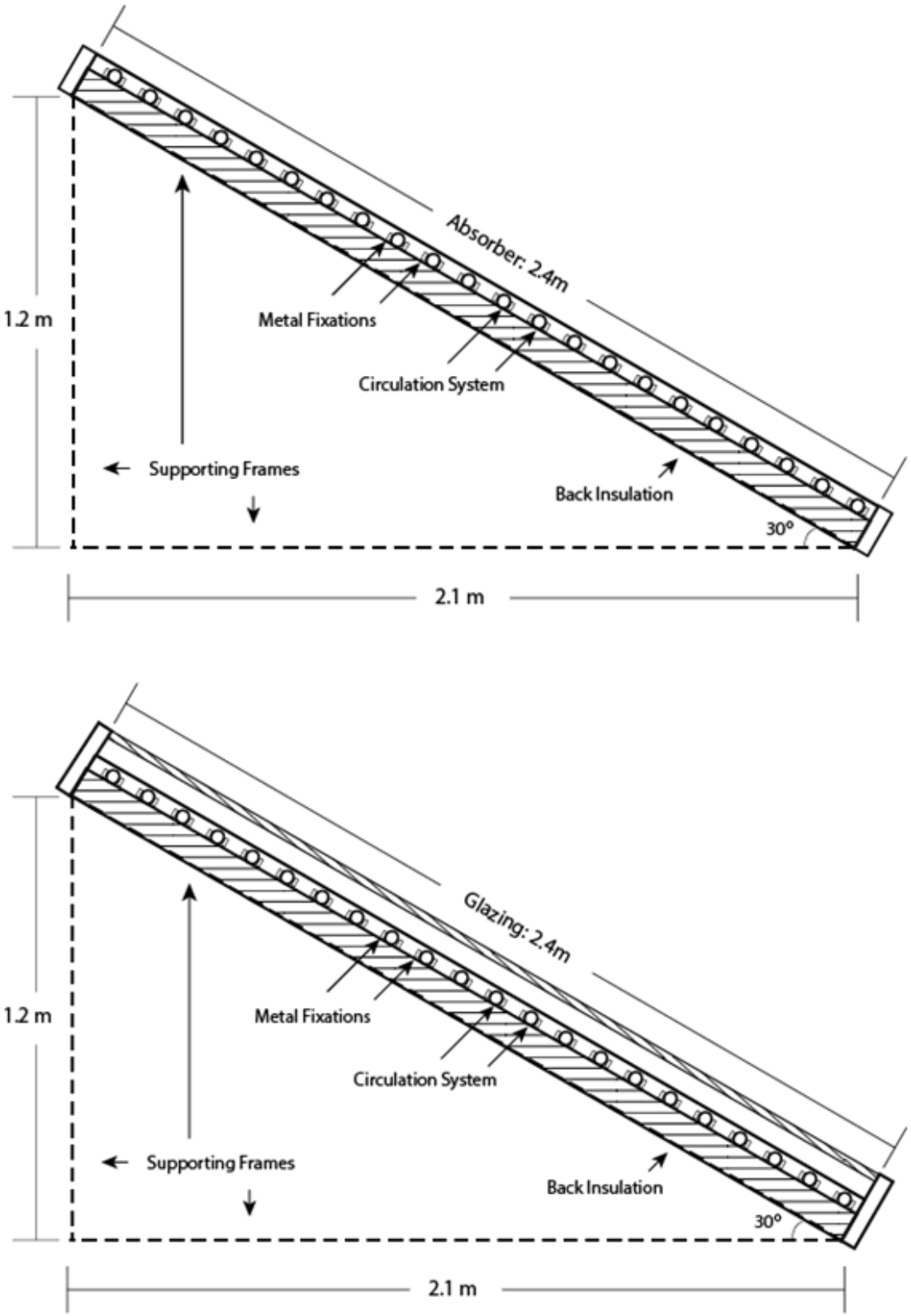

Figure 6.2: Cross-sectional view of the LSFPSC (Up: unglazed; Down: with glazing)

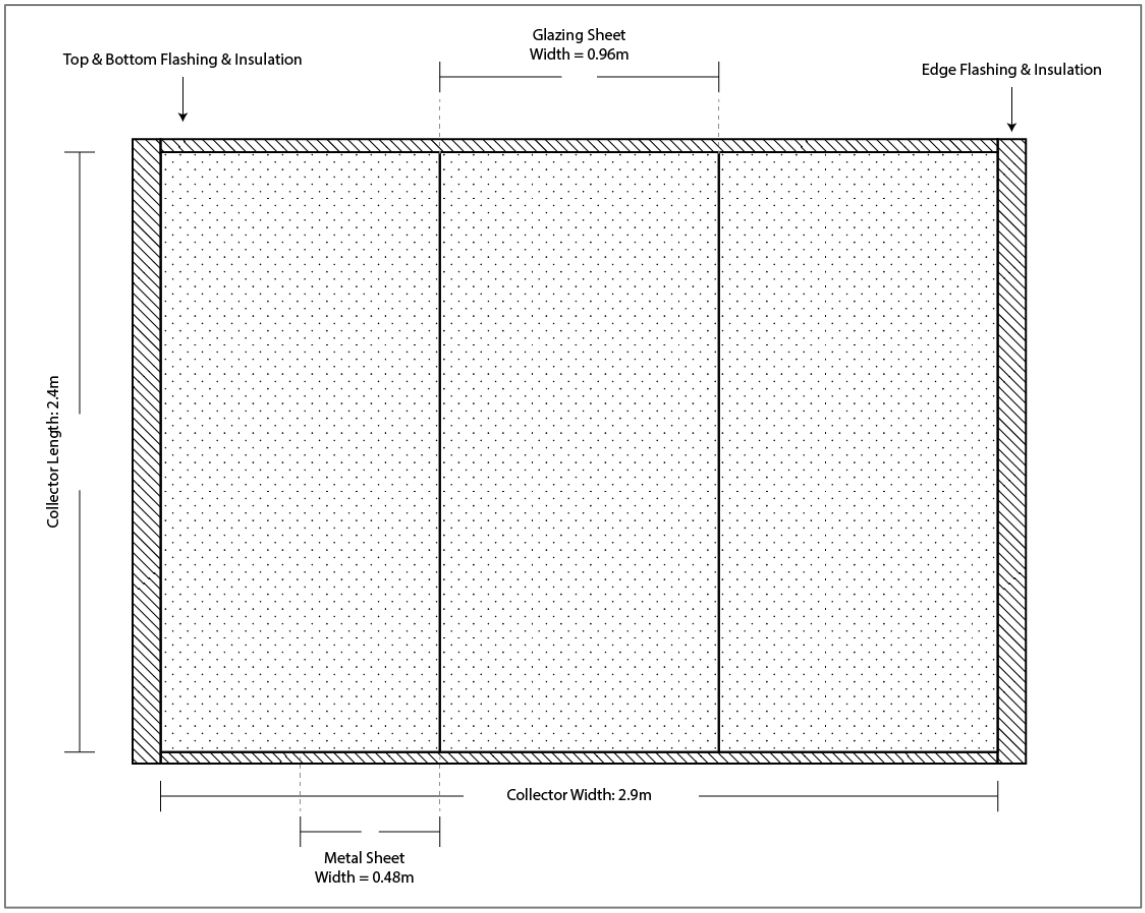

Figure 6.3. Frontal view of the glazed solar collector

The specifications of the modified LSFPSC prototype are provided in Table 6.1.

Table 6.1. Specifications of the LSFPSC prototype system

Components	Parameters	Value	Unit
Absorber	Length	2.4	m
	Width	2.9	m
	Thickness δ_c	0.001	m
	Thermal Conductivity k_c	50	W/m K
	Absorptivity α_c	0.9	
	Emissivity ε_c	0.9	
Circulation System	Total Length L_{cs}	55	m
	Length of each Segment L_{seg}	2.5	m
	Number of Segments N_{seg}	22	
	Interspace between Segments W_{seg}	0.1	m
	Outer diameter D_o	0.01	m
	Inner diameter D_i	0.008	m
	Thermal Conductivity k_{cs}	300	W/m K
	Pump power	43	W
Glazing (Glass)	Length	2.4	m
	Width	2.9	m
	Thickness	0.002	m
	Emissivity ε_{gl}	0.92	
	Transmittance τ	0.9	
Back Insulation	Thickness	0.1	m
	Thermal Conductivity	0.022	W/m K

6.2 Experiment Test-rig

The performance of the LSFPSC prototype was tested in the same indoor experimental facility as described in Chapter 3, with the test-rig schematic of shown in Figure 6.4. A solar simulator equipped with quartz-halogen lamps was employed to provide controllable output of artificial sunlight. Different to the testing in the 1st Stage, a Kipp & Zonen CM3 pyranometer was used to measure the mean irradiance across the surface of the LSFPSC.

The LSFPSC prototype was connected with a storage tank and the circuit was circulated by a centrifugal pump with a flow meter and a pressure transmitter installed for monitoring flow rate and pressure. In order to monitor the temperature distributions of the system, K-type thermocouples were installed based on the configuration described in Table A.2, Appendix A. The circulation system employed 10 mm diameter copper pipes and the parts not underneath the absorber were insulated with 22mm thick Armaflex foam to reduce heat losses to the surroundings.

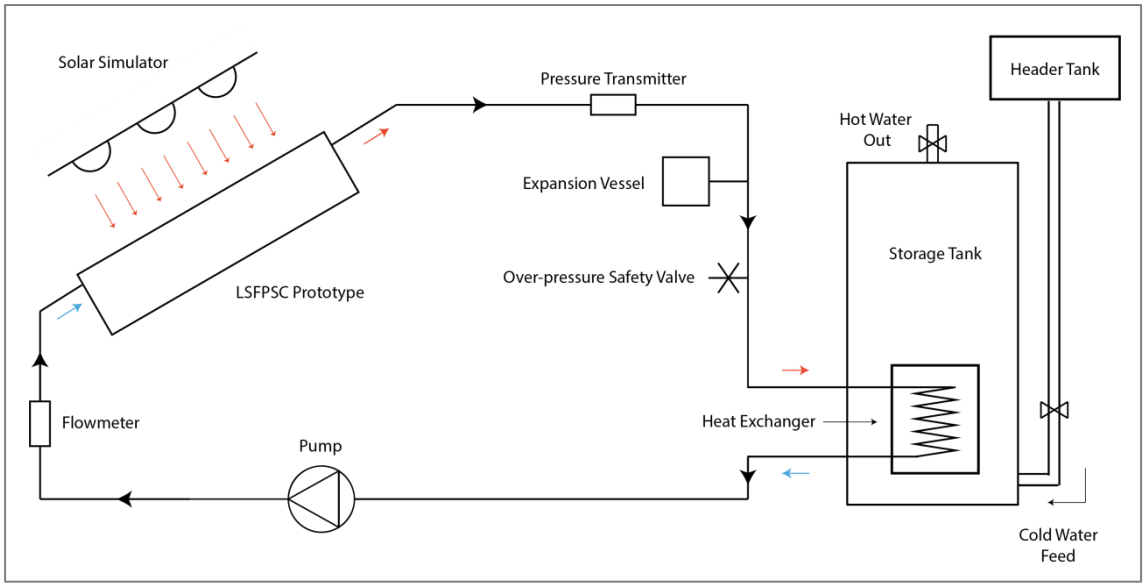

Figure 6.4. Schematic of the test-rig for the indoor testing of the LSFPSC prototype

Water was used as the heat transfer fluid in the closed-loop circulation system that absorbed heat from the LSFPSC and then transferred heat to the cold water in the storage tank via a heat exchanger. A new storage tank was employed with a bigger capacity of 180L instead of 118L that has a finned heat exchanger which is more efficient.

The LSFPSC was tested under a constant irradiance G = 500 W/m^2 over its aperture area for two hours with both the glazed (GL) and unglazed (UNGL) configurations, and the wind speed $V_w < 2\ m/s$. This simulates the conditions during noon with consistent sunlight thus the steady state performance of the LSFPSC can be assessed. During all experiments, the mass flow rates were observed between 0.025 to 0.030 kg/s with a mean mass flow rate $\dot{m}_f$ of 0.028 kg/s. The inlet and outlet temperatures of the circulation system were recorded to calculate the useful energy gain of the collector and its efficiency. The ambient temperature of the testing environment was also recorded during all the experiments.

6.3 Thermodynamic Analysis

Based on the measured inlet and outlet temperatures and the fluid flow rate, the useful energy gain of the solar collector is given as:

$$Q_u = C_f \dot{m}_f (T_o - T_i) \tag{6.1}$$

This equation calculates the basic thermal performance of the collector. However, it is important to understand the conditions that influence the collector performance. In order to do that, data of the influencing conditions are used to characterise the collector by parameters to indicate how the collector absorbs and loses energy to the surroundings. Thus, another expression incorporating important factors such as wind speed, irradiance and ambient temperature is used to describe the thermal performance of a collector operating under steady state conditions:

$$Q_u = A_c F_R [G(\tau\alpha) - U_L (T_i - T_{am})] \tag{6.2}$$

A_c is the aperture area of the LSFPSC, which is given as:

$$A_c = (N_{seg}-1)W_{seg}L_{seg} \tag{6.3}$$

This includes the area of the interspaces between pipe segments and the area of the pipe itself. Solar collector efficiency can be calculated using Equation (6.1) as:

$$\eta = \frac{Q_u}{A_c G} = \frac{C_f \dot{m}_f (T_o - T_i)}{A_c G} \tag{6.4}$$

Also the collector efficiency can be defined with Equation (6.2) as:

$$\eta = \frac{Q_u}{A_c G} = F_R(\tau\alpha) - F_R U_L \frac{(T_i - T_{am})}{G} \tag{6.5}$$

For flat-plate solar collectors, heat losses are generally assumed to be released through the top, bottom and sides of the collector. U_L is defined as the collector overall loss coefficient that is the sum of the top, bottom and side loss coefficients:

$$U_L = U_{top} + U_{bot} + U_{side} \tag{6.6}$$

$$U_{bot} = \delta_{bot}/k_{bot} \tag{6.7}$$

$$U_{side} = \delta_{side}/k_{side} \tag{6.8}$$

For glazed collector, U_{top} can be defined as:

$$U_{top,gl} = \left(\frac{N}{\frac{C}{T_c}\left[\frac{(T_c - T_{am})}{N_{gl} + f}\right]^e} + \frac{1}{h_w} \right)^{-1} + \frac{\sigma_{sb}(T_c + T_{am})(T_c^2 + T_{am}^2)}{\frac{1}{\varepsilon_c + 0.00591 N_{gl} h_w} + \frac{2N_{gl} + f - 1 + 0.133\varepsilon_c}{\varepsilon_{gl}} - N_{gl}} \tag{6.9}$$

$$f = (1 + 0.089h_w - 0.1166h_w\varepsilon_c)(1 + 0.07866N)$$

$$C = 520(1 - 0.000051\beta^2)$$

$$e = 0.43(1 - 100/T_c)$$

For unglazed collectors, U_{top} is given as:

$$U_{top,ungl} = U_{top,rad} + U_{top,conv} \tag{6.10}$$

The top radiation loss is given as:

$$U_{top,rad} = \frac{\varepsilon_c \sigma_{sb}(T_c^4 - T_{am}^4)}{(T_c - T_{am})A_c} \tag{6.11}$$

The top convection loss is given by the McAdams equation (McAdams, 1954):

$$U_{top,conv} = h_w = 5.7 + 3.8V_w \tag{6.12}$$

The overall loss coefficients for the unglazed and glazed configurations calculated for the indoor testing are: $U_{L,ungl} = 12.8\, W/\, m^2K$ and $U_{L,gl} = 6.3\, W/\, m^2K$. The calculation parameters are shown in Table 6.2 and 6.3.

Table 6.2: Calculation Parameters of $U_{L,ungl}$

Stefan-Boltzmann constant	5.67E-08	W/m^2 K^4
Emissivity of the collector	0.9	
Collector aperture area	5.5	m^2
Mean collector temperature T_c	315.08	K
Mean ambient temperature T_a	297.47	K
Wind heat transfer coefficient	11.4	W/m^2 K
Overall loss coefficient $U_{L,ungl}$	12.8	W/m^2 K

Table 6.3: Calculation Parameters of $U_{L,gl}$

Stefan-Boltzmann constant	5.67E-08	W/m^2 K^4
Emissivity of the collector	0.9	
Emissivity of the glazing	0.9	
Collector aperture area	5.5	m^2
Mean collector temperature T_c	315.24	K
Mean ambient temperature T_a	292.77	K
Wind heat transfer coefficient	13.3	W/m^2 K
Overall loss coefficient $U_{L,gl}$	6.3	W/m^2 K

The collector removal factor F_R is the ratio of the heat gained by the heat transfer fluid to the heat gained in the condition that the mean collector temperature equals the inlet fluid temperature, i.e. how effective that absorbed energy can be removed by the heat transfer fluid. For serpentine tube configuration, this is defined as (Zhang and Lavan, 1985):

$$F_R = F_1 F_3 F_5 \left[\frac{2F_4}{F_6\, exp\left(-\sqrt{1-F_2^2}/F_3\right) + F_5} - 1 \right] \tag{6.13}$$

The parameters F_1 through to F_6 are given by:

$$F_1 = \frac{\kappa}{U_L W_{seg}} \frac{\kappa R(1+\gamma)^2 - 1 - \gamma - \kappa R}{[\kappa R(1+\gamma) - 1]^2 - (\kappa R)^2}$$

$$F_2 = \frac{1}{\kappa R(1+\gamma)^2 - 1 - \gamma - \kappa R}$$

$$F_3 = \frac{\dot{m}_f C_f}{F_1 U_L A_c}$$

$$F_4 = \left(\frac{1 - F_2^2}{F_2^2}\right)^{1/2}$$

$$F_5 = \frac{1}{F_2} + F_4 - 1$$

$$F_6 = 1 - \frac{1}{F_2} + F_4$$

And

$$\kappa = \frac{(k_c \delta_c U_L)^{1/2}}{sinh\left[(W_{seg} - D_{outer})(U_L/k_c\delta_c)^{1/2}\right]}$$

$$\gamma = -2\,cosh\left[(W_{seg} - D_{outer})\left(\frac{U_L}{k_c\delta_c}\right)^{1/2}\right] - \frac{D_{outer}U_L}{\kappa}$$

$$R = \frac{1}{C_b} + \frac{1}{\pi D_{inner} h_f}$$

$$C_b = \frac{k_b b}{\gamma}$$

C_b is the bond conductance that determines how effective heat conducts from the absorber to the circulation system. There is only mechanical contact between the absorber and the circulation system in the LSFPSC so even with the help of silicone fillings, the bond thermal conductivity is expected to be small ($0.2 < k_b < 0.5$ W/ m K) considering a combination of direct conductive contacts and indirect convective contacts via small air gaps straight above the circulation tubing. The collector removal factors for the unglazed and glazed configurations were calculated as: $F_{R,ungl} = 50.31\%$ and $F_{R,gl} = 67.26\%$, the calculation parameters are shown in Table 6.4 and 6.5.

Table 6.4: Calculation Parameters of $F_{R,ungl}$

Overall loss coefficient $U_{L,ungl}$	12.8	W/m^2 K
Bond thermal conductivity k_b	0.4	W/m K
Bond thickness γ	0.0015	m
Bond width b	0.01	m
Collector removal factor F_R	50.31%	

Table 6.5: Calculation Parameters of $F_{R,gl}$

Overall loss coefficient $U_{L,gl}$	6.3	W/m^2 K
Bond thermal conductivity k_b	0.4	W/m K
Bond thickness γ	0.0015	m
Bond width b	0.01	m
Collector removal factor F_R	67.26%	

Based on the collected data of the indoor tests, the mean experimental collector efficiency η_{exp} of the steady state testing period was calculated using Equation (6.4). The results were 43.50% for the unglazed configuration and 46.07% for the glazed configuration. The experimental collector efficiencies were made as a function of the term $(T_i - T_a)/G$, which were used to plot the experimental efficiency curves of GL and UNGL configurations of the LSFPSC vs. curves of typical GL and UNGL collectors, shown in Figure 6.5 and 6.6. The data for the typical collectors was adapted from (Duffie and Beckman, 2013).

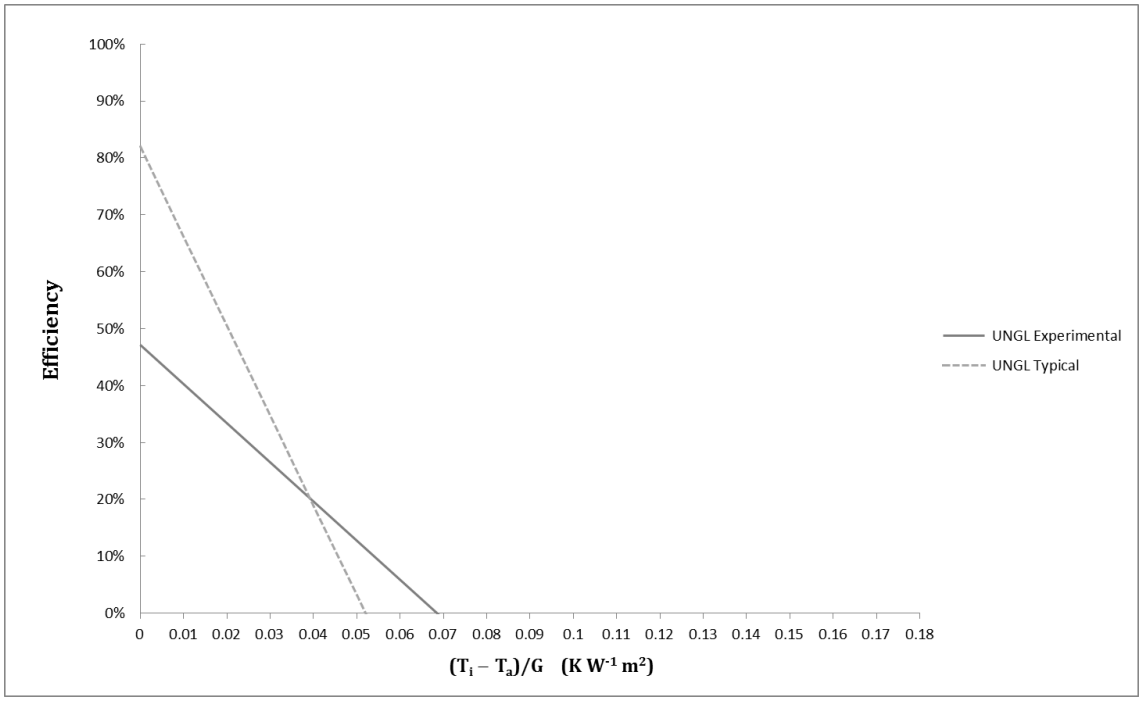

Figure 6.5: Collector efficiency vs $(T_c - T_a)/G$ for UNGL LSFPSC and typical UNGL collector

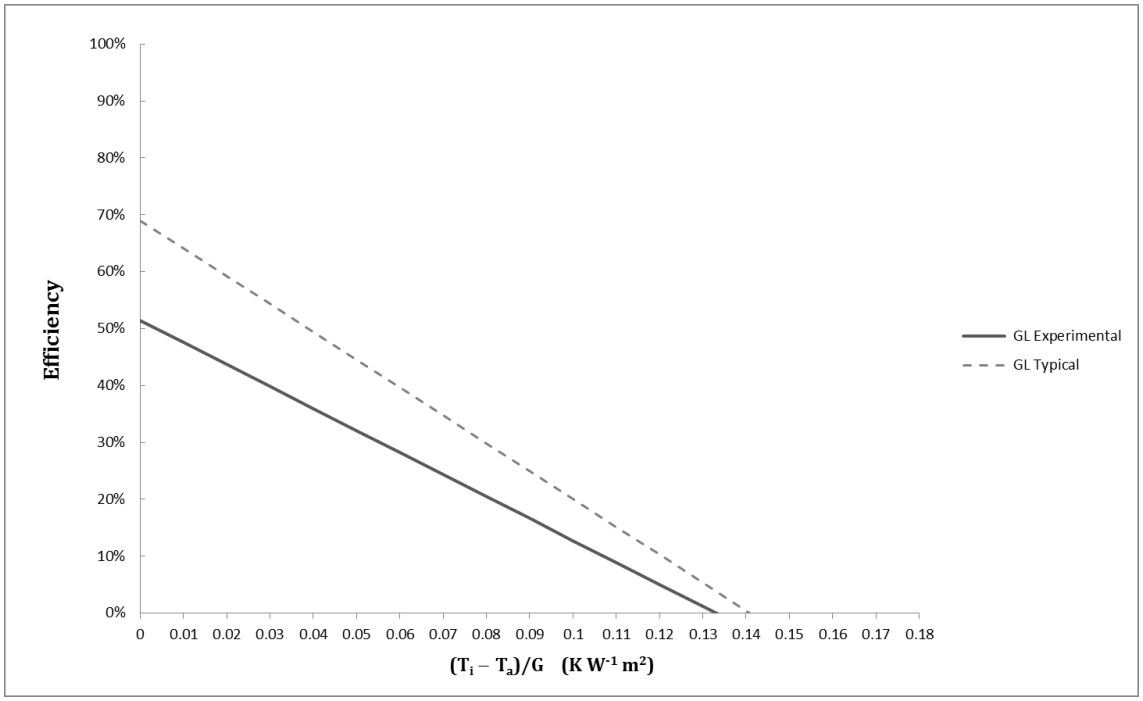

Figure 6.6: Collector efficiency vs $(T_c - T_a)/G$ for GL LSFPSC and typical GL collector

From the graphs, the slope $-F_R U_L$ and the intercept $F_R(\tau\alpha)$ can be adapted for the UNGL and GL experimental curves, based on the relationship described by Equation 6.5. The slope term $-F_R U_L$ is the heat loss factor (describes how energy is lost) and the intercept term $F_R(\tau\alpha)$ is the heat gain factor (describes how energy is absorbed). It is known that the UNGL configuration is much more susceptible to top convection loss caused by wind than the GL configuration as the UNGL absorber is not isolated from the surroundings by glazing. Hence the UNGL configuration has steeper curves. The performances of both configurations of the LSFPSC were reasonably good but not as good as their typical counterparts. This is mainly due to the significantly lower bond conductivity $(0.2 \leq k_b \leq 0.5\ W/m\,K)$ between the circulation system and the absorber than that $(30 \leq k_b\ W/m\,K)$ in the typical ones. Lower bond conductivity means slower heat transfer from the absorber to the circulating system thus the absorber has relatively higher temperature causing more heat losses to the surroundings hence lower collector efficiency. Despite its sacrifice on the collector performance, the mechanical contacts created by clamping greatly simplified the collector installation process as it is similar to installing metal roofing sheets. This saves manufacturing, installation and material costs.

The typical collectors are mounted solar collectors which are completely exposed to the surroundings while the LSFPSC is integrated with the building envelope with insulated, enclosed interior spaces that could have higher temperatures and less air flow than the ambient. Hence they have much better side and back insulation comparing to their typical counterpart that account for the less steep slope of the GL and UNGL efficiency curves shown in Figure 6.5 and 6.6. Even though the LSFPSC has shown lower efficiencies but its materials and production costs are much cheaper (£27.07/m^2 for UNGL and £43.02/m^2 for GL) than commercial flat plate collectors (typically > £200/m^2 for commercial GL collectors). The cost breakdown for the LSFPSC is shown in Table

6.6. This advantage allows the LSFPSC to be installed with much larger collector area (50 – 80% of roof area) to harvest significant amount of solar energy.

Table 6.6: Cost breakdown of the LSFPSC

Collector Components	Cost
Absorber	£11.79/m^2
Circulation Pipe	£6.60/m^2
Insulation	£8.68/m^2
Glazing	£15.95/m^2

6.4 Predictive Modelling

The experimental study showed that the LSFPSC has good efficiency and several advantages allowing it to be competitive against typical commercial flat plate collectors. For the purpose of practical improvement, development and application, it is important to extrapolate the experimental results for further analysis to envisage the potential of the LSFPSC in different conditions. Therefore, predictive efficiency curves of the GL and UNGL configurations were developed based on Equation 6.5 with calculated slope and intercept terms $-F_R U_L$ and $F_R(\tau\alpha)$. The predictive efficiency curves were then plotted vs. the experimental efficiency curves, as demonstrated in Figure 6.7 and 6.8.

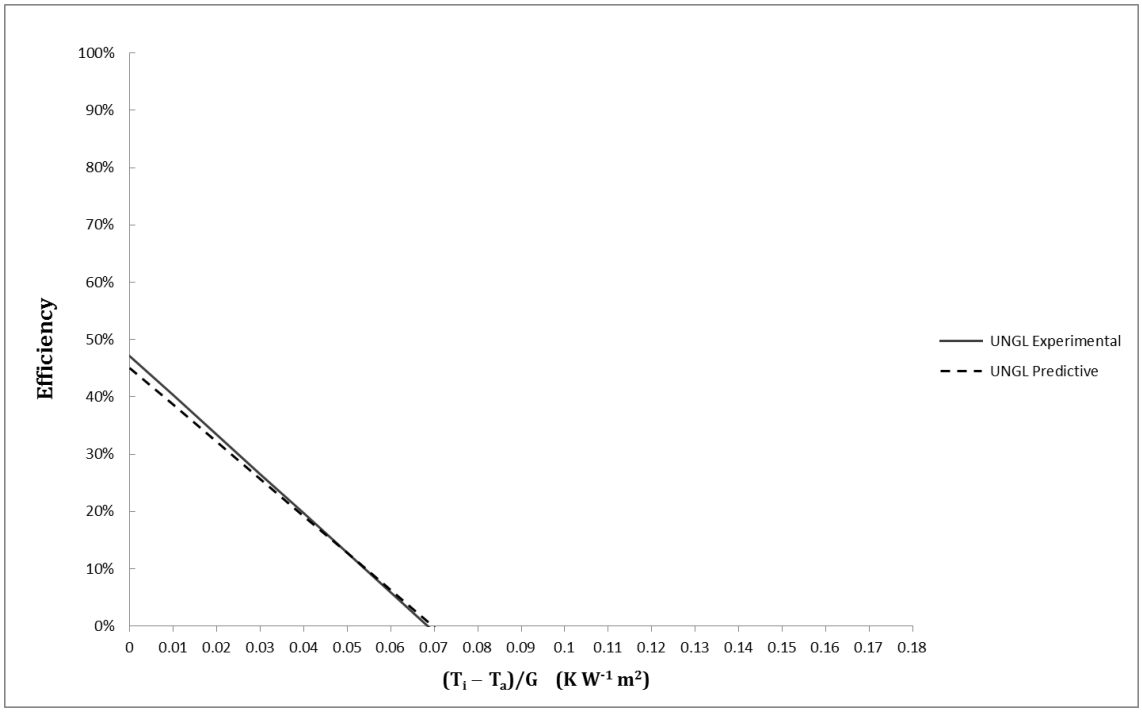

Figure 6.7: Comparison of experimental and predictive efficiencies for UNGL configuration

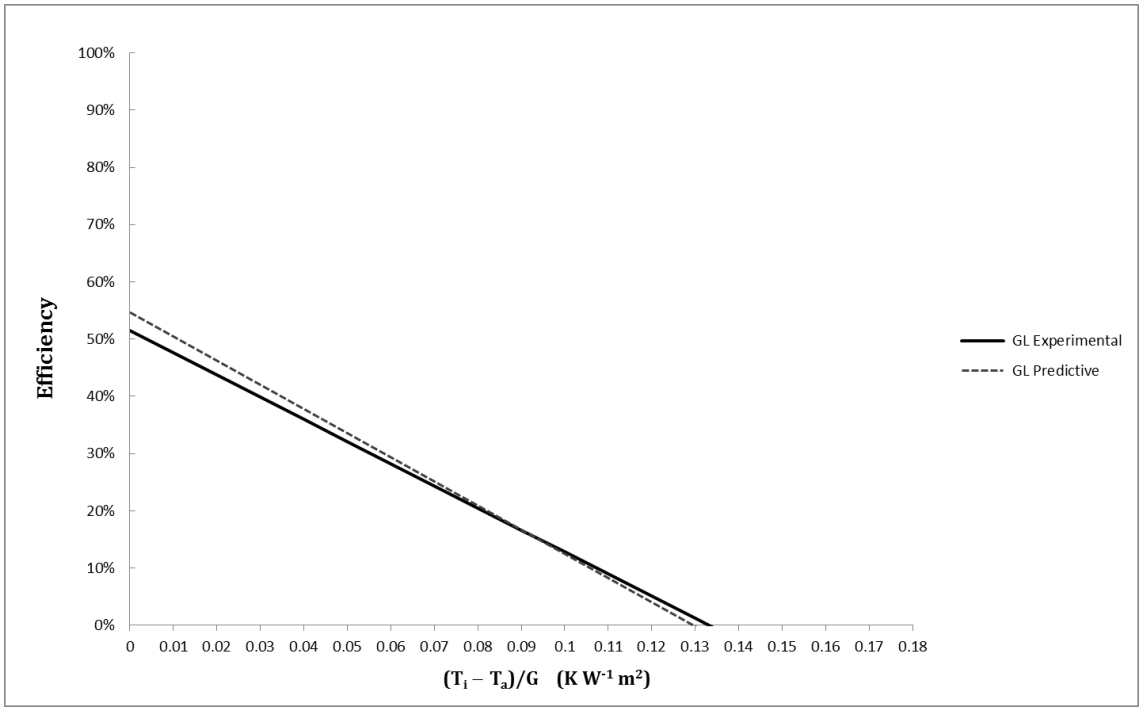

Figure 6.8: Comparison of experimental and predictive efficiencies for GL configuration

The experimental and predictive curves are closely correlated, and the mean predictive collector efficiency η_{pred} is calculated to be 43.72% for UNGL and 46.87% for GL showing satisfactory validation. Hence, the predictive model is suitable for subsequent parametric analysis.

The effects of the fluid mass flow rate on the thermal performance was analysed for the LSFPSC. For better data presentation and extrapolation, the mass flow rate was normalised to a unit collector area as specific mass flow rate $\dot{m}_s$. Figure 6.9 illustrates the steady state solar collector efficiency η_0 as a function of the specific mass flow rate under the conditions: $G = 800\, W\, m^{-2}$, $V_w = 2\, m\, s^{-1}$ and $T_i = T_a$ for both the GL and UNGL configurations.

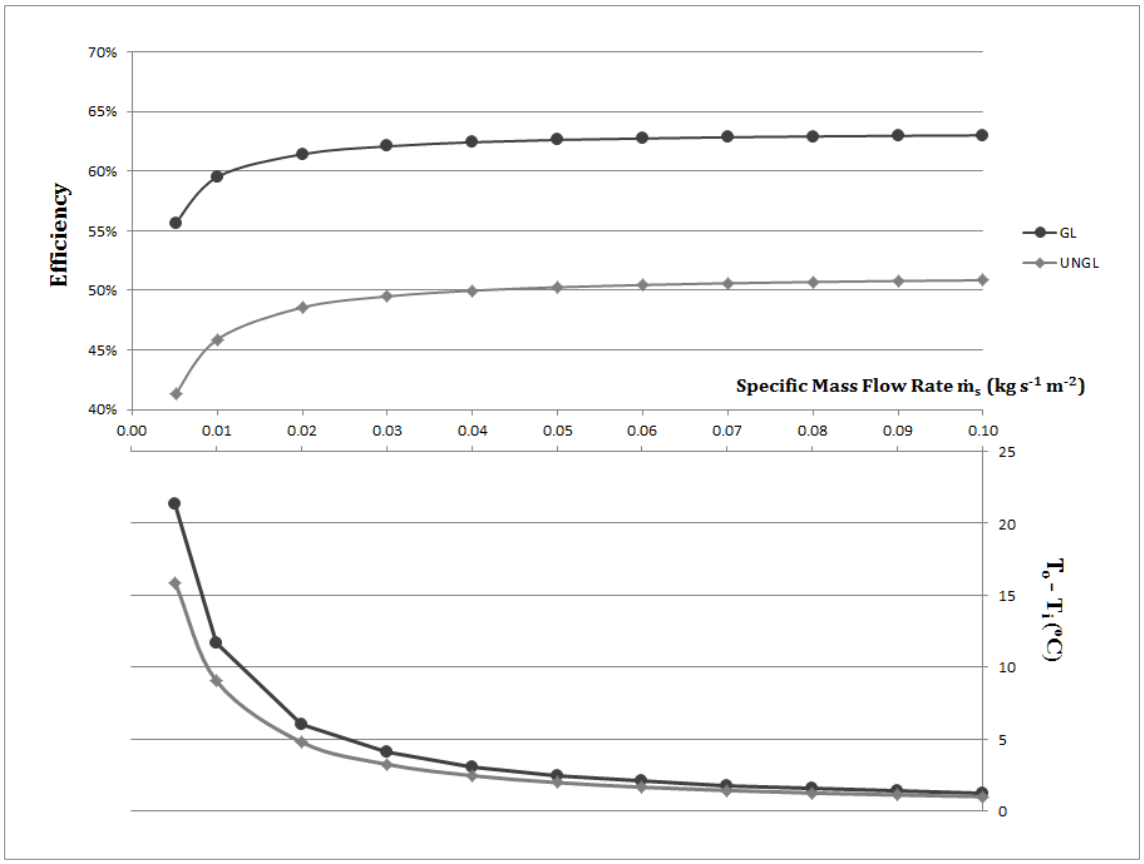

Figure 6.9. Influence of specific mass flow rate on efficiency for GL and UNGL configurations.

Equation (6.2) was used to calculate the useful energy gain which was then substituted into Equation (6.4) for the respective values of $(T_o - T_i)$. It is shown that higher $\dot{m}_s$ allows the heat transfer fluid to remove energy faster from the absorber (higher F_R) thus useful energy can be gained more effectively contributing to higher collector efficiency. However, when the specific mass flow rate increases to more than 0.02 kg s^{-1} m^{-2}, there is no significant increase in collector efficiency and the values of $(T_o - T_i)$ decrease. In practical operations, it is difficult to obtain constant flow rates due to many factors e.g. pressure increase, pump discrepancy, air gaps. Additionally, different output water temperatures may be required for different applications, e.g. swimming pool heating, domestic hot water. Therefore, a range of specific mass flow rate, 0.01 - 0.02 kg s^{-1} m^{-2} is recommended for the LSFPSC based on the design criterion of obtaining $(T_o - T_i)$ between 5 ^{o}C and 10 ^{o}C. For applications with higher temperature requirements, specific mass flow rates smaller than 0.01 kg s^{-1} m^{-2} can be employed.

The wind speed is proportional to the convective heat transfer coefficient of the absorber so it has direct influences on both the heat removal factor F_R and the overall heat loss coefficient U_L. Thus it is important to analyse the relationships between the wind speed and the thermal efficiency for the GL and UNGL configurations. The results are presented in Figure 6.10 and Figure 6.11, with $\dot{m}_s$ = 0.01 kg s^{-1} m^{-2}, $G = 800\ W\ m^{-2}$.

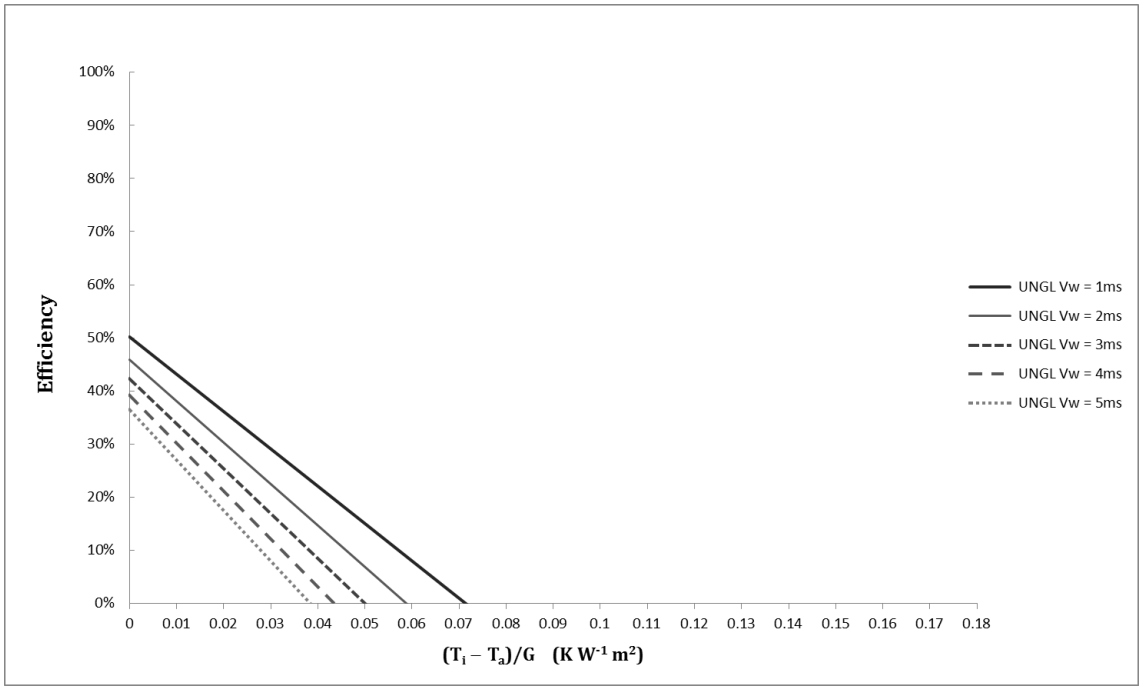

Figure 6.10. Influence of wind speed on the unglazed LSFPSC's thermal efficiency

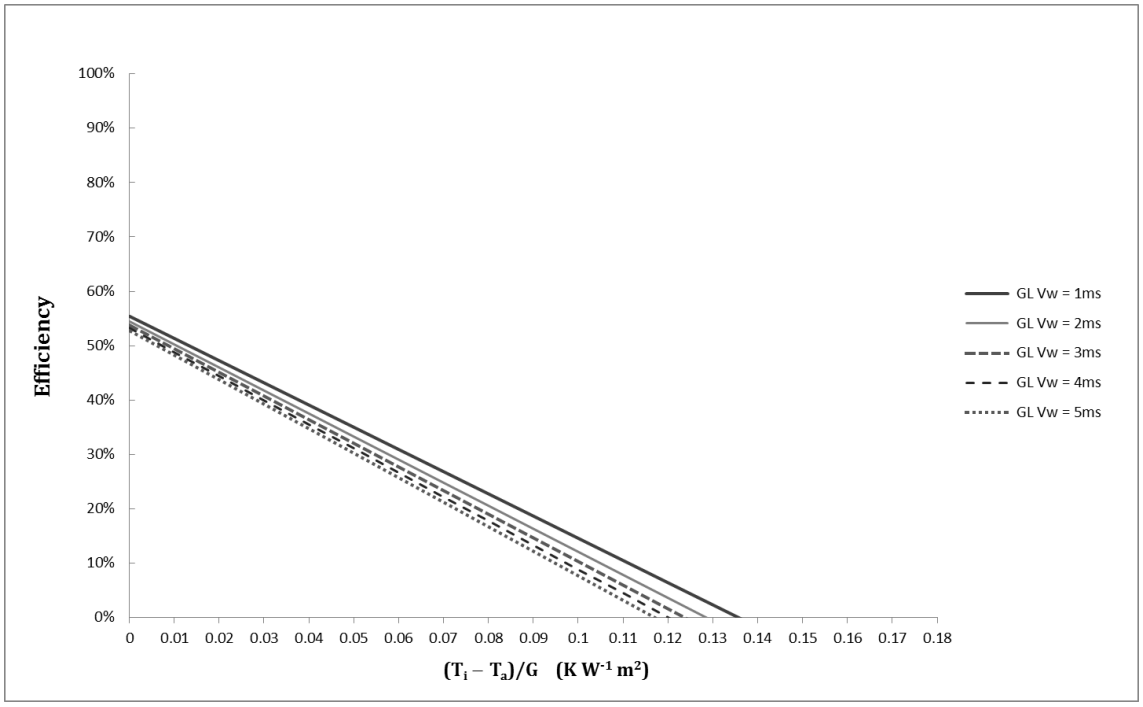

Figure 6.11. Influence of wind speed on the glazed LSFPSC's thermal efficiency

As previously discussed, the GL configuration is less susceptible to convective heat loss caused by wind than the UNGL configuration as it has glazing to isolate the absorber from the surroundings. This allows the GL to operate efficiently under a wide range of climates. However, the UNGL is cheaper than the GL in terms of manufacturing and installation costs and is efficient in hot climate with limited windy conditions. Therefore, it is important to research and identify locations with conditions to help deploying configurations in accordance with economical and operating

requirements. Using the meteorological data provided by Meteonorm, five locations were identified with varied horizontal irradiance G, ambient temperatures T_a and wind speeds V_w. The daily data of these parameters were extracted into monthly and yearly data which are shown in Table 6.7 (monthly data are not included).

Table 6.7. Locations with known yearly averaged G, Ta and V_w, data provided by Meteonorm.

Location, Country	Horizontal Irradiance	Ambient Temperature	Wind Speed	Latitude
	W/m^2	^oC	m/s	
DR of Congo, Kisangani	403.22	27.35	1.15	0.52^o N
India, New Delhi	448.88	26.92	1.76	28.61^o N
Spain, Madrid	363.13	16.29	2.95	40.40^o N
UK, London	200.33	12.11	4.01	51.51^o N
Algeria, Bechar	473.32	22.95	4.98	31.62^o N

Monthly and yearly efficiencies were calculated for each location with T_i = 20^oC assuming the collectors were horizontally installed. The calculated results are illustrated in Figure 6.11, Figure 6.12 and Figure 6.13.

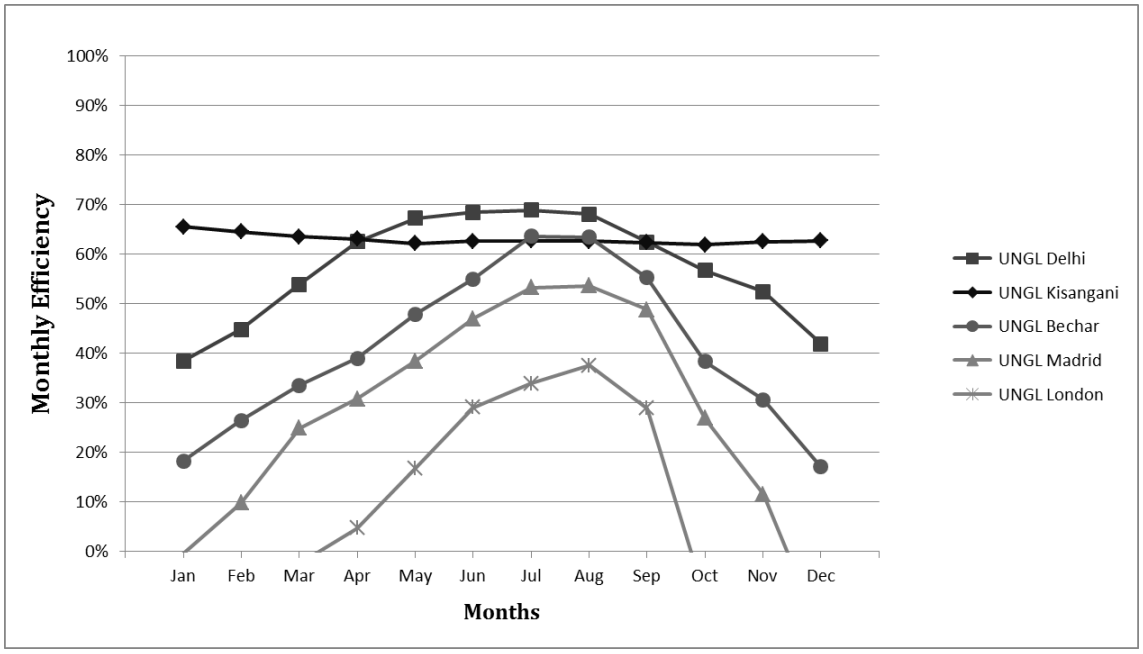

Figure 6.12. Monthly thermal efficiencies of the UNGL LSFPSC in five locations.

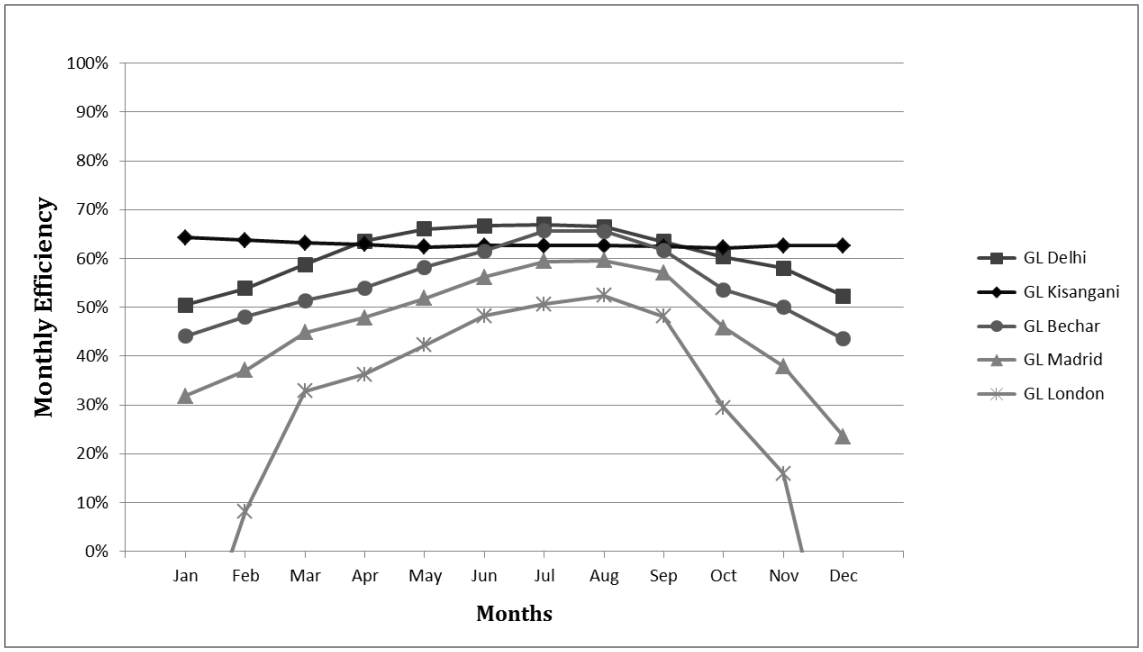

Figure 6.13. Monthly thermal efficiencies of the GL LSFPSC in five locations.

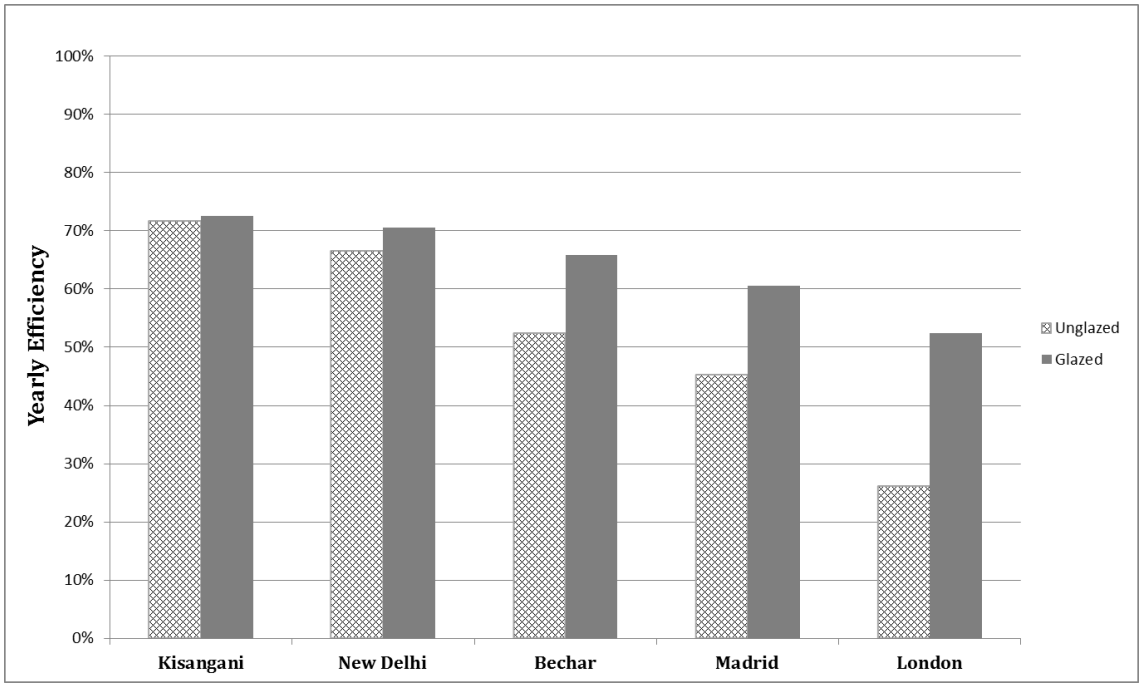

Figure 6.14. Comparison of yearly efficiencies of UNGL and GL LSFPSC in different countries.

The monthly figures showed that the efficiency of the UNGL configuration is highly dependent on the seasonal climate conditions as it has poorer performance in spring and winter compared to summer and autumn for four locations excluding Kisangani. The GL configuration also has reduced performance during spring and winter but not as severe. UNGL configuration is recommended for Kisangani and New Delhi, as it performs at similar levels as GL configuration with less cost. Both GL and UNGL configurations are suitable for Bechar and Madrid depending on the applications. GL configuration is suitable for London as it can operate with reasonable efficiencies from

late spring to early autumn for the purpose of providing domestic hot water while UNGL configuration can be used for swimming pool heating during summer. The results show that the LSFPSC can be employed in locations with varied weather conditions to produce satisfactory outputs.

The sizing of the LSFPSC is another important aspect that requires economical and operational considerations. For a given collector aperture area with uniform and constant irradiance, increasing the length of serpentine tubing underneath to a certain limit will not contribute significantly to the collector efficiency. This is due to the fact that as the heat transfer fluid flows through the serpentine tubing, the temperature gradient between them becomes smaller and approaches equilibrium under steady states. Hence the heat exchange rate is reduced substantially reaching zero. Therefore, it is important to identify optimal collector aperture areas as a large roofing area can be divided into smaller sub-sections for multiple installations of the LSFPSC to maximise the potential of solar energy harvesting. Figure 6.15 and Figure 6.16 illustrate the relationships of collector efficiency vs. N_{seg} and $(T_o - T_i)$ vs. N_{seg} for different L_{seg}, for W_{seg} = 0.1m, G = 800 W/ m^2, $T_i = T_a$ = 15°C and $\dot{m}_s$ = 0.01 kg s^{-1} m^{-2}. The outlet temperature T_o is predicted using the expression:

$$T_o = \exp\left(-\frac{U_L A_c F'}{\dot{m}_f C_f}\right)\left(T_i - T_{am} - \frac{G}{U_L}\right) + T_{am} + \frac{G}{U_L} \tag{6.14}$$

Where F' is the collector efficiency factor:

$$F' = \frac{\frac{1}{U_L}}{W_{seg}\left[\frac{1}{U_L\left[D_o + (W_{seg} - D_o)F\right]} + \frac{1}{C_b} + \frac{1}{\pi D_i h_f}\right]} \tag{6.15}$$

And F is the fin efficiency factor, which is given as:

$$F = \frac{tanh\left[\sqrt{\frac{U_L}{k_c \delta_c}}\frac{(W_{seg} - D_o)}{2}\right]}{\sqrt{\frac{U_L}{k_c \delta_c}}\frac{(W_{seg} - D_o)}{2}} \tag{6.16}$$

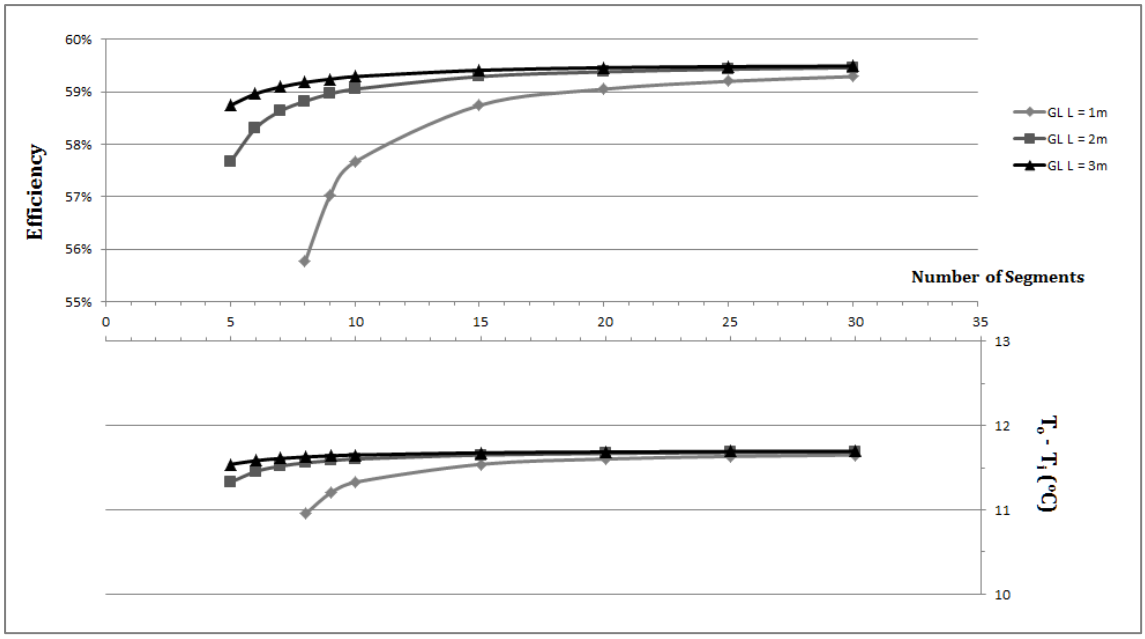

Figure 6.15. Efficiency vs. number of segments for different lengths of segments in GL configuration

For GL configuration, 5 x 2m segments are recommended as this combination has good efficiency and temperature gain. 2m segments are more preferable than 3m segments as they come across less metal roofing sheets horizontally allowing more flexible installation over roofing areas. 10 x 1m segments are not recommended due to the presence of more bends that can cause more turbulent in the heat transfer fluid leading to more energy consumption for the circulating pump; additional labour and energy cost will also incur to create the extra bends.

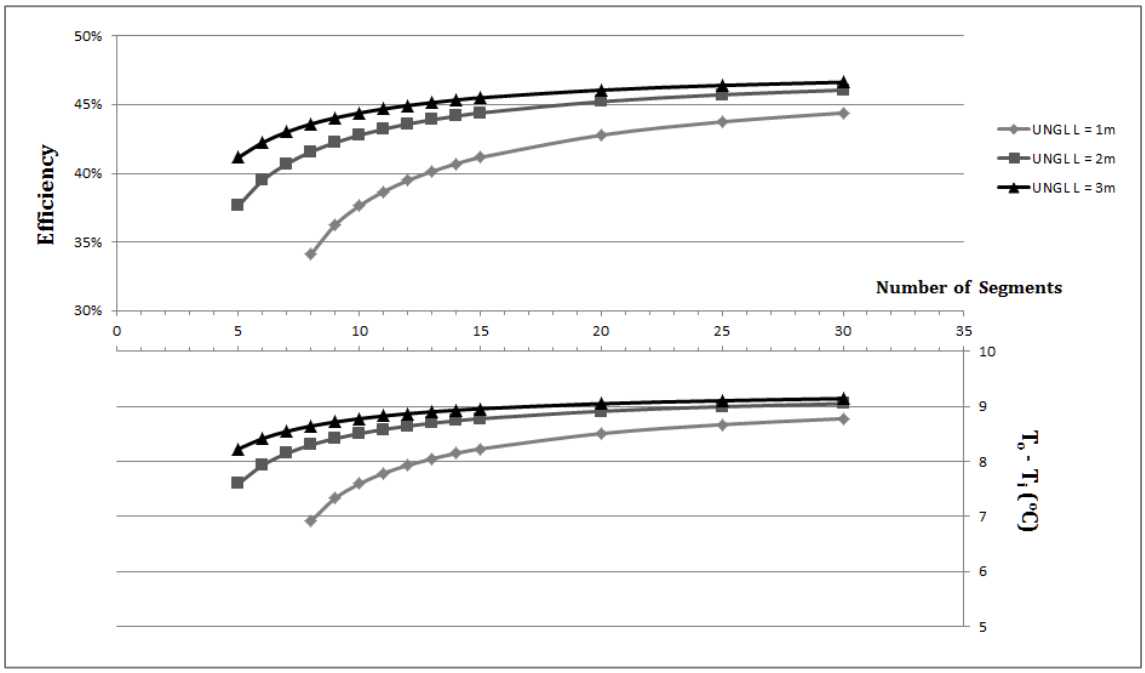

Figure 6.16. Efficiency vs. number of segments for different lengths of segments in UNGL configuration

For UNGL configuration, 10 x 2m segments are recommended for optimal combination of efficiency, temperature output and material costs.

6.5 Summary

The improvement testing results showed that the LSFPSCs have good performance but lower than the typical solar collectors which are mainly due to the mechanical contact between the absorber and the circulating system. This can be compensated by the extensively larger collecting area. The predictive models provided good indication that the LSFPSC can perform effectively under various weather conditions. Next chapter will describe how TRNSYS is used to simulate the performance LSFPSC under a wider range of climate conditions in conjunction with other system components (e.g. heat exchanger and storage tank) for different applications (e.g. water heating, space heating).

CHAPTER 7

7. 3rd Stage – Advanced Modelling and Application Assessment

7.1 Simulation Design and Validation

In the previous chapter, mathematical modelling was conducted for evaluating the performance of the LSFPSC using weather data from five different locations. Even though the modelling results were good indicators of the performance of LSFPSC, but the modelling was for the collector only and didn't include other system components such as the storage tank. Additionally, using mean monthly weather data in the modelling didn't reflect the actual variations of collector performance with daily and hourly weather conditions. Therefore, in order to accurately predict the performance of the LSFPSC under realistic conditions, a computer simulation was designed and developed to simulate the performance of the LSFPSC using realistic weather data with other components used in the actual installation of a fully functioning solar thermal system.

The simulation software used is called TRNSYS which is a quasi-steady state transient simulation program consisting of many subroutines modelling subsystem components (i.e. collector, circulation pump, storage tank etc.). The subsystem components can be linked with each other for solving differential equations and facilitating information output. Each component has its own mathematical description thus once all components comprising a particular system are identified, they can be interconnected for the system simulation process. An information flow diagram of the simulation process is constructed for the purpose of facilitating identification of the components and the flow of information between them. From the flow diagram a deck file is built containing information on all system components, weather data file and the output format. Figure 7.1 shows the information flow diagram of the TRNSYS model for simulating the performance of the LSFPSC prototype under the indoor testing conditions, where the solid lines were used to connect the operating components and the dash lines were used to connect the components with data output facilities.

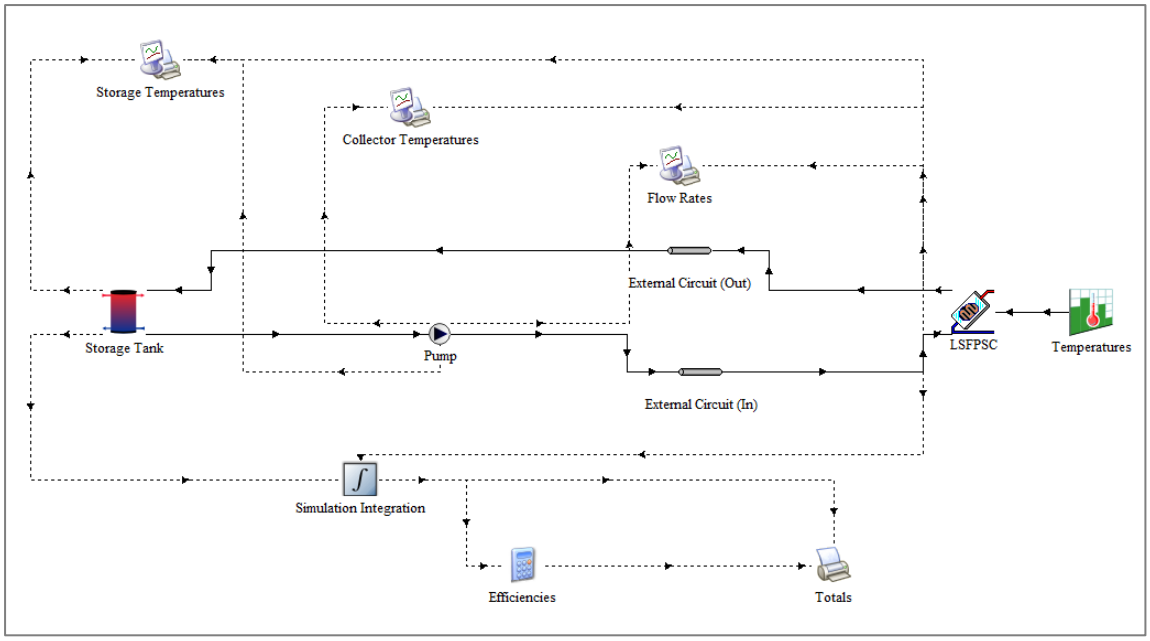

Figure 7.1: Information flow diagram for the simulation of the LSFPSC in indoor testing

The simulation time was set to be 2 hours, which was the same as the indoor testing time with time step of 1 second. Both the LSFPSC and the storage tank had the same parameters as shown in Table 6.1 with the same constant irradiance G = 500 W/m and flow rate $\dot{m}_f = 0.028\ kg/s$. The experimentally measured ambient temperatures were provided to the LSFPSC through the temperature function with compliance to the simulation time step which were used for calculating the values of U_L and F_R. The data output facilities include online plotters (used for showing live simulation data) and a data printer (used for data collection). The performance data (temperatures and flow rates) was integrated over the simulation period and then sent to the calculator function for calculating the collector efficiency which was later recorded by the data printer.

The simulation results of the collector efficiencies were 44.61% for the unglazed configuration and 45.96% for the glazed configuration, which were closely matched with the experimental results (i.e. 43.50% for UNGL and 46.07% for GL). The simulated output of the outlet, inlet and storage temperatures were also closely correlated with the experimental data, as illustrated in Figure 7.2 and 7.3, demonstrating satisfactory validation. This shows the simulation can accurately reflect the operations of the LSFPSC that can be used as a crucial tool for providing comprehensive evaluation of the LSFPSC's performance.

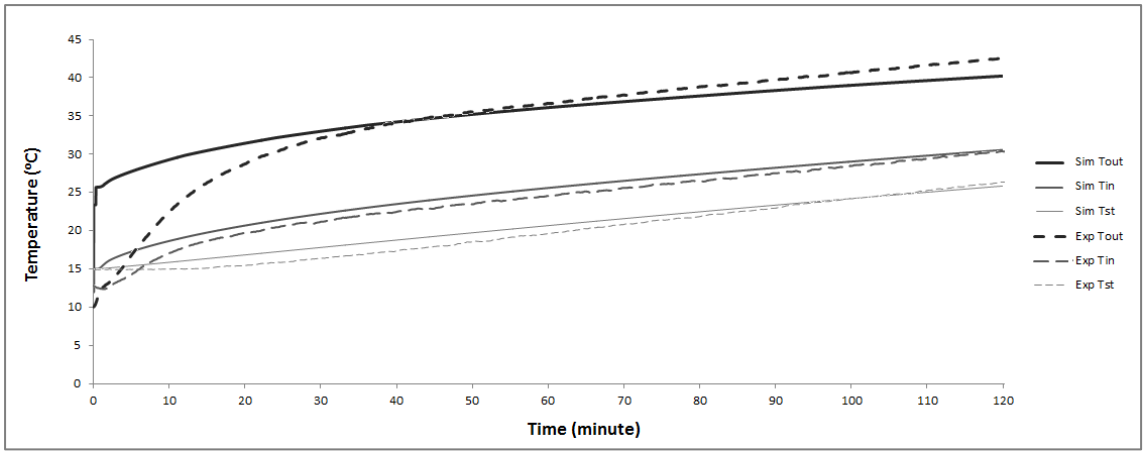

Figure 7.2. Simulated temperature results vs. Experimental temperature results for GL

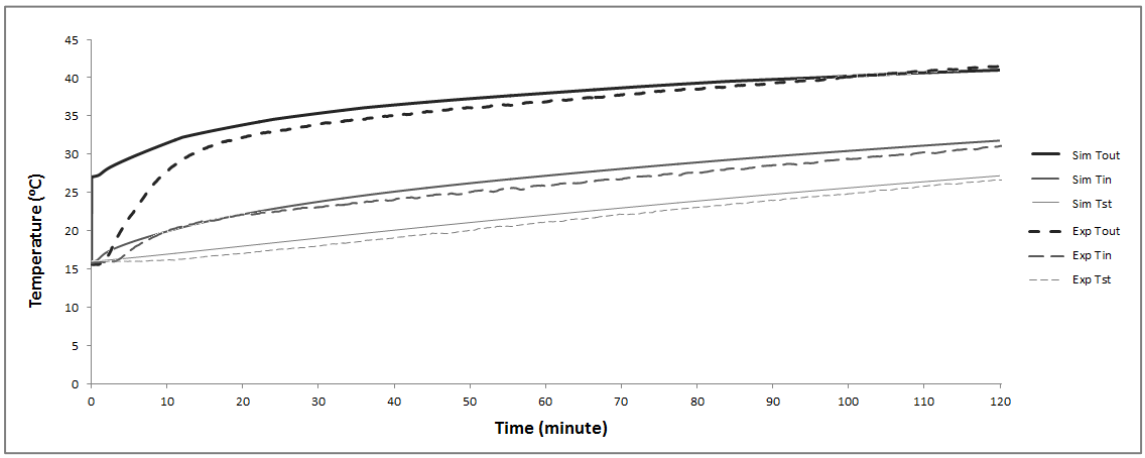

Figure 7.3. Simulated temperature results vs. Experimental temperature results for UNGL

7.2 Advanced Simulation Design

In order to realistically evaluate the potentials of the LSFPSC, it was necessary to simulate its performance when it is used in applications. Thus, the experimentally validated simulation model was modified to simulate the LSFPSC's performance in domestic hot water (DHW) pre-heating and space heating (SH) applications.

It was shown that using longer serpentine tubing can lead to increases collector efficiency and output water temperatures. However, the increases become negligible after increasing the tubing length to a certain limit, and the longer length can also cause higher flow resistance that require extra power consumption for the pump. Thus, it was recommended to employ multiple installations of the serpentine LSFPSC with shorter tubing lengths to fully utilise the roof area to generate useful output effectively and avoid incurring large flow resistance for the pump. In this simulation, both unglazed (UNGL) and glazed (GL) configurations were tested using ten LSFPSC installations that each has a collector area of 2m^2 consisting of 10 x 2m segments with 0.1m space between each other. The design concept of the multiple installations of the LSFPSCs is illustrated in Figure 7.4.

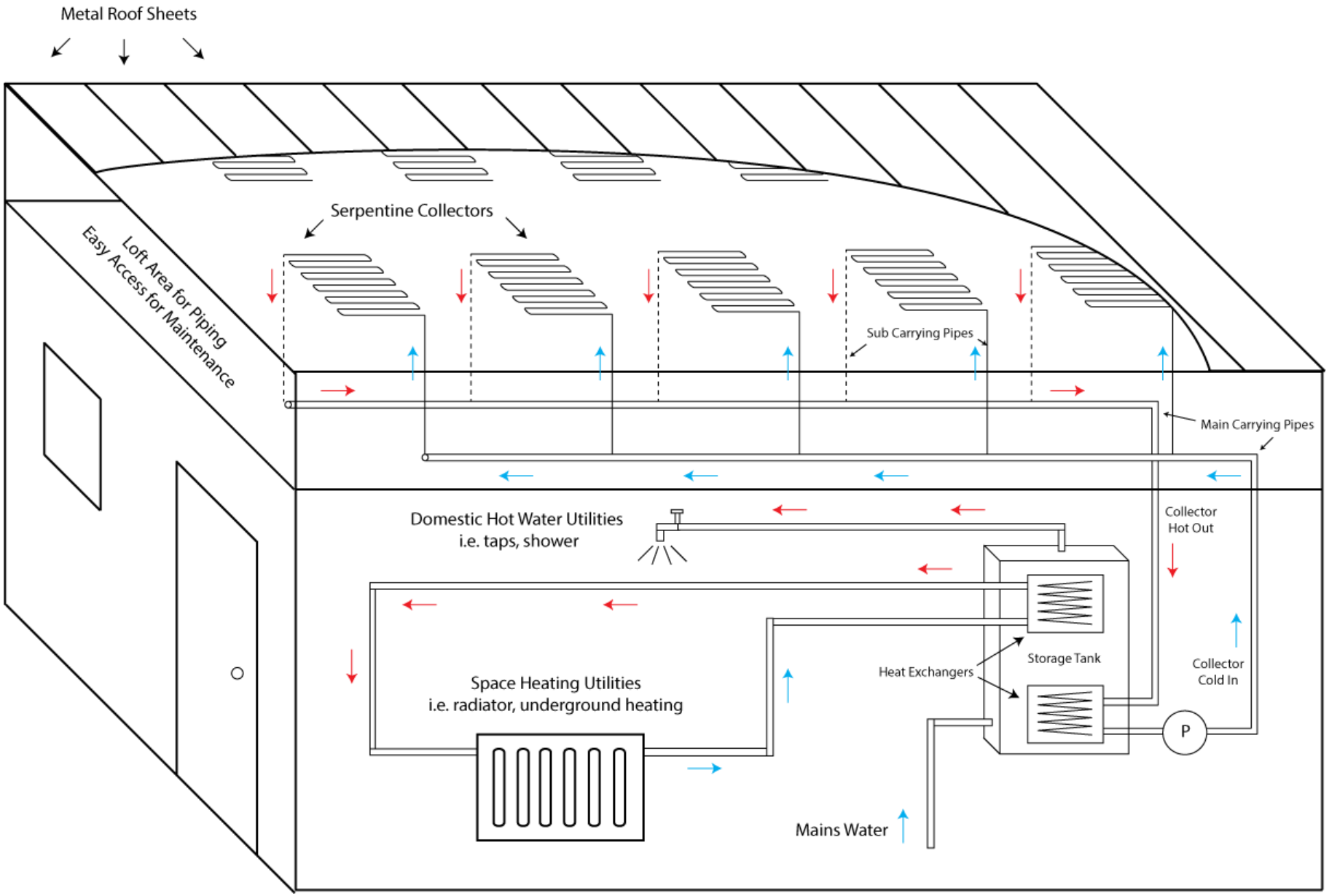

Figure 7.4: Design concept of multiple installations of the LSFPSCs

A reference roof area of 60m^2 was used assuming 1/3 of the roof area could be utilised for collector installation which gives a total collector area of 20m^2 for the installation of 10 LSFPSCs connected in parallel. The absorber (i.e. metal roof sheets) of the LSFPSC has an absorbance $\alpha_c = 0.9$ and an emissivity $\varepsilon_c = 0.9$, assuming only common black paint is used. The back of the LSFPSC is built-in with the building envelope that is not in direct contact with the ambient thus the back losses were assumed to be negligible. The smaller outlet and inlet piping of each LSFPSC are connected to larger main carrying pipes that are installed in the loft area. This places all the tubing joints that are prone to leaking in a location with easy access for maintenance. The well-insulated main carrying pipes are connected to the heat exchanger within a water storage tank.

The storage tank was designed to have a height of 1.5m and a storage volume of 1m^3 insulated by dense foam with mains water inlet on the bottom. For the simulation study, the volume of the water tank was divided equally into 6 nodes that were aligned vertically with node 1 to be the top node and node 6 to be the bottom one. The cold mains water entered the storage tank through the bottom (node 6) and absorbs heat from the coiled heat exchanger which is connected to the solar circuit with hot inlet placed at node 4 and cold outlet placed at node 6. Hot water was extracted from the top (node 1) to load (i.e. DHW and SH utilities). Since space heating is normally not required for regions with hot climate, two simulation designs were employed: one for DHW only and one for DHW and SH (combi system). The schematic diagrams of these two designs are shown in Figure 7.5 and 7.6.

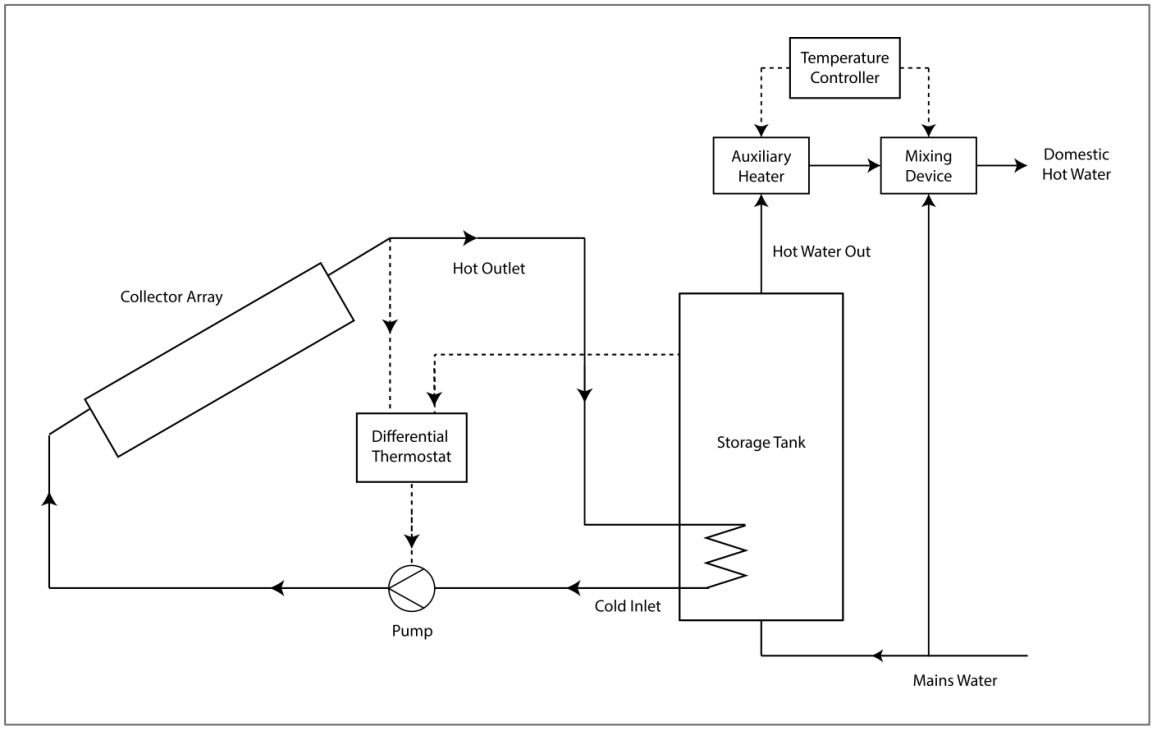

Figure 7.5. Schematic diagram of the DHW pre-heating system

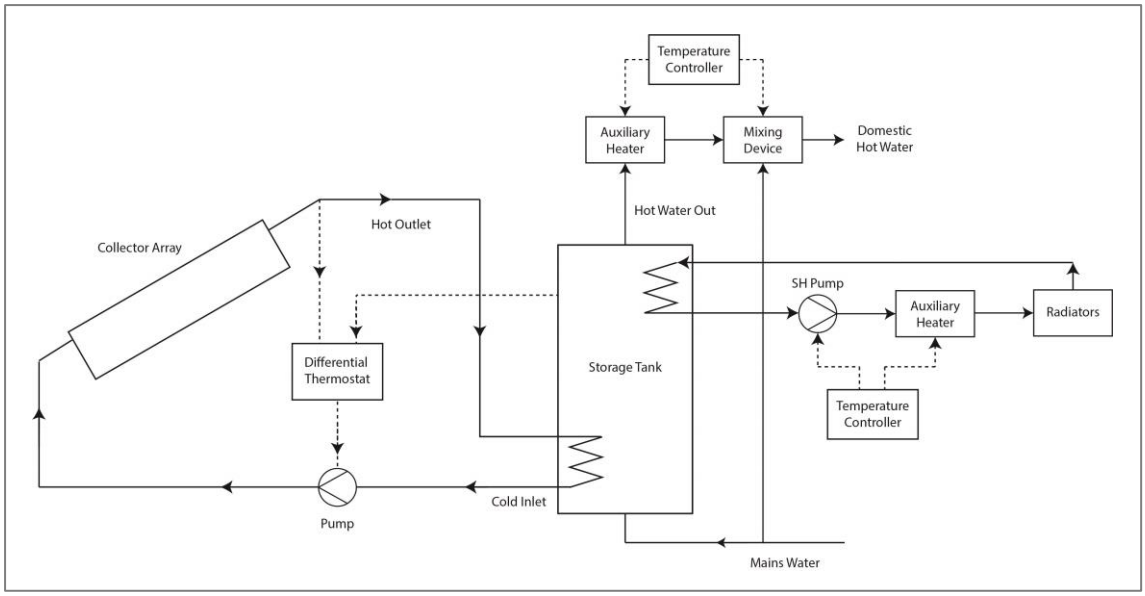

Figure 7.6. Schematic diagram of the DHW pre-heating and space heating (combi) system

A differential thermostat controller operated the solar circuit when the temperature of the fluid near the LSFPSC outlet is at least 10 ^{o}C higher than the fluid near the bottom of the tank. An auxiliary heater was employed to heat the pre-heated DHW to 50 ^{o}C if it is below this set point. The energy consumed by the heater contributed to the auxiliary energy $Q_{aux,DHW}$ and was used to calculate the solar fraction, which is given as:

$$sf_{DHW} = \frac{Q_{DHW}}{Q_{DHW}+Q_{aux,DHW}} \tag{7.1}$$

The combined performance of DHW and SH was studied using a reference building that has an area of 60m^2. An additional heat exchanger was installed near the top (across node 1 and 2) of the storage tank allowing heat to be extracted for the SH circuit while DHW can still be withdrawn from the top of the tank. A controller was used to monitor the room temperature and started the SH pump when the room temperature dropped below 20 ^{o}C. The solar fraction of the combi-system is given as:

$$sf_{combi} = \frac{Q_{DHW} + Q_{SH}}{Q_{DHW}+Q_{SH} + Q_{aux,DHW}+Q_{aux,SH}} \tag{7.2}$$

The information flow diagrams of the TRNSYS simulation models for DHW pre-heating and combi-system are shown in Figure 7.7 and 7.8. Both TRNSYS models reflects the design shown in Figure 7.4, 7.5 and 7.6 to simulate the performance of 10 LSFPSC installations each with collector area of 2 m^2 of which other specifications listed in Table 6.1. The descriptions of TRNSYS components are listed in Appendix C.

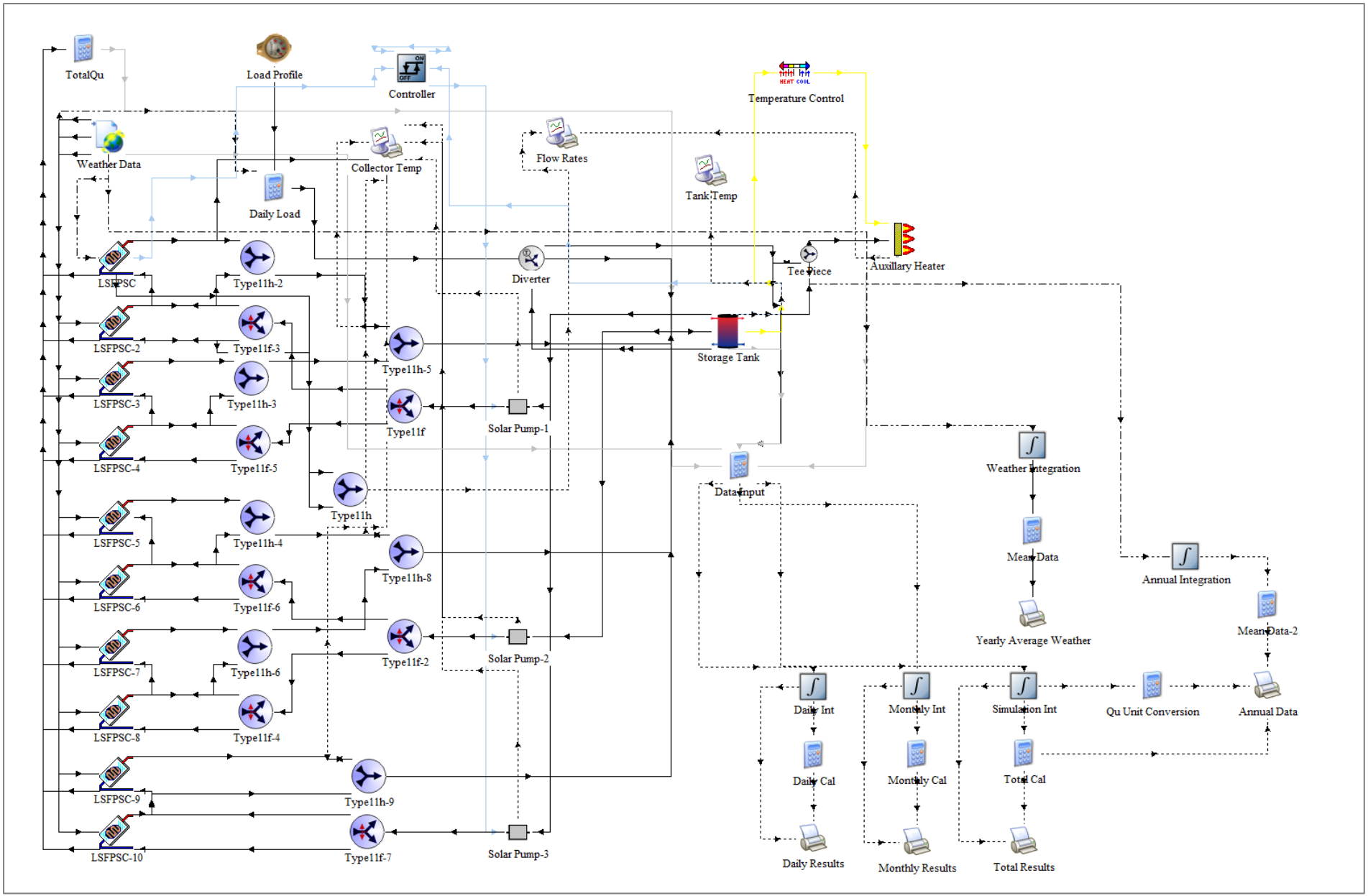

Figure 7.7: Information flow diagram for the simulation of the LSFPSC for DHW application

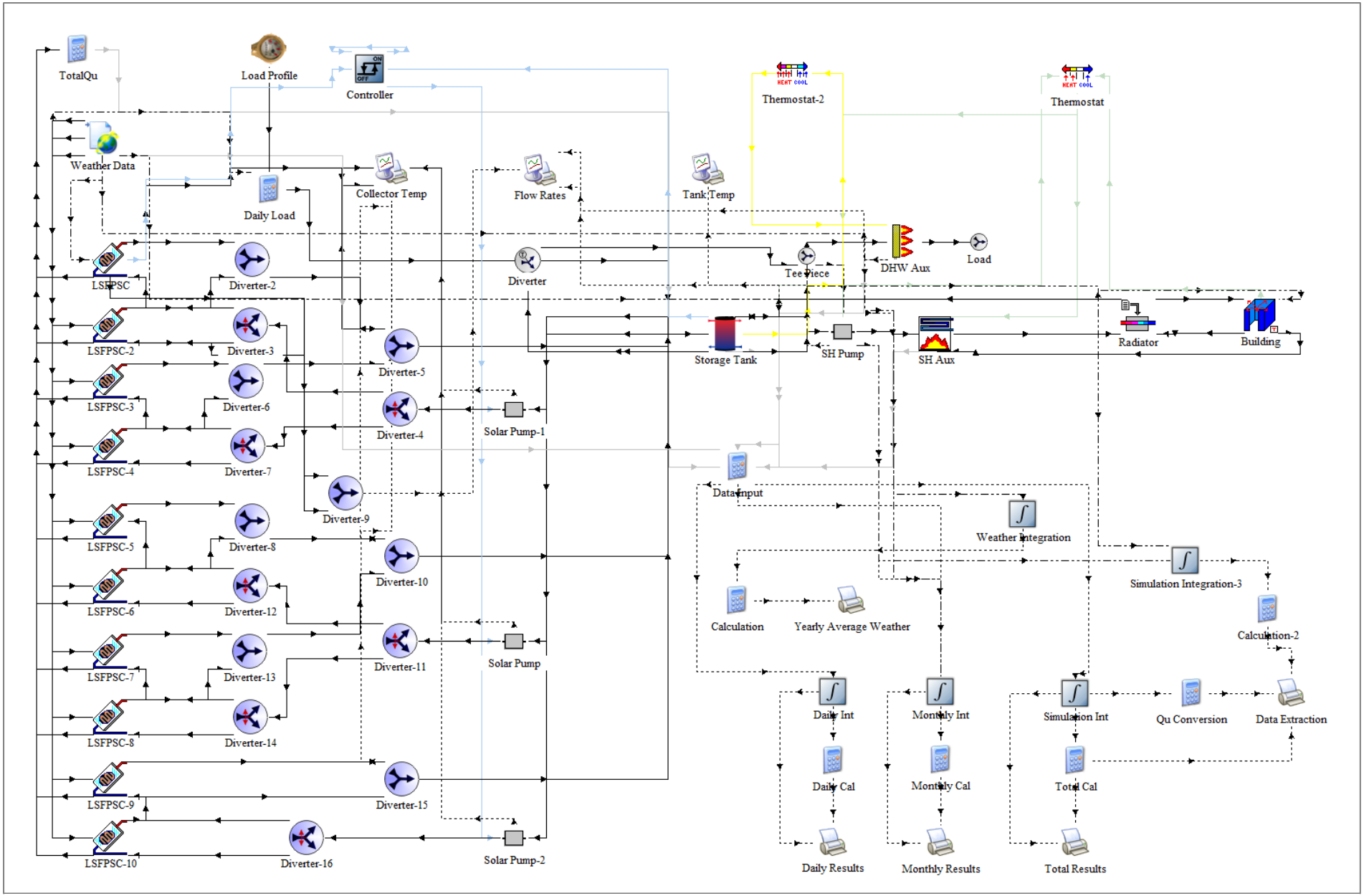

Figure 7.8: Information flow diagram for the simulation of the LSFPSC for DHW & SH application

The simulation time was set to be 8760 hours with simulation time step of 1 hour. The coding of the system components is displayed in Appendix C.

The simulation employed weather data of 36 different locations in 22 countries. The locations were selected based on the world map of Koppen-Greiger climate classification which is shown in Figure 7.9. The selected locations included the five types of main climates (i.e. equatorial, arid, warm temperate, snow, and polar) combined with different precipitation and temperature types representing the majority of populated regions around the world. Two locations were selected for each climate type for comparing performances in the differences in latitude and longitude. The selected locations are shown in Table 7.1.

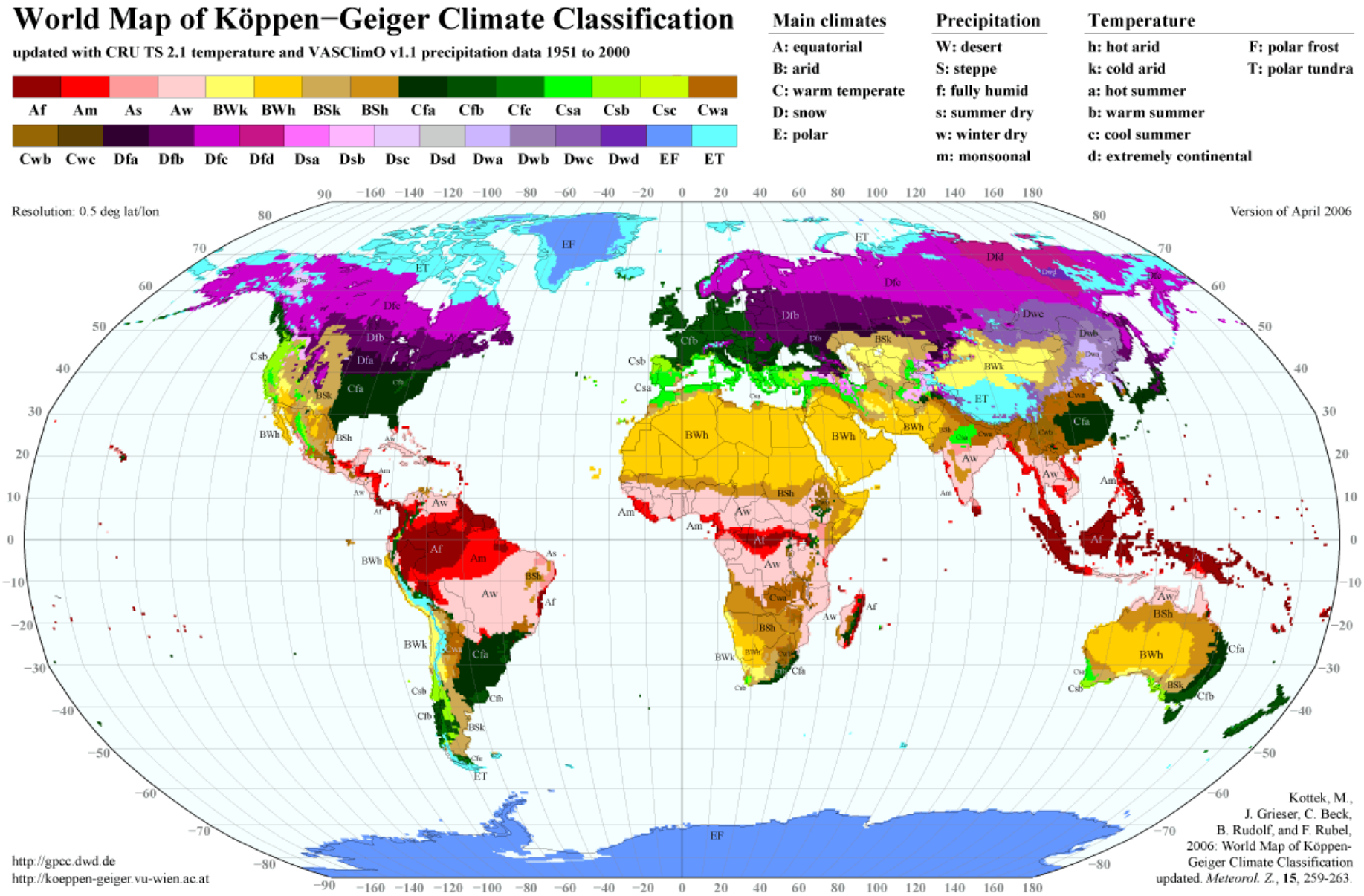

Figure 7.9: World map of Koppen-Greiger climate classification (Rubel and Kottek, 2010)

Table 7.1. Selected climate types for the simulation of LSFPSC

City	Country	Type	Latitude	Longitude	Yearly Mean Climate Conditions			
					I (W/m^2)	V (m/s)	T_{amb} (^oC)	T_{mw} (^oC)
Bogota	Colombia	Af	4.6	-74.08	695	2.20	13.26	16.59
Kuala Lumpur	Malaysia	Af	3.14	101.69	645	2.89	26.45	29.78
Freetown	Sierra Leone	Am	8.48	-13.23	791	2.84	27.23	30.56
Manila	Philippine	Am	14.6	120.98	731	2.79	26.97	30.31
Bankok	Thailand	Aw	13.76	100.5	720	1.19	27.71	31.04
Darwin	Australia	Aw	-12.46	130.84	849	3.26	27.68	31.02
Monterrey	Mexico	BSh	25.69	-100.32	773	4.47	25.09	28.42
New Delhi	India	BSh	28.61	77.21	808	1.43	25.07	28.41
Atyrau	Kazakhstan	BSk	47.09	51.92	627	3.48	9.27	12.60
Mildura	Australia	BSk	-34.21	142.14	755	3.50	16.77	20.10
Mecca	Saudi Arabia	BWh	21.42	39.82	926	1.51	30.65	33.98
Port Hedland	Australia	BWh	-20.31	118.58	944	4.49	26.11	29.44
Ashgabat	Turkmenistan	BWk	37.93	58.37	631	1.61	16.38	19.71
Jiuquan	China	BWk	39.73	98.49	691	2.11	7.26	10.59
Buenos Aires	Argentina	Cfa	-34.6	-58.38	701	4.19	17.42	20.76
Shanghai	China	Cfa	31.23	121.47	540	3.01	15.78	19.11
London	UK	Cfb	51.51	-0.13	380	4.04	10.78	14.11
Sydney	Australia	Cfb	-33.87	151.21	661	4.98	17.91	21.24
Madrid	Spain	Csa	40.42	-3.7	683	2.59	13.91	17.25
Perth	Australia	Csa	-31.95	115.86	796	3.44	18.17	21.50
Porto	Portugal	Csb	41.16	-8.63	641	4.97	14.48	17.81
San Francisco	USA	Csb	37.78	-122.42	714	4.53	13.09	16.42
Lusaka	Zambia	Cwa	-15.42	28.28	852	4.71	21.18	24.52
Xian	China	Cwa	34.34	108.94	639	1.77	13.36	16.69
Johannesburg	S.Africa	Cwb	-26.2	28.05	849	3.41	15.47	18.81
Kunming	China	Cwb	24.88	102.83	703	2.20	14.54	17.87
Chicago	USA	Dfa	41.88	-87.63	588	4.62	9.75	13.09
Volgograd	Russia	Dfa	48.7	44.52	612	4.86	7.57	10.91
Moscow	Russia	Dfb	55.76	37.62	395	1.27	5.01	8.35
Toronto	Canada	Dfb	43.65	-79.38	555	4.15	7.39	10.72
Beijing	China	Dwa	39.9	116.41	533	2.52	11.80	15.13
Seoul	S.Korea	Dwa	37.57	126.98	499	2.44	11.84	15.18
Chongjin	N.Korea	Dwb	41.8	129.78	543	1.15	7.68	11.01
Qiqihar	China	Dwb	47.35	123.92	617	2.88	3.54	6.87
Lhasa	China	ET	29.65	91.17	819	1.79	7.55	10.88
Cusco	Peru	ET	-13.52	-71.98	940	11.90	4.90	15.23

The typical meteorological year (TMY) data of all the selected locations was used in the simulation program. TMY is a collation of selected weather data for a specific location generated from several yearly data sets collected in the past to present the general characteristics of the weather for the specific location. The TMY data of the selected locations was provided by Meteonorm that consisted of hourly measured horizontal

irradiance, wind speed, ambient temperature, and mains water temperature. Horizontal irradiance is used here as the incident irradiance as the LSFPSC was assumed to be installed on horizontal roofs. The building styles vary greatly in the selected locations thus the horizontal performance can be used as a general guideline to describe how well the LSFPSC can perform and could be used as a reference for future analysis of the performance of tilted LSFPSC.

The performance of LSFPSC for DHW preheating was simulated with a consumption (load) profile. The load could vary significantly from day to day and from different consumers, but it is necessary to use a repetitive load profile for conducting performance study. Using a repetitive load profile is not exactly accurate as the DHW demand is generally higher in the summer than in the winter. However, the temperature of the DHW used in summer is not as high as during winter. Consequently, the total thermal energy requirement is reasonably constant throughout the year. The DHW consumption profile for this study is illustrated in Figure 7.10 assuming a daily DHW consumption of 500L for 10 to 20 people (5 to 7 families with average daily DHW consumption of 25 to 50L per person).

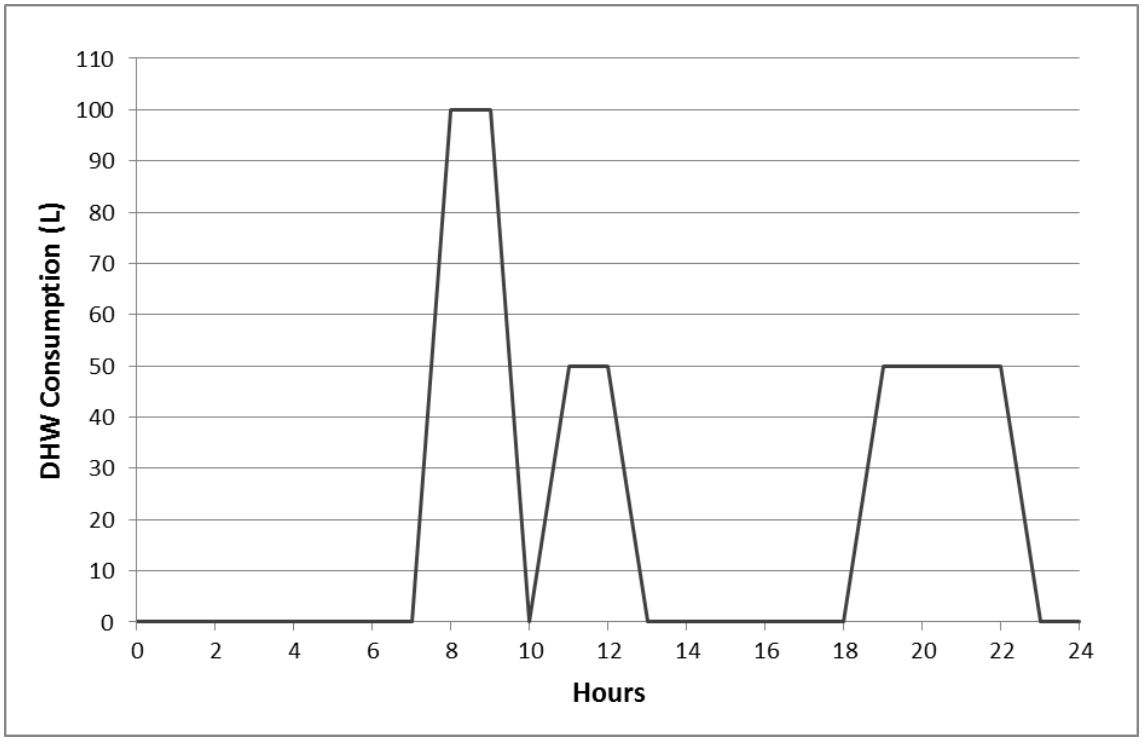

Figure 7.10. DHW daily consumption profile

7.3 Results and Discussion

The simulation was ran for each selected location using daily weather data and the daily results were integrated into annual results for comparative studies. Figure 7.11 shows the annual average temperatures of pre-heated DHW by the LSFPSC. With the glazed configuration, the LSFPSC can produce DHW higher than 50 ^{o}C in 40% of the locations and higher than 40 ^{o}C in 75% of the locations. With the unglazed configuration, the LSFPSC can produce DHW higher than 40 ^{o}C in 40% of the locations. This indicates satisfactory DHW pre-heating temperature outputs for large quantity of usage.

Figure 7.12 shows the simulation results of the annual useful energy Q_u gained by the LSFPSCs and Figure 7.13 shows the annual solar fractions for the selected locations. The LSFPSC is capable of producing at least 15GJ of Qu with unglazed configuration and 20GJ of Qu with glazed configuration meeting more than 50% of the DHW energy demands in the majority of the selected locations. Overall, the glazed configuration (1.29 GJ/m^2/yr or 358 kWh/m^2/yr) performed approximately 30% better than the unglazed configuration (1.00 GJ/m^2/yr or 278 kWh/m^2/yr) in both DHW and DHW + SH applications. However, it is noticed that the unglazed configuration is capable of producing similar amount of useful energy as the glazed configuration on several locations with hot climates.

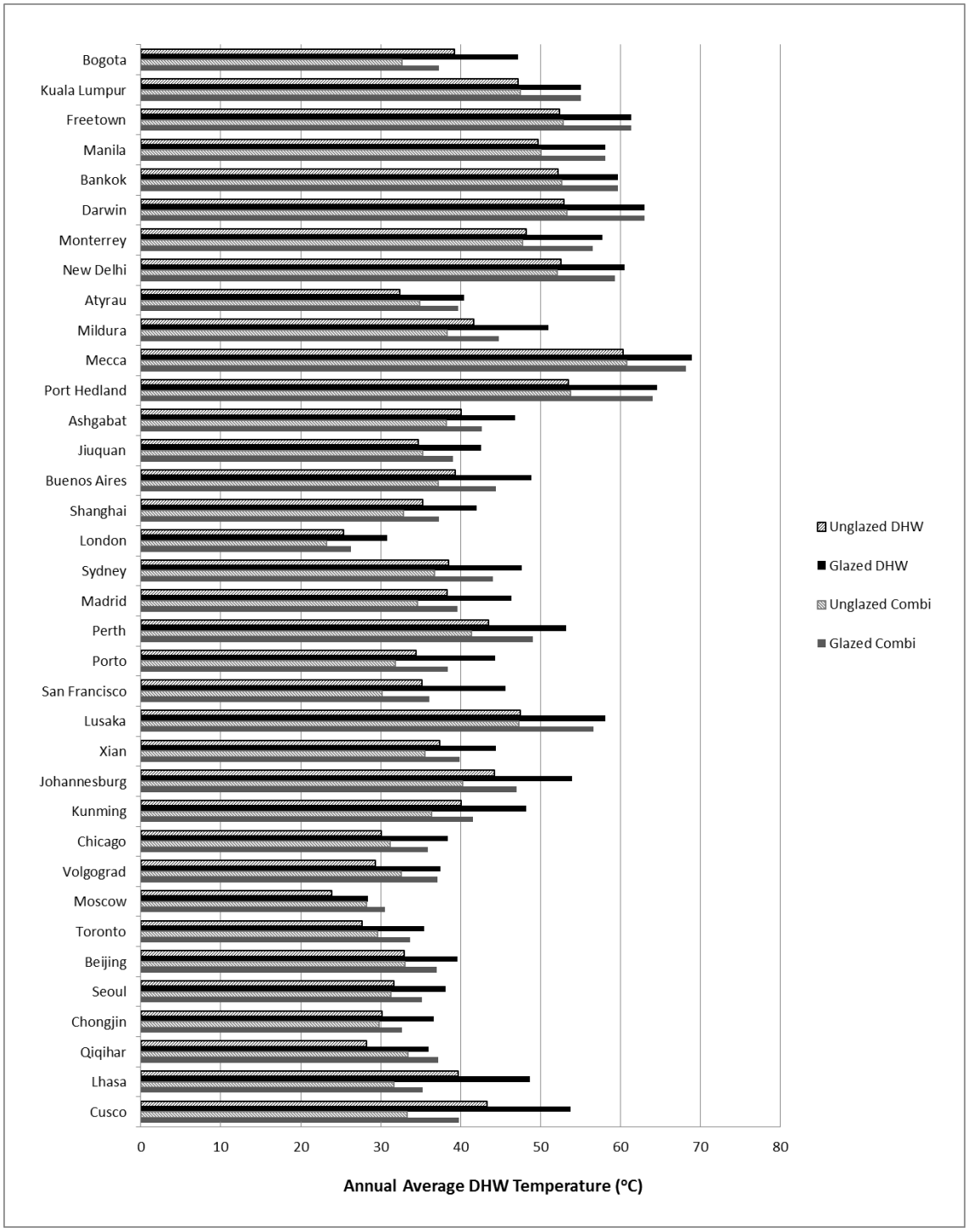

Figure 7.11. Simulation Results of Annual Average DHW Temperatures for the LSFPSC

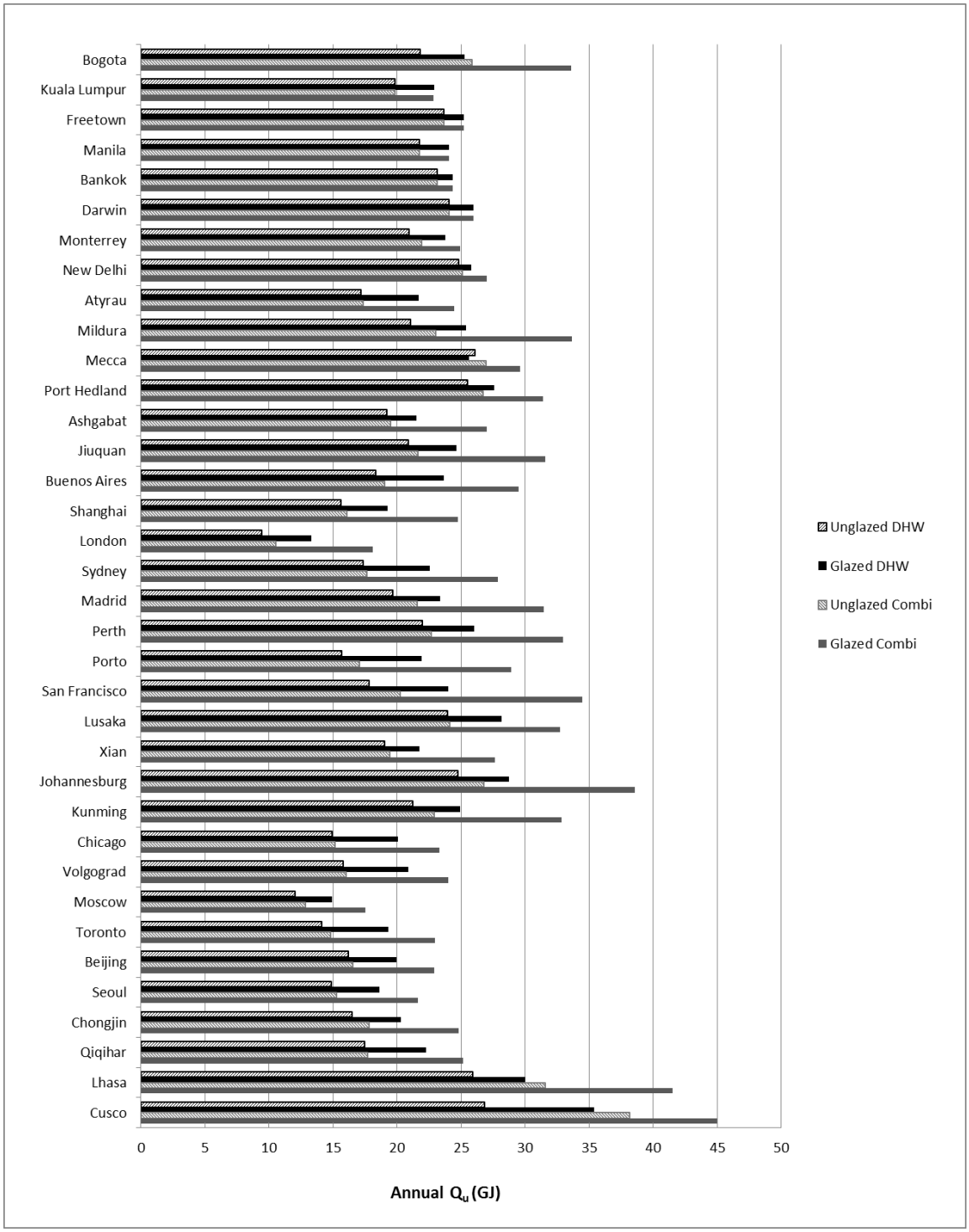

Figure 7.12. Simulation Results of Annual Qu in selected locations for the LSFPSC

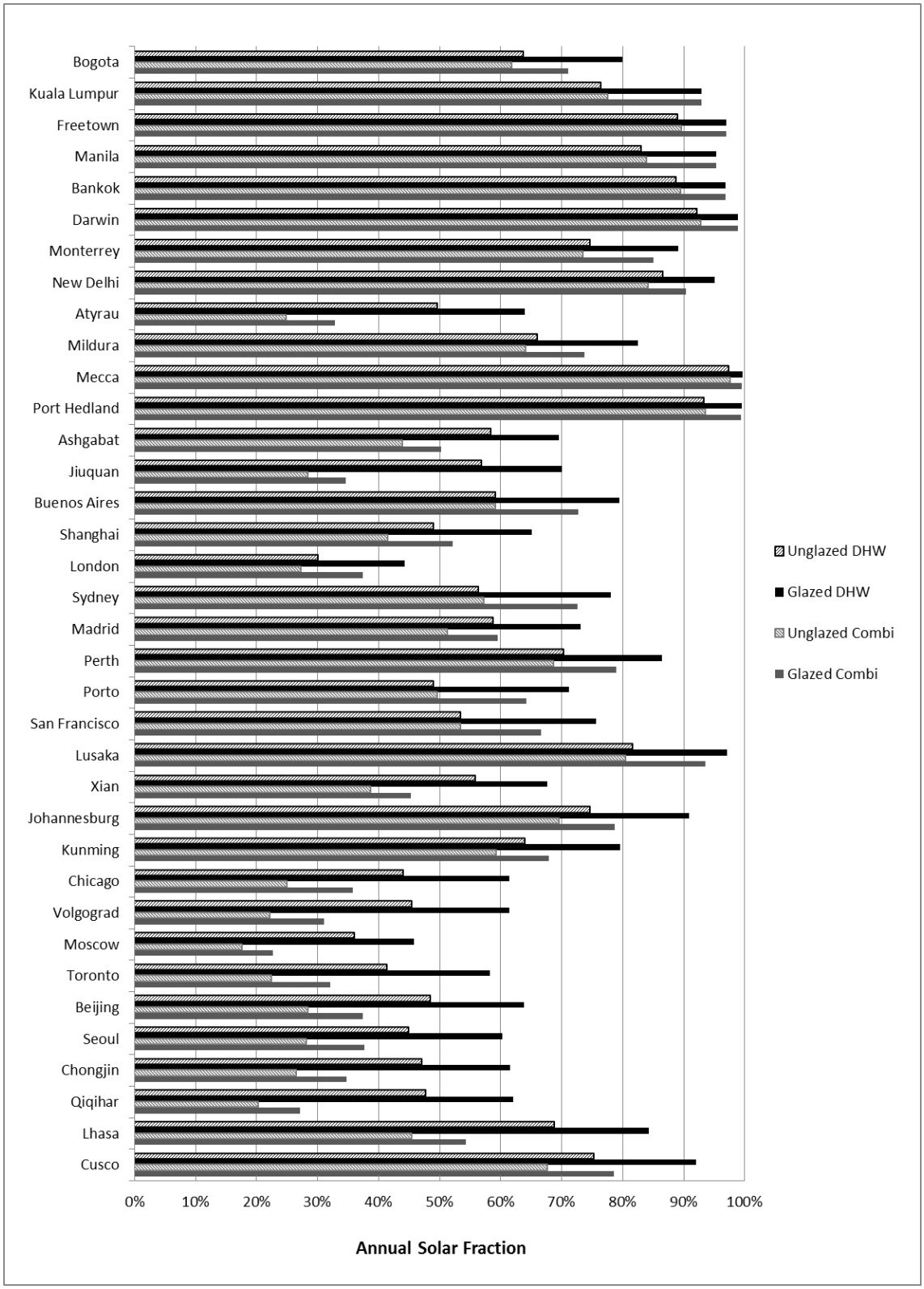

Figure 7.13. Simulation Results of Annual Solar Fraction in selected locations for the LSFPSC

Based on these results, optimal configuration was recommended for each location as shown in Table 7.2.

Table 7.2: Recommended configuration for different locations

City	Country	Type	Optimal Configuration	Solar Fraction	Operating Efficiency	Peak Efficiency
Bogota	Colombia	Af	Glazed Combi	71.02%	28.98%	48.30%
Kuala Lumpur	Malaysia	Af	Unglazed DHW	76.44%	30.42%	57.08%
Freetown	Sierra Leone	Am	Unglazed DHW	89.04%	30.29%	53.93%
Manila	Philippine	Am	Unglazed DHW	83.11%	30.39%	54.67%
Bankok	Thailand	Aw	Unglazed DHW	88.73%	31.69%	55.09%
Darwin	Australia	Aw	Unglazed DHW	92.23%	29.16%	53.84%
Monterrey	Mexico	BSh	Unglazed DHW	74.71%	28.19%	58.67%
New Delhi	India	BSh	Unglazed DHW	86.62%	30.99%	54.21%
Atyrau	Kazakhstan	BSk	Glazed Combi	63.99%	23.33%	45.30%
Mildura	Australia	BSk	Glazed Combi	73.70%	26.01%	52.28%
Mecca	Saudi Arabia	BWh	Unglazed DHW	97.39%	29.53%	61.39%
Port Hedland	Australia	BWh	Unglazed DHW	93.40%	28.47%	59.64%
Ashgabat	Turkmenistan	BWk	Glazed Combi	50.23%	24.62%	52.33%
Jiuquan	China	BWk	Glazed Combi	34.58%	25.57%	47.79%
Buenos Aires	Argentina	Cfa	Glazed Combi	72.68%	24.46%	48.02%
Shanghai	China	Cfa	Glazed Combi	52.14%	25.02%	49.04%
London	UK	Cfb	Glazed Combi	37.47%	24.60%	50.25%
Sydney	Australia	Cfb	Glazed Combi	72.63%	24.57%	46.91%
Madrid	Spain	Csa	Glazed Combi	59.51%	25.54%	48.59%
Perth	Australia	Csa	Glazed Combi	78.99%	24.84%	51.74%
Porto	Portugal	Csb	Glazed Combi	64.25%	24.75%	47.54%
San Francisco	USA	Csb	Glazed Combi	66.62%	27.40%	46.75%
Lusaka	Zambia	Cwa	Glazed Combi	93.59%	23.43%	45.48%
Xian	China	Cwa	Glazed Combi	45.24%	24.65%	48.94%
Johannesburg	S.Africa	Cwb	Glazed Combi	78.69%	26.66%	46.10%
Kunming	China	Cwb	Glazed Combi	67.92%	25.95%	46.61%
Chicago	USA	Dfa	Glazed Combi	35.81%	24.34%	47.92%
Volgograd	Russia	Dfa	Glazed Combi	31.08%	24.62%	47.83%
Moscow	Russia	Dfb	Glazed Combi	22.72%	25.60%	48.13%
Toronto	Canada	Dfb	Glazed Combi	32.12%	24.78%	47.70%
Beijing	China	Dwa	Glazed Combi	37.40%	25.77%	48.52%
Seoul	S.Korea	Dwa	Glazed Combi	37.72%	24.81%	47.59%
Chongjin	N.Korea	Dwb	Glazed Combi	34.79%	26.08%	48.71%
Qiqihar	China	Dwb	Glazed Combi	27.15%	25.14%	47.93%
Lhasa	China	ET	Glazed Combi	54.26%	28.62%	48.05%
Cusco	Peru	ET	Glazed Combi	78.50%	29.55%	45.73%

Glazed DHW was not recommended, because for the locations that require glazing to reduce heat losses SH is also required in colder seasons. Also glazed DHW is not as economical as unglazed DHW in locations with hot climate. Unglazed combi-system was not recommended as its glazed counterpart can perform much better in the locations that require SH providing more energy savings.

The operating efficiency is the mean collector efficiency over the operating periods of the LSFPSC and the peak efficiency is the highest collector efficiency obtained during the operating periods. The unglazed DHW can provide from 75% to 97% of the total DHW demand in the recommended locations with a mean operating efficiency of 29.90% and a mean peak efficiency of 56.50%. It can perform exceptionally well in locations with hot climate making it suitable for sizable applications i.e. multiple families in one apartment building, large families.

The solar fractions for the glazed combi-system varied greatly (from 22.72% to 93.59%) due to the differences in the availability of solar irradiance and ambient temperatures between the recommended locations. Apart from Moscow and Qiqihar, the glazed combi-system can provide more than 30% of the total energy demand for DHW and SH in the recommended locations with a mean operating efficiency of 25.54% and a mean peak efficiency of 48.15%. This shows the glazed combi-system has good performance making it a good alternative energy technology to provide savings for locations with cold seasons.

In summary, these results showed that the LSFPSC can perform well under a wide range of climate conditions in different locations around the world to meet high levels of energy demands for low/medium temperature applications.

CHAPTER 8

8. Conclusions and Recommendations

8.1 Conclusions

- A testing facility has been set up and equipped with measuring instruments for monitoring the key performance parameters (i.e. temperature of different components and flow rate) of the LSFPSC prototype.

- The 1st Stage experimental and analysis results showed that the LSFPSC prototype (unglazed) has an average operating efficiency of around 28% and the sources of energy gains/losses were successfully identified for proposing improvement designs. The improvement designs were studied through mathematically modelling to understand their effects on the collector performance. The results showed that employing glazing cover and replacing the convective heat transfer mechanism with conductive heat transfer can lead to substantial increase in collector performance.

- The modified designs of the LSFPSC and the test-rig were described and illustrated. The experimental results showed that the implemented improvement designs led to increase in collector efficiency: 43.50% for unglazed configuration and 46.07% for glazed configuration. The improved results also showed that the LSFPSC can perform well with the mechanical contacts created by clamping between the absorber and the circulation system. Additionally, further analysis showed the LSFPSC has better insulation capability compared to the typical mounted flat plate solar collectors. The cost analysis showed the materials and production costs per unit area of the LSFPSC are more than 4 times cheaper than commercial flat plate collectors. This makes clear that the LSFPSC has the advantage to be installed with much larger collector area to harvest significant amount of solar energy.

- Predictive models were developed and validated by the experimental data which incorporated important parameters such as the fluid flow rate and wind speeds allowing their relationships with the collector efficiencies to be analysed and extrapolated. The fluid flow rate is strongly correlated with the collector efficiencies and the collector outlet temperatures. An optimal range of specific mass flow rate 0.01 - 0.02 kg s^{-1} m^{-2} is recommended for obtaining $(T_o - T_i)$ between 5 ^oC and 10 ^oC. Specific mass flow rates that are smaller than 0.01 kg s^{-1} m^{-2} can be employed to obtain $(T_o - T_i)$ higher than 10 ^oC, but this will lead to reduced efficiencies. Thus, the actual selection of flow rates must be related to the specific application.

- Five locations were identified that have diversified horizontal irradiances, ambient temperatures and wind speeds. The performance of the LSFPSC was calculated based on the parameters of these five locations to assess the suitability of its GL and UNGL configurations. The UNGL configuration is preferable in Kisangani and New Delhi while both the GL and UNGL configurations are suitable for different

applications in Bechar and Madrid. The GL and UNGL can only perform with reasonable efficiencies from late spring till early autumn for London due to its cold and windy weather during autumn and winter seasons. The results show that the LSFPSC can be employed in locations with varied weather conditions to produce satisfactory outputs.

- Optimal collector aperture areas were identified for both GL and UNGL configurations in terms of length and number of serpentine tubing segments. The arrangements of 5 x 2m segments and 10 x 2m segments were recommended for GL and UNGL configurations respectively. The recommendations were based on optimal collector efficiencies and economic considerations.

- The initial TRNSYS simulation model was designed to reflect the performance of the LSFPSC in our experimental environments using the same parameters e.g. collector absorptivity, lengths of serpentine segments, total loss coefficients etc. The initial simulation outputs (inlet, outlet and storage temperatures) were successfully validated by comparing with the actual outputs to achieve less than 3% difference. The validated TRNSYS model then was modified to construct new models to simulate the performance of 10 installations of LSFPSCs with/without glazing for DHW and SH applications in 36 selected locations around the world. The locations were selected based on the Koppen-Geiger Climate Classification to assess the performance LSFPSC under a widely diverse range of climate conditions.

- The simulation results showed that the LSFPSC is capable of producing large amount of useful energy to meet more than 50% of DHW energy demands in selected locations: averaged 1.29 GJ/m2/year for the glazed configuration and 1.00 GJ/m2/year for the unglazed configuration. This indicates the high suitability of deployment of the LSFPSC in the majority of the regions around the world for effective solar energy utilisation.

8.2 Contribution Statement

Past research has placed efforts on studying the performance of flat plate collector that has manifold tubing design with partial building integration. This research focused on the experimental and simulation study of a large scale flat plate solar collector (LSFPSC) that is an integral part of the building envelope with serpentine-tubed configuration. The LSFPSC can perform well under various climate conditions indicating its great potentials as a clean and sustainable energy solution. The building-integrated designs of the LSFPSC also contribute new architectural concepts of energy generating buildings.

8.3 Limitation

This project has conducted comprehensive simulation study of the LSFPSC performance in different world locations. However, experimental study would be required to provide solid evidence of performance before proceeding with commercialisation in that certain region.

8.4 Recommendations

- The LSFPSC has shown promising performance on producing sizable heat energy. Future work could focus on utilising the abundant useful heat energy to generate electricity that will allow the LSFPSC to be used for a wider range of applications with larger economic benefits.

- In terms of commercialisation, it is recommended for the future work to focus on the standardisation of components, the scaling of manufacturing and the optimisation of installation process.

- Other potential areas for future research include: architectural designs and aesthetics, coupling with other energy generation technologies (e.g. biomass, wind), and optimisation for distributed (decentralised) energy production.

APPENDICES

Appendix A – Configurations of Data Logger

Table A.1: Configuration of Data Logger for 1st Stage

Instrument	Number	Channel	Channel Type	Status	Location	Remark
Thermocouple Type K	6	107 - 112 (S)	Voltage	Installed	Absorber Outer Surface	Detect and monitor temperatures on the outer surface of the metal absorber
Thermocouple Type K	6	201 - 206 (M)	Voltage	Installed	Absorber Inner Surface	Detect and monitor temperatures on the inner surface of the metal absorber
Thermocouple Type K	6	101 - 106 (A)	Voltage	Installed	Air in Exchange Chamber	Detect and monitor temperatures of the air within the exchange chamber
Thermocouple Type K	1	118 (In)	Voltage	Installed	Hot Water In	Detect and monitor temperature of hot water going into the storage tank
Thermocouple Type K	1	119 (Out)	Voltage	Installed	Cold Water Out	Detect and monitor temperature of cold water coming out from the storage tank
Thermocouple Type K	1	120 (Ambient)	Voltage	Installed	Ambient	Fitted on the roof of the testing room, detects ambient temperature within the room
Flowmeter	1	113 (Flowmeter)	Frequency	Installed	External Circuit	Detects and monitors the overall flow rate within the circulation system
Pressure Transmitter	1	221 (Pressure)	DC Current	Installed	External Circuit	Detects and monitors the overall pressure within the circulation system
Channel Type	Total	Used	Available			
Voltage	40	21	19			
Current	4	2	2			

Table A.2: Configuration of Data Logger for Testing Glazing in 2nd Stage

Instrument	Amount	Channel	Channel Type	Status	Location	Remark
Thermocouple Type K	9	101 - 109 (AOS)	Voltage	To be installed	Absorber Outer Surface	Detect and monitor temperatures on the outer surface of the metal absorber
Thermocouple Type K	9	110 - 118 (AIS)	Voltage	To be installed	Absorber Inner Surface	Detect and monitor temperatures on the inner surface of the metal absorber
Thermocouple Type K	1	119 (InEX)	Voltage	To be installed	Hot Water In Heat Exchanger	Detect and monitor temperature of hot water going into the heat exchanger within the storage tank
Thermocouple Type K	1	120 (OutEX)	Voltage	To be installed	Cold Water Out Heat Exchanger	Detect and monitor temperature of cold water coming out from the heat exchanger within the storage tank
Flowmeter	1	121 (Flow)	Current	To be installed	External Circuit	Fitted on the external rig that detects and monitors the overall flow rate within the circulation system
Pressure Transmitter	1	122 (Pressure)	Current	To be installed	External Circuit	Fitted on the external rig that detects and monitors the overall pressure within the circulation system
Thermocouple Type K	9	201 - 209 (GOS)	Voltage	To be installed	Glazing/Air near Unglazed Outer surface	Detect and monitor temperatures of the outer surface for the glazing or air near the surface of unglazed configuration
Thermocouple Type K	9	210 - 218 (AEX)	Voltage	To be installed	Air in Exchange Chamber	Detect and monitor temperatures of the air within the exchange chamber
Thermocouple Type K	1	219 (InST)	Voltage	To be installed	Cold Water in Storage Tank	Fitted in the header tank that provides cold water feeding and applies pressure to the storage tank
Thermocouple Type K	1	220 (OutST)	Voltage	To be installed	Hot Water Out from Storage Tank	Fitted in the exit pipe of the water storage tank
Thermocouple Type K	9	301 - 309 (CS)	Voltage	To be installed	Circulation System	Detect and monitor temperatures of the circulation system underneath the metal absorber
Thermocouple Type K	5	310 - 314 (CS)	Voltage	To be installed	Water Storage Unit	Fitted on water storage tank to detect and monitor the temperature gradient of water in storage
Thermocouple Type K	6	315 - 320 (Amb)	Voltage	To be installed	Ambient	Detect and monitor ambient temperatures and gradients inside and outside the testing room

Channel Type	Total	Used	Available
Voltage	60	60	0
Current	6	2	4

Appendix B – List of Material Candidates

Table B.1: Material Candidates of Heat Transfer Fluid

Material	Manufacturer	Composition	Density (kg/m^3)	Thermal Conductivity (W/m K)	Specific Heat (J/kg K)	Remark
Water	N/A		1000	0.58	4187	Water is the most commonly used heat transfer fluid (HTF) in solar thermal system due to its cheapness and good specific heat capacity. However, when heated, untreated tap water could release dissolved oxygen to form bubbles and release dissolved calcium ions to form limescale, which can cause obstruction to fluid flow hence reducing system performance and decreasing system life.
Heat Transfer Fluid	Fernox	Propylene Glycol 55 - 58% Water Content	993 – 1054	0.514 – 0.613	3630 – 3980	Corrosion inhibitors and anti-freeze chemicals are mixed with water to increase the life of circulation system and prevent freezing damages. However, when evaporation occurs at high temperatures, some dissolved chemicals will be released and may not be mixed back with solvent. HTF will need to be replaced after a certain period of operation.
Heat Transfer Fluid	Sentinel	Propylene Glycol Unknown% Water Content)	1040	0.514 – 0.613 (Approx.)	3630 – 3980 (Approx.)	It is warned that if these HTFs exceed 180 C, immediate degradation will occur. The degradation will cause the HTF to lose its thermodynamic attributes indicating by darkening colour.
Heat Transfer Fluid	RESOL	Propylene Glycol 55 - 58% Water Content	994 – 1056	0.378 – 0.484	3550 – 3990	This type of HTF is reversibly evaporisable meaning it may be suitable to be used in a steam turbine electricity generator. Its reliability must be tested experimentally.

Table B.2: Material Candidates of Absorber

Material	Manufacturer	Density (kg/m^3)	Thermal Conductivity (W/m K)	Specific Heat (J/kg K)	Remark
Pure Copper	N/A	8940 - 8950	390 - 398	383 - 387	Copper has excellent thermal conductivity and is widely used as solar thermal absorber in the form of thin films. However its cost has been increasing.
Pure Aluminium	N/A	2670 - 2730	239 - 249	910 - 960	Aluminium is another commonly used material in solar thermal absorbers. It is cheaper than copper and its thermal conductivity is good.
Stainless Steel SUS410	N/A	7650 - 7850	23 - 27	450 - 500	Stainless steel is less commonly seen in solar thermal absorbers compared to Al and Cu due to its lower thermal conductivity. However its cheap costs allow it to be used in low-medium end solar thermal systems.
Aluminium EN3105	Hydro Aluminium	2670 - 2730	169 - 175	879 - 915	Roof sheet made of this grade of aluminium is a candidate for the absorber of our prototype solar thermal system. As its original purpose is to be employed on buildings, the roof sheets have PVDF (polyvinlidene) coatings as protection measures against corrosion and UV degradation. These coatings may not be able to withstand high temperatures above 100 C. No experiments have been done on this material yet.
Stainless Steel S280	Tata Steel Colorcoat HPS200 Ultra	7800 - 7900	48 - 53	457 - 503	These stainless steel roof sheets were experimented and demonstrated reasonable thermal performance. They have polymer coatings that provide enhanced resistance against corrosion and UV degradation. However, stinky (may be poisonous) fume was observed during bench tests, which was suspected to come from the degradation of polymer coatings under high temperatures.
Ceramic N/A	N/A	2317 - 2368	1.1 - 1.7	621 - 677	Researches showed a new ceramic material with good potentials as solar thermal collector. The ceramic has quite small thermal conductivity. However its production costs are estimated to be less than £5 per m^3, which means this material can be deployed economically in developing countries with very large scale.
Polymer ecoFlare	Magen Eco-Energy	899 - 909	0.197 - 0.205	1880 - 1910	Magen eco-Energy has developed a patented production process of manufacturing copolymer solar thermal collector. The copolymer material is mainly based on polypropylene with the addition of UV degradation inhibitors (other additions unknown). No information of thermal conductivity of the collector is given publicly by the manufacturer, but it is estimated to be very low based on the thermal properties of polypropylene. The production costs are assumed to be very cheap allowing large scale of deployment.

Table B.3: Material Candidates of the Circulation System

Material	Grade	Density (kg/m^3)	Thermal Conductivity (W/m K)	Specific Heat (J/kg K)	Remark
PVC-Al-PVC Underground Heating Pipe	N/A	1300 - 1490	0.147 - 0.209	1000 - 1100	This combination of materials is used in typical underground heating pipes with a maximum service temperature of approximately 95 C. The thermal conductivity is quite low but it is compensated by its thin walls. During tests, the underground heating pipe showed reasonable performance and good stability. However a problem emerged: when placed in direct contact with metal absorber during bench testing, small amount of melting was observed on the outer pipe surface when temperature reached above 120 C. Placing the circulation system in direct contact with metal absorber will be able to improve the system efficiency greatly. Since this underground pipe is unable to withstand high temperatures, it may not be suitable to be used in the circulation system.
PEX-Al-PEX Underground Heating Pipe	N/A	920 - 1240	0.214 - 0.222	1560 - 1620	This type of underground heating pipe is similar to the one described above, but with slightly higher thermal conductivity. It is also not a suitable candidate for our circulation system due to its low maximum service temperatures (40 - 95C).
Pure Copper	Pure	8940 - 8950	390 - 398	383 - 387	Copper is the most widely used material in solar circulation system as it can withstand high temperatures and has very good thermal conductivity that can transfer useful heat energy into heat transfer fluids efficiently. However, it is relatively expensive and difficult to be manufactured into continuous length to meet our shaping requirements.
Stainless Steel 304	304	7850 - 8060	14 - 17	490 - 530	Stainless steel is less commonly used than copper in solar circulation system, but it is much cheaper and has reasonably good thermal conductivity.

Table B.4 Material Candidates of the Back Insulation

Material	Density (kg/m^3)	Thermal Conductivity (W/m K)	Specific Heat (J/kg K)	Remark
Insulation Foam	40 - 80	0.034 - 0.038	1950 - 2010	Widely used insulation on circulation system together with insulation tapes.
Polyurethane Foam	75 - 85	0.024 - 0.028	1470 - 1630	Developed by Magen eco-Energy to be used in a glazed solar flat plate collector as back insulation.
Mineral Wool	20	0.032	840	A very common material used in a glazed solar flat plate collector as back insulation.
Celotex	30 - 32.7	0.022	1400 - 1500	A patented insulation material most commonly used in building (e.g. floor, walls and roofs) insulations with very low thermal conductivity.

Appendix C – TRNSYS Components

C.1 On/Off Differential Controller – Type 2

The on/off differential controller generates a control function which can have a value of 1 or 0.The value of the control signal is chosen as a function of the difference between upper and lower temperatures T_h and T_l, compared with two dead band temperature differences. The new value of the control function depends on the value of the input control function at the previous time step. The controller is normally used with the input control signal connected to the output control signal, providing a hysteresis effect. However, control signals from different components may be used as the input control signal for this component if a more detailed form of hysteresis is desired.

C.2 Pump/Circulator – Type 3

It computes a mass flow rate using a variable control function, which must be between 0 and 1, and a fixed, user-specified maximum flow capacity. Pump or fan power consumption may also be calculated.

C.3 Tee Piece – Type 11 – Mode 2

This mode of Type 11 models a tee piece in which two inlet liquid streams are mixed together into a single liquid outlet stream.

C.4 Tee Piece – Type 11 – Mode 4

This instance of the Type11 model uses mode 4 or mode 5 to model a temperature controlled liquid flow diverter. In mode 4 the entire flow stream is sent through outlet 1 when the inlet temperature is less than the heat source temperature. In mode 5, the entire flow stream is sent through outlet 2 under these circumstances.

C.5 Time Dependent Forcing Function: Water Draw (Load Profile) – Type 14

In a transient simulation, it is sometimes convenient to employ a time dependent forcing function which has a behaviour characterized by a repeated pattern. The pattern of the forcing function is established by a set of discrete data points indicating the value of the function at various times throughout one cycle. Linear interpolation is provided in order to generate a continuous forcing function from the discrete data.

C.6 Weather Data Processor – Type 15

This component serves the purpose of reading data at regular time intervals from an external weather data file, interpolating the data (including solar radiation for tilted surfaces) at timesteps of less than one hour, and making it available to other TRNSYS components. The model also calculates several useful terms including the mains water temperature, the effective sky temperature, and the heating and cooling season forcing functions.

C.7 Integration Function – Type 24

This component integrates a series of quantities over a period of time.

C.8 Data Printer – Type 25

This component is used to output (or print) selected system variables at specified intervals of time.

C.9 Online Plotter – Type 65

The online graphics component is used to display selected system variables while the simulation is progressing. The selected variables will be displayed in a separate plot window on the screen.

C.10 Cylindrical Storage Tank with Immersed Heat Exchangers – Type 534

This subroutine models a fluid-filled, constant volume storage tank with immersed heat exchangers. This component models a cylindrical tank with a vertical configuration. The fluid in the storage tank interacts with the fluid in the heat exchangers (through heat transfer with the immersed heat exchangers), with the environment (through thermal losses from the top, bottom and edges) and with up to two flow streams that pass into and out of the storage tank. The tank is divided into isothermal temperature nodes (to model stratification observed in storage tanks) where the user controls the degree of stratification through the specification of the number of "nodes". Each constant-volume node is assumed to be isothermal and interacts thermally with the nodes above and below through several mechanisms; fluid conduction between nodes, and through fluid movement (either forced movement from inlet flow streams or natural destratification mixing due to temperature inversions in the tank). The user has the ability to specify one of four different immersed heat exchanger types (or no HX if desired); horizontal tube bank, vertical tube bank, serpentine tube, or coiled tube. Auxiliary heat may be provided to each isothermal node individually; through the use if INPUTs to the model. The model also considers temperature-dependent fluid properties for either pure water or a propylene glycol and water solution for both the tank and heat exchanger fluids.

C.11 LSFPSC – Type 565

This component is intended to model a plate-tube type of solar collector where the tube winds itself in a serpentine pattern up the collector absorber plate. The thermal model of this collector relies on algorithms supplied by the "Solar Engineering of Thermal Processes" by Duffie and Beckman.

C.12 Supplemental Firing Device or Hot Water Boiler – Type 659

An auxiliary heater is modelled to elevate the temperature of a flow stream using either internal control, external control or a combination of both types of control. The heater is designed to add heat to the flow stream at a user-designated rate (Qmax *Y) whenever the heater outlet temperature is less than a user-specified maximum (Tset).

By providing a control function between zero and one from a thermostat or controller, this routine will perform like a furnace adding heat at a rate of Q_{max}*Y but not exceeding an outlet temperature of T_{set}. In this application, a constant outlet temperature is not sought and T_{set} may be thought of as an arbitrary safety limit.

C.13 Multi-zone building model component – Type 660

This subroutine models the temperature and humidity level of a simple building zone subject to infiltration effects, ventilation effects, skin losses, internal heat and mass gains, and conductive and convective exchanges with adjacent zones. The model uses two differential equations to solve for the heat and mass balances at each time step.

C.14 Radiator – Type 692

This component models a simple fluid cooler that delivers the user-specified set point temperature for the input flow stream based on the interpolated capacity; which is a function of the sink temperature and the inlet fluid temperature.

C.15 LSFPSC – Type 565 – Source Code

```
SUBROUTINE TYPE565(TIME,XIN,OUT,T,DTDT,PAR,INFO,ICNTRL,*)

C-------------------------------------------------------------------------------------------------------------
C    ACCESS TRNSYS FUNCTIONS
            USE TrnsysConstants
            USE TrnsysFunctions
C-------------------------------------------------------------------------------------------------------------

C-------------------------------------------------------------------------------------------------------------
C    REQUIRED BY THE MULTI-DLL VERSION OF TRNSYS
     !DEC$ATTRIBUTES DLLEXPORT :: TYPE565
C-------------------------------------------------------------------------------------------------------------

C-------------------------------------------------------------------------------------------------------------
C    TRNSYS DECLARATIONS
     IMPLICIT NONE
            DOUBLE PRECISION XIN,OUT,TIME,PAR,T,DTDT,TIME0,TFINAL,DELT
     INTEGER*4 INFO(15),NP,NI,NOUT,ND,IUNIT,ITYPE,ICNTRL
     CHARACTER*3 YCHECK,OCHECK
C-------------------------------------------------------------------------------------------------------------

C-------------------------------------------------------------------------------------------------------------
C    USER DECLARATIONS
     PARAMETER (NP=17,NI=16,NOUT=12,ND=0)
C-------------------------------------------------------------------------------------------------------------

C-------------------------------------------------------------------------------------------------------------
C    REQUIRED TRNSYS DIMENSIONS
     DIMENSION XIN(NI),OUT(NOUT),PAR(NP),YCHECK(NI),OCHECK(NOUT),T(ND),
            1   DTDT(ND)
C-------------------------------------------------------------------------------------------------------------

C-------------------------------------------------------------------------------------------------------------
```

```
C    DECLARATIONS AND DEFINITIONS FOR THE USER-VARIABLES
     DOUBLE PRECISION RDCONV,PI,LENGTH,WIDTH,THICK_ABSORBER,K_ABSORBER,
          1   DIA_TUBE_I,DIA_TUBE_O,R_BOND,CP_FLUID,ABS_PLATE,EMISS_PLATE,
          1   REFR_INDEX,KL_COVER,RHO_DIFFUSE,TAU_ALPHA_N,TAU_ALPHA,FR,T_K,
     1   T_FLUID_IN,FLOW_IN,T_AMB,T_SKY,WINDSPEED,GT,GH,GDH,RHO_GROUND,
          1   ANGLE_INC,SLOPE,U_BACK,U_EDGES,H_FLUID,U_TOP,U_L,AREA,XKAT,
          1   EFFSKY,EFFGND,COSSLOPE,FSKY,FGND,GDSKY,GDGND,XKATDS,XKATDG,
     1   XKATB,T_FLUID_OUT,T_PLATE_MEAN,H_CONV,H_RAD,H_RADIATION,P_KPA,
     1   TMC,TAC,F,C,STF1,STF2,QU,Q_TOP,Q_BACK,Q_EDGES,T_FLUID_OUT_OLD,
     1   W_TUBES,L_TUBES,KAPPA,GAMMA,R,F1,F2,F3,F4,F5,F6,RATIO,X,P_ATM
          INTEGER N_BENDS,ICOUNT,MODE_U,N_COVERS
          CHARACTER(LEN=MAXMESSAGELENGTH)::MESSAGE1,MESSAGE2,MESSAGE3
C-------------------------------------------------------------------------------------------------------------------

C-------------------------------------------------------------------------------------------------------------------
C    DATA STATEMENTS
     DATA RDCONV/0.017453292/
          DATA MESSAGE1/'An illegal overall heat transfer coefficient has be
          1en calculated by the model.  Please check the entering information
     1 carefully.'/
          DATA MESSAGE2/'Unable to find a stable solution for the mean plate
          1 temperature.'/
          DATA MESSAGE3/'The correlation for the serpentine tube collector m
          1ay not be valid for the specified flow rates and collector paramet
     1ers.'/
C-------------------------------------------------------------------------------------------------------------------

C-------------------------------------------------------------------------------------------------------------------
C    GET GLOBAL TRNSYS SIMULATION VARIABLES
     TIME0=getSimulationStartTime()
     TFINAL=getSimulationStopTime()
     DELT=getSimulationTimeStep()
C-------------------------------------------------------------------------------------------------------------------

C-------------------------------------------------------------------------------------------------------------------
C    SET THE VERSION INFORMATION FOR TRNSYS
     IF(INFO(7).EQ.-2) THEN
               INFO(12)=16
               RETURN 1
          ENDIF
C-------------------------------------------------------------------------------------------------------------------

C-------------------------------------------------------------------------------------------------------------------
C    DO ALL THE VERY LAST CALL OF THE SIMULATION MANIPULATIONS HERE
     IF (INFO(8).EQ.-1) THEN
               RETURN 1
          ENDIF
C-------------------------------------------------------------------------------------------------------------------

C-------------------------------------------------------------------------------------------------------------------
C    PERFORM ANY "AFTER-ITERATION" MANIPULATIONS THAT ARE REQUIRED
     IF(INFO(13).GT.0) THEN
               RETURN 1
          ENDIF
C-------------------------------------------------------------------------------------------------------------------

C-------------------------------------------------------------------------------------------------------------------
C    DO ALL THE VERY FIRST CALL OF THE SIMULATION MANIPULATIONS HERE
     IF (INFO(7).EQ.-1) THEN

C      RETRIEVE THE UNIT NUMBER AND TYPE NUMBER FOR THIS COMPONENT FROM THE INFO ARRAY
       IUNIT=INFO(1)
               ITYPE=INFO(2)

C      SET SOME INFO ARRAY VARIABLES TO TELL THE TRNSYS ENGINE HOW THIS TYPE IS TO WORK
       INFO(6)=NOUT
       INFO(9)=1
               INFO(10)=0

C      CALL THE TYPE CHECK SUBROUTINE TO COMPARE WHAT THIS COMPONENT REQUIRES TO WHAT IS
SUPPLIED
               CALL TYPECK(1,INFO,NI,NP,ND)

C       SET THE YCHECK AND OCHECK ARRAYS TO CONTAIN THE CORRECT VARIABLE TYPES FOR THE
INPUTS AND OUTPUTS
```

```
      DATA YCHECK/'TE1','MF1','TE1','TE1','VE1','IR1','IR1','IR1',
     1            'DM1','DG1','DG1','HT1','HT1','HT1','HT1','PR4'/
      DATA OCHECK/'TE1','MF1','PW1','DM1','PW1','PW1','PW1','TE1',
     1            'DM1','HT1','DM1','DM1'/

C         CALL THE RCHECK SUBROUTINE TO SET THE CORRECT INPUT AND OUTPUT TYPES FOR THIS COMPONENT
      CALL RCHECK(INFO,YCHECK,OCHECK)

C      RETURN TO THE CALLING PROGRAM
      RETURN 1

    ENDIF
C-----------------------------------------------------------------------------------------------------------------------

C-----------------------------------------------------------------------------------------------------------------------
C    DO ALL OF THE INITIAL TIMESTEP MANIPULATIONS HERE - THERE ARE NO ITERATIONS AT THE INTIAL TIME
    IF (TIME.LT.(TIME0+DELT/2.D0)) THEN

C      SET THE UNIT NUMBER FOR FUTURE CALLS
      IUNIT=INFO(1)
      ITYPE=INFO(2)

C      READ IN THE VALUES OF THE PARAMETERS IN SEQUENTIAL ORDER
      LENGTH=PAR(1)
            WIDTH=PAR(2)
            THICK_ABSORBER=PAR(3)
            K_ABSORBER=PAR(4)
            N_BENDS=JFIX(PAR(5)+0.5)
            W_TUBES=PAR(6)
            L_TUBES=PAR(7)
            DIA_TUBE_I=PAR(8)
            DIA_TUBE_O=PAR(9)
            R_BOND=PAR(10)
            CP_FLUID=PAR(11)
            ABS_PLATE=PAR(12)
            EMISS_PLATE=PAR(13)
            MODE_U=JFIX(PAR(14)+0.5)
            N_COVERS=JFIX(PAR(15)+0.5)
            REFR_INDEX=PAR(16)
      KL_COVER=PAR(17)

C       CHECK THE PARAMETERS FOR PROBLEMS AND RETURN FROM THE SUBROUTINE IF AN ERROR IS FOUND
      IF(LENGTH.LE.0.) CALL TYPECK(-4,INFO,0,1,0)
      IF(WIDTH.LE.0.) CALL TYPECK(-4,INFO,0,2,0)
      IF(THICK_ABSORBER.LE.0.) CALL TYPECK(-4,INFO,0,3,0)
      IF(K_ABSORBER.LE.0.) CALL TYPECK(-4,INFO,0,4,0)
      IF(N_BENDS.LT.1) CALL TYPECK(-4,INFO,0,5,0)
      IF(W_TUBES.LE.0.) CALL TYPECK(-4,INFO,0,6,0)
      IF(W_TUBES*DBLE(N_BENDS).GT.WIDTH) CALL TYPECK(-4,INFO,0,6,0)
      IF(L_TUBES.LE.0.) CALL TYPECK(-4,INFO,0,7,0)
      IF(L_TUBES.GT.LENGTH) CALL TYPECK(-4,INFO,0,7,0)
      IF(DIA_TUBE_I.LE.0.) CALL TYPECK(-4,INFO,0,8,0)
      IF(DIA_TUBE_O.LE.0.) CALL TYPECK(-4,INFO,0,9,0)
      IF(DIA_TUBE_O.LE.DIA_TUBE_I) CALL TYPECK(-4,INFO,0,9,0)
      IF(R_BOND.LT.0.) CALL TYPECK(-4,INFO,0,10,0)
      IF(CP_FLUID.LE.0.) CALL TYPECK(-4,INFO,0,11,0)
      IF(ABS_PLATE.LE.0.) CALL TYPECK(-4,INFO,0,12,0)
      IF(ABS_PLATE.GT.1.) CALL TYPECK(-4,INFO,0,12,0)
      IF(EMISS_PLATE.LT.0.) CALL TYPECK(-4,INFO,0,13,0)
      IF(EMISS_PLATE.GT.1.) CALL TYPECK(-4,INFO,0,13,0)
      IF(MODE_U.LT.1) CALL TYPECK(-4,INFO,0,14,0)
      IF(MODE_U.GT.2) CALL TYPECK(-4,INFO,0,14,0)
      IF(N_COVERS.LT.0) CALL TYPECK(-4,INFO,0,15,0)
      IF(REFR_INDEX.LE.0.) CALL TYPECK(-4,INFO,0,16,0)
      IF(KL_COVER.LT.0.) CALL TYPECK(-4,INFO,0,17,0)

C            SET THE TRANSMITTANCE-ABSORPTANCE PRODUCT AT NORMAL INCIDENCE AND THE REFLECTANCE OF THE COVER
C      TO DIFFUSE RADIATION
            RHO_DIFFUSE=-1.
      TAU_ALPHA_N=TAU_ALPHA(N_COVERS,0.D0,KL_COVER,REFR_INDEX,
     1     ABS_PLATE,RHO_DIFFUSE)
```

```
C       PERFORM ANY REQUIRED CALCULATIONS TO SET THE INITIAL VALUES OF THE OUTPUTS HERE
        OUT(1)=XIN(1)
        OUT(2:7)=0.
              OUT(8)=XIN(1)
              OUT(9:10)=XIN(1)
              OUT(11)=RHO_DIFFUSE
              OUT(12)=TAU_ALPHA_N

C       RETURN TO THE CALLING PROGRAM
        RETURN 1

      ENDIF
C-----------------------------------------------------------------------------------------------------------------

C-----------------------------------------------------------------------------------------------------------------
C     *** ITS AN ITERATIVE CALL TO THIS COMPONENT ***
C-----------------------------------------------------------------------------------------------------------------

C-----------------------------------------------------------------------------------------------------------------
C     RE-READ THE PARAMETERS IF ANOTHER UNIT OF THIS TYPE HAS BEEN CALLED
      IF(INFO(1).NE.IUNIT) THEN

C       RESET THE UNIT NUMBER
              IUNIT=INFO(1)
              ITYPE=INFO(2)

C       READ IN THE VALUES OF THE PARAMETERS IN SEQUENTIAL ORDER
        LENGTH=PAR(1)
              WIDTH=PAR(2)
              THICK_ABSORBER=PAR(3)
              K_ABSORBER=PAR(4)
              N_BENDS=JFIX(PAR(5)+0.5)
              W_TUBES=PAR(6)
              L_TUBES=PAR(7)
              DIA_TUBE_I=PAR(8)
              DIA_TUBE_O=PAR(9)
              R_BOND=PAR(10)
              CP_FLUID=PAR(11)
              ABS_PLATE=PAR(12)
              EMISS_PLATE=PAR(13)
              MODE_U=JFIX(PAR(14)+0.5)
              N_COVERS=JFIX(PAR(15)+0.5)
              REFR_INDEX=PAR(16)
        KL_COVER=PAR(17)

      ENDIF
C-----------------------------------------------------------------------------------------------------------------

C-----------------------------------------------------------------------------------------------------------------
C       RETRIEVE THE CURRENT VALUES OF THE INPUTS TO THIS MODEL FROM THE XIN ARRAY IN
SEQUENTIAL ORDER
      T_FLUID_IN=XIN(1)
            FLOW_IN=XIN(2)
            T_AMB=XIN(3)
            T_SKY=XIN(4)
            WINDSPEED=XIN(5)
      GT=XIN(6)
      GH=XIN(7)
      GDH=XIN(8)
      RHO_GROUND=XIN(9)
      ANGLE_INC=XIN(10)
      SLOPE=XIN(11)
      U_TOP=XIN(12)
      U_BACK=XIN(13)
      U_EDGES=XIN(14)
      H_FLUID=XIN(15)
      P_ATM=XIN(16)
C-----------------------------------------------------------------------------------------------------------------

C-----------------------------------------------------------------------------------------------------------------
C     CHECK THE INPUTS FOR PROBLEMS
      IF(FLOW_IN.LT.0.) CALL TYPECK(-3,INFO,2,0,0)
      IF(WINDSPEED.LT.0.) CALL TYPECK(-3,INFO,5,0,0)
      IF(GT.LT.0.) CALL TYPECK(-3,INFO,6,0,0)
```

```
      IF(GH.LT.0.) CALL TYPECK(-3,INFO,7,0,0)
      IF(GDH.LT.0.) CALL TYPECK(-3,INFO,8,0,0)
      IF(RHO_GROUND.LT.0.) CALL TYPECK(-3,INFO,9,0,0)
      IF(RHO_GROUND.GT.1.) CALL TYPECK(-3,INFO,9,0,0)
      IF((MODE_U.GT.1).AND.(U_TOP.LT.0.)) CALL TYPECK(-3,INFO,12,0,0)
      IF(U_BACK.LT.0.) CALL TYPECK(-3,INFO,13,0,0)
      IF(U_EDGES.LT.0.) CALL TYPECK(-3,INFO,14,0,0)
      IF(H_FLUID.LE.0.) CALL TYPECK(-3,INFO,15,0,0)
      IF(P_ATM.LE.0.) CALL TYPECK(-3,INFO,16,0,0)
      IF(P_ATM.GT.5.) CALL TYPECK(-3,INFO,16,0,0)
            IF(ErrorFound()) RETURN 1
C-----------------------------------------------------------------------------------------------------------------------

C-----------------------------------------------------------------------------------------------------------------------
C     PERFORM ALL THE CALCULATION HERE FOR THIS MODEL.

C     SET PI
      PI=4*DATAN(1.D0)

C     CALCULATE THE AREA OF THE COLLECTOR
      AREA=LENGTH*WIDTH

C        RETRIEVE THE TRANSMITTANCE ABSORPTANCE PRODUCT AT NORMAL INCIDENCE AND THE
REFLECTANCE TO DIFFUSE
      RHO_DIFFUSE=OUT(11)
      TAU_ALPHA_N=OUT(12)

C     GET THE INCIDENCE ANGLE MODIFIER
      IF(N_COVERS.LT.1) THEN
               XKAT=1.

            ELSE

C        USE THE RELATIONS OF BRANDEMUEHL TO GET THE EFFECTIVE INCIDENCE ANGLES FOR DIFFUSE
RADIATION
         EFFSKY=59.68-0.1388*SLOPE+0.001497*SLOPE*SLOPE
         EFFGND=90.-0.5788*SLOPE+0.002693*SLOPE*SLOPE
         COSSLOPE=DCOS(SLOPE*RDCONV)
         FSKY=(1.+COSSLOPE)/2.
         FGND=(1.-COSSLOPE)/2.
         GDSKY=FSKY*GDH
         GDGND=RHO_GROUND*FGND*GH

C        USE THE TAU_ALPHA FUNCTION FOR THE COMPONENT IAM VALUES
         XKATDS=TAU_ALPHA(N_COVERS,EFFSKY,KL_COVER,REFR_INDEX,ABS_PLATE,
              1      RHO_DIFFUSE)/TAU_ALPHA_N
         XKATDG=TAU_ALPHA(N_COVERS,EFFGND,KL_COVER,REFR_INDEX,ABS_PLATE,
              1      RHO_DIFFUSE)/TAU_ALPHA_N
         XKATB=TAU_ALPHA(N_COVERS,ANGLE_INC,KL_COVER,REFR_INDEX,
              1      ABS_PLATE,RHO_DIFFUSE)/TAU_ALPHA_N

C        CALCULATE THE OVERALL IAM
         IF(GT.GT.0.) THEN
           XKAT=(XKATB*(GT-GDSKY-GDGND)+XKATDS*GDSKY+XKATDG*GDGND)/GT
                ELSE
                  XKAT=0.
                ENDIF
              ENDIF

C     GUESS AN OUTPUT TEMPERATURE
      T_FLUID_OUT=T_FLUID_IN

C     GUESS THE MEAN PLATE ND MEAN FLUID TEMPERATURES
      T_PLATE_MEAN=(T_FLUID_IN+T_FLUID_OUT)/2.

C     INITIALIZE A FEW VARIABLES
      ICOUNT=1
            T_FLUID_OUT_OLD=T_FLUID_OUT


C     SET THE TOP LOSS COEFFICIENCT
100   IF(MODE_U.EQ.1) THEN

C        SET THE TOP LOSS FROM CONVECTION AND RADIATION
               IF(N_COVERS.LT.1) THEN
```

```
                P_KPA=P_ATM*101.325
            T_K=T_AMB+273.15
        CALL WINDCOEF(WINDSPEED,LENGTH,WIDTH,T_K,P_KPA,H_CONV)
            H_CONV=H_CONV*3.6  !CONVERT W/M2/K TO KJ/H/M2.K

                H_RAD=H_RADIATION(T_PLATE_MEAN,T_SKY,EMISS_PLATE)
            U_TOP=H_CONV+H_RAD

C       USE KLEIN'S TOP LOSS CORRELATION
            ELSE

C         SET THE MEAN FLUID TEMPERATURE
                P_KPA=P_ATM*101.325
            T_K=T_AMB+273.15
        CALL WINDCOEF(WINDSPEED,LENGTH,WIDTH,T_K,P_KPA,H_CONV)
            H_CONV=H_CONV*3.6  !CONVERT W/M2/K TO KJ/H/M2.K

        TMC=T_PLATE_MEAN+273.15
        TAC=T_AMB+273.15
        IF (TMC.LE.TAC) TMC=TAC+1.0
        F=(1.0-0.04*H_CONV+5.0D-04*H_CONV*H_CONV)*(1.D0+0.091*
           1        DBLE(N_COVERS))
        C=365.9*(1.0-0.00883*SLOPE+0.0001298*SLOPE*SLOPE)
        STF1=C/TMC*((TMC-TAC)/(DBLE(N_COVERS)+F))**0.33
        STF1=DBLE(N_COVERS)/STF1+1.0/H_CONV
        STF1=1.0/STF1
        STF2=1.0/(EMISS_PLATE+0.05*DBLE(N_COVERS)*(1.0-EMISS_PLATE))
           1        +(2.*DBLE(N_COVERS)+F-1.)/0.88-DBLE(N_COVERS)
        STF2=5.67D-08*(TMC*TMC+TAC*TAC)*(TMC+TAC)/STF2
        U_TOP=(STF1+STF2)*3.6

            ENDIF
          ENDIF

C   SET THE OVERALL LOSS COEFFICIENT
    U_L=U_TOP+U_BACK+U_EDGES
          IF(U_L.LE.0.) THEN
      CALL MESSAGES(-1,MESSAGE1,'FATAL',IUNIT,ITYPE)
            RETURN 1
          ENDIF

C   SET SOME CONSTANTS REQUIRED BY THE SERPENTINE TUBE SOLUTION
    KAPPA=((K_ABSORBER*THICK_ABSORBER*U_L)**0.5)/DSINH((W_TUBES-
          1   DIA_TUBE_O)*((U_L/K_ABSORBER/THICK_ABSORBER)**0.5))
          GAMMA=-2.*DCOSH((W_TUBES-DIA_TUBE_O)*((U_L/K_ABSORBER/
          1   THICK_ABSORBER)**0.5)) - DIA_TUBE_O*U_L/KAPPA
          R=R_BOND+1./PI/DIA_TUBE_I/H_FLUID

    F1=KAPPA/U_L/W_TUBES*(KAPPA*R*((1.+GAMMA)**2.)-1.-GAMMA-KAPPA*R) /
   1      ((KAPPA*R*(1.+GAMMA)-1.)**2.-KAPPA*KAPPA*R*R)
          F2=1./(KAPPA*R*((1.+GAMMA)**2.)-1.-GAMMA-KAPPA*R)
          F3=FLOW_IN*CP_FLUID/F1/U_L/AREA
          F4=((1-F2*F2)/F2/F2)**0.5
          F5=1./F2+F4-1.
          F6=1.-1./F2+F4

C   CALCULATE THE COLLECTOR HEAT REMOVAL FACTOR
    IF(FLOW_IN.GT.0.) THEN
            X=(F6*DEXP(-1./F3*((1.-F2*F2)**0.5))+F5)
      FR=F1*F3*(2.*F5*F4/X-F5)
          ELSE
            FR=0.
          ENDIF

C   CALCULATE THE COLLECTOR USEFUL ENERGY GAIN
    QU=AREA*FR*(GT*XKAT*TAU_ALPHA_N-U_L*(T_FLUID_IN-T_AMB))

C   WARN THE USER IF THE CORRELATION IS OUT OF BOUNDS
    RATIO=FLOW_IN*CP_FLUID/F1/U_L/AREA
          IF((RATIO.LT.1.).AND.(FLOW_IN.GT.0.)) THEN
      CALL MESSAGES(-1,MESSAGE3,'WARNING',IUNIT,ITYPE)
    ENDIF

C   CALCULATE THE COLLECTOR OUTLET TEMPERATURE
    IF(FLOW_IN.LE.0.) THEN
```

```
                    T_FLUID_OUT=GT*XKAT*TAU_ALPHA_N/U_L+T_AMB
                  T_PLATE_MEAN=T_FLUID_OUT

                  Q_TOP=AREA*U_TOP*(T_PLATE_MEAN-T_AMB)
                  Q_BACK=AREA*U_BACK*(T_PLATE_MEAN-T_AMB)
                  Q_EDGES=AREA*U_EDGES*(T_PLATE_MEAN-T_AMB)

                ELSE
                  T_FLUID_OUT=T_FLUID_IN+QU/FLOW_IN/CP_FLUID
                  T_PLATE_MEAN=T_FLUID_IN+QU/AREA*(1.-FR)/FR/U_L

                  Q_TOP=AREA*U_TOP*(T_PLATE_MEAN-T_AMB)
                  Q_BACK=AREA*U_BACK*(T_PLATE_MEAN-T_AMB)
                  Q_EDGES=AREA*U_EDGES*(T_PLATE_MEAN-T_AMB)

      ENDIF

C     SEE IF CONVERGENCE HAS BEEN REACHED
      IF((ICOUNT.LT.50).AND.(DABS(T_FLUID_OUT_OLD-T_FLUID_OUT).GT.0.001)
     1   ) THEN
            ICOUNT=ICOUNT+1
            T_FLUID_OUT_OLD=T_FLUID_OUT
            GOTO 100
          ENDIF

C     WARN THE USER IF CONVERGENCE HAS NOT BEEN OBTAINED
      IF(ICOUNT.GE.50) THEN
        CALL MESSAGES(-1,MESSAGE2,'WARNING',IUNIT,ITYPE)
          ENDIF

C-------------------------------------------------------------------------------------------------------------------------

C-------------------------------------------------------------------------------------------------------------------------
C     SET THE OUTPUTS FROM THIS MODEL IN SEQUENTIAL ORDER AND GET OUT
      OUT(1)=T_FLUID_OUT
      OUT(2)=FLOW_IN
      OUT(3)=QU
          OUT(4)=FR
          OUT(5)=Q_TOP
          OUT(6)=Q_BACK
          OUT(7)=Q_EDGES
          OUT(8)=T_PLATE_MEAN
          OUT(9)=XKAT
          OUT(10)=U_L
C-------------------------------------------------------------------------------------------------------------------------

C-------------------------------------------------------------------------------------------------------------------------
C     EVERYTHING IS DONE - RETURN FROM THIS SUBROUTINE AND MOVE ON
      RETURN 1
      END
C-------------------------------------------------------------------------------------------------------------------------
```

Appendix D – Economic Evaluation

The cost effectiveness of the LSFPSC was evaluated by an estimation of its payback period, which was based on initial capital costs of the LSFPSC and its estimated annual energy savings. Our previous study showed that the LSFPSC with serpentine tubing has significantly lower materials and production costs per unit area ((£27.07/m^2 for UNGL and £43.02/m^2 for GL) than typical flat plate collectors (> £200/m^2). Based on the same roof area (60 m^2) used in the TRNSYS simulation, total costs of UNGL and GL installations are given in Table 7.2 assuming the full roof area can be utilised as solar collector.

Table 0.1. Costs of the LSFPSC for both UNGL and GL configurations

	Materials Costs	Storage Costs	Installation Costs	Total Unit Costs	Installation Size	Total Costs
UNGL	£27/m^2	£20/m^2	£40/m^2	£87/m^2	60 m^2	£5,220
GL	£43/m^2	£20/m^2	£40/m^2	£103/m^2	60 m^2	£6,180

The storage costs include water storage tanks and pipework required to connect to them and the installation costs are the labour costs for installing the LSFPSC assuming a new installation. Both of the costs were extrapolated into costs per unit area. All costs were estimated based on the prices in the UK and they can be significantly lower in other countries with cheaper materials and labour cost. The payback period is estimated by comparing cumulative energy savings to the total investments to estimate the amount of time required to reach break-even point. The payback period is given as:

$$P = \frac{ln\left[1 - \frac{C(d-i)}{(S-c)(1+i)}\right]}{ln\left[\frac{1+i}{1+d}\right]} \tag{0.16}$$

The annual cost of operating the system c is estimated to be 2% of C, which is the total cost of the LSFPSC, given in Table 7.2. The TRNSYS simulation results showed that the average annual amounts of useful energy generated by the LSFPSC per unit area are 278 kWh/m^2/yr for UNGL and 358 kWh/m^2/yr for GL. This is multiplied with energy prices and the collector area to calculate the amount of energy saving, S, produced by the LSFPSC. The energy prices employed here are £0.06/kwh and £0.13/kwh which are the low and high limits of non-renewable energy sources in Europe (IEA & NEA 2010). The costs and benefits over a period of time are considered by using an inflation rate of 2% ($i = 0.02$) and a discount rate of 5% ($d = 0.05$).

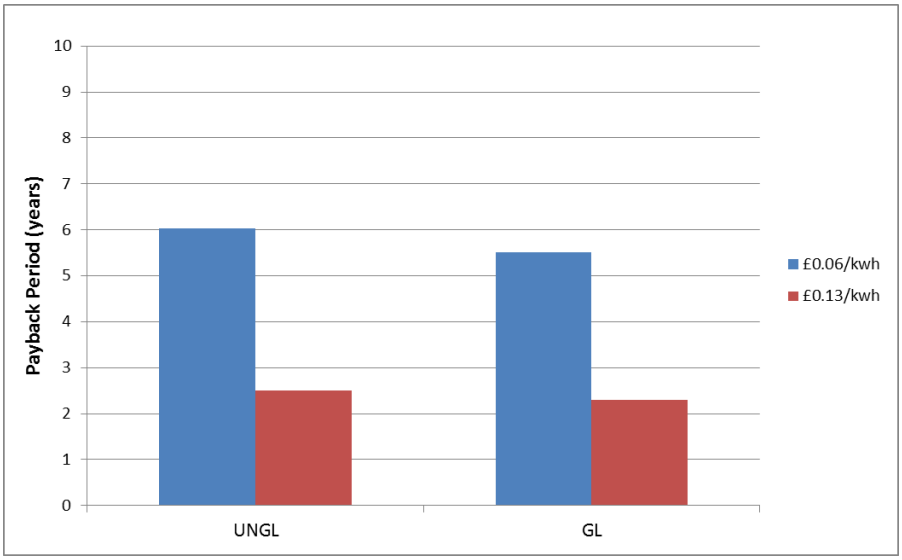

Figure 0.1. Calculated payback periods for the UNGL and GL configurations of the LSFPSC

The calculated payback period for the LSFPSC is between 2.4 to 6.5 years depending on the configuration (GL or UNGL) and energy prices of different sources, shown in Figure 7.13. The GL configuration has shorter payback period due to its capability of generating more useful energy per unit area than the UNGL configuration that compensated for its higher initial investment cost. The payback period of the LSFPSC is much shorter than typical commercial flat plate collectors which have payback period between 8 to 12 years. This clearly indicates the significant economic advantage of the LSFPSC in low/medium temperature applications.

References and Bibliography

06/02796 Integrated collector storage solar water heaters. Smyth, M. et al. Renewable and Sustainable Energy Reviews, 2006, 10, (6), 503–538. *Fuel and Energy Abstracts,* 47**,** 422.

2007. Climate Change 2007. *IPCC fourth assessment report, working group I report "The physical science basis.".* Cambridge ; New York : Cambridge University Press, 2007.

3TIER. 2013. *Global Solar Irradiance Map* [Online]. Available: http://www.vaisala.com/en/energy/support/Resources/PublishingImages/Vaisala_global_solar_map.pdf [Accessed 04 April 2013.

ABDULLAH, A. H., ABOU-ZIYAN, H. Z. & GHONEIM, A. A. Thermal performance of flat plate solar collector using various arrangements of compound honeycomb. *Energy Conversion and Management,* 44**,** 3093-3112.

ABDULLAH, A. H., ABOU-ZIYAN, H. Z. & GHONEIM, A. A. 2003. Thermal performance of flat plate solar collector using various arrangements of compound honeycomb. *Energy Conversion and Management,* 44**,** 3093-3112.

AGBO, S. N. & OKOROIGWE, E. C. 2007. Analysis of Thermal Losses in the Flat-Plate Collector of a Thermosyphon Solar Water Heater. *Research Journal of Physics,* 1**,** 35-41.

AGENCY, N. E. 2010. *Projected Costs of Generating Electricity 2010*, OECD Publishing.

AGHA, K. R. 2009. The thermal characteristics and economic analysis of a solar pond coupled low temperature multi stage desalination plant. *Solar Energy,* 83**,** 501-510.

AKHTAR, N. & MULLICK, S. C. Computation of glass-cover temperatures and top heat loss coefficient of flat-plate solar collectors with double glazing. *Energy,* 32**,** 1067-1074.

AKHTAR, N. & MULLICK, S. C. 2007. Computation of glass-cover temperatures and top heat loss coefficient of flat-plate solar collectors with double glazing. *Energy,* 32**,** 1067-1074.

ALIREZA, H. & KAMRAN, S. 2009. Optimal design of a forced circulation solar water heating system for a residential unit in cold climate using TRNSYS. *Solar Energy,* 83**,** 700-714.

ALTAMUSH SIDDIQUI, M. 1997. Heat transfer and fluid flow studies in the collector tubes of a closed-loop natural circulation solar water heater. *Energy Conversion and Management,* 38**,** 799-812.

ALVAREZ, A., CABEZA, O., MUÑIZ, M. C. & VARELA, L. M. 2010. Experimental and numerical investigation of a flat-plate solar collector. *Energy,* 35**,** 3707-3716.

ANDERSEN, E. & FURBO, S. 2009. Theoretical variations of the thermal performance of different solar collectors and solar combi systems as function of the varying yearly weather conditions in Denmark. *Solar Energy,* 83**,** 552-565.

ARKAR, C., MEDVED, S. & NOVAK, P. 1999. Long-therm operation experiences with large-scale solar systems in Slovenia. *Renewable Energy,* 16**,** 669-672.

AYOMPE, L. M., DUFFY, A., MCCORMACK, S. J. & CONLON, M. 2011. Validated TRNSYS model for forced circulation solar water heating systems with flat plate and heat pipe evacuated tube collectors. *Applied Thermal Engineering,* 31**,** 1536-1542.

BALARAM, K. Performance analysis and optimization of absorber plates of different geometry for a flat-plate solar collector: a comparative study. *Applied Thermal Engineering,* 22**,** 999-1012.

BARBOUR, I., BROOKS, H., LAKOFF, S. & OPIE, J. 1982. *Energy and American values*.

BARTELSEN, B., ROCKENDORF, G., VENNEMANN, N., TEPE, R., LORENZ, K. & PURKARTHOFER, G. 1999. Elastomer–metal–absorber: development and application. *Solar Energy,* 67**,** 215-226.

BEATTIE, D. A. 1997. *History and Overview of Solar Heat Technologies*, MIT Press.

BEAUSOLEIL-MORRISON, I., KUMMERT, M., MACDONALD, F., JOST, R., MCDOWELL, T. & FERGUSON, A. 2012. Demonstration of the new ESP-r and TRNSYS co-simulator for modelling solar buildings. *Energy Procedia,* 30**,** 505-514.

BELUSKO, M., SAMAN, W. & BRUNO, F. 2004. Roof integrated solar heating system with glazed collector. *Solar Energy,* 76**,** 61-69.

BEN BACHA, H., DAMMAK, T., BEN ABDALAH, A. A., MAALEJ, A. Y. & BEN DHIA, H. 2007. Desalination unit coupled with solar collectors and a storage tank: modelling and simulation. *Desalination,* 206**,** 341-352.

BLINDER, S. M. 2004. *Introduction to Quantum Mechanics : In Chemistry, Materials Science, and Biology*, Elsevier.

BLISS JR, R. W. 1959. The derivations of several “Plate-efficiency factors” useful in the design of flat-plate solar heat collectors. *Solar Energy,* 3**,** 55-64.

BO-REN, C., YU-WEI, C., WEN-SHING, L. & SIH-LI, C. Long-term thermal performance of a two-phase thermosyphon solar water heater. *Solar Energy,* 83**,** 1048-1055.

BONHÔTE, P., EPERON, Y. & RENAUD, P. 2009. Unglazed coloured solar absorbers on façade: Modelling and performance evaluation. *Solar Energy,* 83**,** 799-811.

BORSANI, R. & REBAGLIATI, S. 2005. Fundamentals and costing of MSF desalination plants and comparison with other technologies. *Desalination,* 182**,** 29-37.

BP 2011. Statistical Review of World Energy Full Report.

BUDIHARDJO, I. & MORRISON, G. L. Performance of water-in-glass evacuated tube solar water heaters. *Solar Energy,* 83**,** 49-56.

BUDIHARDJO, I. & MORRISON, G. L. 2009. Performance of water-in-glass evacuated tube solar water heaters. *Solar Energy,* 83**,** 49-56.

CADAFALCH, J. 2010. A detailed numerical model for flat-plate solar thermal devices. *Solar Energy,* 83**,** 2157-2164.

CARBONELL, D., CADAFALCH, J. & CONSUL, R. 2013. Dynamic modelling of flat plate solar collectors. Analysis and validation under thermosyphon conditions. *Solar Energy,* 89**,** 100-112.

CARBONI, C. & MONTANARI, R. 2008. Solar thermal systems: Advantages in domestic integration. *Renewable Energy,* 33**,** 1364-1373.

CCGP 2012. Chinese Government Announced a Subsidy Plan of 4 Bilion Yuan of Solar Water Heating Systems.

CHARGUI, R. & SAMMOUDA, H. 2014. Modeling of a residential house coupled with a dual source heat pump using TRNSYS software. *Energy Conversion and Management,* 81**,** 384-399.

CHATURVEDI, S. K., CHEN, D. T. & KHEIREDDINE, A. 1998. Thermal performance of a variable capacity direct expansion solar-assisted heat pump. *Energy Conversion and Management,* 39**,** 181-191.

CHEN, C. J. 2011. *Physics of Solar Energy*, Wiley.

CHEN, X., YANG, H., LU, L., WANG, J. & LIU, W. Experimental studies on a ground coupled heat pump with solar thermal collectors for space heating. *Energy,* 36**,** 5292-5300.

CHONG, K. K., CHAY, K. G. & CHIN, K. H. 2012. Study of a solar water heater using stationary V-trough collector. *Renewable Energy,* 39**,** 207-215.

CHOW, T. T., CHAN, A. L. S., FONG, K. F., LIN, Z., HE, W. & JI, J. 2009. Annual performance of building-integrated photovoltaic/water-heating system for warm climate application. *Applied Energy,* 86**,** 689-696.

COMPAIN, P. 2012. Solar Energy for Water Desalination. *Procedia Engineering,* 46**,** 220-227.

COOK, E. 1971. The Flow of Energy in an Industrial Society. *Scientific American,* 224**,** 135.

COOPER, P. I. & DUNKLE, R. V. 1981. A non-linear flat-plate collector model. *Solar Energy,* 26**,** 133-140.

CRISTOFARI, C., NOTTON, G., POGGI, P. & LOUCHE, A. 2002. Modelling and performance of a copolymer solar water heating collector. *Solar Energy,* 72**,** 99-112.

DE LA CALLE, A., BONILLA, J., ROCA, L. & PALENZUELA, P. 2015. Dynamic modeling and simulation of a solar-assisted multi-effect distillation plant. *Desalination,* 357**,** 65-76.

DE WINTER, F. 1975. Heat exchanger penalties in double-loop solar water heating systems. *Solar Energy,* 17**,** 335-337.

DIERSCH, H. J. G. & BAUER, D. 2015. 7 - Analysis, modeling and simulation of underground thermal energy storage (UTES) systems. *In:* CABEZA, L. F. (ed.) *Advances in Thermal Energy Storage Systems.* Woodhead Publishing.

DORFLING, C., HORNUNG, C. H., HALLMARK, B., BEAUMONT, R. J. J., FOVARGUE, H. & MACKLEY, M. R. The experimental response and modelling of a solar heat collector fabricated from plastic microcapillary films. *Solar Energy Materials and Solar Cells,* 94**,** 1207-1221.

DOVIĆ, D. & ANDRASSY, M. 2012. Numerically assisted analysis of flat and corrugated plate solar collectors thermal performances. *Solar Energy,* 86**,** 2416-2431.

DUFFIE, J. A. & BECKMAN, W. A. 2013. *Solar engineering of thermal processes / John A. Duffie (deceased), William A. Beckman*, Hoboken, New Jersey : Wiley, [2013] Fourth edition.

DUNNET, G. M. 1982. *Oil Pollution And Seabird Populations*.

DUNNET, G. M., CRISP, D. J., CONAN, G. & BOURNE, W. R. P. 1982. Oil Pollution and Seabird Populations [and Discussion]. *Philosophical Transactions of the Royal Society of London B: Biological Sciences,* 297**,** 413-427.

ECEVIT, A., AL-SHARIAH, A. M. & APAYDIN, E. D. 1989. Triangular built-in-storage solar water heater. *Solar Energy,* 42**,** 253-265.

ESLAMI-NEJAD, P. & BERNIER, M. 2011. Coupling of geothermal heat pumps with thermal solar collectors using double U-tube boreholes with two independent circuits. *Applied Thermal Engineering,* 31**,** 3066-3077.

EST. 2013. *UK Feed-In Tariff Scheme* [Online]. Available: http://www.energysavingtrust.org.uk/Generate-your-own-energy/Financial-incentives/Feed-In-Tariffs-scheme-FITs [Accessed 04 April 2013.

FABRICE, M., GILLES, N., CHRISTIAN, C. & JEAN-LOUIS, C. Design and modelling of a new patented thermal solar collector with high building integration. *Applied Energy*.

FACÃO, J. & OLIVEIRA, A. C. 2006. Analysis of a plate heat pipe solar collector. *International Journal of Low Carbon Technologies,* 1**,** 1-9.

FARWATI, M. A. 1997. Theoretical study of multi-stage flash distillation using solar energy. *Energy,* 22**,** 1-5.

FURBO, S. & SHAH, L. J. Thermal advantages for solar heating systems with a glass cover with antireflection surfaces. *Solar Energy,* 74**,** 513-523.

FURBO, S. & SHAH, L. J. 2003. Thermal advantages for solar heating systems with a glass cover with antireflection surfaces. *Solar Energy,* 74**,** 513-523.

GOETZBERGER, A. & ROMMEL, M. 1987. Prospects for integrated storage collector systems in central Europe. *Solar Energy,* 39**,** 211-219.

GREENPEACEINT, SOLARPACES & ESTELA 2009. Concentrating Solar Power Outlook.

GREINER, W. 2001. *Quantum mechanics: an introduction*, Springer Verlag.

GUOYING, X., XIAOSONG, Z. & SHIMING, D. Experimental study on the operating characteristics of a novel low-concentrating solar photovoltaic/thermal integrated heat pump water heating system. *Applied Thermal Engineering,* 31**,** 3689-3695.

GUOYING, X., XIAOSONG, Z. & SHIMING, D. A simulation study on the operating performance of a solar–air source heat pump water heater. *Applied Thermal Engineering,* 26**,** 1257-1265.

GUPTA, C. L. & GARG, H. P. 1968. System design in solar water heaters with natural circulation. *Solar Energy,* 12**,** 163-170,IN3,171-182.

HAMED, O. A., AL-SOFI, M. A. K., IMAM, M., MUSTAFA, G. M., BA MARDOUF, K. & AL-WASHMI, H. 2000. Thermal performance of multi-stage flash distillation plants in Saudi Arabia. *Desalination,* 128**,** 281-292.

HASSAN, M. M. & BELIVEAU, Y. 2007. Design, construction and performance prediction of integrated solar roof collectors using finite element analysis. *Construction and Building Materials,* 21**,** 1069-1078.

HATAMI, N. & BAHADORINEJAD, M. Experimental determination of natural convection heat transfer coefficient in a vertical flat-plate solar air heater. *Solar Energy,* 82**,** 903-910.

HELLSTROM, B., ADSTEN, M., NOSTELL, P., KARLSSON, B. & WACKELGARD, E. 2003. The impact of optical and thermal properties on the performance of flat plate solar collectors. *Renewable Energy,* 28**,** 331-344.

HILMER, F., VAJEN, K., RATKA, A., ACKERMANN, H., FUHS, W. & MELSHEIMER, O. NUMERICAL SOLUTION AND VALIDATION OF A DYNAMIC MODEL OF SOLAR COLLECTORS WORKING WITH VARYING FLUID FLOW RATE. *Solar Energy,* 65**,** 305-321.

HIROSHI, T. Solar thermal collector augmented by flat plate booster reflector: Optimum inclination of collector and reflector. *Applied Energy,* 88**,** 1395-1404.

HOLLANDS, K. G. T. & STEDMAN, B. A. 1992. Optimization of an absorber plate fin having a step-change in local thickness. *Solar Energy,* 49**,** 493-495.

HOTTEL, H. C. & WHILLIER, A. 1955. Evaluation of Flat Plate Solar Collector Performance. *Transactions of the Conference on the use of Solar Energy: The Scientific Basis,* II, Part 1, Section A**,** 74 - 104.

HUANG, B. J., LEE, J. P. & CHYNG, J. P. 2005. Heat-pipe enhanced solar-assisted heat pump water heater. *Solar Energy,* 78**,** 375-381.

HUANG, J., PU, S., GAO, W. & QUE, Y. 2010. Experimental investigation on thermal performance of thermosyphon flat-plate solar water heater with a mantle heat exchanger. *Energy,* 35**,** 3563-3568.

HUGO, A. & ZMEUREANU, R. 2012. Residential Solar-Based Seasonal Thermal Storage Systems in Cold Climates: Building Envelope and Thermal Storage. *Energies (19961073),* 5**,** 3972-3985.

IEA 2007. Energy Use in the New Millennium: Trends in IEA Countries.

IEA 2010. World Energy Outlook. Paris.

IEA 2011. Solar Energy Perspectives. Paris: International Energy Agency.

IEA 2012. Solar Heating and Cooling: Technology Roadmap. Paris: International Energy Agency.

INCROPERA, F. P. & DEWITT, D. P. 2002. *Fundamentals of heat and mass transfer*, New York ; Chichester : Wiley, c2002.

5th ed.

JAISANKAR, S., ANANTH, J., THULASI, S., JAYASUTHAKAR, S. T. & SHEEBA, K. N. A comprehensive review on solar water heaters. *Renewable and Sustainable Energy Reviews,* 15**,** 3045-3050.

JAISANKAR, S., RADHAKRISHNAN, T. K. & SHEEBA, K. N. Experimental studies on heat transfer and friction factor characteristics of forced circulation solar water heater system fitted with helical twisted tapes. *Solar Energy,* 83**,** 1943-1952.

JAISANKAR, S., RADHAKRISHNAN, T. K. & SHEEBA, K. N. Experimental studies on heat transfer and thermal performance characteristics of thermosyphon solar water heating system with helical and Left–Right twisted tapes. *Energy Conversion and Management,* 52**,** 2048-2055.

JI, J., LUO, C., CHOW, T.-T., SUN, W. & HE, W. 2011. Thermal characteristics of a building-integrated dual-function solar collector in water heating mode with natural circulation. *Energy,* 36**,** 566-574.

JOHAN, V., JAN-OLOF, D. & MATS, R. Movement and mechanical stresses in sealed, flat plate solar collectors. *Solar Energy,* 86**,** 339-350.

JUAREZ-TRUJILLO, A., MARTÍN-DOMÍNGUEZ, I. R. & ALARCÓN-HERRERA, M. T. 2014. Using TRNSYS Simulation to Optimize the Design of a Solar Water Distillation System. *Energy Procedia,* 57**,** 2441-2450.

KALOGIROU, S., TRIPANAGNOSTOPOULOS, Y. & SOULIOTIS, M. Performance of solar systems employing collectors with colored absorber. *Energy & Buildings,* 37**,** 824-835.

KALOGIROU, S., TRIPANAGNOSTOPOULOS, Y. & SOULIOTIS, M. 2005. Performance of solar systems employing collectors with colored absorber. *Energy and Buildings,* 37**,** 824-835.

KALOGIROU, S. A. 2004a. Environmental benefits of domestic solar energy systems. *Energy Conversion and Management,* 45**,** 3075-3092.

KALOGIROU, S. A. 2004b. Solar thermal collectors and applications. *Progress in Energy and Combustion Science,* 30**,** 231-295.

KARMARE, S. V. & TIKEKAR, A. N. Analysis of fluid flow and heat transfer in a rib grit roughened surface solar air heater using CFD. *Solar Energy,* 84**,** 409-417.

KAUSHIK, S. C., KUMAR, R. & GARG, H. P. 1995. Effect of baffle plate on the performance of a triangular built-in-storage solar water heater. *Energy Conversion and Management,* 36**,** 337-342.

KAUSHIK, S. C., KUMAR, R., GARG, H. P. & PRAKASH, J. 1994. Transient analysis of a triangular built-in-storage solar water heater under winter conditions. *Heat Recovery Systems and CHP,* 14**,** 337-341.

KAUSHIKA, N. D. & SUMATHY, K. 2003. Solar transparent insulation materials: a review. *Renewable and Sustainable Energy Reviews,* 7**,** 317-351.

KAYS, W. M. & LONDON, A. L. 1998. *Compact Heat Exchanger,* Malabar, Fla Krieger Pub. Co.

KHALFALLAOUI, S., SEGUIN, D., ABDELGHANI-IDRISSI, M. A., MOUHAB, N., MILLER, A. & IP, K. 2011. Theoretical and experimental unsteady-state thermal behaviour of domestic solar water heating. *International Journal of Sustainable Energy,* 30**,** 129-148.

KOEHL, M., SAILE, S., PIEKARCZYK, A. & FISCHER, S. 2014. Task 39 Exhibition – Assembly of Polymeric Components for a New Generation of Solar Thermal Energy Systems. *Energy Procedia,* 48**,** 130-136.

KONG, X. Q., ZHANG, D., LI, Y. & YANG, Q. M. Thermal performance analysis of a direct-expansion solar-assisted heat pump water heater. *Energy,* 36**,** 6830-6838.

KOTB, O. A. 2015. Optimum numerical approach of a MSF desalination plant to be supplied by a new specific 650 MW power plant located on the Red Sea in Egypt. *Ain Shams Engineering Journal,* 6**,** 257-265.

KOTHARI, C. R. 2004. *Research Methodology : Methods & Techniques*, New Age International [P] Ltd.

KOVARIK, M. 1978. Optimal distribution of heat conducting material in the finned pipe solar energy collector. *Solar Energy,* 21**,** 477-484.

KUANG, Y. H., SUMATHY, K. & WANG, R. Z. 2003. Study on a direct-expansion solar-assisted heat pump water heating system. *International Journal of Energy Research,* 27**,** 531-548.

KUDISH, A. I., SANTAMAURA, P. & BEAUFORT, P. 1985. Direct measurement and analysis of thermosiphon flow. *Solar Energy,* 35**,** 167-173.

KUNDU, B. 2002. Performance analysis and optimization of absorber plates of different geometry for a flat-plate solar collector: a comparative study. *Applied Thermal Engineering,* 22**,** 999-1012.

KUNDU, B. & LEE, K. S. 2012. Fourier and non-Fourier heat conduction analysis in the absorber plates of a flat-plate solar collector. *Solar Energy,* 86**,** 3030-3039.

LAMBERT, A. A., CUEVAS, S. & RÍO, J. A. D. Enhanced heat transfer using oscillatory flows in solar collectors. *Solar Energy,* 80**,** 1296-1302.

LAN, Q., LI, M., XIA, C. & JI, X. Design And Heating Performance Of Solar-Assisted Heat Pump Water Heater With Truncated-Cone-Type Evaporator. Power and Energy Engineering Conference (APPEEC), 2010 Asia-Pacific, 28-31 March 2010 2010. 1-4.

LAUGHTON, C. & EARTHSCAN 2010. *Solar Domestic Water Heating: The Earthscan Expert Handbook for Planning, Design, and Installation*, Earthscan.

LAVILLE, S. 2005. Panic buying begins as motorists fear petrol blockades. *The Guardian*, 14 September 2005.

LEON, M. A. & KUMAR, S. Mathematical modeling and thermal performance analysis of unglazed transpired solar collectors. *Solar Energy,* 81**,** 62-75.

LI, S., KARAVA, P., SAVORY, E. & LIN, W. E. 2013. Airflow and thermal analysis of flat and corrugated unglazed transpired solar collectors. *Solar Energy,* 91**,** 297-315.

LI, X., ZHIFENG, W., GUOFENG, Y., XING, L. & YI, R. 2012. A new dynamic test method for thermal performance of all-glass evacuated solar air collectors. *Solar Energy,* 86**,** 1222-1231.

LI, Y. W., WANG, R. Z., WU, J. Y. & XU, Y. X. 2007. Experimental performance analysis on a direct-expansion solar-assisted heat pump water heater. *Applied Thermal Engineering,* 27**,** 2858-2868.

LI, Z., CHEN, C., LUO, H., ZHANG, Y. & XUE, Y. 2010. All-glass vacuum tube collector heat transfer model used in forced-circulation solar water heating system. *Solar Energy,* 84**,** 1413-1421.

LIU, W., DAVIDSON, J. & MANTELL, S. 2000a. Thermal Analysis of Polymer Heat Exchangers for Solar Water Heating: A Case Study. *Journal of Solar Energy Engineering,* 122**,** 84-91.

LIU, W., DAVIDSON, J. & MANTELL, S. 2000b. Thermal analysis of polymer heat exchangers for solar water heating: A case study. *Journal of Solar Energy Engineering, Transactions of the ASME,* 122**,** 84-91.

LJILJANA, T. K. & ZORAN, T. P. Optimal position of flat plate reflectors of solar thermal collector. *Energy & Buildings,* 45**,** 161-168.

MAATOUK, K. & SHIGENAO, M. Theoretical approach of a flat-plate solar collector taking into account the absorption and emission within glass cover layer. *Solar Energy,* 80**,** 787-794.

MAMMOLI, A., VOROBIEFF, P., BARSUN, H. & BURNETT, R. Design guidelines for a robust and reliable solar thermal heating and cooling system. *In:* VILLACAMPA ESTEVE, Y., BREBBIA, C. A. & MAMMOLI, A. A., eds., 2011. Southampton, WIT Press, 3-12.

MANN, P., GAHAGAN, L. & GORDON, M. B. 2005. Tectonic setting of the world's giant oil and gas fields. *AAPG Memoir***,** 15-105.

MATRAWY, K. K. & FARKAS, I. 1997. Comparison study for three types of solar collectors for water heating. *Energy Conversion and Management,* 38**,** 861-869.

MATUSKA, T. & SOUREK, B. 2006. Façade solar collectors. *Solar Energy,* 80**,** 1443-1452.

MCADAMS, W. H. 1954. *Heat Transmission,* New York, McGraw-Hill.

MEDVED, S., ARKAR, C. & ČERNE, B. 2003. A large-panel unglazed roof-integrated liquid solar collector—energy and economic evaluation. *Solar Energy,* 75**,** 455-467.

MEDVED, S., JERSIN, K., ARKAR, C. & NOVAK, P. 1994. New solutions for a wider use of solar energy. *Energija i zastita okolisa,* 1**,** 389-395.

MIGUEL, B. & JOHANE, B. A dimensionless model for the outlet temperature of a nonisothermal flat plate solar collector for air heating. *Solar Energy,* 86**,** 647-653.

MING, Y., PENGSU, W., XUDONG, Y. & MING, S. 2012. Experimental analysis on thermal performance of a solar air collector with a single pass. *Building and Environment,* 56**,** 361-369.

MONDOL, J. D., SMYTH, M. & ZACHAROPOULOS, A. 2011. Experimental characterisation of a novel heat exchanger for a solar hot water application under indoor and outdoor conditions. *Renewable Energy,* 36**,** 1766-1779.

MONDOL, J. D., ZACHAROPOULOS, A. & SMYTH, M. A State-of-the-Art Solar Simulation Facility for Multidisciplinary Research on Sustainable Technologies. *In:* SAYIGH, A. A. M., ed., 2010. Brighton, WREC, 195.

MORRISON, G. L. & BRAUN, J. E. 1985. System modeling and operation characteristics of thermosyphon solar water heaters. *Solar Energy,* 34**,** 389-405.

MOTAHAR, S. & ALEMRAJABI, A. A. 2010. An analysis of unglazed transpired solar collectors based on exergetic performance criteria. *International Journal of Thermodynamics,* 13**,** 153-160.

MUMMA, S. A. 2011. Over Thirty Years of Experience with Solar Thermal Water Heating. *ASHRAE Transactions,* 117**,** 57-63.

MYRNA DAYAN, S. K., WILLIAM BECKMAN. 2000. *Analysis of Serpentine Collectors in Low Flow Systems* [Online]. Madison: University of Wisconsin-Madison. Available: http://www.geocities.ws/myrna_dayan/AsesCollector.pdf.

NEA & OECD 2010. Projected Costs of Generating Electricity 2010.

NWS. 2013. *The Relationship Between Length of Day and Temperature* [Online]. National Weather Service. Available: http://www.weather.gov/cle/Seasons [Accessed 04 April 2013.

O'BRIEN-BERNINI, F. C. & MCGOWAN, J. G. 1984. Performance modeling of non-metallic flat plate solar collectors. *Solar Energy,* 33**,** 305-319.

ONG, K. S. 1974. A finite-difference method to evaluate the thermal performance of a solar water heater. *Solar Energy,* 16**,** 137-147.

ONG, K. S. 1976. An improved computer program for the thermal performance of a solar water heater. *Solar Energy,* 18**,** 183-191.

ONG, K. S. 1995. Thermal performance of solar air heaters: Mathematical model and solution procedure. *Solar Energy,* 55**,** 93-109.

OPEC 2013. OPEC Basket Price.

OSTWALD, W. 1907. The modern Theory of Energetics. *Monist,* 17**,** 481-515.

PALMERO-MARRERO, A. I. & OLIVEIRA, A. C. 2006. Evaluation of a solar thermal system using building louvre shading devices. *Solar Energy,* 80**,** 545-554.

QUASCHNING, V. 2004. Solar thermal water heating. *Renewable Energy World***,** 95 - 99.

RAUPACH, M. R., CANADELL, J. G., MARLAND, G., CIAIS, P., LE QUÉRÉ, C., KLEPPER, G. & FIELD, C. B. 2007. Global and regional drivers of accelerating CO 2 emissions. *Proceedings of the National Academy of Sciences of the United States of America,* 104**,** 10288-10293.

REHIM, Z. S. A. 1998. A new design of solar water heater. *Proceedings of the Indian Academy of Sciences: Chemical Sciences,* 110**,** 373-384.

REN21 2012. Renewables 2012 Global Status Report. Paris: REN21 Secretariat: Renewable Energy Policy Network for the 21st Century.

REYNOLDS, T. S. 2002. *Stronger Than a Hundred Men: A History of the Vertical Water Wheel*, Johns Hopkins University Press.

RIFFAT, S. B. & ZHAO, X. 2004. A novel hybrid heat-pipe solar collector/CHP system—Part II: theoretical and experimental investigations. *Renewable Energy,* 29**,** 1965-1990.

RISTINEN, R. A. & KRAUSHAAR, J. J. 2006. *Energy and the Environment*, Wiley.

RITTIDECH, S. & WANNAPAKNE, S. Experimental study of the performance of a solar collector by closed-end oscillating heat pipe (CEOHP). *Applied Thermal Engineering,* 27**,** 1978-1985.

ROBERTS, D. E. & FORBES, A. 2012. An analytical expression for the instantaneous efficiency of a flat plate solar water heater and the influence of absorber plate absorptance and emittance. *Solar Energy,* 86**,** 1416-1427.

ROMMEL, M. & MOOCK, W. 1997. Collector efficiency factor F' for absorbers with rectangular fluid ducts contacting the entire surface. *Solar Energy,* 60**,** 199-207.

RONNELID, M. & KARLSSON, B. 1999. THE USE OF CORRUGATED BOOSTER REFLECTORS FOR SOLAR COLLECTOR FIELDS. *SOLAR ENERGY -PHOENIX ARIZONA THEN NEW YORK-,* 65**,** 343-351.

RÖNNELID, M. & KARLSSON, B. 1999. THE USE OF CORRUGATED BOOSTER REFLECTORS FOR SOLAR COLLECTOR FIELDS. *Solar Energy,* 65**,** 343-351.

SANTAMOURIS, M. 2003. *Solar thermal technologies for buildings : the state of the art*, London : James & James, c2003.

SHAOBO, H., ZHANG, Z., HUANG, Z. & XIE, A. 2008. Performance optimization of solar multi-stage flash desalination process using Pinch technology. *Desalination,* 220**,** 524-530.

SHATAT, M., WORALL, M. & RIFFAT, S. 2013. Opportunities for solar water desalination worldwide: Review. *Sustainable Cities and Society,* 9**,** 67-80.

SMYTH, M., EAMES, P. C. & NORTON, B. 2006. Integrated collector storage solar water heaters. *Renewable and Sustainable Energy Reviews,* 10**,** 503-538.

SMYTH, M., MCGARRIGLE, P., EAMES, P. C. & NORTON, B. Experimental comparison of alternative convection suppression arrangements for concentrating integral collector storage solar water heaters. *Solar Energy,* 78**,** 223-233.

SMYTH, M., MCGARRIGLE, P., EAMES, P. C. & NORTON, B. 2005. Experimental comparison of alternative convection suppression arrangements for concentrating integral collector storage solar water heaters. *Solar Energy,* 78**,** 223-233.

SOKOLOV, M. & VAXMAN, M. 1983. Analysis of an integral compact solar water heater. *Solar Energy,* 30**,** 237-246.

SONNENENERGIE, D. G. F. 2005. *Planning and Installing Solar Thermal Systems: A Guide for Installers, Architects, and Engineers*, Earthscan.

SOPIAN, K., ZULKIFLI, R., SAHARI, J. & OTHMAN, M. Y. Thermal performance of thermoplastic natural rubber solar collector. *Journal of Materials Processing Tech.,* 123**,** 179-184.

SOPIAN, K., ZULKIFLI, R., SAHARI, J. & OTHMAN, M. Y. 2002. Thermal performance of thermoplastic natural rubber solar collector. *Journal of Materials Processing Technology,* 123**,** 179-184.

STERLING, S. J. & COLLINS, M. R. 2012. Feasibility analysis of an indirect heat pump assisted solar domestic hot water system. *Applied Energy,* 93**,** 11-17.

STOJANOVIĆ, B. & AKANDER, J. 2010. Build-up and long-term performance test of a full-scale solar-assisted heat pump system for residential heating in Nordic climatic conditions. *Applied Thermal Engineering,* 30**,** 188-195.

STOJANOVIĆ, B., HALLBERG, D. & AKANDER, J. A steady state thermal duct model derived by fin-theory approach and applied on an unglazed solar collector. *Solar Energy,* 84**,** 1838-1851.

STOJANOVIĆ, B., HALLBERG, D. & AKANDER, J. 2010. A steady state thermal duct model derived by fin-theory approach and applied on an unglazed solar collector. *Solar Energy,* 84**,** 1838-1851.

SWEET, M. L. & MCLESKEY JR, J. T. 2012. Numerical simulation of underground Seasonal Solar Thermal Energy Storage (SSTES) for a single family dwelling using TRNSYS. *Solar Energy,* 86**,** 289-300.

TANAKA, H. 2011. Theoretical Analysis of Solar Thermal Collector with a Flat Plate Bottom Booster Reflector. *Energy Science & Technology,* 2**,** 26-34.

TANISHITA, I. 1970. *Present situation of commercial solar water heaters in Japan*, ISES.

TERZIOTTI, L. T., SWEET, M. L. & MCLESKEY JR, J. T. 2012. Modeling seasonal solar thermal energy storage in a large urban residential building using TRNSYS 16. *Energy and Buildings,* 45**,** 28-31.

TIAN, Y. & ZHAO, C. Y. 2013. A review of solar collectors and thermal energy storage in solar thermal applications. *Applied Energy,* 104**,** 538-553.

TODOROV, T. K., TANG, J., BAG, S., GUNAWAN, O., GOKMEN, T., ZHU, Y. & MITZI, D. B. 2013. Beyond 11% Efficiency: Characteristics of State-of-the-Art Cu2ZnSn(S,Se)4 Solar Cells. *Advanced Energy Materials,* 3**,** 34.

TOORAJ, Y., FARZAD, V., EHSAN, S. & SIRUS, Z. 2012. An experimental investigation on the effect of Al2O3–H2O nanofluid on the efficiency of flat-plate solar collectors. *Renewable Energy,* 39**,** 293-298.

TREUT, L., H., R. S., CUBASCH, U., DING, Y., MAURITZEN, C., MOKSSIT, A., PETERSON, T. & PRATHER, M. 2007. Historical Overview of Climate Change. *In:* SOLOMON, S., QIN, D., MANNING, M., CHEN, Z., MARQUIS, M., AVERYT, K. B., TIGNOR, M. & MILLER, H. L. (eds.) *Climate Change 2007: The Physical Science Basis. Contribution of Working Group I to the Fourth Assessment Report of the Intergovernmental Panel on Climate Change.* Cambridge, United Kingdom and New York, NY, USA.

TRIPANAGNOSTOPOULOS, Y., SOULIOTIS, M. & NOUSIA, T. 2000. Solar collectors with colored absorbers. *Solar Energy,* 68**,** 343-356.

TSILINGIRIS, P. T. Back absorbing parallel plate polymer absorbers in solar collector design. *Energy Conversion and Management,* 43**,** 135-150.

VERMASS, W. 1998. An Introduction to Photosynthesis and Its Applications. *The World & I,* March 1998**,** 158 - 165.

VIDAL, J. 2012. Rare minerals dearth threatens global renewables industry. *The Guardian*, 27 January 2012.

VIGNAROOBAN, K., XU, X., ARVAY, A., HSU, K. & KANNAN, A. M. 2015. Heat transfer fluids for concentrating solar power systems – A review. *Applied Energy,* 146**,** 383-396.

VIKRAM, D., KAUSHIK, S., PRASHANTH, V. & NALLUSAMY, N. ISEC2006-99090 An Improvement in the Solar Water Heating Systems by Thermal Storage Using Phase Change Materials. 2006. New York, ASME, 409-416.

VIOREL, B. 2007. Optimal control of flow in solar collectors for maximum exergy extraction. *International Journal of Heat and Mass Transfer,* 50**,** 4311-4322.

WAHIDABANU, R. S. D. & RAJAN, J. 2012. Solar Thermal Power Plant (Combined plant of solar thermal power and gas plant). *Golden Research Thoughts,* 1**,** 1-7.

WANG, H., QI, C., WANG, E. & ZHAO, J. 2009. A case study of underground thermal storage in a solar-ground coupled heat pump system for residential buildings. *Renewable Energy,* 34**,** 307-314.

WANG, Z., DUAN, Z., ZHAO, X. & CHEN, M. 2012. Dynamic performance of a façade-based solar loop heat pipe water heating system. *Solar Energy,* 86**,** 1632-1647.

WAZWAZ, A., SALMI, J., HALLAK, H. & BES, R. Solar thermal performance of a nickel-pigmented aluminium oxide selective absorber. *Renewable Energy,* 27**,** 277-292.

WCA 2013. Coal Use & the Environment.

WEISS, W. & MAHTHNER, F. 2012. Solar Heat Worldwide: Markets and Contribution to the Energy Supply 2010. *IEA Solar Heating & Cooling Programme.* Gleisdorf, Austria: AEE Institute for Sustainable Technologies.

WEISS, W. & MAUTHNER, F. 2012. Solar Heat Worldwide. *In:* PROGRAMME, I. S. H. C. (ed.). Gleisdorf, Austria: AEE Institute for Sustainable Technologies.

XI, H., LUO, L. & FRAISSE, G. 2007. Development and applications of solar-based thermoelectric technologies. *Renewable and Sustainable Energy Reviews,* 11**,** 923-936.

XU, G., ZHANG, X. & DENG, S. 2011. Experimental study on the operating characteristics of a novel low-concentrating solar photovoltaic/thermal integrated heat pump water heating system. *Applied Thermal Engineering,* 31**,** 3689-3695.

YADAV, A. S. & BHAGORIA, J. L. Heat transfer and fluid flow analysis of solar air heater: A review of CFD approach. *Renewable and Sustainable Energy Reviews,* 23**,** 60.

YADAV, A. S. & BHAGORIA, J. L. 2013. Heat transfer and fluid flow analysis of solar air heater: A review of CFD approach. *Renewable and Sustainable Energy Reviews,* 23**,** 60-79.

ZHANG, H.-F. & LAVAN, Z. 1985. Thermal performance of a serpentine absorber plate. *Solar Energy,* 34**,** 175-177.

ZHIYONG, L., CHAO, C., HAILIANG, L., YE, Z. & YANING, X. All-glass vacuum tube collector heat transfer model used in forced-circulation solar water heating system. *Solar Energy,* 84**,** 1413-1421.